



HAL
open science

Wavefront sensing in the longwave infrared using thin scattering media

Anwesh Bhattacharya

► **To cite this version:**

Anwesh Bhattacharya. Wavefront sensing in the longwave infrared using thin scattering media. Signal and Image Processing. Université Paris sciences et lettres, 2023. English. NNT : 2023UPSLS035 . tel-04452742

HAL Id: tel-04452742

<https://pastel.hal.science/tel-04452742v1>

Submitted on 12 Feb 2024

HAL is a multi-disciplinary open access archive for the deposit and dissemination of scientific research documents, whether they are published or not. The documents may come from teaching and research institutions in France or abroad, or from public or private research centers.

L'archive ouverte pluridisciplinaire **HAL**, est destinée au dépôt et à la diffusion de documents scientifiques de niveau recherche, publiés ou non, émanant des établissements d'enseignement et de recherche français ou étrangers, des laboratoires publics ou privés.



THÈSE DE DOCTORAT
DE L'UNIVERSITÉ PSL

Préparée à l'École Supérieure de Physique
et de Chimie Industrielles de la ville de Paris

**Wavefront sensing in the longwave infrared
using thin scattering media**

**Détection de front d'onde dans l'infrarouge
à l'aide de diffuseurs minces**

Defended by

Anwesh Bhattacharya

July 11, 2023

Doctoral School n°564

**Ecole Doctorale Physique
en Ile-de-France**

Speciality

Physics

Prepared at

Institut Langevin, ESPCI-PSL Paris

Jury:

Alexandra FRAGOLA ISMO, Université Paris Saclay	Présidente de jury
Aurélien BRUYANT L2n, Université de Technologie de Troyes	<i>Rapporteur</i>
Michel KAZAN Dept. of Physics, American University of Beirut	<i>Rapporteur</i>
Florian FORMANEK HORIBA Jobin Yvon	<i>Examineur</i>
Yannick DE WILDE Institut Langevin, ESPCI-PSL Paris	<i>Directeur de thèse</i>
Gilles TESSIER Institut de la Vision, Sorbonne Université, Paris	<i>Co-directeur</i>

For

Baba

Maa

Bonu

Dedicated to

All the working and oppressed peoples of this world!

Acknowledgments

A doctoral thesis is an attempt at pushing the collective boundaries of human knowledge, and if I have succeeded in doing so to a minuscule degree, I owe it solely to the giants who have propped me up and let me take a peek at the smooth pebbles and beautiful shells lying in front of the great ocean of truth, which lies all but discovered before us. In this doctoral sojourn, I have been graced by the immense generosity and warmth of extremely talented, smart and compassionate humans, all of whom can rightfully partake in the achievements on this avenue, for without their hands holding on to mine, I might have faltered much earlier on this marathon of a journey. I express my sincerest gratitude to each one of my benefactors for always having had my back, and for their intricate presence in this odyssey, in ways which might even be unbeknownst to me.

The rough outline of this PhD project was born about four years ago at Institut Langevin, and I want to begin by thanking my doctoral mentor Yannick De Wilde, for shaping an ambitious doctoral topic marrying speckle physics to infrared physics that immediately piqued my interest when I chanced upon it. My first meeting with Yannick in the fall of 2018 to discuss the doctoral project introduced me to the richness of infrared physics, as well as to a mentor who invested his time wholeheartedly into his students' projects. From that day till now, he has continually kept abreast of the goings on in the thesis, and shared his precious time, even after assuming the directorship of the laboratory. I have been fortunate to have learnt from him numerous experimental tips, ambitious and sometimes quirky ideas of exploring experimentally the infrared world to develop our intuition and knowledge, become much more proficient at troubleshooting in the laboratory, and experienced the rigour and dedication that is necessary to carry out world-class research. His childlike enthusiasm inspired us to remain ever curious, in science and beyond. Being a talented artist himself, I admired his paintings every time I visited his office, and I cherish the good humour we shared during these past three years feeding birds, discovering great art and culture, and sharing ideas for youthful travel follies. I am glad to have finished my doctoral studies working with someone who we jovially refer to as our 'academic father' in the sub-wavelength physics group at Institut Langevin. Alongside Yannick as my thesis director, I was lucky again to have found a co-director in Gilles Tessier, whose sharp physics acumen and radiant positivity, encouraged me to keep working and not despair, particularly when the going got tougher. My first memory of Gilles remains etched clearly in my mind's eye as if it happened just yesterday, when Gilles refrained from asking me additional questions for a second time in my PhD interview, by highlighting that I had already mentioned in my presentation that I considered him a collaborator in the project. Gilles' simplicity, uplifting positivity and an acute eye for going straight to the heart of a problem were crucial in reaching

the culmination of this thesis, and I remain in his debt forever for his mentorship and kindness. In hindsight, I believe that amidst many of the challenges surrounding the thesis, Yannick and Gilles' presence and stewardship ensured its successful culmination, with the limitations being entirely mine, of course! Merci beaucoup to my two *gurus* :)

I would like to thank Pascal Berto, who was one of the most critical collaborators in this project, who treated it as his own and gave me his incredible support throughout my thesis; without you, Pascal, it would have been unthinkable to have achieved what we have, and I hope to see this thrive in myriad ways in the future as well. Pascal's willingness to go into the nitty-gritties of the experimental work, and our mutual wrangling to arrive at a tenable solution remain some of the most informative research lessons in my thesis, and I surely benefitted from his keen insight and abundant feedback in my work. I also benefitted from the support of Tengfei Wu, whose timely insights at critical junctures of my thesis kept my focus aligned at those phases when multiple experiments still do not lead to conclusive conclusions. His humour and goodwill and suggestions of restaurants and research groups in the same breath are well-remembered! I am deeply indebted to Valentina Krachmalnicoff and Ignacio Izeddin for their early feedback on regular project discussions, being instrumental in defining the project and helping me train on building a visible speckle imaging setup, and for being readily available to discuss my many questions while managing their busy schedules. Ignacio also graciously accepted to step down from my thesis jury to aid in its organization, and I am humbled in the presence of such kind researchers, who have shown me the humane-ness still extant in academia. I am grateful to Marc Guillon, member of my thesis tracking committee, for his nuanced insights into my doctoral project and for his experiential advice on my thesis work. The other member of my Comité de Suivi, Remi Carminati, ensured my academic upbringing in the field of waves in complex media - through his courses, a wonderfully written book on the broad field of light scattering and transport, and other valuable literature that he made me abreast of. His insights into the theoretical aspect of my work was rich, and I benefitted immensely from his stellar scholarship and research in this field, which he proffered during the thesis meetings, in his office amidst his brimming schedule, and many times impromptu on the corridors or coffee machine of Institut Langevin. His suggestion of analytically treating the transmission of light through our scattering medium based on an early seminal paper of his is an interesting work that I envisage to carry out in the future.

I am thankful to the members of my thesis jury for having kindly accepted to read my thesis and adjudicate the thesis defence, at a relatively short notice - the chairperson of the journey Alexandra Fragola, the reviewers of my thesis Michel Kazan and Aurélien Bruyant, and the examiner Florian Formanek. I am glad to have had the opportunity to present my thesis to them and field interesting questions on my work, many of which have given rise to new questions and ideas, and for having pronounced me successful in the thesis defence which very nicely rounded out these nerve-wracking years of learning, experimenting and getting results in a novel yet challenging topic, rife with possibilities for applications. I would like to especially

thank the head of the EDPIF doctoral school, Frederic Chevy, for having facilitated an easy navigation of the cumbersome process of my thesis defence organization, by accommodating my many constraints for my benefit. Having had the good fortune to have worked in his group at LKB, Paris for my Masters dissertation, I had known him already as a brilliant physicist and kind human, and my interactions with him in this official capacity reinforced those notions. I am also in the debt of Suzanne Rera of the ESPCI's doctoral student office who aided me in organizing the thesis defence, being always willing to provide cogent information to get things moving as quickly as possible, sometimes even quicker than what is considered normal. Without such kindness and graciousness in helping me out of their ways, I would have had a much more difficult time defending my thesis - considering that it is already not an easy task to do so in the first place.

Over the course of my doctoral studies, I have been incessantly entertained and helped by the amazing secretaries at Institut Langevin - Christelle, Nathalie, Catherine, Anne-Sophie, and Loïc in furnishing mission orders, purchase slips and other such administrative tasks (which have already become much smoother due to Romain Pierrat's development of the Jetlag application), by David in everything related to IT, by Emmanuel in his versatile Superman-like role in the lab and for offering me to be the lab's Santa Claus at Christmas luncheons, by Jean-Marie on many experimental aspects of my PhD and on safety issues while also introducing me to Manga, and by Christian as well. I am indebted to Abdel from IPGP as well, who never denied any request for help during these past years in the machine shop, even as he was not bound to aid non-IPGP researchers. I have also been fortunate to have been aided in many administrative aspects by the wonderful UPtoParis team - Rositsa, Virginie, Alexandra and Lucie - who always had a smile on their faces whenever (and it was many times) I had any questions regarding official French government paperwork and the like.

I have been blessed to have completed my PhD at the Institut Langevin, which is not only a leading research lab in the field of wave physics, but which is also incidentally the point of genesis of many of the key developments in the field of wave transmission through complex media. I would especially like to thank Arnaud Tourin, the director of the lab for the greater part of my stay there, as well as the renowned researchers spanning many generations, for creating such a conducive atmosphere for the exchange of scientific ideas that serves as a great hub of learning for students through the regular seminars, lab conferences and poster sessions, and fostering scientific dialogue in the daily lab routine. Much as I have gained from the scientific exchanges at the lab, I have equally (if not more) cherished the conviviality of every member of the lab who did not let even a day go by without some joyful occurrence. There comes a time when everyone declares how they have enjoyed their stay in the best PhD students' office in the lab, but in my case, I have to acquiesce that it is true indeed - for nothing can beat the camaraderie of the R31 office. It is my good fortune in life to have had the pleasure of sharing this incredible office space with stalwarts like Joris, Jules, Paul, Maxime, Julie, Slava, Kamel, Antoine, Chloë, Alexandre, Yao, Serena, Francois, Jad, and Ahmed - the countless memories we have created

remain permanently etched in my heart, as also my huge digital photo-repository. While my office was full of revolutionary fervour and peppered with moments of frolic everyday, I was equally excited to be working in the R63 lab due to the humour and warmth that emanated from that place (in spite of the ACs being on full blast during thermal experiments). From my first visit to the lab to working for the past years with Joris, Loubnan, Patricia, Serena, Sylvio, Victor, Clémence, Guillaume, Claire, Laure, Ismael and Hugo, I have enjoyed the presence of such cool researchers as them every single day of my stay here, sometimes working till late nights followed by the not infrequent trips to Les Arenes afterwards.

Having had the privilege of being friends with most of the members of Institut Langevin, I have nevertheless soothed the occasional (or not quite so!) bitterness of a doctoral day gone awry by immersing myself with people like Camilo - who was the first person from IL I became friends with, Loubnan - with whom I shared almost my entire PhD journey and consider now as family, Samer - who was 'jokingly' my unofficial supervisor for my thesis, Guyu - whose soothing voice and green teas brought much calm and respite amidst chaos, Yamil - whose solution for any question would be to 'take two bottles of wine', and Deboleena - during our daily afternoon coffee breaks badgering away in Bengali. I still feel excited thinking about plans that we would make with the IL Foreign Legion - Bart, Margoth, Kevin, Nariaki, Clement, the happening Salsa sessions with Samuel, Max, Claudia, Houssam, Daniel, the diverse conversations with Jana and Yao, attending pension reform protests and discussing socialism with Dimitri, learning the French language and *verlan* with Romain, Jeanne, Matthieu, Noet, and Jerome (je suis dead!). The many trips to sushi buffet restaurants and bars along Rue Mouffetard with the full cohort of international students of our doctoral programme UPtoParis are events that I crave often; it was so commonplace back then that the rarity of those moments is now being adequately felt. I have to confess that being friends with such a diverse bunch of talented folk opened the doors for me to much of the world's local cultures from where each of them were, and at whose thesis defences I was able to sample local delicacies from their home countries, experienced the diverse forms of music and dance, and learnt their vernacular slang. I am aware that I cannot list every single person with whom I have vibrant memories at IL, primarily due to the lack of space, but rest assured that they remain well-kept in my cherished memoria, and each of whom remains safe in the cockles of my heart.

I consider it my great privilege to have carried out my doctoral studies in Paris, widely touted as the world's cultural hub. I came to Paris for love, following my dear friend Nandz, for the first time in 2018 when I carried out my Masters dissertation at LKB. The city of love then swept over me, and with the aid of friends like Nandz, who encouraged me to apply for this PhD project even when faced with a conflict of interest, and Subha, a fellow IISERite and UPtoParis student who helped me prepare my UPtoParis interview presentation, my childhood dream of visiting the workplace of venerated Maria Sklodowska Curie turned into a reality. Not only was I going to be a Marie Curie fellow working at ESPCI, but I found out after a few days at IL that my office was next to the small laboratory where Marie Pierre Curie carried out their research

on radioactivity for several years. I had the rare opportunity of living such a dream, which also brought other challenges that required dodgy perseverance and dogged determination to reach the finishing line.

My sanity (or insanity) over these years was kept in check by the many loving families and friends I am proud to have known over the course of my PhD. I have to begin with the people who brought me home from the CDG airport the day I arrived in Paris in the fall of 2019 to begin my PhD. Firstly, Nandu, who I have known ever since I made a telephone call before joining IISER Pune to ask about what utensils to bring to college, for whom I came to Paris and then fortunately stayed on during both our PhDs, I give my warmth and love. From together honing academic applications to bring talented folks for their international education, to exploring the streets of Rueil-Malmaison over long walks and chats, to regularly discussing academics and research challenges, I believe that the journey that began from Pune and continued in Paris with Nandz, will hopefully take us to a place anew and until we meet then, you have my love! Thanks are due to my dear friend Rutuja, who came to the airport with a note mentioning 'from Mr. to Dr. Anwesh', and truly, without her presence along the way, it would have been much tougher to tread on this journey. While to the world outside, she was an acclaimed process engineer and business administrator, I was blessed to have seen how she could whip up delectable dishes in a jiffy while talking to Neha Aunty and Uncle, who shared with me night time readings of Charlie Brown comics so that we would sleep happy irrespective of the day's travails, and our impromptu singing and dancing parades in the middle of household chores. As I was begin to settle down into my doctoral work gradually, the SARS CoV 2 struck. It is unthinkable to imagine the way our mood was always bubbly even in the first two months of absolute lockdown in France, if not for the joy we all shared in our confined *Rueil Parivaar*. From dancing with our cute toddler neighbours Sonia and Mariam, to binge-watching movies together, I am thankful that I shared the confinement with Nandu, Rutuja, Pooja and Vaibhav - my classmate from IISER Pune who doubled up here as our European Outreach coordinator, and who should soon become Dr. Ingale in a few days at Brest, France. Travelling beyond the perimeters of Rueil-Malmaison, I was glad to have been able to share my home in Nanterre during the later half of my PhD with Pooja and Nidhi. Having met Pooja when she was a fellow undergraduate at India's prestigious space institute, I have been fortunate to have learnt so much from her, and shared such joyous moments over the course of my PhD, and it absolutely gladdens me to write here how just before my thesis defence, the news of her selection as a Marie Curie doctoral fellow in Artificial Intelligence (AI) research at Copenhagen, brought joy to my heart and emboldened me to defend with more conviction than earlier. Nidhi, on the other hand, has risen high above her modest roots and has shone like such an ace that there is a shortage of laurels and accolades to bestow on her. The exhilarating inspiration that I have regularly been fortunate to have witnessed by being in the midst of such talented people has helped me grow, while also acknowledging that no worthwhile feat is achieved without sacrifices and challenges. Amidst all the trials and tribulations of our Parisian lives, our home was peppered with thoughtful birthday celebrations, countless gastronomic experiments that mostly

turned out successful, and soaking up the photographic memories of numerous small trips we made across France. Our beloved junior from IISER Pune also deserves special mention for being the uncomplaining dishwasher at home, relieving me from my duties after a yearlong stint in the greywaters. I could not have wished for better companions to live with during my stay in Paris, and to each of them I pay my gratitude.

Few people are blessed with a felicitous life during their stay abroad where they can count on childhood friends to carry on the jolly good humour of youth even when living far away. I have been opportune enough to have such accomplished childhood friends who also came to Paris around the same time as me, and together we rediscovered our evening Thunder hangouts while gazing at the city of lights. Pranjali came to pick me up at the airport in Paris, and again came back all the way from Barcelona for my thesis defence, rounding out his role in my PhD. Thanks to Shaoni who first dreamt of coming to Paris for a day back in 2017, which spurred my earlier trip to Paris for my Masters thesis work, and who invited me to nice homecooked meals at her artsy studio followed by long candid afternoon or evening chats. I am at a loss for words to highlight how intricately linked my dear friend Shubham's journey was to mine, and for whom immense love wells in me even now as I just reminisce the great times we spent together (and which we shall share again soon)! From me bringing Shubham home his first day in Paris, to him graduating with a Masters in AI from Centrale Supélec, to his attending my thesis defence live while being on Zoom meetings back at his workplace at Barcelona, I have known what it is to be truly cared for by a friend. Even if time was sometimes against us, Shubham and his equally beautiful and kind partner Jiya ensured that my birthdays were celebrated well, that we partied and danced together, and also lazed around after being full from Chef Bissu's cooked meals on gloomy afternoons. Thank you mates for being there for me far away from home, ensuring that none of us truly felt the absence of that which was 8000 kilometres away!

I have also been lucky in having become friends with such lovely, kind, witty, and sharp people for the first time in Paris as Gentle - who taught me how to handle lasers, Yash Bhatiji lives on ji - our dearest eternal friend who never shied away from making me happy with his guitar and movie suggestions (and whose Fellini on Fellini book remains a veritable treasure of him on my bookshelf) as well as hosting parties with Amritansh at the drop of a hat, Ayush - who gracefully shared with me his home and grocery stocks, Setsen - who brought context to my nickname of 'Tatar' and who fed me milk tea with salt during our many cultural expeditions and long conversations (I await the launch of Scientific Mongolian sooner rather than later!), Pulkit - who I have now known for about a decade and who still takes care of many things for me in Paris, and whose house parties are the most lit ones I have been to, as Souradeep and Nirmal at IPGP who were kind enough to share their offices with me and both of whom are in the process now of soon becoming Drs. themselves, the entire Indian Alliance Paris group that emerged out of spontaneous political demonstrations against developments in India (including but not limited to Saurabh, Manuj, Ritam, Sagnik, Abhishek) for keeping me sane in trying political times, and for sharpening my political education at the whetstones of Global South radical literature

by introducing me to The People's Forum of New York, and the unique potpourri of friendships created at the CIUP campus which will last beyond my stay in Paris. Thanks are due to Rasika "madam" as well, who ensured that I could stay in one of the best student residences in Paris - the CIUP - during the first few months of my PhD at the Korean House. My deepest thanks are also due to the many families who have taken care of me and brought humour into my life when there was very little - the entire Bengali Pujo *poribaar* which I dearly miss now, comprising of Ruby Mashi, Bithi Mashi, Shipra Mashi, Jhumu Mashi, Pabitra da Debasmita di, Arun da Moumita di, Avigyan da Atreyee di, Satadru da Arpita di, Shameek da Soumi di, Rohan da Soumi di, Dr. Atreya Tista, Bulti, Oindrila, and Anambar - who were always punctual in our weekend feasts of Bengali fare (*maach, mangsho*) and with whom theatre rehearsals for Durga Puja in Paris were invariably snacking rehearsals in practice, to Rajesh bhaiyya Radhika di who fed me pasta the very first weekend of my stay in Paris and who were always available for guidance on life in France, to Rahul bhaiyya Simar di for their calming presence, extremely filling lipsmacking food, and for regaling us with funny and informative stories, to Amit Pandeyji Savitaji for their warm hospitality and sharing the mutual joy in organizing Bihar Foundation events, to Priyanka Kakima and Mrinal Kaku for their kind invitations to what would seem to me mini-Kharagpur get-togethers replete with delicious fares to sample - to each one of them, including the kids who coloured my palate merry - I owe my warmest affection and regards!

Even as IISER Pune has become my alma mater for a few years now, our network has grown all the more tightly knit and it has been my greatest pleasure to have stayed in Europe with many classmates and friends from my undergrad days. Danish has been my fellow doctoral traveller during her stay at IFPEN, Rueil-Malmaison, and having written two acknowledgments with her now, I am thankful for her lasting friendship that permeated the many weekend vacations I took at her and Tomin macha's place in Sevres, frolic and follies around Paris, feeling like being back home when Aunty visited and brought boxes of 'Rewari Barfi' for us, and the day long conversations on mundane things as well as chats about education and mental health that deeply enriched me. I hope that she enjoys all her endeavours until our theatre group opens up! The joy of meeting Raghuram for special events in Paris or St Remy les Chevreuse, of harking about old days with Surabhi at Institut Langevin - who has remained my labmate from IISERP till IL, of curiously wondering at astronomical discoveries with Tomin and then fighting about politics to watching Malayali movies together, taking a week-long break from thesis writing in the woods of Palaiseau with Amar, afternoon chats with Abhisikth on thesis writing, to Christmas break shenanigans with Mahendra, visiting Montpellier with Sarthak, touring non-chalantly the hidden gems of places in Lille with Anurag, Sravan and the entire Lille gang, enjoying the much-awaited visits of IISER family members like Dhriti's long stay in Paris when we hung out together and relived our days in Pune while also experiencing what Paris had to offer to paint our nostalgia greener, to the incessant visits of Sagnik to his second home in Paris except for when true necessity was thrown to the wind, to his sharing of musical classics - Paris never made me feel the need to let go of Pune, for it always 'seems like old times' with such old friends mingling about. The occasional visits from IISERP family members also brought back cheerful

memories of Pune and a chance to reconnect with the alma mater - thanks to Hari, Amrita, Sudha, Amogh and John for dropping by and cheering me up, not to forget the amazing food and culture we invariably added to our tasks during those meet-ups. I was fortunate to have hosted many old friends due to my being in Paris, and it is thanks to them that I know Paris as much as I do. And the same warmth and generosity was extended to me when I visited them - in Lyon at Amit Sahuji's lavish apartment looking down at the Saône, in Stanford at Dhriti's dorm room which she cleared out to host me and for chaperoning me on our trip to the Bay Area and San Francisco, in Miami at Mice's Spanish villa replete with tropical fans and during our long drives on American freeways down the Florida coast, in New York at Ajith Nair's NJ apartment where we also found Shrikhand after many years searching for it in Europe, to getting guided tours of NY at the leisure of friends like Sayantika and Uddipan (who I believe has now been repaid in kind during his visit to Paris for Durga Puja 2022), in wintry Berlin at Swarnshikha's (Tia) spacious yet warm apartment coupled with her witty banter and sloth-like approach to sightseeing - all of them made my trips so much more warm and exciting.

I am also indebted to friends like Vishal whose lipsmacking chicken recipes made Parisian winters *tres chaud*, to Kartikey for his affable presence and for taking me along to poetry evenings that resonated with me deeply at times when the joy and merriment needed to take a short break to allow some creativity to flow, to Arnab for his jolly good French, Rabindrasangeet and art along the Seine by the Jardin Tino Rossi in the last lap of my thesis writing, to Himanshu for his musical monologues and the pleasure of calm conversation and good food, Sambuddha (Shubho da) for hanging out with me in Paris inspite of my many detours and enroute conversations with friends, to Anwai for his delightful visits that brought hearty cheer to our faces and for clicking great photographs when in town, to Anwaar and Issam who were kind enough to share their time with Loubnan and touched me with their familial affection (and through whom I wish Sophie grows up well!), to old hags like Shubham, Suraj, Dimple, Shrunal and Mukul, who would be ever present to assuage my many procrastinatory periods and provided me with the nitro boost to continue writing my thesis and working along towards my defence, to Anambar for bringing additional colour to my merry life and for putting forbidden red ink on my forehead in jest, and to Upasika for her assurances and de-stressing conversations full of laughter during the last course of writing and for always being such a nice and kind accomplice to many dark crimes :P.

I am thankful to have been blessed with such dear companions as Anwasha who cared for me from afar, showered me with beautiful handmade presents, and whose presence, even from afar, soothed my frayed nerves and kept me sailing. On the other hand, I feel almost sinful in craving those days when I would go home to have lunch from the lab, prepared with love by Deepika, and not wanting to go back again. I am deeply grateful to her good sense that she ensured I was promptly kicked out to go work on my PhD first before evening plans could be drawn up again. I am deeply thankful for such amazing times in my life that made my stay in Paris worthwhile, made me a daily TGV traveller, and even brightened my beautiful trip to

Kerkyra and Athena in Greece.

A mention of my immense gratitude to all my dear friends who organized the *pot de these* on the day of my thesis defence without me having to worry about it all, seems appropriate here. Thanks to Pooja who single-handedly cooked many of the homemade dishes, to Ajay who did much of the shopping, to Nageshji for his aid in going drinks hunting, to Upasika for managing the entire organization, to Neha for being the IPGP liaison for all the tasks in setting up and wrapping up the pot, to Rounak who came all the way from Basel to peel potatoes for my thesis pot and brought delectable Swiss cheese alongside, to Ruby Mashri for preparing the *payesh* dessert that everyone licked off their plates, to Deboleena di for helping set things rolling and for enlisting Rita and the postdocs for their aid, to Himanshu for cleaning all the champagne glasses without complain, and to Naimisha for herself preparing an expertly crafted dessert cake especially for my thesis pot. After a taxing day presenting my thesis, it gave me great joy to see everyone enjoying the spread of Indian fare at the pot and all credit for it goes to my wonderful friends who put in the hard yards to make it happen. I want to especially single out and mention Sunil, who was constantly beside me the day of my defence, and who ensured that I could soundly defend my thesis even though I was delayed by traffic in reaching my own defence. I am eternally grateful at the many gifts I was presented by my friends and labmates - including a colourful speaker on which I keep playing music daily - even as I have to insist that the gift of their affectionate company over these years is beyond any material gift that I can ever receive. Thank you for making it an honour for me to stay amidst you folks, and complete my doctoral thesis!

Now that the time has come for this list to be wrapped up, as it invariably will, it makes me bittersweet to write about the people who have been behind me, whatever the situation, throughout the years of my doctoral studies, and much before and beyond. Even as my cousin brother Rounak was the only representative from my family who came all the way from Switzerland to grace my defence, my extended family has supported me all through my life, given me countless memories to cherish, and been reservoirs of love whenever I have needed to dip into one. My maternal grandmother *Didu* has always blessed our academic endeavours, even though she hasn't studied beyond elementary school, and her loving presence motivates us daily to try to do our best in whatever we do. Monima, Mama, Mami, and Diya have always been ready to regale me with conversations and photographs of tasty food and humorous memes during our weekly or biweekly video-calls, and all of them made it a point to attend my defence online. I should also thank Kaku for his contribution in my educational upbringing that has enriched me over the years, introducing me to Arundhati Roy's writings on India's working and oppressed people. I have also been blessed with the love and affection of my other families spread across places - Shiv Devi aunty at Gaya, Neetu didi, Jijaji, Sanchit and Veer, Tarun Uncle and Nandini Aunty, Gurudev Ghanshyam Gunwanti Babaji's perennial watch over me, Amarendra Bhaiyya and Pooja ki mummy, Sonu and Chintu at Haspura, the rocking Thunder families, Swati didi, Jethu and Jethi at Dhanbad, Anu aunty in Pune, Dr. and Mrs. Mathew who rest well beyond

Vishranti, Joy da and Ritika di in London, Harsh Bhaiyya and Alka di at Metz - all of their love and warmth has filled me to the brim.

I would have definitely loved for my own parents and sister to have been in Paris for my defence, but alas, we still reside in a neoliberal imperialist world ruled by capital where states are desperate to control the free movement of the world's united people. However, Baba, Ma and Bonu left no stone unturned in giving suggestions towards the preparation of my defence, even reducing their continual qualms about when I would fly back home, and sharing this important milestone in my academic journey glued to a broadcast screen at home. Over the almost three decades of my life till now, Baba has shown me the inherent importance and routine joys of carrying out research and it is in his footsteps that I have tried to tread in doing justice to this thesis, even though I am sure it is not even close. Being born when his thesis was being written, and also being named as a seeker of knowledge and truth, I believe that my impetus in carrying out a doctoral thesis has stemmed from all these years of immersion in academic culture. Ma, on the other hand, ensured that I had the necessary life skills to survive on this daunting journey far from home, and without fail checked on my well being regularly, all in the hope that I could work calmly but diligently. All of the good things that are in my character can be traced to their impeccable upbringing, while my imperfections are my own, despite their immaculate parenting. I am truly thankful to have been born to them, to have been taught by them as teachers of life and in studies, and to have come towards a major step in my academic journey under their watchful eyes. The happiness and joy in the family however emanates from our archaeologist and historian in training, Miss Nenikumari Shontu or also known as Bonu, without whom the joys of life would have diminished manifold. Even as I have missed her presence in Paris, the knowledge that there is someone taking care of all of us and who'll be there, no matter what happens, is a veritable blessing amidst the tribulations of life. To all of you, my family, goes my warmest love and Ghujumujus!

I would fall short in finishing the acknowledgments if I did not record my deep appreciation for everything that Neha Bawa has done for me, in a very short duration, but the crucial duration of the final phase of my thesis writing and my defence. Having known each other while working on both of our theses, I am glad to call her my joint pal, jointly lazing around the Seine on weekday evenings, sampling the few authentic Indian restaurants in Paris, to getting to know Montreuil again in all its working class glory. My fathomless affection lies with her for her ever calming and helpful presence in my life, and who ensured that I finished my work even when I was lax in doing so. Merci beaucoup for your companionship, and to you I say - Suka Cyka!

To all that is joyful in this world, and to all the revolutionary people striving for a more just world, I pay my greatest respects and lay myself down at the altar of humanity's advancement!

Abstract

Long wave infrared (LWIR) radiation between 7-14 μm allows passive imaging and is the fingerprint region for spectroscopy. Infrared (IR) imaging has wide-ranging applications in thermography, airborne atmospheric sensing, fault detection, and non-invasive medical testing. However, existing cameras are only sensitive to the amplitude, but not to the phase of IR radiation. The technique of speckle imaging enables the detection of phase or intensity through complex scattering media - at visible and IR wavelengths. We have developed a novel broadband LWIR speckle imaging configuration for wavefront sensing, utilizing a thin diffusive medium and an uncooled microbolometric camera. Taking advantage of the large angular memory effect of the diffuser, deformations in the speckle image can be ascribed to local variations in the phase of the impinging wavefront. The spatial shifts of the speckle grains in the images are registered using a rapid diffeomorphic image registration algorithm, generating a high-resolution mapping of the local phase gradients. The local phase gradients are then integrated in 2-D to reconstruct the wavefront profile. We have successfully demonstrated thermal wavefront reconstruction using LWIR speckle imaging in infrared optical samples, ranging from optical lenses to fabricated complex phase samples. The experimental setup and technique are characterized, keeping in mind its utility for promising future applications in imaging through visually non-transparent media like semiconductor wafers, engineered nano-electronic surfaces, and infrared optics.

Keywords: Phase imaging, Infrared imaging, Wavefront sensing, Complex media

Résumé

Le rayonnement infrarouge à ondes longues (LWIR), entre 7 et 14 μm , permet l'imagerie passive et constitue une gamme spectrale cruciale pour la spectroscopie. L'imagerie infrarouge (IR) a de nombreuses applications dans les domaines de la thermographie, de la détection aérienne et atmosphérique, de la détection des défauts et des tests médicaux non invasifs. Les motifs de tavelures, ou "speckle", permettent de détecter la phase ou l'intensité en utilisant des milieux diffusants complexes - aux longueurs d'onde visibles et infrarouges. Nous avons mis au point une nouvelle configuration d'imagerie du front d'onde, en utilisant un milieu diffusif mince et une caméra microbolométrique non refroidie travaillant dans la gamme LWIR. En exploitant le fort effet mémoire de diffuseurs minces, les déformations locales de la figure de speckle permettent de remonter à une information quantitative sur les gradients locaux de la phase optique. Ceux-ci sont ensuite intégrés en deux dimensions pour reconstruire le profil du front d'onde. Nous avons démontré avec succès la reconstruction d'un front d'onde LWIR dans des échantillons optiques infrarouges, allant de lentilles optiques et jusqu'à des échantillons de phase complexes. Le dispositif expérimental et la technique sont caractérisés, en gardant à l'esprit leur utilité pour des applications futures prometteuses dans l'imagerie à travers des milieux visuellement non transparents tels que les semi-conducteurs, les surfaces nano-électroniques et les optiques pour l'infrarouge.

Mots clés : Imagerie de phase, Imagerie infrarouge, Imagerie de front d'onde, Milieux complexes

Contents

1	Infrared imaging using scattering media	1
1.0.1	Infrared (IR) radiation	2
1.0.2	Long wave infrared (LWIR) radiation	3
1.0.3	Infrared imaging using complex media	4
1.0.4	Infrared wavefront sensing	6
1.0.5	Thesis outline	7
2	Speckle imaging for wavefront sensing	8
2.1	Phase imaging	9
2.1.1	Holography & interferometry	11
2.1.2	Digital holography	15
2.1.3	Wavefront sensing	17
2.1.4	Imaging with complex media	19
2.1.4.1	Wavefront reconstruction using Demons algorithm	23
2.1.4.2	Chromaticity and multiplexing	27
2.1.5	Infrared phase imaging	28
2.2	Speckles	29
2.2.1	Speckle as random walk	31
2.2.2	Speckle parameters	33
2.2.2.1	Intensity correlation function	35
2.2.2.2	Rayleigh probability distribution of speckle intensity	35
2.2.2.3	Memory effect	38
2.2.2.4	Speckle grain size	39
2.2.2.5	Spatial correlation function of a speckle	40
2.3	Summary	41

3	Longwave infrared speckle imaging - experimental setup development	42
3.1	Diffuser	45
3.1.1	Diffuser requirements	45
3.1.1.1	Intensity loss from interface reflection	45
3.1.2	Infrared transparency and transmission properties	46
3.1.3	Initial diffuser trials	48
3.1.3.1	Sodium chloride (NaCl)	48
3.1.3.2	Gallium arsenide (GaAs)	50
3.1.3.3	Powdered materials - salts and oxides	51
3.1.4	Silicon wafer diffuser	53
3.2	Infrared source	58
3.2.1	Blackbody	59
3.2.1.1	Planck's law of blackbody radiation	59
3.2.1.2	Emissivity	60
3.2.2	Soot as blackbody source	61
3.2.3	Coiled filament source	61
3.2.3.1	Penetration depth	64
3.2.4	Silicon nitride globalbar source	67
3.2.5	Silicon carbide globalbar source	69
3.3	Point source	71
3.3.1	Coherence length and time	73
3.3.1.1	Coherence of light with Gaussian emission spectrum	74
3.3.1.2	Coherence of thermal radiation	75
3.3.1.3	Lateral coherence for speckle observation	79
3.4	Infrared detector	79
3.4.1	Bolometers	79
3.4.2	Microbolometers	81
3.4.3	Microbolometer detector responsivity	83
3.4.3.1	Temperature coefficient of resistance	83
3.4.3.2	Pink (1/f) noise characteristics	84
3.4.3.3	Detector resistivity	85
3.4.4	FLIR longwave infrared camera	85
3.4.5	Summary	87
4	Wavefront Reconstruction	88

4.1	Processing of the speckle images	89
4.2	Wavefront reconstruction algorithm	92
4.3	Angular memory effect characterization	94
4.3.1	Angular memory effect for varying diffuser - speckle imaging plane distances	100
4.4	Speckle grain size estimation	101
4.5	Lens phase imaging experiments	106
4.5.1	Reconstructed lens wavefronts	109
4.5.1.1	Zinc Selenide (ZnSe) lens ($f = 1$ m)	109
4.5.1.2	Wavefront radius of curvature estimation	111
4.5.1.3	Zinc Selenide (ZnSe) lens ($f = 50$ cm)	112
4.5.2	Wavefront sensing for various curvatures	112
4.5.3	Wavefront sensing with varying diffuser - speckle imaging plane distances	115
4.6	LWIR speckle imaging challenges	119
4.6.1	Camera noise analysis	119
4.6.2	Frame averaging of speckle images	124
4.6.3	Intensity inhomogeneities	125
4.6.4	Infrared focussing	126
4.7	Wavefront reconstruction of a complex phase mask	127
4.8	Qualitative and quantitative aspects of phase reconstruction	131
4.9	Summary	138
5	General conclusions and outlook	140
5.1	Future prospects	143
	Bibliography	145
	Appendices	175
A	Analytical Modelling of Speckle	175
A.1	Speckle generation due to scattering from a rough surface	175
A.1.1	Scatterer topography and correlation function	175
A.1.2	First-order perturbation theory to compute transmitted electric field	176
A.1.3	Scatterer topography and speckle contrast	179

List of Figures

1.1	Electromagnetic spectrum	2
1.2	Atmospheric transmittance	3
1.3	LWIR and visible camera comparison	5
2.1	Plane wave wavefront illustration	10
2.2	Basic holography setup	13
2.3	Hologram formation	14
2.4	Hologram reconstruction	14
2.5	Shack-Hartmann wavefront sensor	19
2.6	Wavefront shaping	21
2.7	Memory effect illustration	22
2.8	Phase encoding with thin diffuser	24
2.9	Maxwell's demons thought experiment	25
2.10	Demons algorithm as a diffusion model	25
2.11	Demons algorithm image registration	26
2.12	Red laser beam reflection	29
2.13	Laser beam transmission through paper	30
2.14	Ultrasound image with speckles	31
2.15	Synthetic Aperture Radar (SAR) images with speckles	32
2.16	2-D complex plane random walk	33
2.17	Scattering slab with plane wave illumination	34
2.18	Rayleigh probability density function	36
2.19	Scattering sequence in a medium	37
2.20	Memory effect graphical representation	39
3.1	Simple setup for imaging through scattering media	43

3.2	IR speckle imaging setup through scattering media	44
3.3	Compatible materials for infrared applications	47
3.4	IR spectrum of ZnSe slab	48
3.5	IR spectrum of NaCl slab	49
3.6	Microscope image of NaCl crystal	49
3.7	Lab-prepared NaCl disks and IR images	50
3.8	Infrared transmission through different scatterers	51
3.9	GaAs wafer and scattered IR images	51
3.10	IR spectrum of TiO ₂ and ZnO nanoparticles	52
3.11	Powders on substrates as scattering media and IR images	52
3.12	First IR speckle with silicon wafer	53
3.13	Silicon wafer diffusers	54
3.14	IR spectrum of double side polished silicon wafer	55
3.15	RMS surface roughness	55
3.16	AFM topography of polished silicon wafer	56
3.17	Height distribution of polished silicon wafer	56
3.18	AFM topography of unpolished silicon wafer	57
3.19	Height distribution of unpolished silicon wafer	57
3.20	Blackbody radiation	60
3.21	Homemade blackbody source	61
3.22	Scitec IR 30K blackbody source	62
3.23	Scitec IR 30K source beam	62
3.24	IR speckle with Scitec IR 30K source	63
3.25	Refractive indices and penetration depth for glass	64
3.26	Penetration depth for quartz	65
3.27	Penetration depth comparison between glass and quartz	66
3.28	Scitec IR-Si 253 Si ₃ N ₄ global source	67
3.29	IR speckle with Si ₃ N ₄ global source	68
3.30	Scitec reflector mount for Si ₃ N ₄ global source	68
3.31	Scitec IR-Si 207 SiC global source	69
3.32	IR-Si 207 global source temperature vs. voltage plot	70
3.33	Emission spectrum of IR-Si 207 SiC global	71
3.34	Lateral angular coherence range illustration	80
3.35	Bolometer schematic	81
3.36	Microbolometer pixel cross-section	82

3.37	FLIR A655sc microbolometric camera	86
4.1	Raw averaged speckle image	90
4.2	Gaussian low-pass filter for smoothing raw averaged speckle image	91
4.3	Low-pass Gaussian filtered averaged speckle image	92
4.4	Speckle pattern as a unique fingerprint of incident wavefront	94
4.5	LWIR speckle setup to characterize angular memory effect of scattering medium	95
4.6	Angular memory effect characterization of Silicon diffuser in LWIR setup	97
4.7	Estimated global speckle translation shift versus incidence angle plot	98
4.8	2-D Gaussian surface fitting for cross-correlation peak localization	99
4.9	Angular memory effect characterization at varying distances	100
4.10	Speckle pattern from spherical wavefront on ZnS lens	102
4.11	Histogram of LWIR and visible speckle pattern intensity values	103
4.12	Speckle grain size estimate using 2-D normalized autocorrelation function	104
4.13	Speckle grain size comparison with varying conditions	107
4.14	Setup for acquiring reference LWIR speckle images from plane wavefront	108
4.15	Setup for imaging sample speckle pattern after phase object distortion	108
4.16	Converting plane wavefront to converging spherical wavefront with lens	109
4.17	Ideal LWIR wavefront from ZnSe lens at 2 cm from diffuser	110
4.18	Reconstructed LWIR wavefront from ZnSe lens at 2 cm from diffuser	110
4.19	Ideal LWIR wavefront from ZnSe lens at 50 cm from diffuser	112
4.20	Reconstructed LWIR wavefront from ZnSe lens at 50 cm from diffuser	113
4.21	Comparison of reconstructed wavefront radii for $f = 1$ m lens	114
4.22	Comparison of reconstructed wavefront radii at different distances for $f = 1$ m lens	115
4.23	Comparison of reconstructed wavefront radii at different distances for $f = 50$ cm lens	116
4.24	Reconstructed wavefront radii comparison with ideal values	118
4.25	Image stack for obtaining one processed image in thermal camera	120
4.26	Pixel-wise mean of intensity values for 100 frame background image	121
4.27	Histogram of pixel-wise mean values for 100 frame background image	121
4.28	Pixel-wise standard deviation of intensity values for 100 frame background	122
4.29	Histogram of pixel-wise standard deviation values for 100 frame background	122
4.30	Signal-to-noise ratio (SNR) computed for individual pixels over 100 frames	123

4.31	Average SNR values for increasing number of frame averages	124
4.32	3D design of smiley pattern for nanoscribe fabrication	127
4.33	Optical microscope image of nanoscribe fabricated smiley pattern	128
4.34	Refractive indices of SU(8) photoresist used for fabricating LWIR phase samples	129
4.35	LWIR image of smiley pattern illuminated by plane wavefront	130
4.36	Reconstructed LWIR wavefront when smiley pattern distorts plane wavefront	131
4.37	3-D surface plot of optical path difference between reference speckle images	132
4.38	Optical path difference range and standard deviation for reference speckle residuals	133
4.39	3-D surface plot of residuals for reconstructed spherical wavefront	135
4.40	Optical path difference range and standard deviation for reconstructed spher- ical wavefront residuals	136
4.41	Reconstruction of a converging spherical wavefront	137
4.42	Reconstruction of a diverging spherical wavefront	137
5.1	1951 USAF resolution test chart sample as nanoscribe fabricated phase sample design	144
5.2	Thermal image through silicon substrate showing a gold resistor	144

List of Tables

- 3.1 Refractive indices of materials with infrared transmission at 10 μm 47
- 3.2 Coherence length and coherence time values computed for longwave infrared radiation in air centred at 10 μm 78

Chapter 1

Infrared imaging using scattering media

Contents

1.0.1	Infrared (IR) radiation	2
1.0.2	Long wave infrared (LWIR) radiation	3
1.0.3	Infrared imaging using complex media	4
1.0.4	Infrared wavefront sensing	6
1.0.5	Thesis outline	7

Our universe is made up primarily of matter and energy. It is therefore useful for us to be able to detect matter and energy in its different forms. The human eye can detect energy, as photons, in only a very limited range of the entire electromagnetic (EM) spectrum, with photon wavelengths ranging from approximately 400 to 700 nanometers, which is consequently known as the visible range of the electromagnetic spectrum. A lot of physical phenomena produce photons that cannot be seen by the human eye, and it is therefore important to create instruments that can detect such photons. All objects with a temperature above absolute zero Kelvin (0 K) emit thermal radiation, which emerges from the conversion of the kinetic energy of motion of its constituent charged particles into electromagnetic energy. The wavelength region of photons involved in thermal radiation, i.e. heat transfer, corresponds to the infrared region of the electromagnetic spectrum, for bodies whose temperature is between room temperature (~ 300 K) and 3000 K approximately.

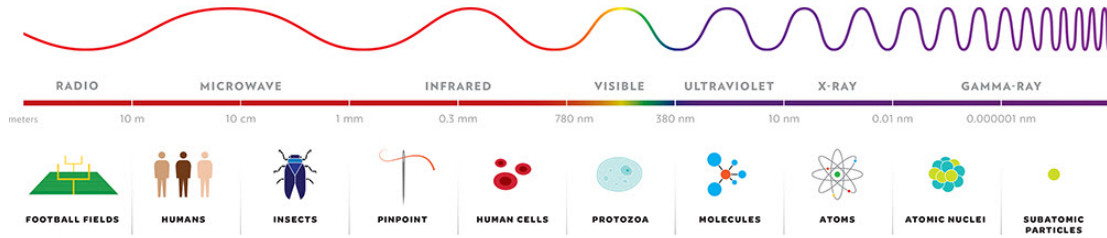


Figure 1.1: The entire electromagnetic spectrum [1].

1.0.1 Infrared (IR) radiation

The infrared region of the EM spectrum lies between the visible region and the radiowave region, between the wavelengths 700 nm - 1 mm. There are further sub-divisions in the infrared band, with some key applications in those ranges listed below:

1. Near infrared (NIR) - 0.75–1.4 μm : corresponding to the transition from the visible to the infrared and leading up to the first local maxima of water absorption in the infrared, with applications in low attenuation silica-based fibre optic telecommunications, night vision devices, pulse oximetry, and NIR spectroscopy [2].
2. Short wavelength infrared (SWIR) - 1.4-3 μm : leads to a peak in water absorption, and is the dominant window for long-distance fiber-optic telecommunications. At this range, indium gallium arsenide (InGaAs) detectors and mercury cadmium telluride (MCT / $\text{Hg}_{1-x}\text{Cd}_x\text{Te}$) cryogenically cooled detectors work.
3. Mid wavelength infrared (MWIR) - 3-7 μm : a part of this range falls in the atmospheric transmittance window (as shown in Figure 1.2) and is used for passive heat-seeking technology in aerospace applications. Indium antimonide (InSb), lead selenide (PbSe) and MCT detectors work in this range.
4. Long wavelength infrared (LWIR) - 7-14 μm : the infrared region where passive thermal imaging of objects near room temperature works best, as well as aerospace applications and spectroscopy (as discussed in further detail in Section 1.0.2), being facilitated by MCT detectors [3] as well as microbolometers (which we use in our experimental setup, and are discussed in greater detail in Section 3.4.2).
5. Far infrared (FIR) - 14-1000 μm : useful for passive human detection, therapeutic medicine, and in infrared astronomy for detecting galactic signatures.

Different sub-regions of the infrared are useful for various applications like thermography (heat profiling), thermophotovoltaic conversion and the spectroscopic identification of chemical compounds.

1.0.2 Long wave infrared (LWIR) radiation

The long wavelength infrared (LWIR) region from 7-14 μm is known as the "thermal infrared" region, since photons emanating from room temperature thermal radiation lie in this region. Sensors in this range can obtain a completely passive image of objects - like the human body with an average body temperature of about 37 $^{\circ}\text{C}$ - based on thermal emissions only and requiring no external illumination, which makes this wavelength range particularly conducive for thermal imaging [4]. The LWIR also coincides with a region of the earth's atmosphere's transmittance window, as shown in Figure 1.2. The overlap with the transmittance window of the earth's atmosphere makes the LWIR useful for atmospheric and space applications [5] as well. A lot of chemical compounds and molecules also emit or absorb infrared radiation when transitioning between their vibrational-rotational states, which are excited when there is a change in the dipole moment of the molecules. Numerous molecules have their rotational-vibrational energy states in the LWIR, and LWIR spectroscopy can be utilised to precisely detect specific molecules, due to which the LWIR is also christened as the IR spectroscopy fingerprint region [6], as well as being a useful wavelength range to study these specific rotational and vibrational energy states of the molecules.

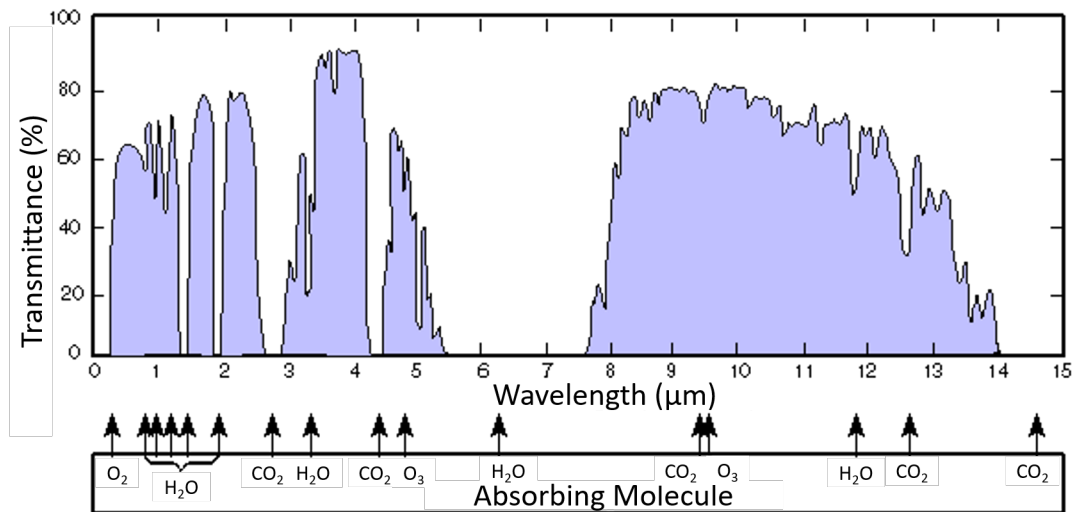


Figure 1.2: Atmospheric transmittance [7]

One of the broad applications of long wave infrared radiation is thermography or thermal imaging, which is the detection of LWIR radiation emitted by objects and the surroundings to create pseudo-colour images. LWIR thermography is widely used in scientific, industrial, defense and medical applications [8], due to the novel thermal image information obtained in the process, and the ability to track changes in different systems from the variation in their heat signatures. Infrared thermography is used for face recognition [9], building diagnostics [10], livestock monitoring [11], non-invasive beehive population analysis [12], passive three dimensional (3D) object detection [13], non-invasive studies of thermal physiology [14] - like peripheral blood flow measurements, respiratory physiological probing, and the detection of skin cancer [15] and breast cancer [16], functional brain imaging [17], mammal tracking in ecological research [18], non-destructive testing [19], studying thermal landscape dynamics [20], food safety assessment [21], and traffic management [22], among others.

LWIR radiation is also important in developing novel strategies for tackling climate change [23] by engineering thermal radiation that can exit through the Earth's atmosphere like in daylight radiative cooling [24] and energy harvesting antenna designs [25]. Thermal infrared remote sensing for mineral exploration [26], LWIR hyperspectral imaging [27] - for airborne landmine detection [28], chemical agent detection [29], gas-phase remote sensing of chemical clouds [30], LWIR free-space optical communications [31], development of LWIR transmitting optical fibres [32], infrared heat-seeking in aerospace applications [33], infrared deicing systems [34], LWIR cameras in space climatology [35], infrared astronomy [36], space applications [37], and infrared reflectography in art analysis [38] are other domains in the vast repertoire of LWIR applications.

1.0.3 Infrared imaging using complex media

In addition to the utility of longwave infrared radiation in investigating phenomenon that is uniquely in the LWIR spectral domain, it also allows the examination of processes or materials with unique signatures that extend beyond the visible regime, either as complementary to visible light inspection [39] or as alternative standalone examinations in the LWIR wavelength range, as shown in Figure 1.3. Recently, beyond these advantages, the idea of thermal inspection through obstacles like scattering media or in a non-line-of-sight light propagation context has taken shape [40]. While imaging through scattering media has been demonstrated in the visible spectrum extensively, it is completely novel in the LWIR and has not been done before. Thermal imaging through complex media extends the

imaging capability in the LWIR beyond conventional ballistic light propagation, i.e. where light travels between the scene object and the detector without any significant impediment even when passing through a scattering medium. It allows imaging through obstacles like scattering media to probe deeper into materials, and to look around corners when the object and detector are not in a straight optical path. This promises new applications, that were hitherto not possible, ranging from the ability to look through obstacles and around corners for rescue and emergency services, material analysis in physically constrained environments, autonomous navigation, among others. The LWIR is favourable for thermal imaging through scattering media due to the ability to carry out passive imaging from objects which behave as thermal sources themselves, and due to lesser scattering at relatively larger LWIR wavelengths compared to visible wavelengths.

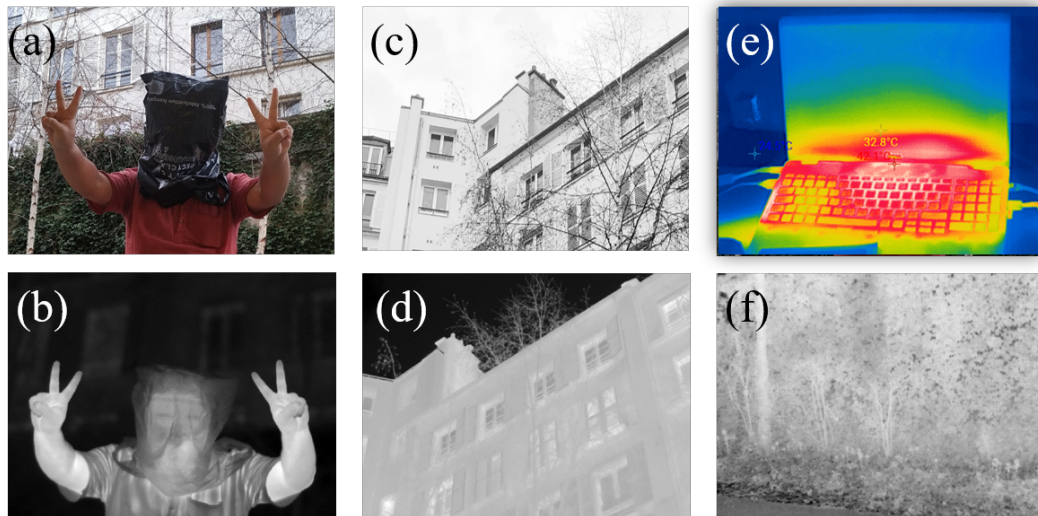


Figure 1.3: Long wave infrared Thermography enables us to detect LWIR radiation that is not captured by visible cameras, while imaging in both wavelength regions can create complementary visual information. In (a), we see a visible-light camera image of a human being behind a plastic bag, while the same person when imaged in the LWIR in (d) becomes visible due to the plastic bag being translucent in the LWIR. Additionally, we can gather a heat profile of the person’s body and clothing. By contrasting (b) which shows a monochrome visible-light image of a building and the sky, and (e) which shows an LWIR pseudo-color image of the same surroundings, it is evident that glass has different optical properties in the visible (where it is transparent) and in the LWIR (where it is strongly emissive), and also that the thermogram (heat map) of a building and the sky can provide alternate visual information about the surroundings. (c) shows a thermogram of a laptop where the upper portion of the screen is much cooler than the lower portion which contains the central processing unit (CPU). (f) shows an LWIR image of foliage which is quite dissimilar from one in the visible.

1.0.4 Infrared wavefront sensing

Thermal radiation provides a way to investigate thermal sources, while the development of tailored unconventional thermal sources [41] enable the altering of thermal emission for innovative applications like creating more energy efficient materials [24]. Thermal sources, with no particular surface structuration, are typically broadband with low spatial and temporal coherence, thus radiating near-isotropically over a broad angular range and spectrum. Surface structuration on polar and plasmonic materials using gratings have been successfully developed to control and alter the emitted thermal radiation [42] [43]. Recently, metasurfaces composed of sub-wavelength Metal-Insulator-Metal (MIM) resonators of various geometries have enabled spatial and spectral control of infrared radiation [44] as well as their characterization [45]. These atypical thermal sources thus necessitate the need to characterize the infrared emitters themselves. In the visible and in the infrared, detectors are usually sensitive to the intensity and not to the phase. Our specific interest lies in carrying out phase imaging and / or wavefront sensing in the LWIR for reconstructing thermal wavefronts, which can be used in investigating the thermal emission from IR nano-antennas in the far field and other applications.

To carry out thermal wavefront sensing, it is necessary to encode the phase of the IR radiation in an intensity pattern since it cannot be directly measured by a camera. IR holography [46] is a possible technique, but the difficulty of sourcing optical components in the IR and its careful alignment demand an alternative approach. We take inspiration from wavefront sensing developed in the visible region of the electromagnetic spectrum [47], and the growing field of wavefront shaping in complex media in the visible region as well (see [48] for a detailed review). Visible wavefront sensors map the local wavevectors directly onto a two-dimensional image to obtain a phase map [49]. Self-referenced techniques for wavefront sensing utilize an optical mask placed before the camera that encodes the phase in an intensity image through speckle patterns [50], where small deformations due to local phase gradients allow the reconstruction of the incident wavefront with high fidelity [51].

Thesis Objective: Our objective in this thesis is to develop a speckle-based wavefront imaging system in the LWIR that can function using non-transparent media and reconstruct thermal wavefronts by carrying out LWIR phase imaging through scattering media. By utilizing the theoretical techniques and experimental tools developed in the visible region of the EM spectrum, we seek to adapt to the LWIR spectrum, towards building a wavefront sensing imaging modality in a complemen-

tary region of the EM spectrum that was hitherto inaccessible to thermal imaging. This is a topic that has fundamental relevance in infrared optics, along with numerous potential applications.

1.0.5 Thesis outline

This thesis is arranged into 5 chapters. Chapter 1 presents a brief overview of long wave infrared radiation and its applications, introduces the background of imaging through complex media and wavefront sensing, and describes the objective of the thesis - to develop an LWIR speckle imaging technique based wavefront sensor. In Chapter 2, an overview of current phase imaging techniques in the visible and LWIR spectral regions is presented, followed by a review of the basic theoretical concepts involved in the description of speckles - which forms the basis of our experiments - and a summary of some of the key developments in speckle imaging in other wavelength regions that have built the foundations necessary for our LWIR speckle imaging technique. In Chapter 3, we discuss the development of our novel experimental setup for LWIR speckle imaging, and review the design considerations of the key components of the setup which needed to be adapted for their operation in the LWIR. In Chapter 4, we describe the methodology for wavefront reconstruction using our LWIR speckle imaging technique, present the key results in thermal wavefront sensing, and discuss some of the challenges in LWIR speckle imaging. Chapter 5 concludes the thesis with a global summary of the work in this thesis, a brief glance at the applications of our LWIR wavefront sensing technique, as well as a report on the future prospects of the work presented in this thesis. References are listed at the end of the thesis in a complete bibliography.

Chapter 2

Speckle imaging for wavefront sensing

Contents

2.1 Phase imaging	9
2.1.1 Holography & interferometry	11
2.1.2 Digital holography	15
2.1.3 Wavefront sensing	17
2.1.4 Imaging with complex media	19
2.1.5 Infrared phase imaging	28
2.2 Speckles	29
2.2.1 Speckle as random walk	31
2.2.2 Speckle parameters	33
2.3 Summary	41

An electromagnetic wave - like a light wave - is a periodic wave that can be described in terms of its intensity (or amplitude, whose square is the intensity) and phase. While the intensity is a measure of the average energy transferred per unit time and per unit area in a plane perpendicular to the direction of propagation of the wave, the phase signifies the fractional position in a full cycle of the oscillating wave at a given time. The electric field

for a time-varying wave can be written as:

$$E(t) \propto \text{Re}\{\sqrt{I(t)}e^{i(\omega_0 t - \phi(t))}\} \quad (2.1)$$

where, $I(t)$ is the intensity and $\phi(t)$ is the phase of the wave. The temporal derivative of the phase gives access to the instantaneous frequency of the wave. The phase information of a wave is information complementary to the intensity information. However, classical detectors like photodiodes and cameras are only sensitive to the intensity, and totally blind to the phase. An important and relevant part of the optical information is therefore lost. The ability to measure the relative phase of a wave gives rise to numerous applications in phase imaging, which are not possible only by using intensity information.

A locus of points in space that have an equal optical phase is known as a wavefront. Every point on a wavefront, therefore, has the same phase. Figure 2.1 shows plane wavefronts which are generated by a plane wave propagating perpendicular to the constant-phase wavefront surfaces. A wave's phase variability is quantified by coherence. Temporal coherence is a measure of the degree of systematic and predictable evolution of the phase over time, while spatial coherence quantifies the correlation between the phases at different points in space. Light propagation inside a medium introduces optical phase delays which are proportional to the distance of propagation, with the constant of proportionality being the wavenumber - that is related to the refractive index. Most optical elements introduce some kind of phase change to a light beam, like a spherical lens producing a curved wavefront depending on the convergence or divergence of the lens used. While wavefront distortions can sometimes be a problem, they can also be utilized to detect phase variations as we shall see in the following sections.

2.1 Phase imaging

We have seen above that a light wave can be expressed in terms of its intensity and phase. This implies that a light beam can be altered by changing a combination of these two parameters, independently of each other. Biological objects like single cells and thin tissue slices [52], optical components like conventional lenses and more recently developed metalenses [53] [54], materials such as nanoparticles and polymer filaments [55], or any object with a refractive index differing from that of its environment are phase objects, i.e. ob-

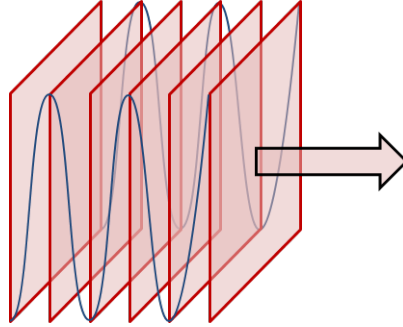


Figure 2.1: The wavefronts (marked red) of a plane wave (represented by the blue curve) are also planes, perpendicular to the direction of propagation of the wave (marked in black).

jects that significantly affect the phase of the incident electric field but not necessarily its amplitude, at least in the visible part of the electromagnetic spectrum. Here, we consider that absorption is not the primary phenomenon of light modulation that is experienced by an incident beam when passing through typical phase objects. In most cases, such phase samples are usually only weakly scattering, thereby necessitating the measurement of the phase shifts by imaging to identify such structures in an intrinsically low contrast intensity imaging mechanism. However, since the phase of a light wave cannot be directly measured by a camera whose pixels are only sensitive to the intensity, it needs to be encoded in an intensity pattern for imaging purposes. The development of different techniques to optimally perform these measurements of phase differences forms the core of the field of phase imaging. The various techniques and their improvements in imaging phase contrast is briefly reviewed below. Readers interested in more details can refer to G. Popescu's cogent review of quantitative phase imaging techniques, which focuses on the predominant visible region of the EM spectrum where such state-of-the-art methods have been developed [56]. We shall first look at the state-of-the-art techniques for phase imaging in the visible region of the EM spectrum, where extensive work has been carried out first in its historical evolution, and then look at the state-of-the-art methodologies for phase imaging specifically in the infrared in Section 2.1.5. Finally, we will delve into the underlying theory of speckles in Section 2.2 in order to gain a basic understanding of speckle physics.

From the development of the precursors of modern light microscopes in the 17th century by inventors like Cornelis Drebbel and Galileo Galilei [57] to the first visual inspection of cells under a microscope by Robert Hooke [58] and the study of micro-organisms using an improved high-magnification (upto 300x) single lens microscope by Antonie van Leeuwenhoek [59], the field of microscopy has continually expanded to revolutionize science itself,

by providing innovative means to probe the physical world optically. Over the course of microscopy's developments, the key focus has been to improve the resolution and the contrast of microscope images [60]. While Ernst Abbe proposed a theoretical resolution limit of microscopes in 1873 to be close to half the wavelength of light [61], newly developed far-field fluorescence microscopy techniques like stimulated emission depletion (STED) microscopy [62], photo-activated localization microscopy (PALM) [63], stochastic optical reconstruction microscopy (STORM) [64] have pushed this limit greatly. Novel methods like non-linear structured illumination microscopy have alluded to theoretically unlimited resolution [65], and the use of near-field techniques have broken the diffraction barrier as well [66]. The usage of contrast agents like dyes [67] and gene expressing markers like the green fluorescent protein [68] have also aided optical contrast enhancement in microscopy even as they require treatment of the sample itself. Deep-tissue imaging techniques like confocal microscopy [69] [70] and full-field optical coherence tomography (FF-OCT) [71] have also enhanced microscopy contrast. Most of these techniques have been developed in the visible region of the EM spectrum. However, in the infrared, microscopy applications are very limited, mainly because of the strong limitations on resolution (owing to diffraction), but also due to instrumental limitations (lenses and detectors are scarce and more expensive in the infrared) and inherent limitations of the infrared spectrum (like absorption of infrared in water limiting biological applications).

2.1.1 Holography & interferometry

The consideration of image formation as an interference problem [72] enabled novel improvements in imaging contrast using interferometry, leading to the development of phase contrast microscopy by Frits Zernike [73] [74], where the phase information is coupled to the intensity information in the phase contrast image, and gives access to the phase information without manipulating the sample itself. When treating imaging as an interference phenomenon, the scattered and incident electric fields are considered as the object wave and the reference wave in an interferometric setup, respectively [75]. The total electric field, $U(x, y)$, can be written as:

$$U(x, y) = |U| e^{i\phi(x, y)} \approx |U| [1 + i\phi(x, y)] \quad (2.2)$$

where, $|U|$ is the amplitude of the electric field and $\phi(x, y)$ is the local phase. When consid-

ering transparent objects, the term $|U|^2$ carries little information and contrast, but the phase term can be informative. In phase contrast microscopy, an additional phase shift, usually $\pi/2$, is introduced between the illumination and transmitted or scattered light to enhance the contrast of the interferogram, which makes them antiphase to each other. The resulting field of the phase contrast image, $U_{pci}(x, y)$, then becomes:

$$U_{pci}(x, y) = |U| [1 + i\{\phi(x, y)\}] \approx |U| e^{-\phi(x, y)} \quad (2.3)$$

with the additional $\pi/2$ phase shift in the resulting field term converting the complex exponential into a real exponential and translating phase modulation into amplitude modulation in the final image. With an additional attenuation of the incident field's power to enhance the scattered field's contribution, phase contrast microscopes enable the visualization of unlabelled transparent objects in great detail. However, the non-linear coupling of the phase in the intensity image has long prevented the quantitative retrieval of the contrast, i.e. the relative phase between the scattered and unscattered light, with phase contrast remaining mostly qualitative. The development of holography by Dennis Gabor in 1948 [76] enabled the utilization of the interferogram recording - which is generated by the interference between the primary illuminating (reference) wavefront and the secondary object emitted wavefront - to access the amplitude and phase information through imaging to record the light field itself.

The basic principle of holography is based on the diffraction of light by an object and the interference of this diffracted light beam with the reference beam to create an intensity image of the interference pattern, known as a hologram which can then be illuminated or digitally treated to reveal the object [78]. The basic elements of an optical holography setup, as shown in Figure 2.2, consist of a coherent laser beam that is divided into two beams - a reference beam and an illumination beam - by means of a beamsplitter. While the illumination beam interacts with the object and produces an object beam upon transmission or reflection, the reference beam follows a different path, unhindered by the object and is therefore entirely known (usually a plane wave). The reference beam and the illumination beam are then made to intersect each other, thereby producing an interference pattern which is recorded to produce the hologram. When two plane waves from the same source superimpose to form a hologram, a diffraction grating is obtained whose fringe spacing is determined by the wavelength of light and the angle between the two plane waves. Sim-

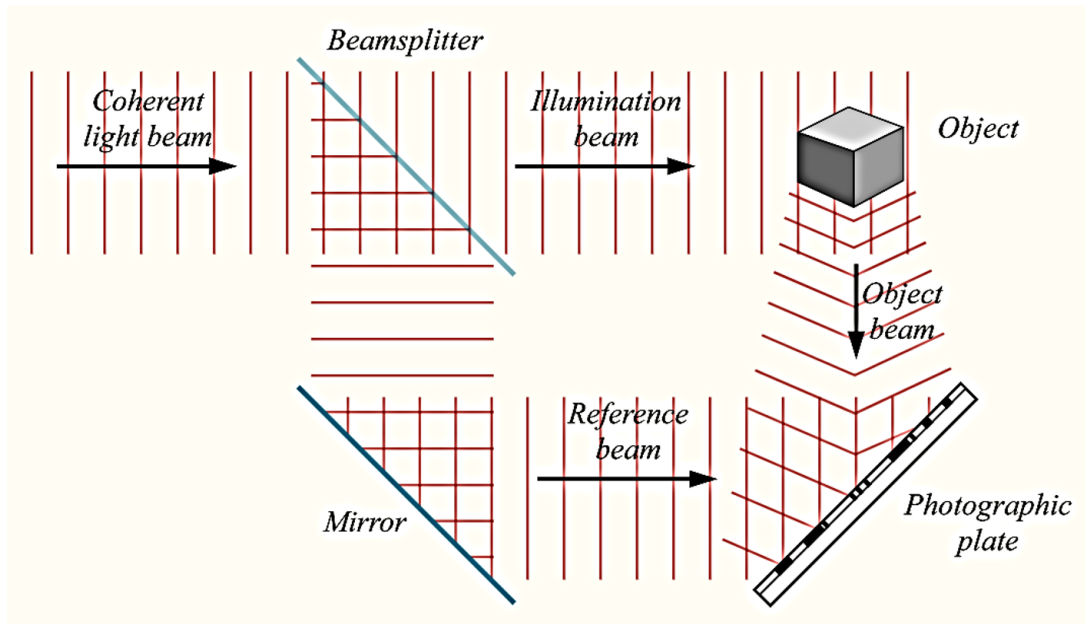


Figure 2.2: Basic holography setup - A coherent light beam is split into a reference and illumination beam - which after encountering the object becomes the transmitted or reflected object beam - that recombine to produce an interference pattern known as a hologram [77].

ilarly, when a spherical wave coming from a point source interferes with a plane wave incident normally, the resulting hologram is known as a Fresnel zone plate - an interference pattern of concentric dark and bright fringes. A complex object can be considered as a collection of point sources, and hence an object beam is a sum of waves emerging from point sources, which interfere with the reference beam, to produce a complex superimposition of such zone plates, as depicted in Figure 2.3.

To reconstruct the original light wavefronts of the object beam in classical holography, the recorded hologram, shown in Figure 2.3, needs to be converted into an absorption and dephasing pattern first. Then, it needs to be illuminated by the original reference beam, which reproduces the object beam in such a manner that an observer views it as emerging from a virtual image of the object located at the precise original object location (with respect to the hologram), as shown in Figure 2.4. Alternatively, a conjugate beam - where all the light rays are exactly opposite to the reference beam - can be used to illuminate the back of the hologram to produce a real image of the object at its original location with respect to the hologram. This real image can be recorded directly, and precludes the need for a lens to capture an image. Therefore, a hologram is both a record of the interference between the object beam and the reference beam, as well as being a projection of the object

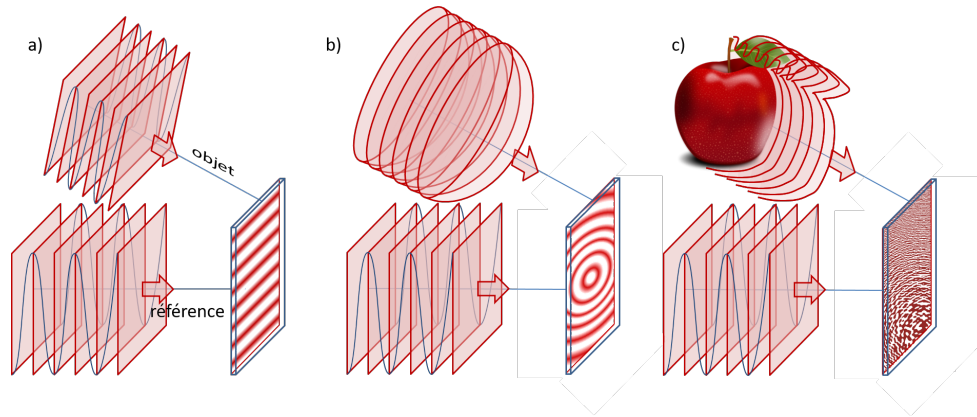


Figure 2.3: The formation of a hologram which records the interference pattern between an object wavefront and a reference wavefront in the case of the object wavefront being (a) a plane wavefront, (b) a spherical wavefront, and (c) a complex wavefront emanating from an object like an apple. (Illustration courtesy of G. Tessier)

when illuminated with the reference beam.

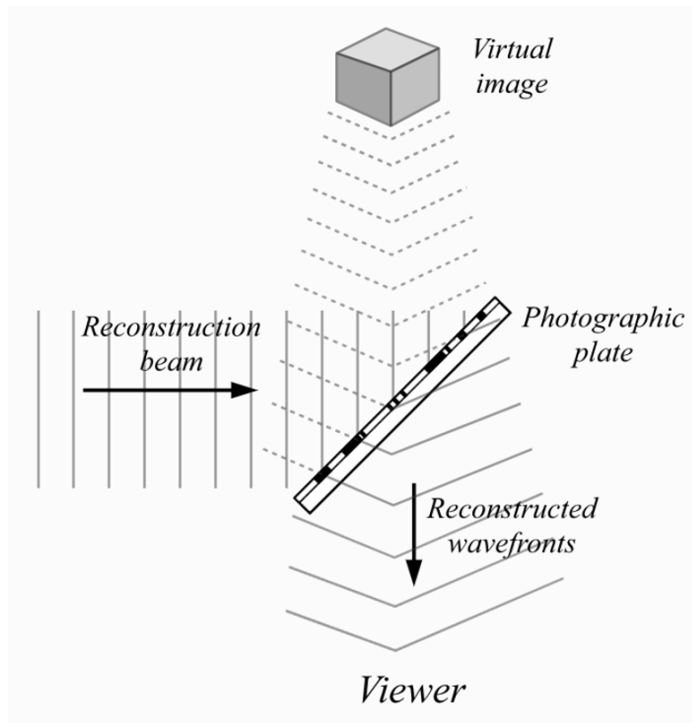


Figure 2.4: Reconstruction of the actual object by illuminating a recorded hologram with the original reference beam which reproduces the object beam and generates wavefronts that appear to emerge from a virtual object to an observer [79].

Since a hologram represents a recording of the light field information, it can generate differ-

ent reconstructed images when viewed from different angles, akin to observing the object in a similar fashion, albeit with the added advantage of being able to do so anytime after the hologram has been recorded. Holography is also a lens-less recording process, since the hologram is recorded without the need for any image formation as in a conventional optical camera or microscope. An additional advantageous feature of holography is that each point on a hologram contains information from every point in the scene, which means that a subset of a hologram can also generate scene information unlike a photograph where a subset of an image does not represent the other parts of the scene outside it.

2.1.2 Digital holography

After the first publications on holography, the field became dormant until the seminal publication by E. Leith and J. Upatnieks in 1963 demonstrating the first successful laser hologram [80]. This was due in no small part to the development of the laser at that time [81] [82]. Another significant development was the publication of how holography could be ingeniously combined with natural color photography by Y. Denisyuk [83]. In 1971, concurrent with the award of the Nobel prize to D. Gabor for holography, the first paper on digital holography was published [84], which gave rise to the next remarkable phase of development in the field of holography.

Digital holography is a holographic technique in which a hologram containing the information from an object wavefront is recorded digitally and reconstruction of the object wavefront is also carried out using a computer. The utilisation of digital computers for reconstructing wave fields led to active research in digital holography, and alongside the development of the main ideas, various possibilities of digital holography were tested, like fabricating computer-generated optics for information processing and holographic displays. However, the development of digital holography was thwarted by the limited computing technology of that time, and also the lack of optimal digital recording and storage media for digital holograms. This led to another hiatus in the field of holography, which was revived in the 1990s owing to the advent of fast microprocessors, high-resolution electronic optical sensors and the fabrication of micro-lenses and mirror arrays. The digital recording of holograms in real-time and real-time data processing enabled digital holography to become extremely fast and efficient. Digital holography has incorporated optical holography with information processing using digital computers and is a manifestation of information optics [85]. Just as the development of the laser led to the first realisation of the principle of holography, the subsequent development of digital holography was spurred by the

mass production of powerful computers and the introduction of the fast Fourier transform algorithm in 1965 by J. Cooley and J. Tukey [86], which is ubiquitous in digital image processing and is an extremely useful numerical algorithm in many different fields [87].

Beyond the development of the laser and of affordable highly sensitive detector matrices like EM CCD and s-CMOS cameras that led to the advent and growth of digital holography from the 1960s [88], key improvements to the holographic technique have been proposed that have augmented the basic principle of optical holography. The emergence of new techniques like off-axis holography, pioneered by E. Leith & J. Upatnieks, where the two beams recombine with an angular tilt between their propagation directions [89], increased its use in phase microscopy [90]. The off-axis holographic method spatially separated the twin images found in an in-line configuration, thereby improving reconstruction. The first steps towards digital holography involved the digitization of optically sampled holograms and their numerical reconstruction [91]. The direct recording of Fresnel holograms with charged coupled device (CCD) cameras allowed the direct numerical recording of both the amplitude and the phase information, and ushered in an era of digital holography where the holograms were recorded and processed completely digitally, without the need for intermediate photographic plate recording [92]. A more detailed treatment on digital holography can be found in the thesis of S. Suck [93], carried out earlier in our group, where digital holography is utilized to conduct photothermal studies.

The numerous advantages of digital holography have led to its widespread usage today. The numeric encoding of the hologram eliminates the need for any photographic processing for reconstructing the real object. Since the reconstructed wavefront in digital holography is a complex function, both the intensity and phase can be computed, as opposed to only the intensity being reconstructed in the case of an optical hologram. It is also possible to reconstruct from the recorded wavefront, the wavefield at any arbitrary plane located between the object and the recording plane [94]. Holographic or interferometric techniques are currently used in phase contrast microscopy [95], for quantitative phase-contrast imaging [96], digital in-line holography for biological applications [97] [98] like dry cell mass estimation [99], nanoparticle tracking [100] using digital holographic microscopy (DHM) [101], DHM in the near infrared [102], for 3D electric field reconstruction from a near-field probe [94], holographic interferometry for radiation dosimetry [103], interferometric vibration analysis [104], interferometric microscopy [105], holographic data storage [106], in optical astronomical imaging [107], and for creating visual arts [108]. Digital hologra-

phy has been utilized for metrology [109], multi-dimensional imaging applications [110], and multi-modal imaging [111] in addition to promising future avenues of application and development [112]. In the infrared region of the EM spectrum, digital holography presents interesting applications for 3D imaging and display [113], owing to the ability to have shorter recording distances in the infrared, larger field of view, higher system stability as well as the possibility to investigate materials that are transparent to infrared radiation [114].

2.1.3 Wavefront sensing

Beyond holography, an alternative approach to carry out phase imaging is wavefront sensing. In wavefront sensing, the distortions in the light wavefront originating from phase shifts caused by interaction of the incident wavefront with a sample are measured, and this without the need for a separate reference beam as required in holographic or conventional interferometric techniques. One of the most common wavefront sensors is the Shack-Hartmann microlens array wavefront sensor [115].

A Shack-Hartmann wavefront sensor consists of a contiguous array of evenly spaced microlenses, each with the same geometry and focal length, focussed on an image sensor which is placed in the common focal plane of the microlenses [116]. When the sensor is uniformly illuminated in such a configuration, as shown in Figure 2.5, the wavefront gradient across a microlens is proportional to the displacement of the focal spot [117]. By measuring a wavefront having phase distortions with the microlens array, these local focal spot displacements can then be measured leading to a reconstruction of the entire wavefront itself [118]. The Shack-Hartmann sensor was proposed by Shack and Platt in 1971 [119], which improved upon the Hartmann screen developed in 1904 where an array of holes (apertures) in an opaque optical mask was used to trace individual light rays through a telescope to test its image quality [120]. While the contiguous sampling due to the microlens array, and the small size and large separation between the focal spots allow a good phase measurement using the recorded tilts, the Shack-Hartmann sensor is unable to detect sharp phase discontinuities like steps in the wavefront. The Shack-Hartmann wavefront sensor has a spatial resolution which is limited by the number of microlenses. Shack-Hartmann wavefront sensors are used for measuring optical aberrations in the human cornea [121] [122], in an inverse configuration for user-friendly portable optometry [123], non-invasive jet flow turbulence analysis [124], in space telescope optics [125], and in adaptive optics [126] for visible and infrared applications [127].

The earliest reported technique proposed to increase the resolution in wavefront sensing is lateral shearing interferometry [128]. In lateral shearing interferometry, the incident field is divided by a grating into two similar but tilted wavefronts which interfere with each other. The two wavefronts are generated due to the reflection of the incident beam twice at the two different interfaces of a tilted slab which introduces a spatial shift (shear). However, a unidirectional interference is insufficient to reproduce the two-dimensional (2D) phase information, and later improvements like multiwave interferometry have been successful in doing so due to the generation of more than one gradient direction [129]. Quadri-wave lateral shearing interferometry (QWLSI) couples the use of two dimensional (2D) lateral shearing interferometry technique with a modified Hartmann mask [130] that is used to generate multiple identical wavefronts that interfere with each other and generate a 2D interference pattern that can be used to measure phase gradients along perpendicular directions, and enables the estimation of both intensity and phase [131]. Some of the applications of these techniques include high speed detection of tumour cell dynamics [132], optical focusing and imaging through biological tissues [133], quantitative phase microscopy of living cells [134] [135], the development of self-referencing wavefront sensors for in-situ testing [136], quantifying laser beam divergence [137], thermal imaging using optical phase analysis [138], the study of micro-bubble generation and water super-heating [139], enhanced 3D spatial resolution using spatially incoherent illumination [140], temperature shaping using plasmonic nanoparticle assemblies [141], and the optical characterization of 2D materials [142] and nanoparticles [143].

Wavefront sensing has multiple advantages over conventional interferometric methods to carry out phase imaging, like higher speed, sensitivity and temporal resolution with less complex optical setups. [134] The lack of a reference arm in wavefront sensing methods as compared to double-beam methods ensures better fidelity due to higher tolerance to vibrations and other disturbances. In addition, wavefront sensing does not necessarily require a highly coherent source as required in holographic techniques. Owing to the acquisition of single images for wavefront sensing, the temporal resolution can also be higher, but with a trade-off in having lower spatial resolution as each measured focal spot for the phase is spread over multiple pixels on the camera sensor. With a magnification in the imaging, though, the phase sampling can be increased while satisfying the Nyquist-Shannon sampling criterion to effectively improve the resolution.

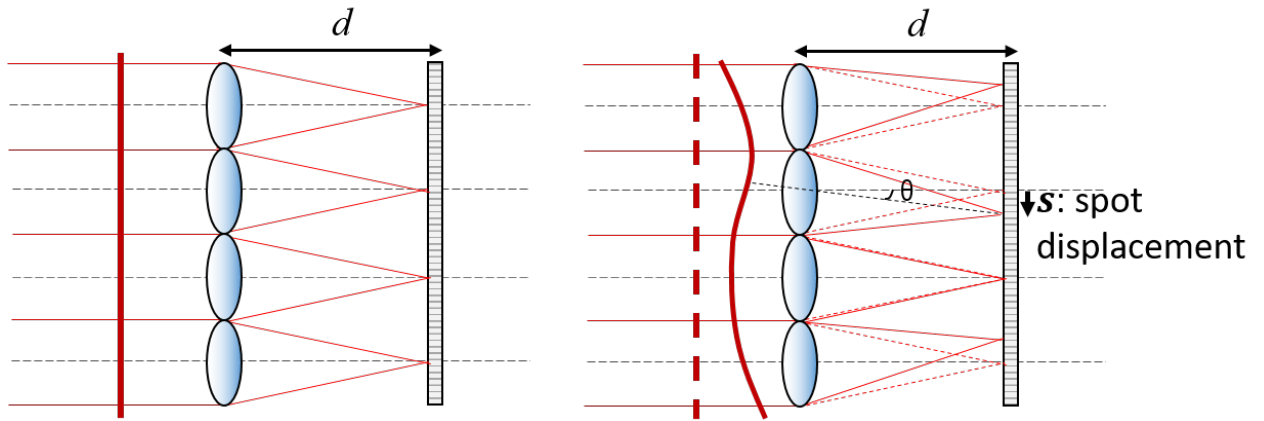


Figure 2.5: Shack-Hartmann wavefront sensor schematic: On the left, a plane wavefront is incident on the Shack-Hartmann microlens array whose focal plane is then populated by the focal spot of each microlens. On the right, a distorted wavefront (solid line) is incident on the Shack-Hartmann sensor, which produces displacements of the microlens focal spots by an amount proportional to the phase tilt of the incoming wavefront (solid line) with respect to the plane wavefront (dotted line) at each microlens. By measuring the individual spot displacements from the reference condition, the phase map of the incident distorted wavefront is then reproduced. (Illustration courtesy of P. Berto)

2.1.4 Imaging with complex media

Since the invention of the maser in 1953 [144], and its later refinement to the laser (Light Amplification by Stimulated Emission of Radiation) in 1960 [145], there has been an easily-accessible technique to generate coherent light in a narrow spectral band. However, spectrally narrow laser light gives rise to significant wavelength dependent interference patterns which are seen quite clearly when reflected off a diffuse and rough (unpolished) surface, like a wall [146]. The mutual interference pattern between multiple coherent wavefronts generated when coherent light is incident on a disordered material is called a speckle pattern.

The initial scientific reaction to the observation of speckle patterns was to treat them as noise [147], and reduce speckles or to improve the signal-to-speckle ratio in applications where the high coherence of a laser beam was of primary importance [148]. Even as inhomogeneities in the local refractive index of materials causes strong scattering of light [149] in various materials of interest for applications [150], studies in holography have demonstrated that when light is scattered in time-invariant media, the full incident light field information is not lost irretrievably [151]. The information is scrambled but present in the disordered speckle patterns [152]. This is due to the high degree of spatial correlation

in the speckle images that is still preserved after transmission through the thin diffuser, as seen in the high degree of similarity between the autocorrelation of a speckle pattern and the autocorrelation of the same object imaged by conventional lenses [50]. The first ideas of retrieving the interference information encoded in speckle patterns was proposed in the field of astronomy by A. Labeyrie in 1970 [153]. The seminal theoretical paper led to the development of speckle interferometry which is still widely used in astronomy. While techniques like OCT are adept at removing the contributions from multiply scattered waves [154], various other techniques such as those in adaptive optics [155] [156], and stellar speckle interferometry [157] enable the use of speckles to carry out distortion-free imaging by retrieving the information from the speckle pattern. Once demonstrated, the ability to exploit speckle patterns to retrieve the encoded transmission medium or object information, which would otherwise be lost, was widely adopted in diverse fields.

A speckle pattern can also be observed when coherent light undergoes transmission through a scattering medium like white printing paper. While the random scattering of light gives rise to the opaque nature of materials like white paint and paper, repeated and random scattering and interference in the scattering medium ensures that the incident wavefront is distorted so strongly that all or nearly all spatial coherence in the initially coherent light is lost during transmission. The incident coherent light waveform diffuses through the scattering medium and gives rise to a speckle pattern where spatial correlation on a scale larger than the wavelength of light is not present. The theory of wave transmission in the multiple scattering regime through complex disordered material has been developed during the 1990s, which is reviewed in [48], as well as precursors like time reversal of waves [158] which later facilitated optical imaging through complex media.

In 2007, I. M. Vellekoop and A. P. Mosk published a pioneering paper reporting their work on focusing coherent light through strongly scattering opaque media [159]. They bypassed wavefront correction methods used in adaptive optics, which were inadequate in controlling the propagation of light due to the complete scrambling of the field during random diffusive transmission. Instead, they demonstrated the focusing of coherent light through disordered scattering media - with the focus being about 10 times tighter than the one observed before scattering [160] [161] - by constructing wavefronts designed to control the diffusion channels of light through the scattering medium using spatial light modulators in order to maximize the intensity of one speckle grain [162]. Their method relied on interference, and it was applicable universally to various scattering media, irrespective of

their scattering strengths and material composition. Wavefront shaping, as demonstrated by Vellekoop and Mosk, can be mathematically considered as phase conjugation [163], which can counteract phase scrambling due to the single scattering of light [164], and has been implemented for reversing wavefronts in tissue [165].

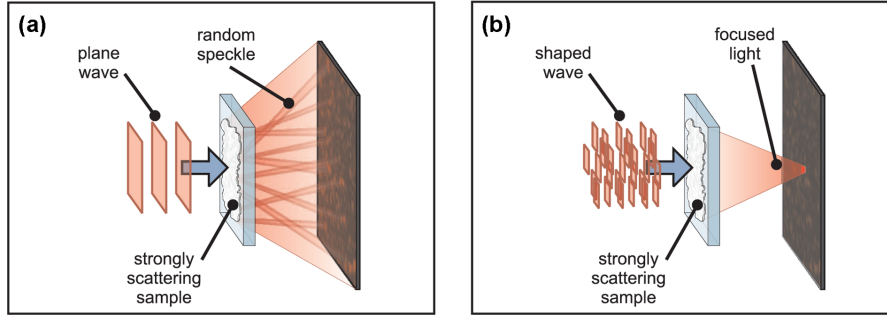


Figure 2.6: Design of the experiment: (a) A plane wave is focused on a disordered medium, and a speckle pattern is transmitted. (b) The wavefront of the incident light is shaped so that scattering makes the light focus at a predefined target [159].

The output characteristics of a wave after transmission through a scattering medium, in relation to the input characteristics of the wave is completely described by a transmission matrix. After the first demonstration of the measurement of the transmission matrix by S. M. Popoff *et al.* in 2010 [166], where they measured the transmission matrix for an 80 μm ZnO layer deposited on a microscope slide by using a method based on a spatial phase modulator together with a full-field interferometric measurement on a camera, various techniques for the measurement of the transmission matrix of complex disordered materials have been proposed [167]. It was also shown that knowing the transmission matrix of a scattering medium enabled its usage in imaging as a lens [168], as first proposed by Freund [151]. However, the efficient measurement of the transmission matrix is still quite intractable for most real-life scattering media, and is therefore an active field of research. In spite of (or due to) this problem, speckle-based information retrieval applications have been developed, thanks to the ability to reconstruct a majority of the encoded speckle information through long-range correlations that do not necessarily need the full knowledge of the precise transmission matrix of the scattering medium.

In 1988, S. Feng *et al.* theoretically predicted the memory effect for the first time, where long-range correlations preserve spatial correlation of object information in the final speckle pattern generated after wave transmission through a complex scattering medium [169]. In the same year, I. Freund & M. Rosenbluh experimentally demonstrated the memory effect in a scattering medium [170], leading to subsequent research where complex scattering me-

dia have been used to retrieve object information from a speckle pattern. Recent work like the characterization of the chromato-axial memory effect has simplified the manipulation of light beams for imaging as well as facilitating wavelength tuning while imaging [171].

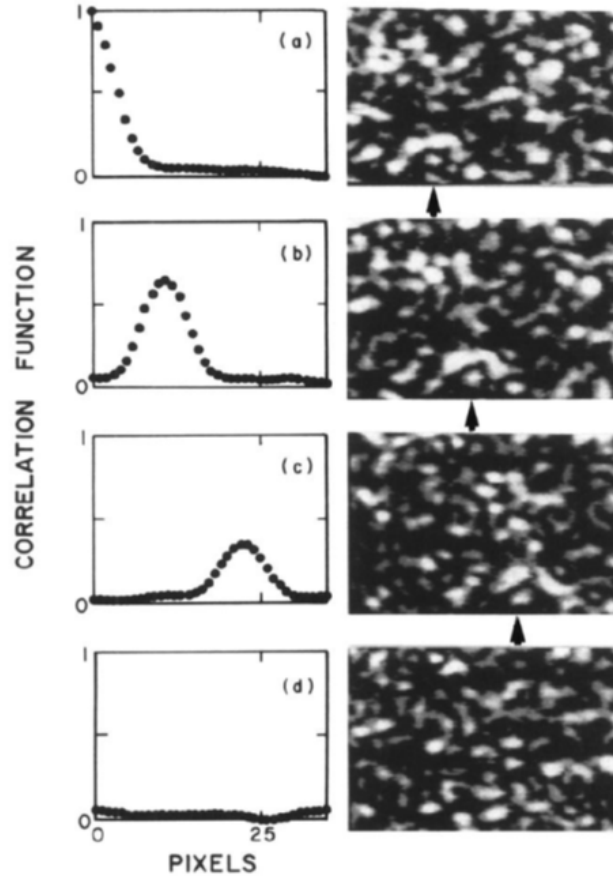


Figure 2.7: First experimental demonstration of memory effect: Auto-correlation function and zoomed-in speckle pattern clearly shows tracking of laser beam spot as the incident laser beam is rotated by (a) 0° (b) 0.01° and (c) 0.02° . Speckle pattern (d) is uncorrelated to (a), and therefore only shows expected small statistical fluctuations about zero, as expected for uncorrelated speckle patterns [170].

Based on this, P. Berto *et al.* in 2017 demonstrated the method of single-shot spatial and high-resolution phase imaging of the wavefront from a coherent source through a thin diffusing medium in the visible region of the electromagnetic spectrum, after a one-time speckle-to-wavefront calibration step, thanks to the memory effect of speckle correlations [51]. Considering that the angle θ between the local wavefront distortions is small, which is true for paraxial rays, the wavefront slope or the local phase gradient $\nabla_{\perp}\varphi$ can then be calculated by computing the ratio of the local spot displacement, s , to the distance between

the wavefront and the sensor, d .

$$\theta \simeq \tan \theta \simeq \sin \theta = \|\nabla_{\perp} \delta\| \quad (2.4)$$

$$\nabla_{\perp} \delta = \frac{\nabla_{\perp} \varphi}{k_0} \simeq \frac{\mathbf{s}}{d}, \quad (2.5)$$

where, d is the distance between the diffuser and the speckle, φ is the wavefront's phase, δ is the optical path difference, and $k_0 = \frac{2\pi}{\lambda}$ is the wavenumber, as depicted in Figure 2.8. This relation connecting the phase of the wavefront to the speckle grain displacement allows the phase to be computed from the intensity images themselves. In this respect, a thin diffuser can be seen as a phase mask - much like the modified Hartmann mask of QWLSI, or the Shack-Hartmann microlens array - albeit a complex and random mask. Like other phase masks, it also allows the encode the amplitude and the phase in a single intensity image. We would like to point out here that we have taken inspiration from this specific approach to carry out wavefront sensing in the longwave infrared, as we shall discuss later in greater detail.

2.1.4.1 Wavefront reconstruction using Demons algorithm

In order to reconstruct the wavefronts from the acquired speckle images, the popular demons algorithm for image registration is useful. The demons algorithm is a non-parametric method used to align two images by iteratively deforming one image (the moving image) to match another image (the fixed image).

The Demons algorithm was first proposed in [172] as an image matching algorithm that borrowed from thermodynamics concepts for image processing in the context of biomedical image registration. In the original thought experiment devised by James Clerk Maxwell, he considered a container containing a mixture composed of two different types of gaseous particles a and b (see Figure 2.9) - one of which was hot and the other cold - which are separated by a semi-permeable membrane. The semi-permeable membrane has a set of beings called Demons that are able to discern the specific kind of particle coming to the barrier, and only allows particles of the type a to diffuse to the side A while those of the kind b are allowed to only diffuse to the side B . Eventually, the box containing this gaseous mixture will contain only particles of a on side A and particles of b on side B ,

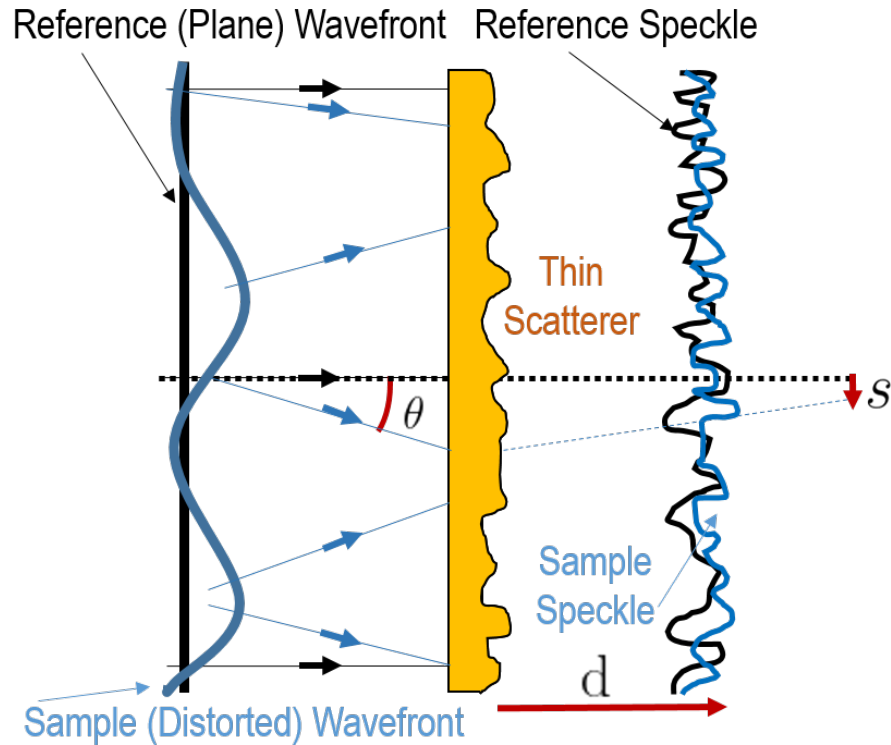


Figure 2.8: Phase encoding using a thin scattering medium, similar to using a Shack Hartmann wavefront sensor as shown in Figure 2.5. A plane wavefront is incident on the thin diffuser that produces a reference speckle pattern after transmission, while a distorted sample wavefront produces a different sample speckle. The local displacement of the speckle grains between the reference and sample speckles, denoted by s , is related to the local wavefront slope θ between the two wavefronts and the distance between the diffuser and the speckle d , which allows the computation of the wavefront profile of the sample wavefront w.r.t. the reference wavefront by estimating the speckle grain displacements.

which leads to a decrease in the system's entropy. This is a violation of the second law of thermodynamics. However, this paradoxical situation is resolved by considering that the demons also need to expend energy to recognise the particles and act on them, and if that is included, the total entropy of the system actually increases without violating the second law of thermodynamics.

Building on this notion of Maxwell's demons, the idea is applied to information theory and specifically, image matching. As illustrated in Figure 2.10, a model image M needs to be matched to a scene image S . A specific contour in S is chosen to act as the membrane and demons are positioned on this contour. At every local point in the contour in S , it is assumed possible to determine a vector perpendicular to the contour and with a specified

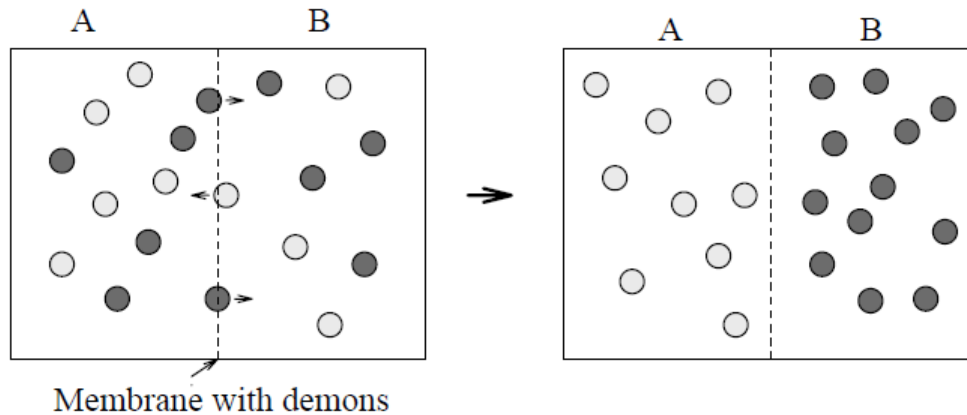


Figure 2.9: Maxwell's demons thought experiment schematic - Light coloured particles are of the type a and dark coloured particles are of the type b with the sides A and B separated by a semi-permeable membrane on which sit the Demons [172].

orientation from the inside of the object to the outside, like the gradient for example. This notion of polarity, signified as inside or outside the contour, is the central parameter on which the demons act and try to match the images to each other.

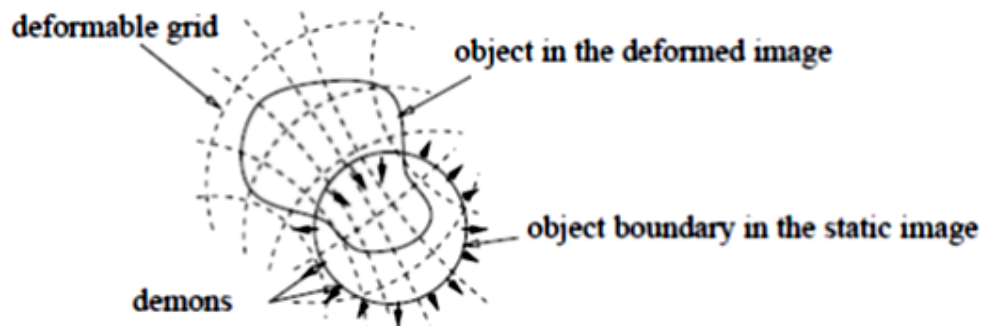


Figure 2.10: Demons algorithm as a diffusion model - the model image M is the deformable grid which diffuses through the static scene image S 's contours depending on the polarity-dependent forces applied by the Demons on the contours of S [172].

Now, the model image M is considered as a deformable grid whose vertices are treated as particles and assigned a polarity i.e. inside or outside based on the relations between these vertices themselves and the models used to assign the polarities. Now, having knowledge of the polarities, the demons situated on the membrane in S now effect deformation of the grid M locally by pushing points in M inside or outside S depending on their polarity. Eventually, the image grid M has been deformed locally by the demons to have the closest match of M to the static scene image S .

Subsequent developments in the image processing field developed a more rigorous mathematical framework for the proposed Demons algorithm [173] by showing that the diffusion forces that are effected by the demons can be better understood as an approximation of a second order gradient descent on the criterion of the sum of square of intensity differences between the scene image S and model image M 's points. There is also a regularization term to ensure that the algorithm works well with small values of the image gradient, and this can be modelled as a minimization problem which needs to be adapted to the specific image processing requirement to still be computationally efficient.

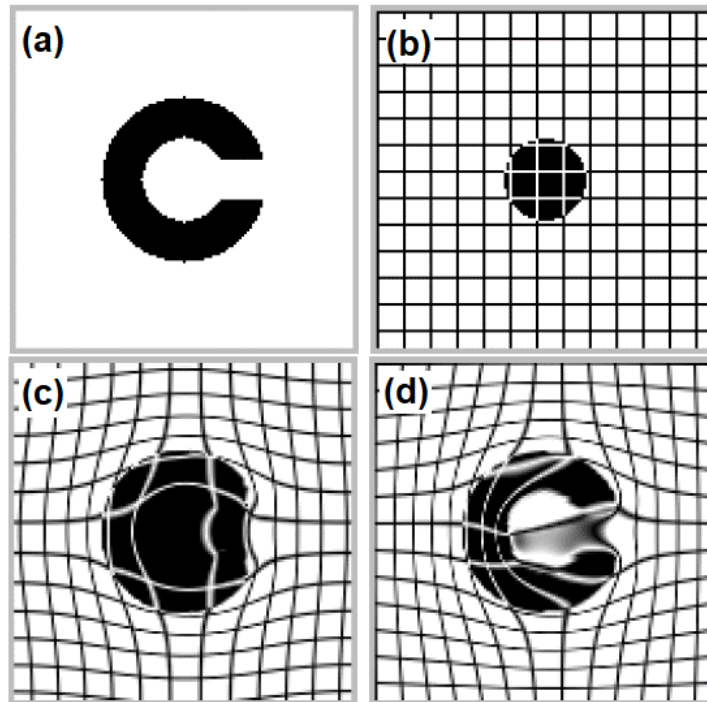


Figure 2.11: A simple illustration of how the Demons algorithm registers an image of a circular spot to fit to an image of the letter C by deforming the image grid (grid added for visualization later): (a) shows the reference image, (b) shows the image to be registered, (c) shows the registration results with Demons algorithm, and (d) shows the registration using a method simulating elastic deformations [173].

A further development to the Demons algorithm is to adapt it to a diffeomorphic image registration technique, as reported and discussed in detail in [174], which is also the current version of the algorithm that is used as the MATLAB function *imregdemons* [175]. A diffeomorphism is an invertible structure-preserving mapping between smooth differentiable manifolds where both the differentiable map between the two manifolds and its inverse are differentiable. This invertibility is quite useful to ensure smooth transformations, while also being able to preserve the topology of the surfaces being dealt with, so that folding is

handled effectively in real images. A diffeomorphic map can also be good input data when no prior information about an image and the spatial transformations are available.

The non-parametric diffeomorphic image registration algorithm proposed in [174] based on the demons algorithm of [172] is therefore an adaptation of the optimization process on the entire space of displacement fields to an optimization on the space of diffeomorphic transformations. It introduces smoother deformations which have much less folding artefacts, are computationally efficient, and rests on a much more well-developed mathematical framework than initially developed. An example of the diffeomorphic Demons algorithm in Figure 2.11 shows a simple image-matching exercise as an illustration of the technique.

The Demons algorithm is an useful tool to carry out wavefront reconstruction using speckle images. We shall now move on to discussing how speckles themselves are useful for multiplexing information contained in a light beam.

2.1.4.2 Chromaticity and multiplexing

Speckle pattern formation is strongly wavelength-dependent, as the scattering path in the complex medium is directly related to the wavelength of the transmitted wave. A multi-spectral speckle pattern is a superposition of multiple speckle patterns generated by each narrow spectral band in the entire spectral region of interest. It is possible to spectrally decorrelate the integrated speckle pattern sufficiently so that the individual spectral speckle patterns are retrievable during speckle image reconstruction. For this purpose, the scattering medium has to be chosen appropriately, i.e. - 1. the scatterer must transmit in the spectrum of interest, and 2. the spatial dimensions of the scatterer should be enough to spectrally decorrelate the speckle patterns generated by two different spectral bands [176]. In 2018, S. Sahoo *et al.* demonstrated the spatial and spectral information retrieval from a broadband white light source using a thin diffuser (scattering medium) and a speckle-imaging camera [177]. Spatial correlation of speckles allows us to reconstruct spatial information while spectral decorrelation of speckles allows us to retrieve the spectrum of the scene or object behind the scattering medium. Within the constraints imposed by the imaging system, the multiplexed spatial and spectral information could be retrieved together [178] [179], albeit with trade-offs on the resolution of either due to the lack of an infinite imaging sensor. Other interesting applications like nanoscale light localization in metamaterials [180], in-situ wavefront correction [181], and selective light-focussing on nano-objects [182] have been demonstrated by shaping waves through complex media.

2.1.5 Infrared phase imaging

In this chapter, we have seen till now the various techniques employed for phase imaging as well as the multitude of their applications. However, most of these developments have been carried out in the visible region of the electromagnetic spectrum, as well as in the near infrared. We will now review the application of some of these aforementioned techniques in the longwave infrared, and also highlight the state-of-the-art in infrared phase imaging through scattering media, which to the best of our knowledge, is quite limited.

Applications in the longwave infrared include speckle interferometry used to combine holography (the first infrared holography experiment being reported in [46]) and thermography in a single sensor for non-destructive testing [183], aeronautics material flaw detection using a mobile speckle interferometer [184], single-pixel sensor based imaging of thermal objects [185], simultaneous temperature and deformation measurement using LWIR speckle interferometry [186], vibration analysis [187], infrared optical metrology using quadriwave lateral shearing interferometry [188], LWIR digital holography [189], digital in-line holographic interferometry for metrology [190], LWIR Shack Hartmann wavefront sensors [191] for space telescope mirror measurements [192], and high-power CO₂ laser beam correction [193]. In the mid-wavelength infrared, the group of A.T. Watnik has demonstrated imaging through scattering media using speckle correlations [194], wavefront sensing in deep turbulence [195], and wavefront correction [196]. Commercial wavefront sensors in the LWIR are also available from PHASICS [197], even as the details of their internal mechanism is not readily available.

Speckle imaging in the visible has shown that it is possible to do single-shot phase reconstruction of objects through a scattering medium. The diverse applications and versatility of speckle imaging in the visible region has prompted us to consider it for applications in the infrared. **The aim of this work is therefore to develop a compact one-shot LWIR wavefront sensor based on speckle imaging that is able to work in the entire LWIR spectrum.** In addition to developing LWIR phase imaging, it is also an opportunity to study infrared speckle physics, both of which are relatively new domains of research.

We will now introduce the basic concepts related to the understanding and characterization of speckles, as well as the fundamental principles about light propagation through scattering media. This will allow us to appreciate the essential theoretical considerations when generating speckles and utilizing them to carry out imaging for wavefront sensing.

2.2 Speckles

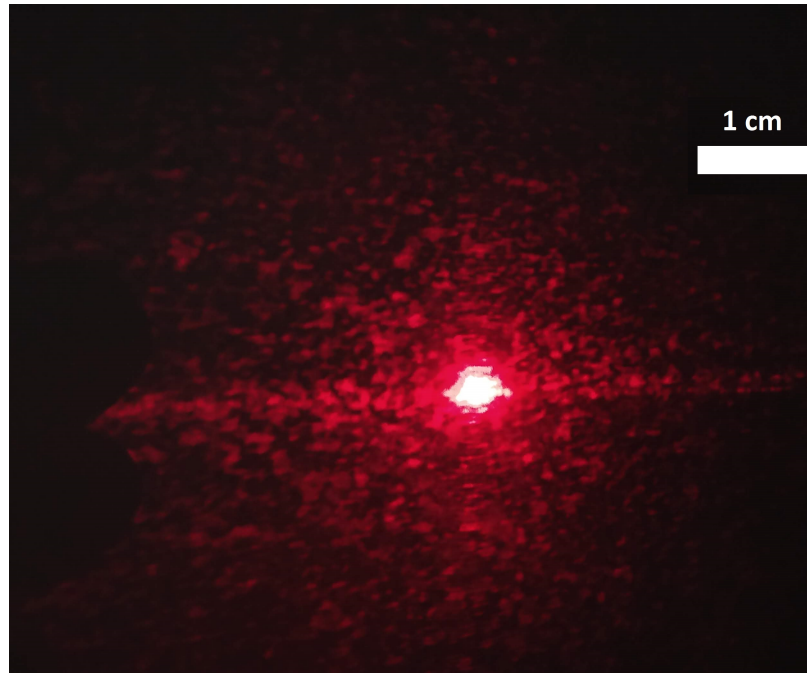


Figure 2.12: Red laser beam (671 nm) reflected off the surface of a wall [198]

When laser light is reflected off materials like paper or the surface of a wall, an observer looking at the laser spot on the wall sees a fine-scale complicated granular pattern with high contrast, i.e. alternating bright and dark spots that are much smaller than the size of the reflected beam spot, as shown in Figure 2.12. Even though a laser beam has relatively uniform illumination, measurement of the intensity of the granular pattern shows that the fine-scale fluctuations exist in space. This granular pattern is termed a speckle.

The origin of a speckle pattern is the irregular roughness of the surface that reflects the incident light. Most materials in the world, when not polished, exhibit a surface roughness of the order of an optical wavelength ($\sim 1 \mu\text{m}$). Different microscopic parts of the rough irregular surface produce elementary contributions possessing random phases to the total observed field. These randomly phased partial contributions interfere with each other, giving rise to a resultant intensity pattern, whose strength closely depends on the particular configuration of the random phase contributions present. Therefore, a rough surface microscopically dephases the coherent wavefront of laser light upon reflection, which then interferes to produce the fine-scale local intensity interference pattern that is seen by an observer.

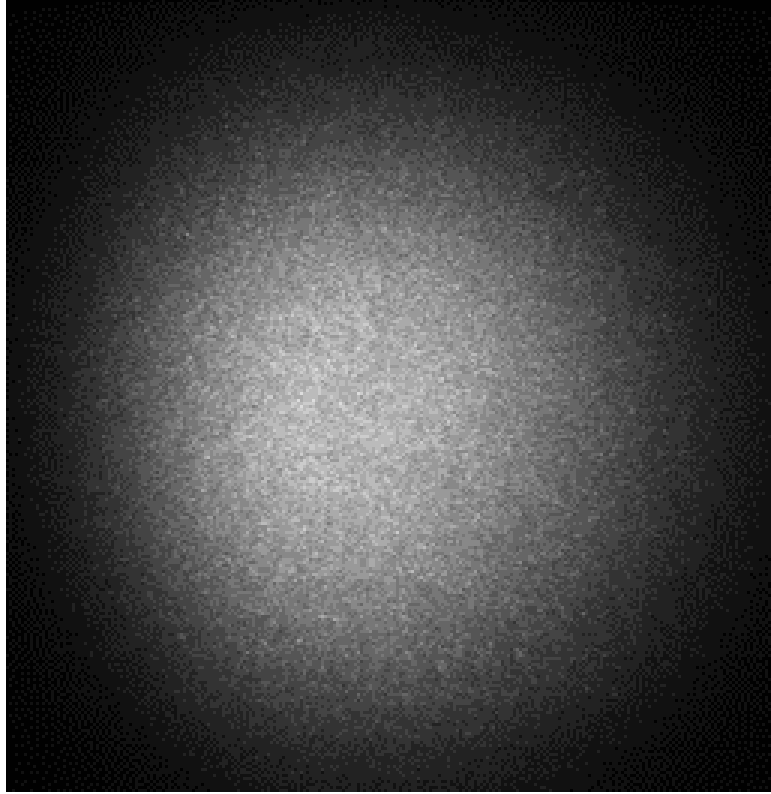


Figure 2.13: Laser beam (638 nm) transmitted through white paper

A speckle can also be seen upon transmission through a scattering medium, like printing paper, as shown in Figure 2.13, with the underlying basis for the generation of a speckle pattern being similar in both transmission and reflection. The component light rays of the incident light beam undergo different optical paths and / or scattering due to variations in the thickness and refractive index inside the transmissive medium. Since the exact configuration inside the medium is random, the optical paths of different component light rays vary significantly. These optical path variations are on the order of the wavelength of light, which leads to randomly dephased light rays that interfere beyond the transmission medium to create a speckle pattern.

Definition: *A speckle is the mutual interference pattern between multiple incoherent wavefronts generated when coherent light is reflected by or transmitted through a disordered material, whose surface roughness on the scale of an optical wavelength introduces fine-scale local random dephasing.*

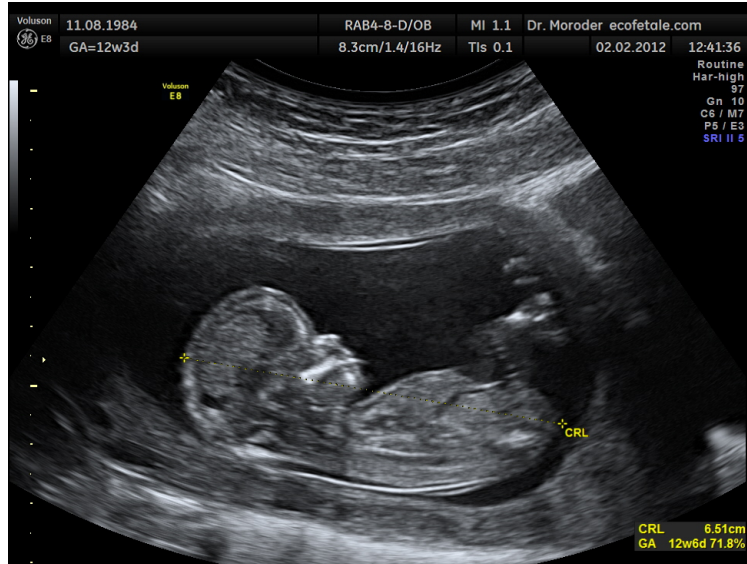


Figure 2.14: Ultrasound image with speckles, of a fetus in the womb, viewed at 12 weeks of pregnancy (Image courtesy of Wolfgang Moroder [199])

Speckle patterns are seen in different kinds of transmission media, ranging from solid surfaces like paper, to white paint on a wall, and even in suspensions of particles. A speckle is frequently observed in many optical transmission or reflection examples, but it is not limited to optical systems alone. Speckles are ubiquitous in ultrasound images, as seen in figure 2.14, where they appear as large blobs with a high contrast [200]. Speckles are also seen in microwave images, like in figure 2.15, where the surface roughness is on the order of a wavelength.

2.2.1 Speckle as random walk

A speckle pattern can be intuitively understood by considering the addition of individual component optical paths during the stochastic scattering process as resembling a random walk [202]. A speckle is composed of multiple complex components with independent individual phases that additively combine to form the final speckle pattern. Each individual complex component can have different random (independent) lengths, i.e. amplitudes, and random (independent) directions, i.e. phases. The individual components are complex in nature as they are usually phasors with an amplitude and phase, representing signal components with a sinusoidal behaviour. The addition of all the complex components is similar to a random walk process in 2-D, where the final resultant vector depends on the relative phases of the individual components. The resultant intensity, which is the

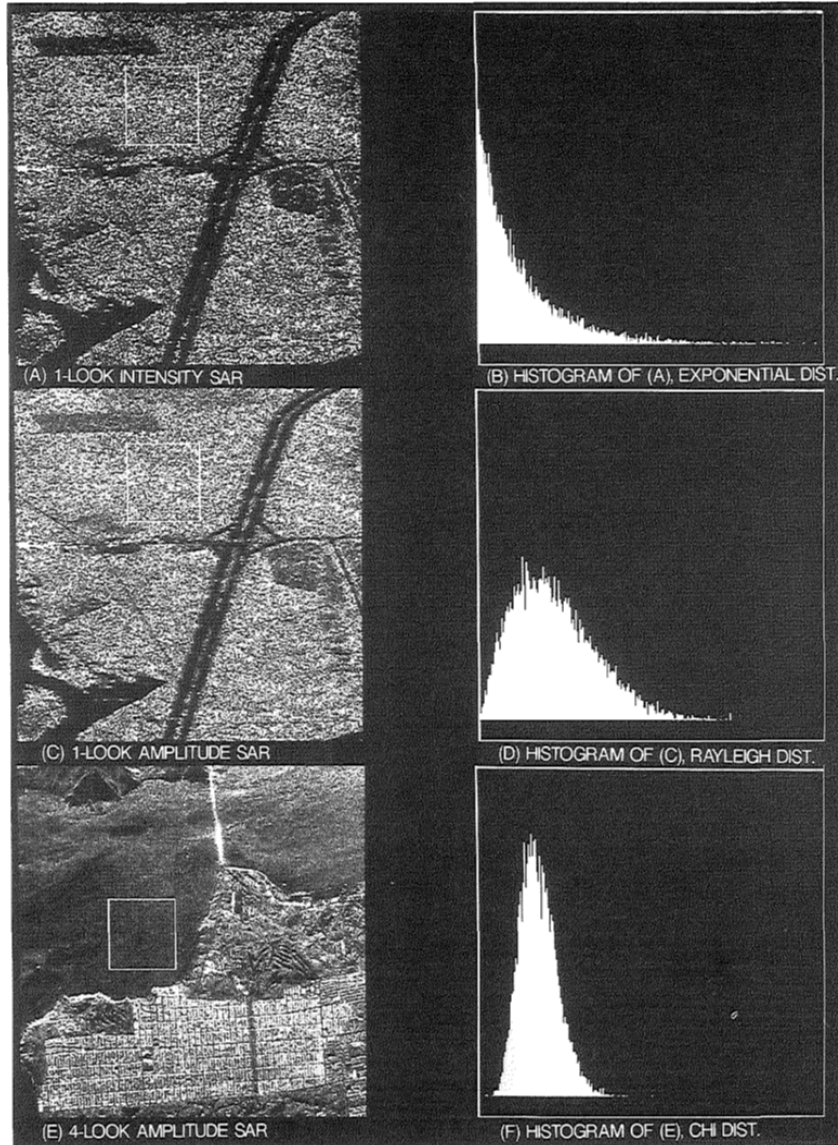


Figure 2.15: Synthetic Aperture Radar (SAR) images with speckles taken from a NASA / JPL aircraft over the San Francisco bay area[201]

resultant amplitude-squared, i.e. square of the vectorial length, depends on whether the phases additively contribute towards constructive interference or destructive interference.

In figure 2.16, the cases with a constructive interference (large resultant amplitude) and destructive interference (small resultant amplitude) are seen, which is primarily due to the different nature of the contributory phase components. It is also quite evident that no single vector dominates the sum, and that both the amplitudes (vector lengths) and phases (vector directions) are random and independent of each other, which is akin to the physical picture

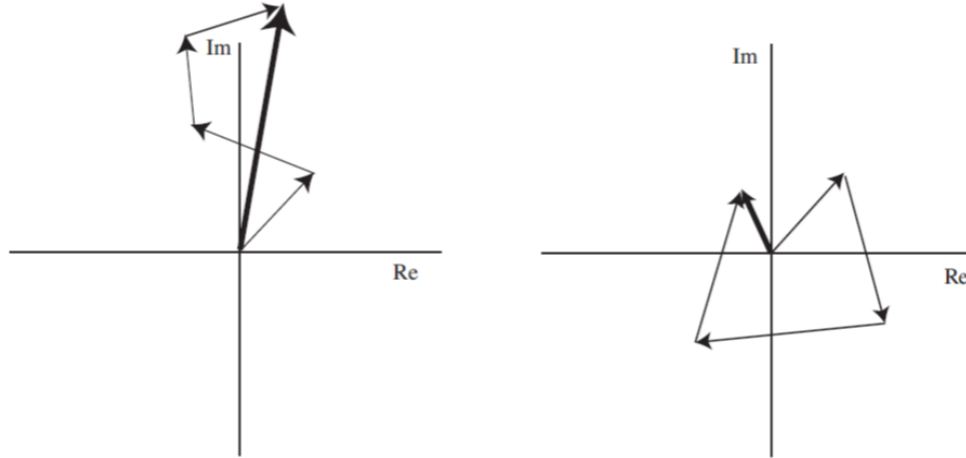


Figure 2.16: Random walk in the 2-D complex plane showing constructive addition (left) and destructive addition (right) [203]

of scattering inside a medium. Having seen such an equivalence between the scattering process that gives rise to a speckle pattern and a random walk, we can expect that the physics of speckle formation is similar to many other real-world phenomenon which can be modelled by a similar 2-D random walk process.

2.2.2 Speckle parameters

The foremost physical characteristic of a speckle is its granularity. In figure 2.17, we see that for an illumination along the direction \mathbf{k}_a , the transmitted speckle intensity collected along \mathbf{k}_b is denoted I_{ba} . Here, \mathbf{k}_a and \mathbf{k}_b are the wavevectors in the directions shown in the figure. We can see from the figure that the observed speckle intensity I_{ba} changes depending on the direction of observation, \mathbf{k}_b . The direction \mathbf{k}_b can be tuned in such a manner that the fluctuations in the observed intensity δI_{ba} become of the order of the mean intensity $\overline{I_{ba}}$, i.e.

$$\delta I_{ba} = \overline{I_{ba}} \quad (2.6)$$

It follows simply that the total intensity can be locally zero, $2\overline{I_{ba}}$, or any value in between.

$$I_{ba} = \overline{I_{ba}} \pm \delta I_{ba} \quad (2.7)$$

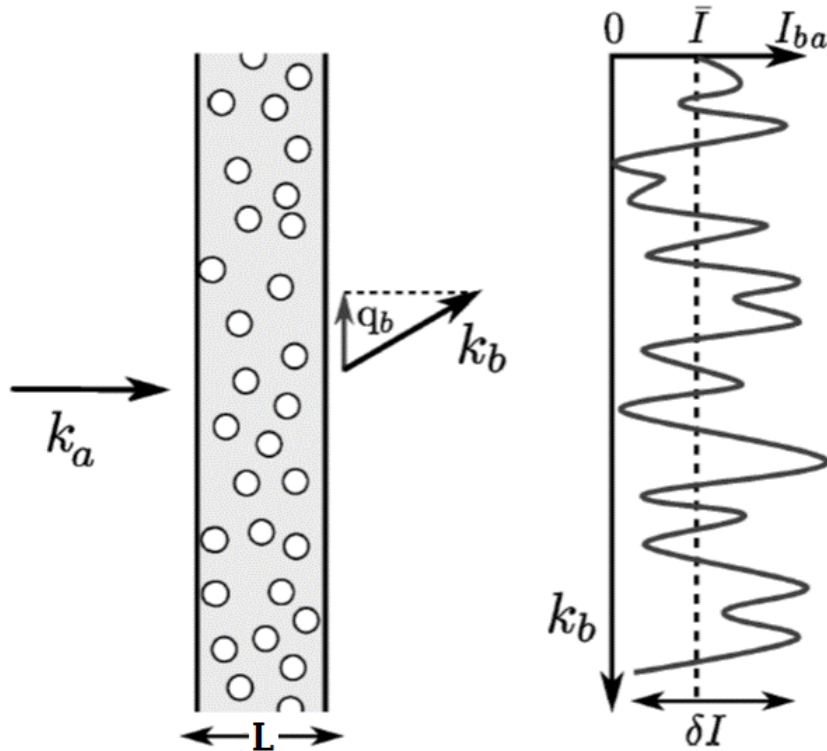


Figure 2.17: Schematics of a disordered slab illuminated by a plane wave, giving rise to a speckle pattern in transmission. [204]

We see therefore that the speckle pattern has a large contrast, being however dependent on the direction of transmitted intensity collection, i.e. k_b . We will now consider the intensity correlation between two different speckle patterns, $\langle I_{ba} I_{b'a'} \rangle$, and see how it can lead us to understand:

- the large fluctuations in the intensity
- the typical size of speckle grains
- what happens when the speckle illumination is shifted, angularly (as a tilt) and spatially
- whether the speckle preserves and carries information of an object placed before the scattering medium even after transmission
- the possibility to retrieve encoded information from a speckle to reconstruct an image of the object.

2.2.2.1 Intensity correlation function

We define a correlation function,

$$C_{bab'a'} = \frac{\langle I_{ba}I_{b'a'} \rangle - \langle I_{ba} \rangle \langle I_{b'a'} \rangle}{\langle I_{ba} \rangle \langle I_{b'a'} \rangle} \quad (2.8)$$

where, I_{ba} and $I_{b'a'}$ are intensities along b and b' for illumination directions a and a' , respectively, and $I_{ba} = |E_{ba}|^2$. For the case when $a = a'$ and $b = b'$, we can easily see that the auto-correlation function turns out to be:

$$C_{baba} = \frac{\langle I_{ba}^2 \rangle}{\langle I_{ba} \rangle^2} - 1 = 1 \quad (2.9)$$

which turns out to be an expression of the granularity condition of speckles.

2.2.2.2 Rayleigh probability distribution of speckle intensity

From the fact that the electric field E is a Gaussian complex random variable, it can be demonstrated that the probability distribution of the speckle intensity I_{ba} will correspond to a Rayleigh distribution, as shown in Figure 2.18 (see [204] or [203] for proof), given by

$$p(I_{ba}) = \frac{1}{\langle I_{ba} \rangle} e^{-I_{ba}/\langle I_{ba} \rangle} \quad (2.10)$$

In fact, to see a speckle pattern, it is not necessary to be in the diffusive regime, i.e. when $L > l^*$, where L is the thickness of the scattering sample and l^* is the transport mean free path inside the scattering medium.

A quick proof of the result above can be obtained by using the central limit theorem. The central limit theorem is a key idea in the theory of probability, which states that the appropriately normalized sum of independent random variables tends towards a normal distribution (i.e. a bell curve), even if the original variables are not normally distributed themselves. Considering $E = X + iY$, where X and Y are independent identically distributed Gaussian variables, we obtain,

$$p(I) \sim p(X)p(Y) \sim e^{X^2/2\sigma^2} e^{Y^2/2\sigma^2} \sim e^{-I/\langle I \rangle} \quad (2.11)$$

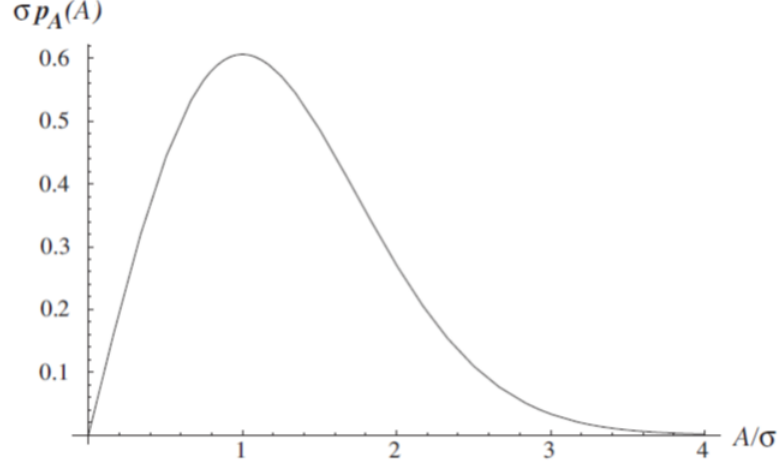


Figure 2.18: Rayleigh probability density function, where $p_A(A)$ is the marginal probability density function of the amplitude (length) A of the resultant phasor [203]

We can decompose the field E_{ba} over all the possible trajectories of scattering events inside the system, as

$$E_{ba} = \sum_S E_S \quad (2.12)$$

where E_S is the output field representative of a particular scattering configuration, as seen in figure 2.19. From the decomposition above, we can consider $X = \sum_S \text{Re}(E_S)$ and $Y = \sum_S \text{Im}(E_S)$, the real and imaginary sums, respectively, as a summation over a large number of independent identically distributed variables. Now, by using the central limit theorem, we obtain:

$$p(X) = \frac{1}{\sqrt{2\pi}\sigma} e^{-X^2/2\sigma^2} \quad (2.13)$$

$$p(Y) = \frac{1}{\sqrt{2\pi}\sigma} e^{-Y^2/2\sigma^2} \quad (2.14)$$

In the equations above, $\sigma^2 = \langle X^2 \rangle = \langle Y^2 \rangle = \langle I \rangle / 2$. The joint probability distribution then reads,

$$p(X, Y) = p(X)p(Y) = \frac{1}{\pi \langle I \rangle} e^{-I/\langle I \rangle} \quad (2.15)$$

The probability distribution for $I = X^2 + Y^2$ then follows by changing variables,

$$p(I) = \int_{-\infty}^{\infty} dX \int_{-\infty}^{\infty} dY p(X, Y) \delta(X^2 + Y^2 - I) \quad (2.16)$$

$$= \int_0^{2\pi} d\theta \int_0^\infty dR R \frac{e^{-R^2/\langle I \rangle}}{\pi \langle I \rangle} \delta(R^2 - I) \quad (2.17)$$

$$= \frac{1}{\langle I \rangle} e^{-I/\langle I \rangle} \quad (2.18)$$

where the following property was used in the last step,

$$\delta[g(x)] = \sum_i \frac{1}{|g'(x_i)|} \delta(x - x_i) \quad (2.19)$$

for a function g with roots x_i .

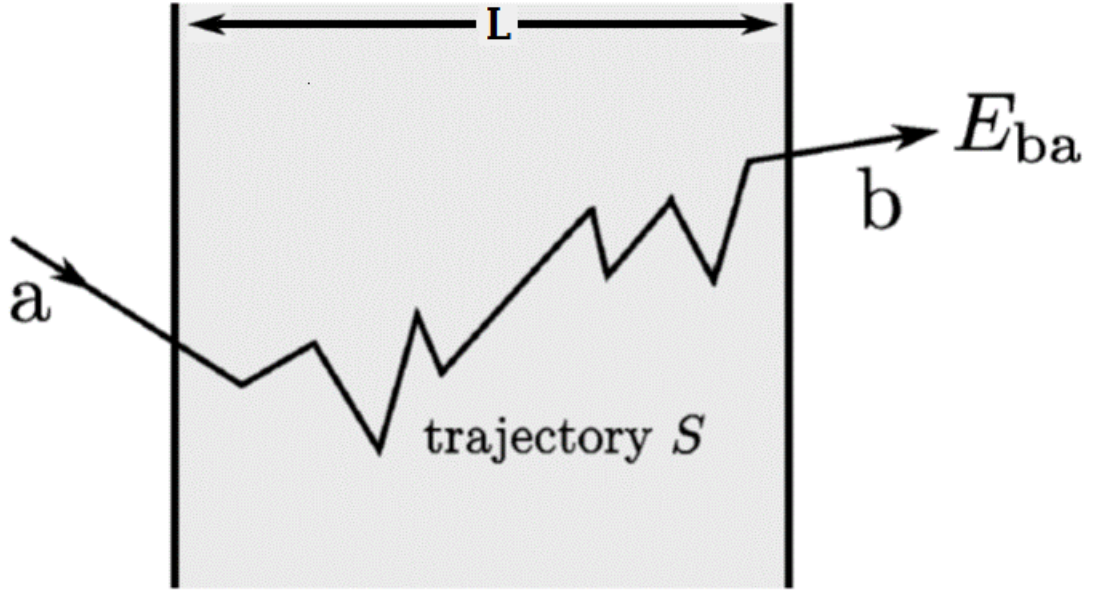


Figure 2.19: A typical scattering sequence inside the scattering medium contributing to the output field. [204]

$Re(E_S)$ and $Im(E_S)$ have been taken as independent, which is a direct consequence of the independence of the amplitude and phase of E_S , which has been implicitly assumed throughout the equations above. The phase of E_S is also uniformly distributed over $[0, 2\pi]$.

By the central limit theorem, we note that both the field components X and Y are symmetrically distributed. However, when the algebraic condition $I > 0$ is imposed, which is true for a physical system, the symmetry does not hold. This asymmetry in the Rayleigh distribution for the intensity gives an indication that the observation of a dark spot has a higher probability than the observation of a bright spot in a speckle pattern.

The angular correlator can be evaluated to give us the form (see proof in [204]),

$$C_{bab'a'} = \left[\frac{\Delta q_a L}{\sinh(\Delta q_a L)} \right]^2 \delta_{\Delta q_a, \Delta q_b} \quad (2.20)$$

which extends over the range of values of Δq_a satisfying $\Delta q_a \lesssim 1/L$. Here, \mathbf{q} refers to the transverse momentum, i.e. the momentum perpendicular to the direction of propagation of radiation. The total momentum \mathbf{k} is split into a longitudinal component (parallel to the direction of propagation) k_z and the transverse momentum \mathbf{q} . The momentum difference is defined as $\Delta \mathbf{q}_a = \mathbf{q}_a - \mathbf{q}_{a'}$ and $\delta_{\Delta q_a, \Delta q_b}$ is the correlation between the input illumination and the output speckle. This result is obtained by taking into account the conservation of the transverse momentum, and is valid in the diffusive regime where $L \gg l$, i.e. the thickness of the scattering medium is significantly larger than the transport mean free path. It is interesting however to note that the correlator does not have an explicit dependence on the transport mean free path l . When $a = a'$ and $b = b'$, we see that $C_{baba} = 1$, which is the result that the contrast of a speckle pattern is equal to 1, as already seen in Equation 2.9, which was arrived at for this specific case without the need for a detailed calculation of the angular correlation function.

2.2.2.3 Memory effect

In the angular correlator in Equation 2.20 above, the term $\delta_{\Delta q_a, \Delta q_b}$ shows that strong correlations between the post-transmission speckle pattern and the input illumination beam always exist, irrespective of the strength of the disorder of the scattering medium. This signifies that an angular tilt in the illumination beam from \mathbf{k}_a to $\mathbf{k}_{a'}$ will result in the same speckle pattern, albeit globally shifted translationally by an amount equal to Δq_b which is proportional to Δq_a , as can be seen in figure 2.20.

The factor $[\Delta q_a L / \sinh(\Delta q_a L)]^2$ is a measure of the range of the memory effect, which can be measured experimentally as shown in [50]. The typical width of the range of the memory effect is around $\Delta q \sim 1/L$. We know that $q = k \sin \theta$, and this relation corresponds to an angular range equivalent to $\Delta \theta \simeq \Delta q / k$. Therefore, the angular range of the memory effect can be approximated as,

$$\Delta \theta|_{memory} \sim \frac{1}{kL} \quad (2.21)$$

with $k = 2\pi/\lambda$. It can be easily seen that the angular range of the memory effect is significant when the thickness of the scattering sample is thin, and that the angular range

Memory effect graphical representation]

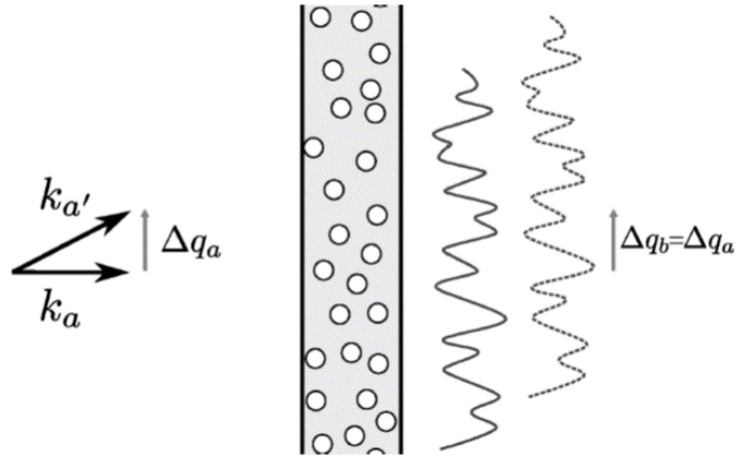


Figure 2.20: Graphical representation of the memory effect [204]

also scales proportionately with the wavelength of light. Therefore, the angular range of the memory effect can be tuned by controlling the light wavelength and the scatterer thickness. In the longwave infrared range, this memory effect is therefore longer than in the visible. It should be noted that this equation is valid in the diffusive regime, where the following inequality holds, $L \gg l \gtrsim \lambda$. Typically, for visible light, the highest memory angle is about $\Delta\theta \sim 0.1^\circ$, when considering $\lambda \lesssim 1 \mu\text{m}$. Even though this angle is quite small, it is possible for the entire extent of an object to fall within the angular range of the memory effect, if it is placed sufficiently far from the scattering medium. In the longwave infrared, considering the wavelength to be $10 \mu\text{m}$, and the thickness of the scattering medium to be at least 10 times the wavelength to be in the diffusive regime, the angular range of the memory effect turns out to be approximately 1° . We shall see later in Section 4.3 that in our longwave infrared experiments, the range of the angular memory effect of our scattering medium is of the same order of magnitude.

2.2.2.4 Speckle grain size

The mean size of a speckle grain in the far field is given by the width of the angular correlator defined above in Equation 2.20. However, when we put in $a = a'$, we see that the width turns out to be zero, which is unrealistic since speckle grains do have a finite size. It turns out that this result arises from the fact that both the illumination and the scattering system are assumed to be invariant along the transverse direction. Since we illuminate a finite portion of the scattering medium in any real experiment, we shall consider a finitely sized

illumination beam having a transverse illumination profile $P(\boldsymbol{\rho})$. This loss of invariance along the transverse direction modifies the transverse input illumination state from $|\Delta\mathbf{q}_a\rangle$ to,

$$|\Delta\tilde{\mathbf{q}}_a\rangle = \int d\boldsymbol{\rho} P(\boldsymbol{\rho}) \langle \boldsymbol{\rho} | \Delta\mathbf{q}_a \rangle | \boldsymbol{\rho} \rangle \quad (2.22)$$

where $\boldsymbol{\rho}$ is the transverse coordinate (perpendicular to the direction of propagation, with $\mathbf{r} = (z, \boldsymbol{\rho})$) and $\Delta\mathbf{q}$ is the transverse momentum. The bra-ket notation more conveniently represents the bases $\boldsymbol{\rho}$ and \mathbf{q} , such that $E(\boldsymbol{\rho}) = \langle \boldsymbol{\rho} | E \rangle$ and $E(\mathbf{q}) = \langle \mathbf{q} | E \rangle$ is the Fourier transform of $E(\boldsymbol{\rho})$.

Therefore, the angular correlator in equation 2.20 now becomes,

$$C_{bab'a'} = \left[\frac{\Delta q_b L}{\sinh(\Delta q_b L)} \right]^2 P(\Delta\mathbf{q}_a - \Delta\mathbf{q}_b)^2 \quad (2.23)$$

where $P(\mathbf{q})$ is the Fourier transform of the transverse illumination profile $P(\boldsymbol{\rho})$. Considering the typical width of $P(\boldsymbol{\rho})$ to be W , the angular size of a speckle grain will be

$$\Delta\theta|_{grain} \sim \min\left(\frac{1}{kL}, \frac{1}{kW}\right) \quad (2.24)$$

We know from experiments that usually $W \gg L$, and it follows that $\Delta\theta|_{grain} \sim \frac{1}{kW}$. This result also holds in the quasi-ballistic regime, i.e. where $L \sim l$, as it arises from the diffraction of the illumination beam.

2.2.2.5 Spatial correlation function of a speckle

We have seen results above originating from the angular correlation function in a few physical cases. It is also instructive to compute the spatial correlation function. Without going into the calculation itself, it is important to mention here that unlike the angular correlation result leading to a memory effect, there is no correlation between the input and the output light waves in real space. Hence, there is no spatial memory effect through a scattering medium. This is a valuable result since this means that a speckle pattern is not only a unique fingerprint of an object even after undergoing transmission or reflection through a scattering medium, but a speckle also uniquely encodes the spatial positional information of an object. This would allow us to retrieve the position of an object by analyzing its speckle pattern. This kind of a retrieval of the positional information would not be possible if there were a spatial memory effect as well. Through the spatial correlation function, the

size of a speckle grain can be computed, and it turns out to be,

$$\Delta x|_{\text{grain}} \sim \lambda \quad (2.25)$$

a result which holds for a speckle even inside the disordered scattering medium. The result above is also independent of the size of the inhomogeneities present in the scatterer.

2.3 Summary

The basic concepts involved in understanding speckles have been discussed in Section 2.2, while a more complete review of the theories related to the propagation of waves in scattering media like radiative transfer theory [205] and particle diffusion can be found in [48] and [206]. The majority of studies carried out till now on speckle-based information retrieval, specifically spatial imaging, phase sensing and spectrometry, have all been carried out in the visible region of the electromagnetic spectrum or in the near-infrared band of the electromagnetic spectrum.

The theories of speckle formation and wave transmission in complex media predict that these effects should be similar at all wavelengths. Also, to the best of our knowledge, these techniques have never been developed in the thermal infrared band or the long-wave infrared band of the electromagnetic spectrum. Therefore, **we seek to study speckle-based imaging and spectrometry in the thermal infrared from 8 to 14 μm** . The motivation for such a research objective is the experimental observation and subsequent understanding of fundamental speckle physics in the thermal infrared region, and the possible development of novel applications in the same spectral region. This work will require specifically developed optimization techniques for problems emerging in the thermal infrared region due to the overlapping thermal emission from the background, which we shall see in the following Chapter.

Chapter 3

Longwave infrared speckle imaging - experimental setup development

Contents

3.1 Diffuser	45
3.1.1 Diffuser requirements	45
3.1.2 Infrared transparency and transmission properties	46
3.1.3 Initial diffuser trials	48
3.1.4 Silicon wafer diffuser	53
3.2 Infrared source	58
3.2.1 Blackbody	59
3.2.2 Soot as blackbody source	61
3.2.3 Coiled filament source	61
3.2.4 Silicon nitride global source	67
3.2.5 Silicon carbide global source	69
3.3 Point source	71
3.3.1 Coherence length and time	73
3.4 Infrared detector	79
3.4.1 Bolometers	79
3.4.2 Microbolometers	81

3.4.3	Microbolometer detector responsivity	83
3.4.4	FLIR longwave infrared camera	85
3.4.5	Summary	87

In the previous chapters, we have seen the necessity of developing a longwave infrared speckle imaging system for wavefront sensing, as well as looked at the major theoretical and experimental developments that are essential in building such an experiment. In this chapter, we shall discuss

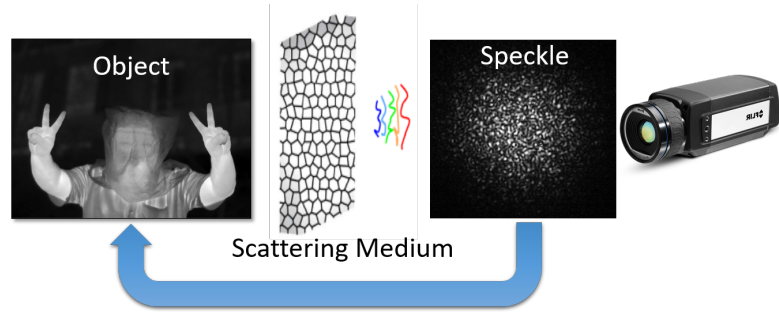


Figure 3.1: Minimal experimental setup for imaging through scattering media

the development of an LWIR speckle imaging system, which to the best of our knowledge, is the first demonstrated in literature. The experimental apparatus designed for imaging in the longwave infrared through a scattering media is described in this chapter. It is a novel design that incorporates the basic elements of imaging through scattering media as known from the literature in the visible range of the electromagnetic spectrum [177] [51], while also being adapted for specific requirements of longwave infrared imaging to a certain degree. In addition to the design itself, the materials used for the optical components and especially the scattering medium required a careful consideration of the choices available in the limited range of materials that transmit in the longwave infrared. After an introduction of the design of the setup, we will discuss in detail the key individual elements that comprise the experimental setup.

The essential components of an imaging setup through scattering media are an imaging object, a scattering medium, and a detector to record the scattered light, as shown in Figure 3.1. In our case, we have worked with a configuration that works in transmission, i.e. the detector is positioned to record the scattered light after transmission through the scattering medium’s length along the direction of light propagation. As depicted in Figure 3.2, we use a heated blackbody as a thermal source, which is then imaged onto an iris to control its spatial extent. The image of the primary source on the iris serves as our homogeneous secondary source. This secondary source is then collimated to produce a plane wavefront

that impinges on a phase object, thereby distorting the wavefront. The distorted wavefront is then incident on a thin surface scatterer which forms a speckle in transmission. The transmitted speckle is finally imaged using an objective lens onto a FLIR uncooled microbolometric camera.

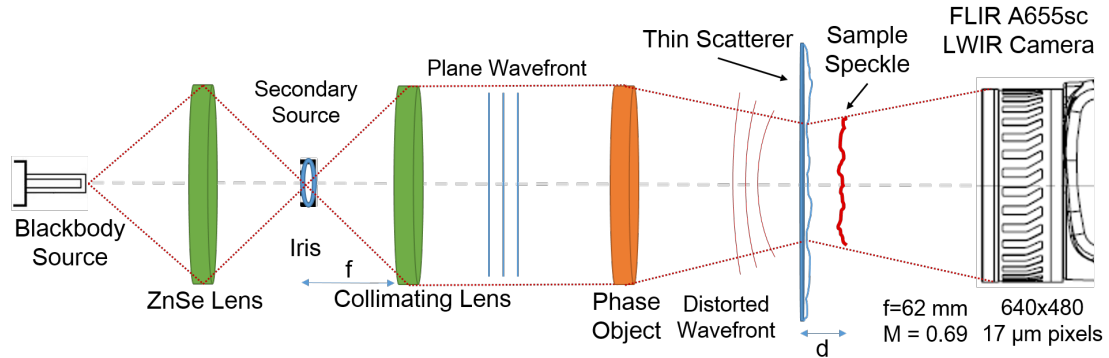


Figure 3.2: Experimental setup for longwave infrared speckle imaging through scattering media

In the case of a similar setup for speckle imaging in the visible part of the electromagnetic spectrum, which is the classical case in this field, there are multiple options and choices in obtaining key optical components necessary for the setup. Firstly, all the materials that are usually available in the visible for optical components do not work in the longwave infrared. For example, the glass material N-BK7 [207], which is ubiquitous in visible optical glass applications, does not transmit longwave infrared radiation, as can be seen in Figure 3.3. Secondly, the choice of an optical source is also limited in the longwave infrared compared to the diverse types of lasers and alternative sources available in the visible region. In our case, due to the inability to use a strong laser in conjunction with our sensitive camera, we had to resort to using blackbody sources whose choice is limited by the materials available that can produce adequate incident power in the longwave infrared and in a desirable geometry. The limitation of choices of optical materials in the longwave infrared, in addition to the fact that the emission of the surroundings is also in the same wavelength region, prompted the necessity for us to develop a novel setup optimised for longwave infrared speckle imaging. We now discuss the key elements of our setup and some of the design choices that arose from practical considerations to optimise the detection of speckles in the longwave infrared, in the following sections.

3.1 Diffuser

A diffuser is any material that scatters light incident on the material. The scattering medium is the most important element for carrying out imaging through such a medium, and an optimal choice is necessary for the success of the imaging technique.

3.1.1 Diffuser requirements

There are multiple parameters to consider when choosing an appropriate scattering medium, like:

1. Transmission in the wavelength region of interest (7 - 14 μm , in our case)
2. Scattering strength - related to the surface roughness
3. Scattering dimension - surface scattering or volumetric scattering
4. Scatterer geometry - thickness and shape of the scattering medium

An ideal scattering medium would have significant transmission (>80%) in the longwave infrared region and a relatively low refractive index to ensure that the incident infrared radiation would not be reflected off, as discussed in the next Section 3.1.1.1.

3.1.1.1 Intensity loss from interface reflection

At every interface, due to the refractive index difference between the propagation medium (air, in our case) and the scattering material or different optics, the incident beam undergoes a reflection and this leads to a fractional loss of incident power. The Fresnel equations for any isotropic, linear, homogeneous and dielectric or non-magnetic media (i.e. where the magnetic permeability of both the media, $\mu_1 = \mu_2 = \mu_0$) give us the amplitude reflection coefficient r_{\perp} and the amplitude transmission coefficient t_{\perp} for an electric field \vec{E} that is perpendicular to the plane of incidence as [208]:

$$r_{\perp} \equiv \left(\frac{E_{0r}}{E_{0i}} \right)_{\perp} = \frac{n_i \cos \theta_i - n_t \cos \theta_t}{n_i \cos \theta_i + n_t \cos \theta_t} \quad (3.1)$$

$$t_{\perp} \equiv \left(\frac{E_{0t}}{E_{0i}} \right)_{\perp} = \frac{2n_i \cos \theta_i}{n_i \cos \theta_i + n_t \cos \theta_t} \quad (3.2)$$

with E_0 being the amplitude, n the refractive index of the medium, θ the angle and i, r, t respectively being the incident, reflected and transmitted components of the variables.

Similarly, the Fresnel equations for the case of the electric field \vec{E} being parallel to the plane of incidence gives us the amplitude and transmission coefficients r_{\parallel} and t_{\parallel} as:

$$r_{\parallel} \equiv \left(\frac{E_{0r}}{E_{0i}} \right)_{\parallel} = \frac{n_t \cos \theta_i - n_i \cos \theta_t}{n_i \cos \theta_t + n_t \cos \theta_i} \quad (3.3)$$

$$t_{\parallel} \equiv \left(\frac{E_{0t}}{E_{0i}} \right)_{\parallel} = \frac{2n_i \cos \theta_i}{n_i \cos \theta_t + n_t \cos \theta_i} \quad (3.4)$$

The fraction of incident power that is reflected at an interface is known as the reflectance R , which is the square of the amplitude reflection coefficient r . In the case of normal incidence, the reflectance and similarly, the transmittance T simplifies to:

$$R = R_{\parallel} = R_{\perp} = \left(\frac{n_t - n_i}{n_t + n_i} \right)^2 \quad (3.5)$$

$$T = T_{\parallel} = T_{\perp} = \frac{4n_t n_i}{(n_t + n_i)^2} \quad (3.6)$$

The reflectance losses of various infrared materials are computed with respect to air in Table 3.1.

3.1.2 Infrared transparency and transmission properties

The first thing that we had to consider was the transparency of the material that would be used as a scattering medium in the longwave infrared, which is quite different from those that are used in the visible, as can be clearly seen in Figure 3.3.

Some candidates that were considered were Sodium Chloride (NaCl), Potassium Chloride

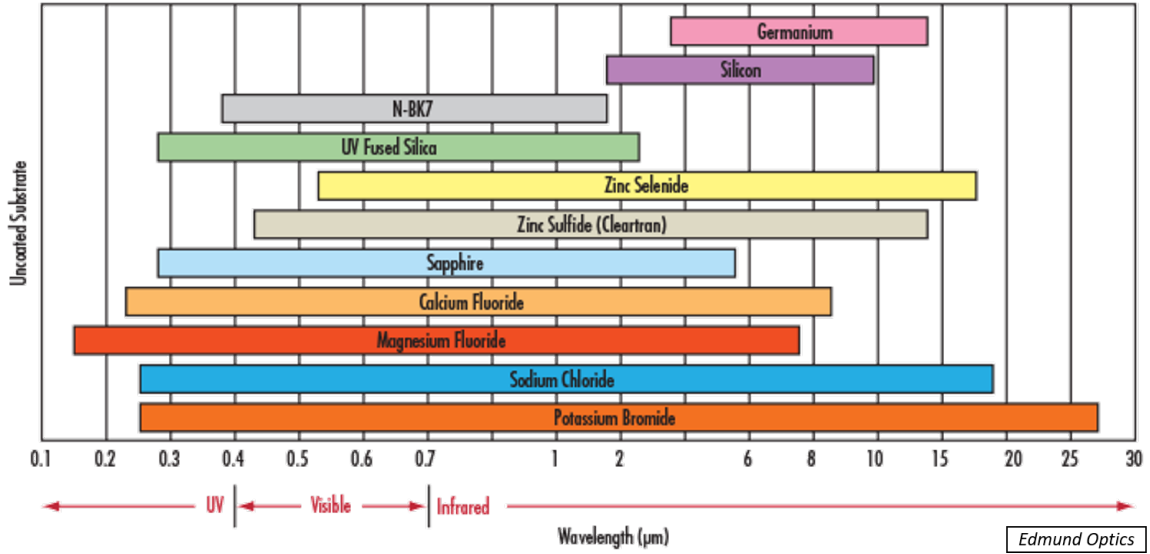


Figure 3.3: Materials with a refractive index and transmission coefficient compatible with infrared applications [209]

Material	Refractive Index at 10 μm	Infrared Transmission at 10 μm	Interface Reflectance Loss (w.r.t. air)
Potassium Chloride (KCl)	1.46	>90%	3.50%
Sodium Chloride (NaCl)	1.49	90%	3.87%
Potassium Bromide (KBr)	1.53	>85%	4.39%
Zinc Sulfide (ZnS)	2.20	>75%	14.10%
Zinc Selenide (ZnSe)	2.40	70%	17.00%
Gallium Arsenide (GaAs)	3.30	>55%	28.60%
Silicon (Si)	3.47	>30%	30.50%
Germanium (Ge)	4.00	>45%	36.00%

Table 3.1: Refractive indices of materials with infrared transmission at 10 μm

(KCl), Potassium Bromide (KBr), Gallium Arsenide (GaAs), Zinc Selenide (ZnSe), Zinc Sulfide (ZnS), Silicon (Si) & Germanium (Ge) [210], some of whose infrared transmission spectra are shown in Figures 3.4, 3.5 and 3.14.

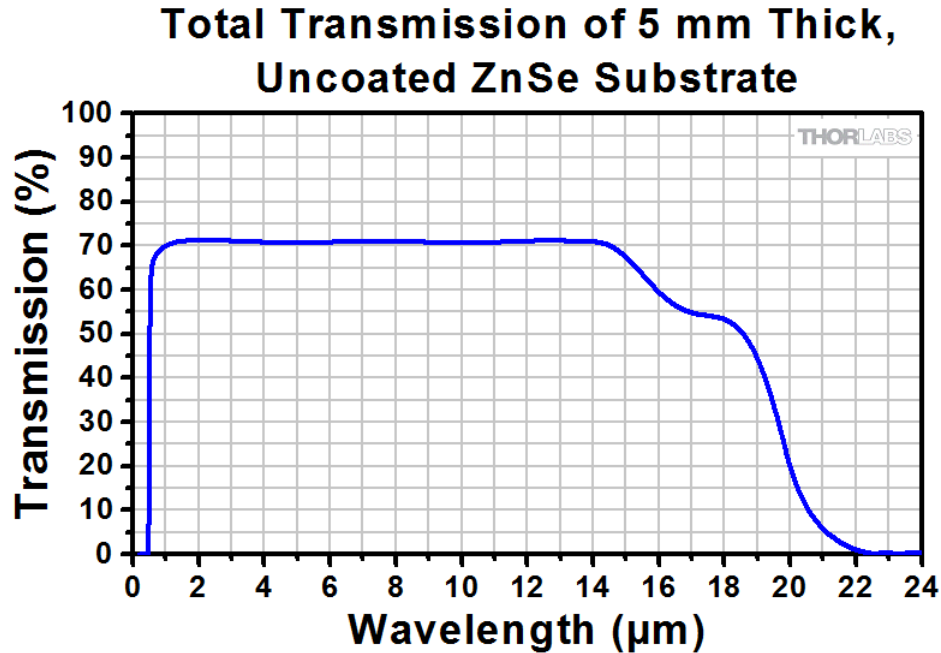


Figure 3.4: Infrared transmission spectrum of 5 mm thick Zinc Selenide (ZnSe) slab [211]

3.1.3 Initial diffuser trials

3.1.3.1 Sodium chloride (NaCl)

Initially, we tried to evaporate a supersaturated solution of grains of table salt (NaCl) to form discs of thickness between 1-5 mm and diameters between 5-10 cm as a scattering medium (see Figure 3.7 [a,b]). Additional chemical or physical treatment was not carried out, and the resulting discs had salt clusters that were big enough to block light transmission except for some ballistic light that could pass through (see Figure 3.7 [e,f]). Some parts of the discs had crystalline structures, the smallest of which was about 50 μm in size, as shown in Figure 3.6.

Subsequently, we tried to ground NaCl to a fine powder using a mixer and grinder and then bake it in an oven to form a more homogeneous salt disc (see Figure 3.7 [c]). These discs blocked both visible and longwave infrared light transmission almost uniformly since their thickness turned out to be larger than those prepared using the evaporative method. An attempt to drizzle NaCl grains on a scotch tape and coat it for use as a scattering medium also demonstrated that such large grains did not effectively scatter light (see Figure 3.8 [a]), with most of the scattering arising from the scotch tape’s surface roughness itself. There was also a significant fraction of ballistic light when imaging through the scotch tape

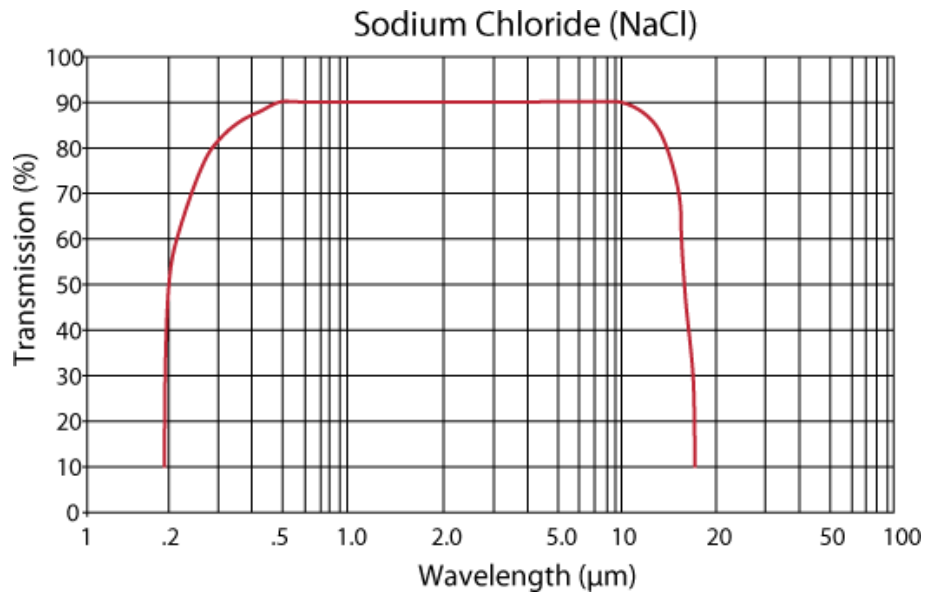


Figure 3.5: Infrared transmission spectrum of a 2 mm thick Sodium Chloride (NaCl) slab [212]

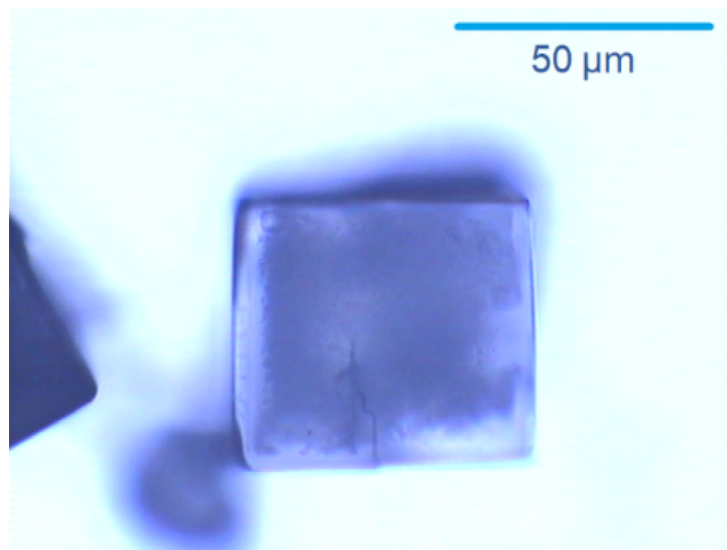


Figure 3.6: Microscope image of a lab-prepared Sodium Chloride (NaCl) disk showing a single crystal

surface.

Since fabricating NaCl windows was not possible in the lab due to the need for applying high pressure to NaCl to create such windows, commercially available salt windows were tested for their performance as scattering media in the longwave infrared. Windows made from NaCl and KCl of various diameters ranging from 2-6 mm with a thickness of 1-2 mm

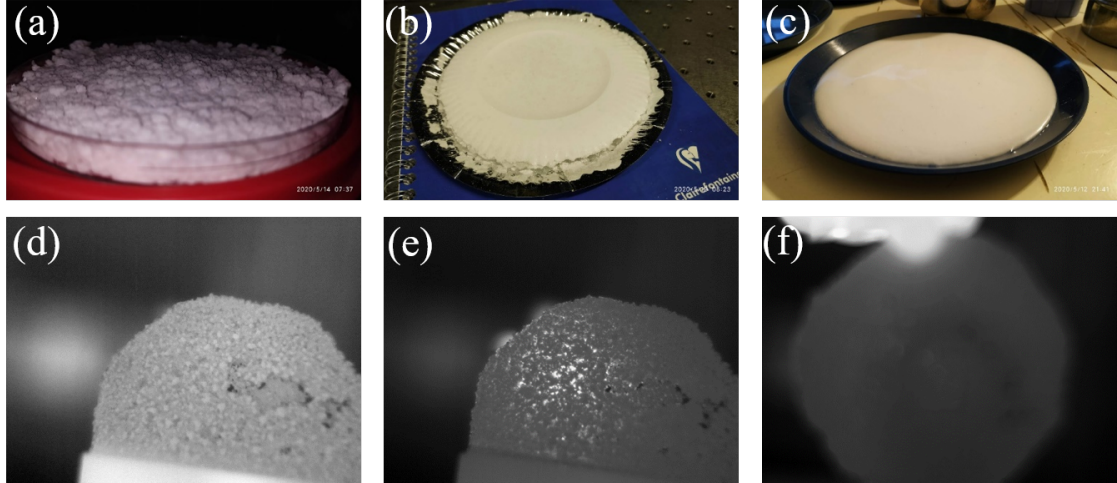


Figure 3.7: Sodium Chloride (NaCl) disks prepared in the lab by (a) & (b) evaporative drying, and (c) finely powdering and baking, and the corresponding observed infrared images of the NaCl disk shown in [a] (d) without any incident infrared radiation, (e) in-focus, with incoming infrared radiation from a blackbody source scattered and ballistically propagating, and (f) NaCl disk shown in [c] blocking infrared light.

were tested as scattering media. Even though they scattered light and reduced the ballistic transmission of infrared light through them, no speckle pattern was produced and instead a wide diffuse region was observed. It was believed that the surface of the salt windows were too smooth to create a speckle pattern, and consequently we polished the surface with water and coarse sandpaper and allowed it to evaporatively dry to check for an improvement in the observed post-scattering transmitted light. Sandpapers of various grain dimensions ranging from 100-500 μm were then used to polish a single surface of the salt windows but without much success (see Figure 3.8 [c]), which thwarted their possible use as longwave infrared scattering media.

3.1.3.2 Gallium arsenide (GaAs)

At this stage, single side polished Gallium Arsenide (GaAs) wafers were also tested to see their efficacy as scattering media, but it did not work as well. The unpolished surface had surface features with height differences above 20 μm , as shown in Figure 3.9, which would mean that the optical path difference $\delta = (n_{\text{GaAs}} - n_{\text{air}}) \times \text{roughness} \approx (3.3 - 1) \times 20 \mu\text{m} = 46 \mu\text{m}$, i.e. approximately 5 times if we consider 10 μm as the reference wavelength of longwave infrared light.

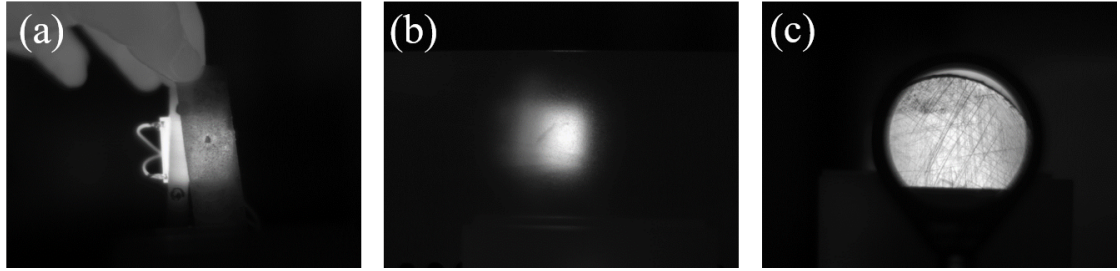


Figure 3.8: Images of transmitted infrared radiation scattered through (a) a scotch tape sprinkled with powdered NaCl grains, (b) finely powdered NaCl sprinkled on a measuring ruler with a rough surface on the order of a few hundred micrometers, and (c) NaCl windows roughly polished with sandpaper.

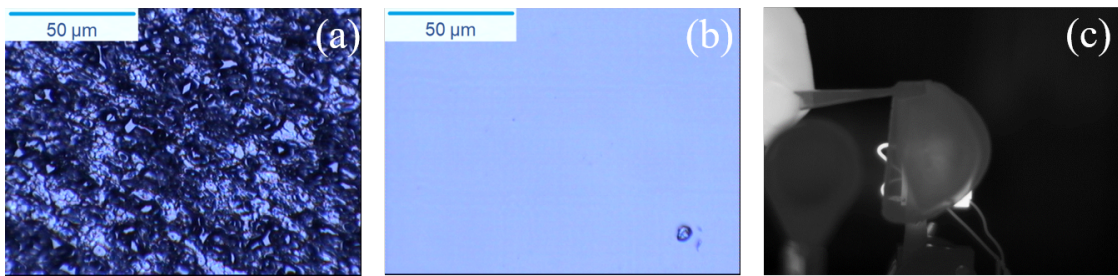


Figure 3.9: Gallium Arsenide (GaAs) wafer - Microscope images of the (a) unpolished surface, and (b) polished surface, and (c) the scattered infrared radiation imaged in transmission through the wafer.

3.1.3.3 Powdered materials - salts and oxides

An alternative strategy to control the surface structuration of the scattering media was to deposit powdered material over relatively flat surfaces. This required a change in the orientation of the setup from a horizontal to a vertical configuration. The first candidate diffuser that was tried was NaCl grains of diameter ~ 1 mm deposited on a 2 cm diameter KCl window (see Figure 3.11 [a]), but without obtaining a speckle in the transmitted pattern that was imaged (see Figure 3.11 [d]). It was evident at this stage that a scattering medium with finer surface features could be more suitable to obtain a transmitted speckle. Therefore, we used a single side polished Silicon wafer whose surface was smoother than those of the salt windows as a substrate for depositing powdered white paint particles. White paint has been successfully used as a scattering medium for visible speckle imaging [50], and the materials that we chose - Zinc Oxide (ZnO) and Titanium Dioxide (TiO_2) - both have an appreciable transmission in parts of the longwave infrared, as you can see in Figure 3.10 where 714 cm^{-1} - 1429 cm^{-1} corresponds to $14 \text{ }\mu\text{m}$ - $7 \text{ }\mu\text{m}$ with 1000 cm^{-1} being equivalent

to 10 μm . ZnO has been used for visible imaging through turbid tissues [213], while TiO_2 has been used in visible laser speckle imaging for measuring blood flow dynamics [214] as well as being used in planar meta-lenses at visible wavelengths [215].

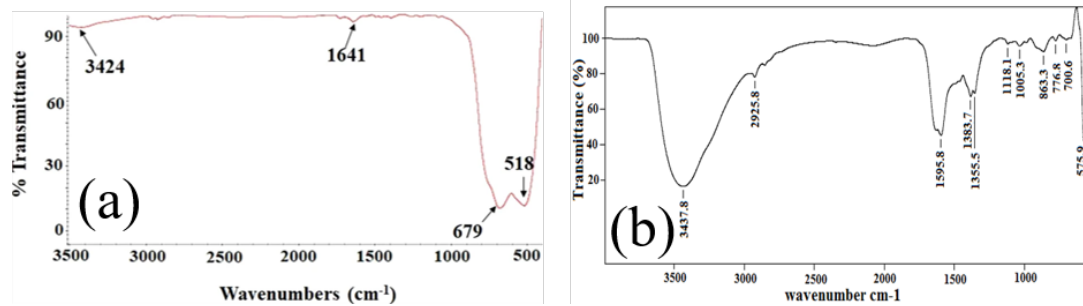


Figure 3.10: Infrared transmission spectrum of (a) TiO_2 nanoparticles of particle size between 70-90 nm [216] and (b) ZnO nanoparticles of size about 20 nm [217].

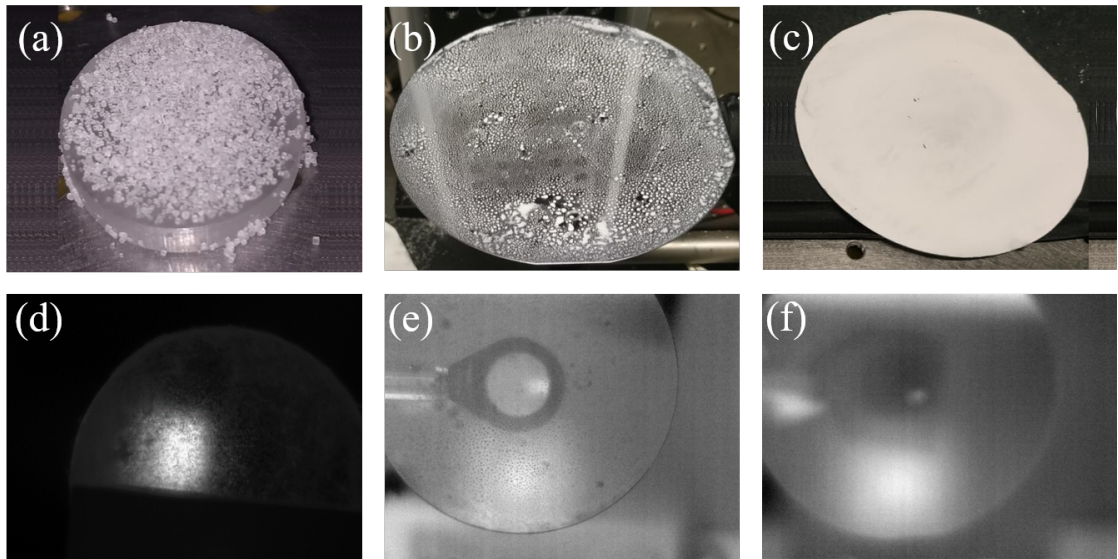


Figure 3.11: Powdered material on substrates as scattering media: (a) NaCl grains of size ~ 1 mm on a 2 cm diameter KCl window, (b) < 100 nm particles of Titanium Oxide (TiO_2) airbrushed onto a 10 cm diameter single side polished Silicon wafer, and (c) 500 nm particles of Zinc Oxide (ZnO) spin-coated and airbrush deposited onto a 10 cm diameter single side polished Silicon wafer, and the corresponding images of scattered infrared radiation after transmission through the scatterers (d-f).

100 nm particles of powdered TiO_2 and 500 nm particles of powdered ZnO, both white in colour, were deposited on single side polished Silicon wafer substrates, using two different processes of spin-coating and deposition using an airbrush (see Figure 3.11 [b,c]). The transmitted scattered light pattern resembled a very diffuse speckle pattern (see Figure 3.11

[e,f]), which reinforced the notion that the surface of the previous samples was too rough to create a speckle pattern.

At this stage, there was still a fraction of ballistic light that was being transmitted (see Figure 3.11 [e,f]). We intuitively tried to create a thick layer of candle wax on the Silicon wafer substrate to attenuate the ballistic light transmission while producing a scattering medium. Some types of wax have a longwave infrared transmittance close to 70%, but also a high reflectance of the same magnitude, in addition to having a transmittance dip around 1175 cm^{-1} [218]. A deposit of molten candle wax was poured onto the Silicon wafer which later solidified to obtain a flat wax-coated surface of 2-3 mm on the wafer substrate. It reduced the ballistic light transmitted through the Silicon wafer, as desired, but did not produce a well-formed speckle pattern. A test experiment without any deposit and just the Silicon wafer substrate turned out to exhibit the first signs of a longwave infrared speckle, as can be seen in Figure 3.12, thus enabling us to settle on a choice of scattering material to work with.

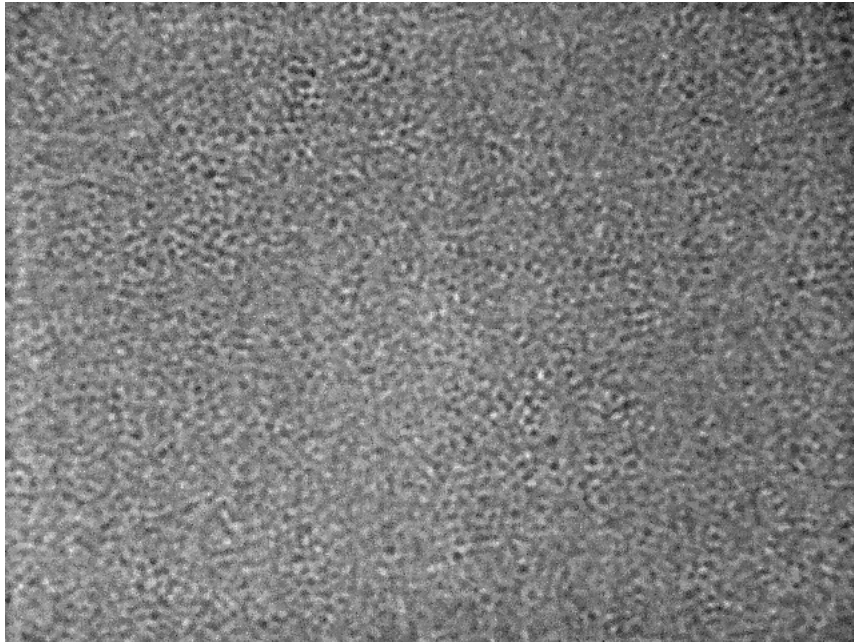


Figure 3.12: First longwave infrared speckle observed using a single side polished Silicon wafer as the scattering medium

3.1.4 Silicon wafer diffuser

The diffuser that we use for the current setup is a single-side-polished Silicon wafer of thickness $250\text{ }\mu\text{m}$ and diameter 10 cm, as shown in Figure 3.13. Atomic force microscopy



Figure 3.13: Single side polished Silicon wafer diffusers of thickness 250 μm and diameter 10 cm (with a measuring ruler alongside for scale)

(AFM) measurements of the two wafer surfaces were carried out to determine its surface topography that was crucial in its utility as a diffuser that created a longwave infrared speckle pattern in transmission. We used a WiTec Alpha 300S AFM microscope to measure the surface topography of the Silicon wafer, over a $150 \mu\text{m} \times 150 \mu\text{m}$ area, in a 256×256 point grid matrix, at a scan speed of $5 \mu\text{m}/\text{s}$.

The average surface roughness, as depicted in the case of one dimension (1D) in Figure 3.15, is measured by calculating the root mean squared (RMS) value of the height measurement over all the data points R_{rms} , which is essentially the standard deviation of the height values σ_h . Let the height at any point (x, y) on the surface be $h(x, y)$, with there being $N_x \times N_y$ points in total, then the average RMS roughness is calculated as:

$$R_{rms} = \sigma_h = \sqrt{\frac{1}{N_x - 1} \frac{1}{N_y - 1} \sum_{i=1}^{N_x} \sum_{j=1}^{N_y} |h(x, y)_{ij} - \mu_h|^2} \quad (3.7)$$

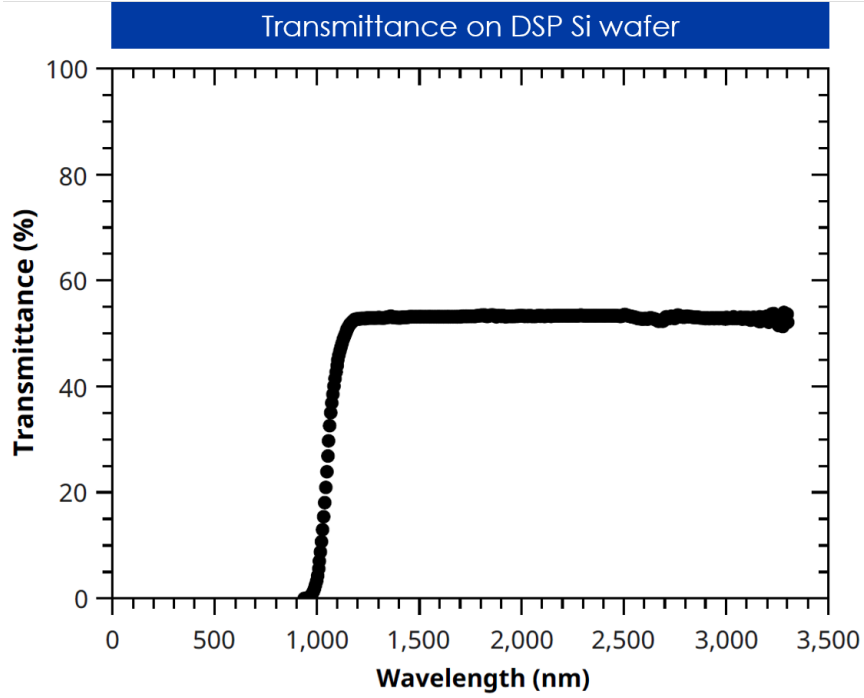


Figure 3.14: Infrared transmission spectrum of double side polished Silicon (Si) wafer [219]

with the mean of the height values, μ_h , being:

$$\mu_h = \frac{1}{N_x} \frac{1}{N_y} \sum_{i=1}^{N_x} \sum_{j=1}^{N_y} h(x, y)_{ij} \quad (3.8)$$

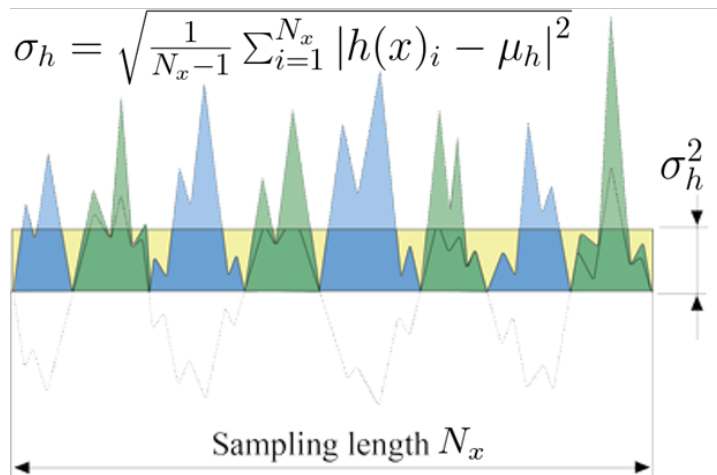


Figure 3.15: Sketch of average RMS surface roughness in 1D [220]

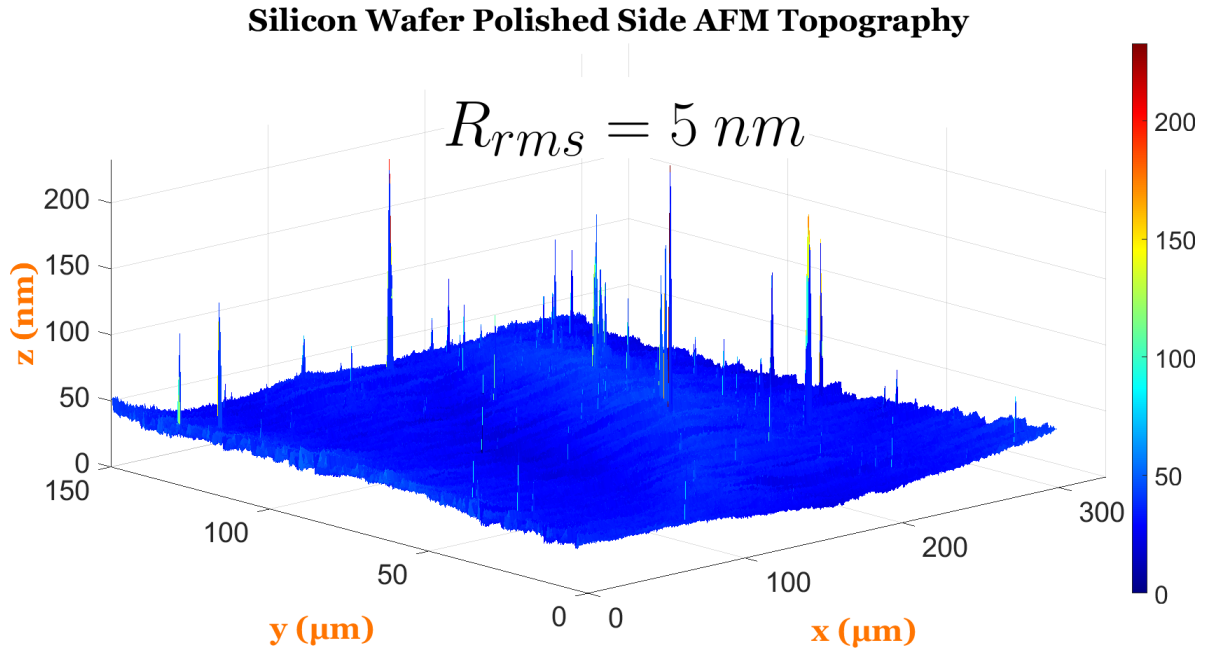


Figure 3.16: AFM topography of the polished side of a silicon wafer over a $150 \mu\text{m} \times 150 \mu\text{m}$ area with an average RMS roughness of 5 nm.

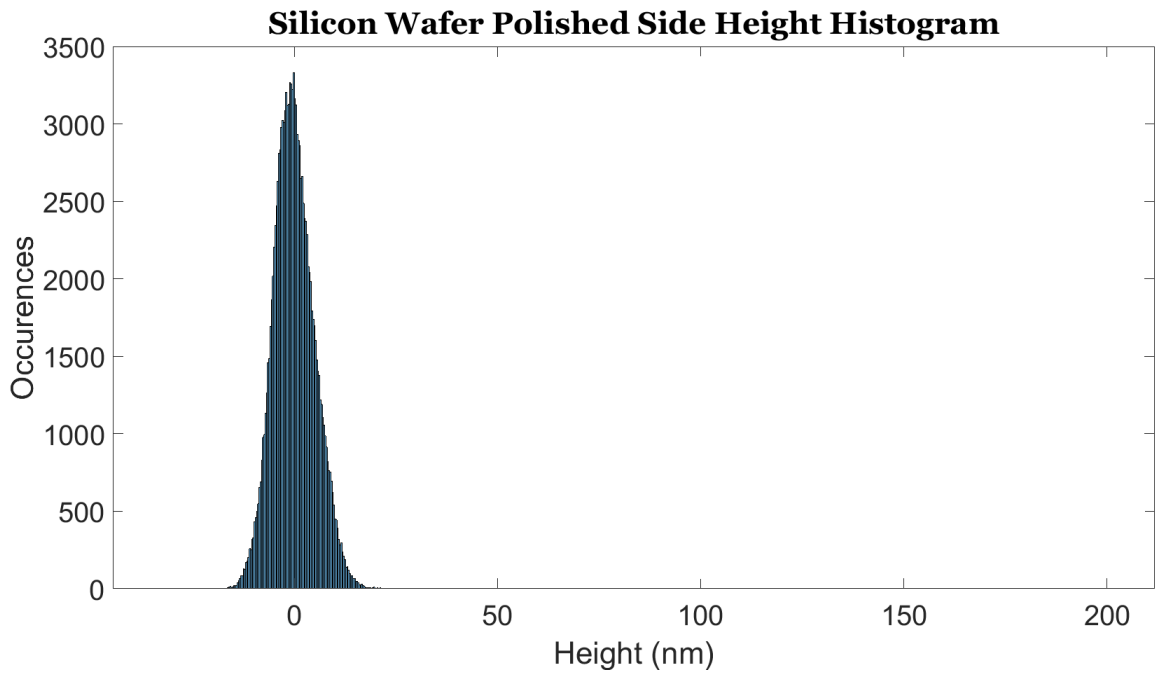


Figure 3.17: Height distribution of the polished side of a silicon wafer from an AFM measurement.

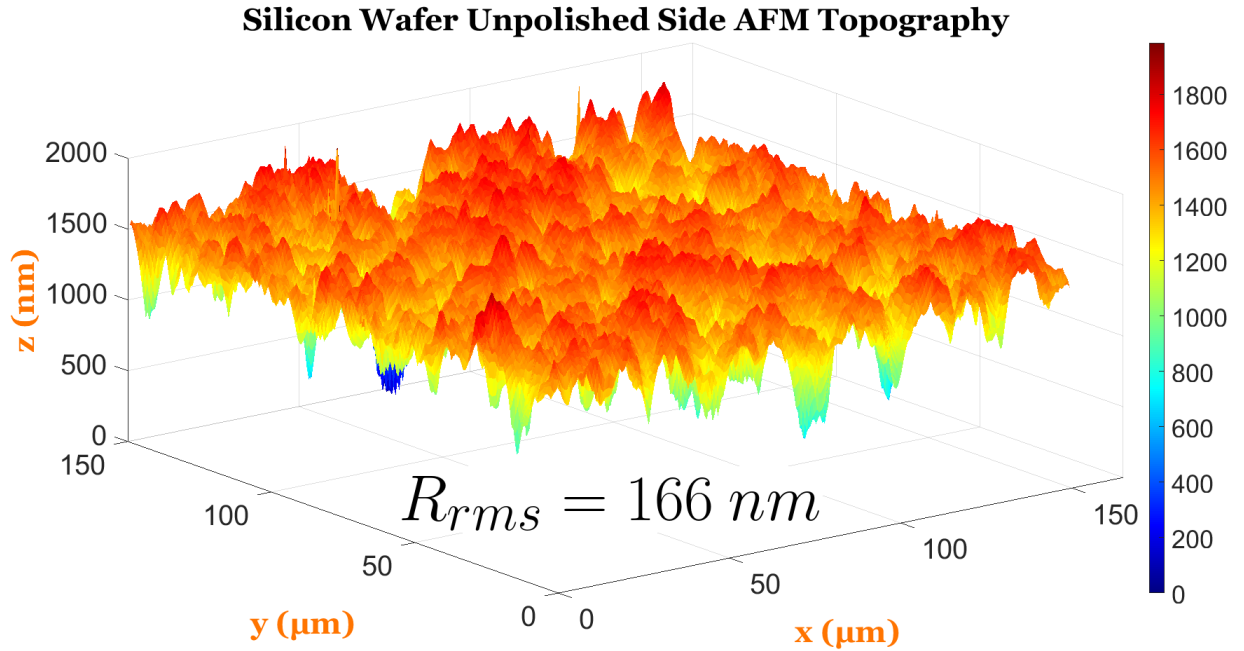


Figure 3.18: AFM topography of the unpolished side of a silicon wafer over a $150 \mu\text{m} \times 150 \mu\text{m}$ area with an average RMS roughness of 166 nm.

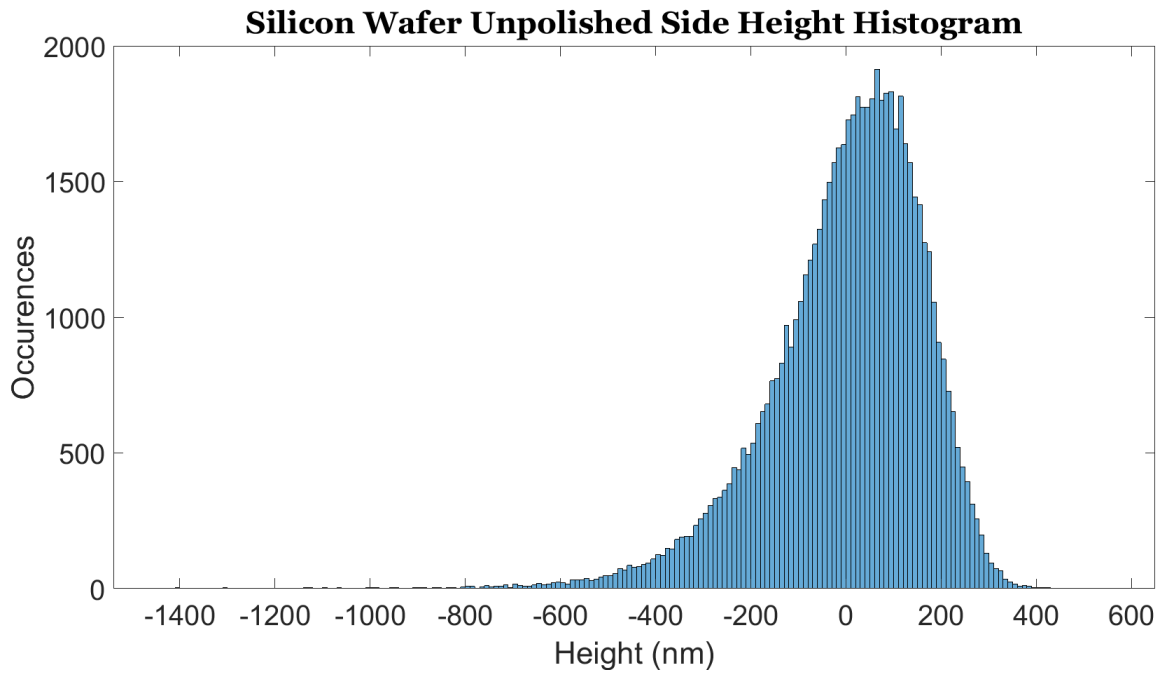


Figure 3.19: Height distribution of the unpolished side of a silicon wafer from an AFM measurement.

As can be seen from the Figure 3.16, the polished surface of the diffuser is very smooth with an average RMS surface roughness of 5 nm, while the unpolished surface topography, shown in Figure 3.18 has crests and troughs across its surface with an average RMS surface roughness of 166 nm. The polished side is essentially flat with the average roughness being on the order of $\lambda/2000$, while the unpolished side is on the order of $\lambda/60$, w.r.t. the reference wavelength of 10 μm .

The histogram representation of the height measurements from the AFM image are also shown for the polished side in Figure 3.17 and for the unpolished side in Figure 3.19. The spread of the height values for the polished surface is very narrow and quite symmetric around the zero mean value. In the case of the unpolished surface, the distribution is more spread out and not symmetric, with a significant tail of negative height values which indicate valleys. The occurrence of extremely deep troughs is albeit quite low.

From the average surface roughness value of the unpolished side of the silicon wafer, the optical path difference turns out to be, $\delta = (n_{Si} - n_{air}) \times roughness \approx (3.5 - 1) \times 166 \text{ nm} = 415 \text{ nm}$, which is in agreement with and on the same order of magnitude as the average speckle grain size of a typical longwave infrared speckle (as shown in Figure 4.1). Clearly, the average surface roughness of the earlier diffuser candidates was much larger than this value in most cases, which hindered our ability to image a transmitted speckle.

3.2 Infrared source

In our setup, we need to create an infrared illumination source, as depicted in Figure 3.2. To do so, we elected to use a blackbody source due to the inability of our camera to withstand high incoming intensities from a focused laser beam. An additional consideration was to develop our infrared imaging methodology with a broadband and incoherent source, which is more practical in applications than using an infrared laser which requires specialized equipment and is cumbersome. The use of a broadband source also broadens the applicability of the technique by not constraining the use of sources to only narrow-band and coherent sources. However, it was necessary to use a source that has a variable temperature while being high enough to produce adequate intensity for the formation of a speckle pattern, which also means that a material of high emissivity would be required, as briefly discussed below in Section 3.2.1.2. We also required a homogeneous source with a high luminance so that a sub-region of the source could be filled using an iris diaphragm and be

collimated by a lens to produce a plane wavefront. The plane wavefront is essential for obtaining a sufficiently intense well-collimated speckle pattern in our experiments. Another important consideration was to use a source which would resemble as best as possible a point source in order to increase the spatial coherence, which is discussed later in Section 3.3.

3.2.1 Blackbody

A blackbody is an ideal body which absorbs all electromagnetic radiation incident on it, without any surface reflection and without allowing any exit after absorption due to internal scattering, irrespective of the frequency of the incident radiation or the angle of incidence. It is therefore a body that absorbs electromagnetic radiation from all wavelengths and all directions. When it is at a constant temperature with no net energy flow between the environment and itself, considered as thermal equilibrium, it also emits electromagnetic radiation in every direction equally (isotropically). The spectral emission has a dependence solely on the temperature and not on any other physical characteristic like size, shape or composition. It is a perfect diffuse emitter and is considered to be a surface emitting the highest amount of radiant energy possible among thermal sources at a given temperature [221] [222].

3.2.1.1 Planck's law of blackbody radiation

The electromagnetic radiation emitted by a blackbody at constant temperature T is given by Planck's law, which describes the spectral radiance of a body L_0 , i.e. the radiant flux emitted by a body per unit area per unit solid angle per unit wavelength, as [205]:

$$L_0(\lambda, T) = \frac{2hc^2}{\lambda^5} \frac{1}{e^{\left(\frac{hc}{\lambda k_B T}\right)} - 1} \quad (3.9)$$

where the spectral radiance at a given wavelength L_0 is only a function of the emission wavelength λ and temperature T , h is the Planck constant, c is the speed of light in the propagation medium, and k_B is the Boltzmann constant. Planck's law of blackbody radiation clearly shows that as the temperature of the blackbody increases, the total radiated energy of the body increases as well as shifting the peak of the emitted radiation spectrum to shorter wavelengths, as can be seen in the plots in Figure 3.20.

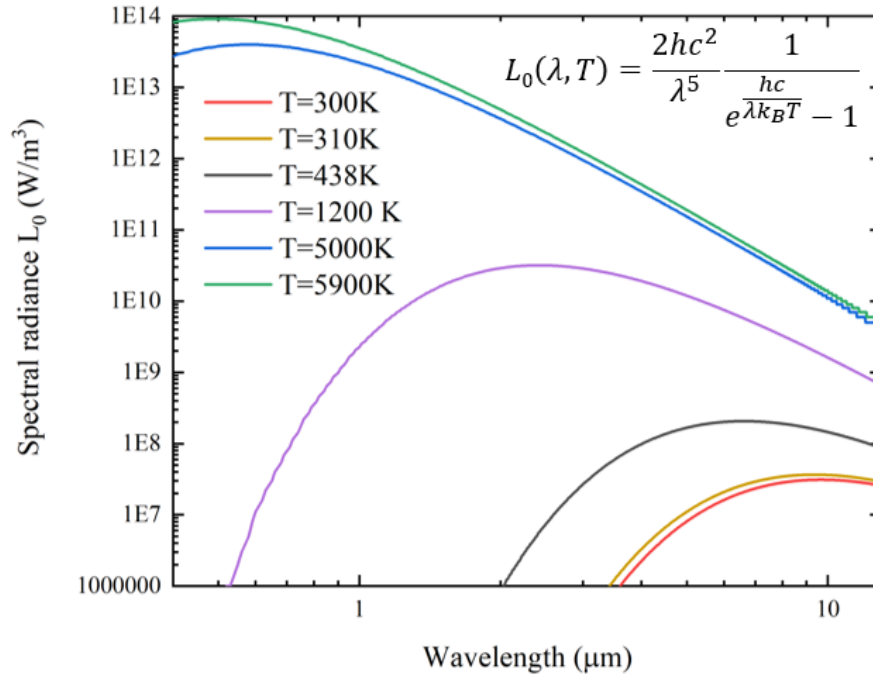


Figure 3.20: Blackbody radiation at different temperatures according to Planck’s law (see Equation 3.9) which also demonstrates Wien’s displacement law for the emission maximum (see Equation 3.29). Both axes are logarithmic.

3.2.1.2 Emissivity

A blackbody is an ideal body, by definition, and all real objects only emit a fraction of a blackbody’s electromagnetic radiation at thermal equilibrium. The physical quantity of emissivity is a measure of a body’s thermal radiation compared to that of a blackbody at the same temperature. Emissivity, specifically the total hemispherical emissivity, is defined as the ratio between the radiant flux per unit area emitted by a surface M_e and the radiant flux per unit area emitted by a black body, M_e^0 , where the blackbody is at the same temperature as the surface, as:

$$\varepsilon = \frac{M_e}{M_e^0} \tag{3.10}$$

A blackbody in thermal equilibrium, by definition, has an emissivity of 1. Objects at the same temperature but having different emissivity values will have different apparent temperatures, as having emissivity values farther from the ideal value of 1 confers objects with properties of transparency or reflectivity, which then mirror the temperature of the

surroundings also.

3.2.2 Soot as blackbody source

As a first blackbody source, we designed a small resistive heating element in our laboratory with a glass slide and a flat resistive element connected to an electrical DC power supply. Soot, having an emissivity of 0.95 [223] [224], was deposited on a square-cut glass slide to create a blackbody and the square surface resistor was placed in contact beneath it to heat the glass surface through conduction. The two pieces were held to each other using a metallic crocodile clip, with the entire blackbody surface measuring 2 cm x 2 cm, as shown in Figure 3.21. The temperature of the blackbody source could be controlled using the resistor to heat the soot-coated glass slide to about 200°C, which is the maximum temperature which could be reached using the flat resistive element. We found out that the luminance of this source was not high enough and had to work with alternate ones.



Figure 3.21: Lab-made blackbody source using soot deposited on a glass slide and heated up to 200°C using a flat resistive element underneath.

3.2.3 Coiled filament source

In order to increase the intensity and luminance of the source beam, we changed the infrared source to a commercial Scitec IR 30K 4.2 Watt coil-wound filament source mounted on a TO-5 header, shown in Figure 3.22. At steady state, the coiled filament - made of Kanthal resistance wire (an iron-chromium-aluminium (FeCrAl) alloy) - operates at ~950°C. It has an emissivity of 0.75. With an active area of 1.8 mm x 1.8 mm, the source produced a nearly

elliptical beam after collimation but with the filament edges still visible when viewed with our infrared camera (see Figure 3.22 [b] for the geometry and Figure 3.23 for the source beam image). Some of the first longwave infrared speckles that we observed were obtained with this coiled filament source, even as the inhomogeneous surface of the source filament was clearly distinguishable in the observed speckle images, as seen in Figure 3.24.

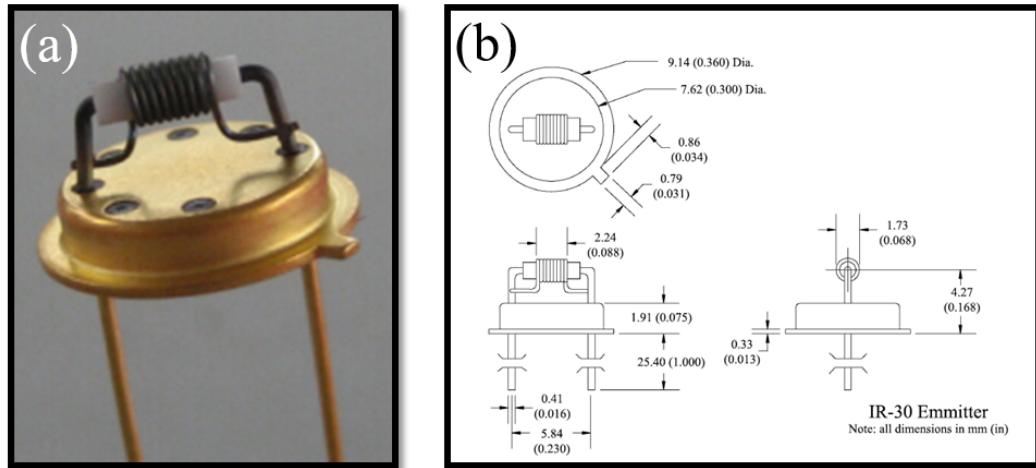


Figure 3.22: Scitec IR 30K coiled filament blackbody source operating at a temperature of 950°C: (a) upright view, and (b) sketch of geometrical dimensions. [225]

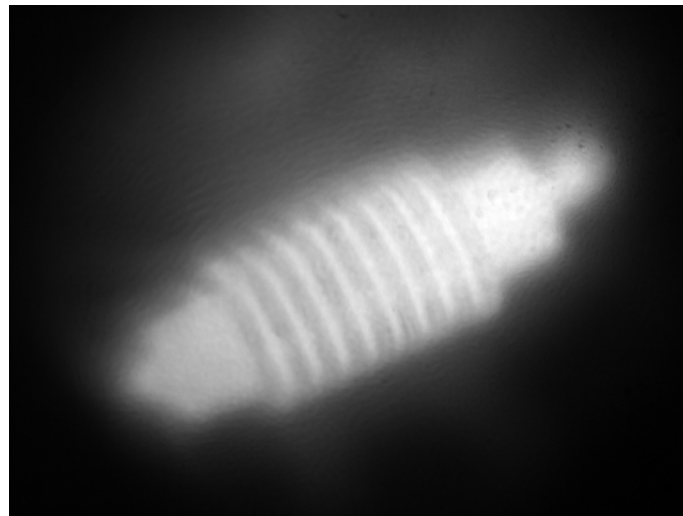


Figure 3.23: Nearly elliptical beam from Scitec IR 30K coiled filament blackbody source seen using our infrared camera, with clearly observable geometrical features of the source as shown in Figure 3.22.

To obtain a better point source and a more homogeneous source beam, the collimating lens was adjusted to only allow a magnified portion of the coiled filament infrared source

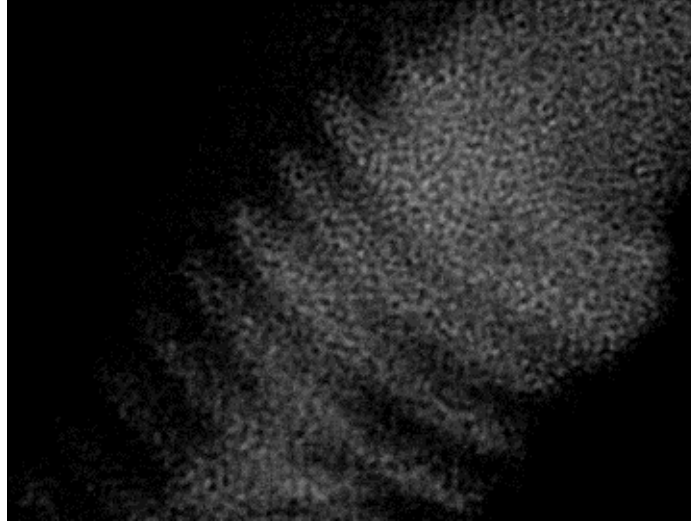


Figure 3.24: Longwave infrared speckle observed using a Scitec IR 30K coiled filament blackbody source as shown in Figure 3.22, with clearly observable source features, in conditions where the beam should be collimated.

to be visible during speckle imaging. This produced nearly homogeneous speckles but still contained intensity inhomogeneities that needed to be rectified. In addition, due to the geometry of the coiled filament source, the radiation emanating from the source was from different planes between the tip of the filament and the header holding the filament - a distance of 4.27 mm (see Figure 3.22 [b]). A possible solution that was tried was to place the infrared source in contact with a glass slide of thickness 1.2 mm [226] so that the glass slide could be heated by the source through conduction and subsequently radiate from its surface, acting as a secondary infrared source. This experimental idea took advantage of the low penetration depth of glass - $0.71 \mu\text{m}$ at a wavelength of $10 \mu\text{m}$ [227] - which would mean that the radiation emanating from the surface would come from a thin planar volume located at the focal plane of the collimating lens and also be more homogeneous than just using the coiled filament source by itself. However, the glass slide either cracked or softened (i.e. the state of matter before the phase change to melting) after just a few contacts due to the high temperature of $\sim 900^\circ\text{C}$ of the filament in contrast to the softening temperature of microscope glass slides being 720°C [228]. The glass slide was replaced by using a pure quartz slide instead of glass, which in contrast has a skin depth of $2.02 \mu\text{m}$ at the wavelength of $10 \mu\text{m}$ [229] [230], and a softening temperature of 1250°C [231]. The values of the refractive indices, n & k , are plotted with respect to the wavelength for soda lime glass in Figure 3.25 and for fused silica quartz in Figure 3.26. A brief description of the concept of penetration depth is presented in Section 3.2.3.1 and plots of the values for

both glass and quartz are comparatively presented in Figure 3.27.

3.2.3.1 Penetration depth

The penetration depth, also referred to as the skin depth, of a material is the distance up to which the incident radiation can traverse through the medium before being attenuated to $1/e$ times the incident intensity (or electric field, when talking of skin depth). This distance is a characteristic property of materials that interact with light, being dependent on the extinction coefficient, i.e. the imaginary part of the refractive index, and also on the wavelength or frequency of the radiation.

The complex refractive index of a material allows us to conveniently account for the absorption and scattering of light through the material, since all real materials attenuate light to varying degrees.

$$\bar{n} = n + ik \quad (3.11)$$

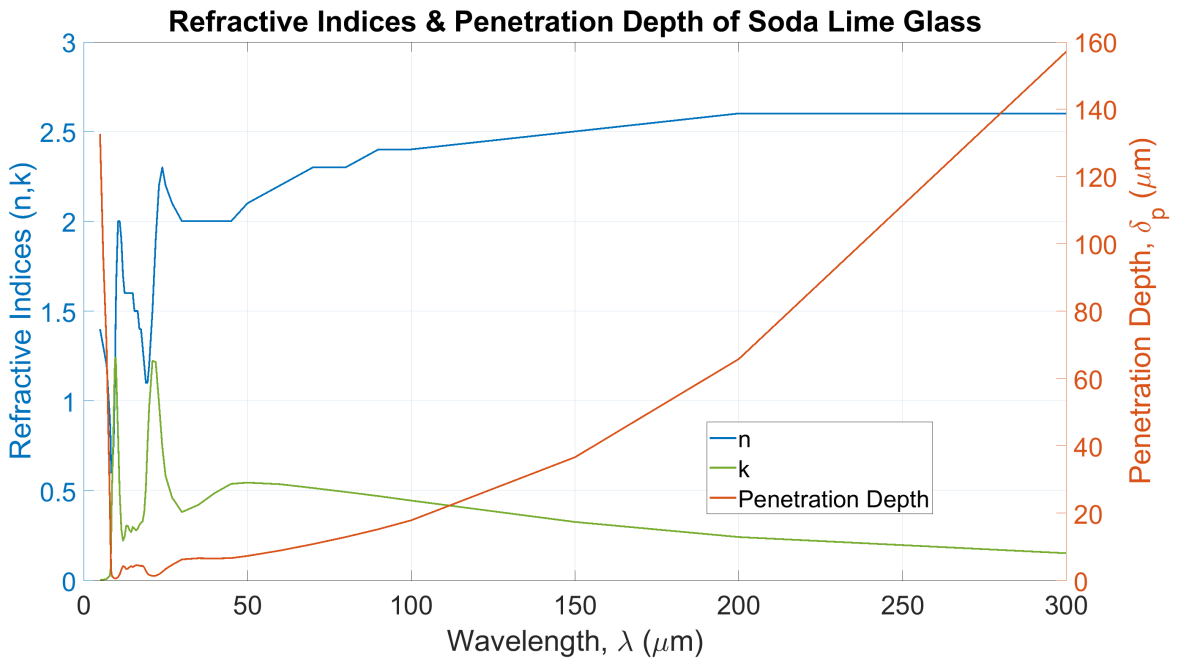


Figure 3.25: Values of the refractive indices, n and k , from [227], and the calculated penetration depth, δ_p , in the wavelength region of 5 - 300 μm , for soda lime glass which is used to manufacture microscope glass slides [226].

The real part of the refractive index, n , indicates the phase velocity of the light wave, while

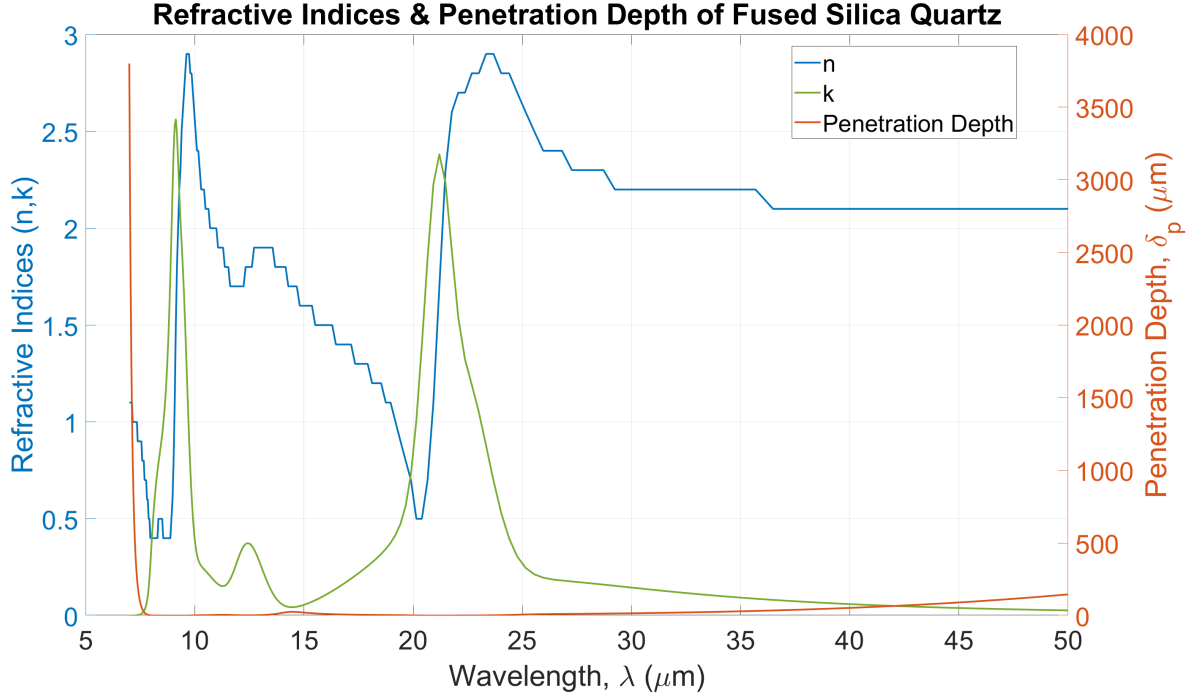


Figure 3.26: Values of the refractive indices, n and k , from [229], and the calculated penetration depth, δ_p , in the wavelength region of 7 - 50 μm , for fused silica quartz which is used to manufacture microscope quartz slides [231]. We can see that even though the variation in the penetration depth (δ_p) values in the broad wavelength range depicted in this figure seems minor (according to the right-hand y-axis scale), the sharp change in the values of the penetration depth between 7 to 7.4 μm demonstrates the strong dependence of the penetration depth on the imaginary part of the refractive index, k .

the imaginary part k refers to the extinction or attenuation coefficient, which is the sum of the absorption coefficient and the scattering coefficient. We can relate the complex wave number \bar{q} to the complex refractive index \bar{n} through:

$$\bar{q} = 2\pi\bar{n}/\lambda_0 \quad (3.12)$$

where, λ_0 is the wavelength of light in vacuum. We can insert this expression into the electric field equation for a plane electromagnetic wave travelling in the x-direction as:

$$\begin{aligned} \mathbf{E}(x, t) &= \text{Re}[\mathbf{E}_0 e^{i(\bar{q}x - \omega t)}] = \text{Re}[\mathbf{E}_0 e^{i(2\pi(n+ik)x/\lambda_0 - \omega t)}] \\ &= e^{-2\pi kx/\lambda_0} \text{Re}[\mathbf{E}_0 e^{i(qx - \omega t)}] \end{aligned} \quad (3.13)$$

We see that the extinction coefficient leads to an exponential decay of the electric field. Similarly, we know from the Beer-Lambert Law that the intensity at the position x is related to the initial intensity and the absorption coefficient by an exponential law, with the following simplified relation in the case of uniform attenuation and if we consider that the attenuation coefficient is invariant with x . Therefore, combining the two, we get:

$$I(x) = I_0 e^{-\alpha x} = I_0 e^{-4\pi k x / \lambda_0} \implies \alpha = 4\pi k / \lambda_0 \quad (3.14)$$

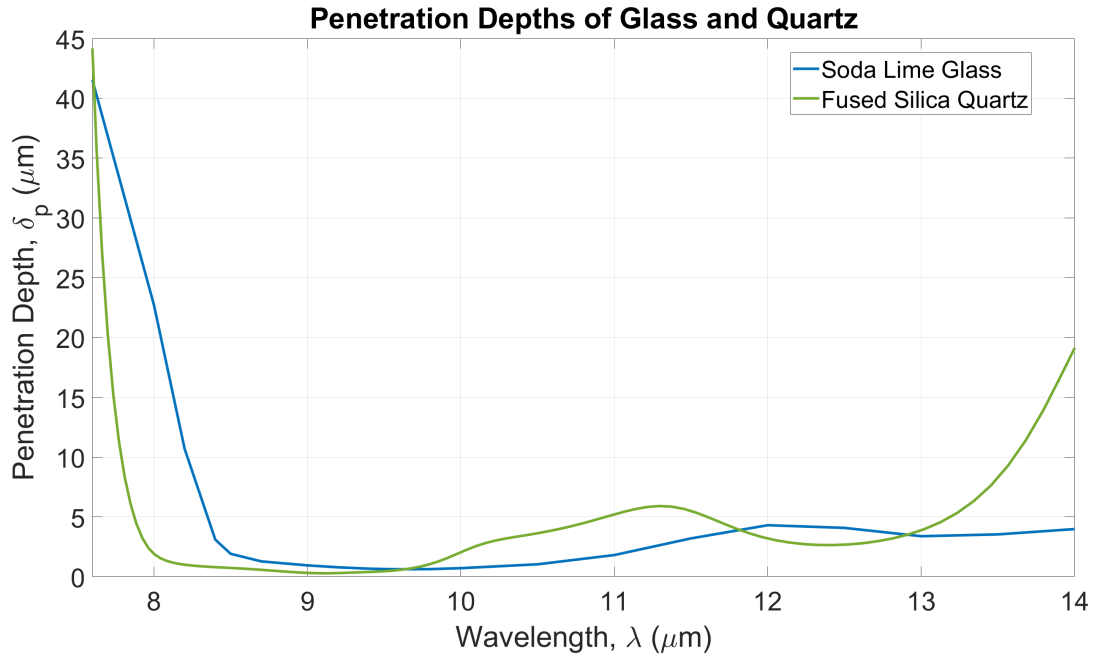


Figure 3.27: Comparison of the calculated penetration depth values, δ_p , in the wavelength region of 7.5 - 14.0 μm , for soda lime glass and fused silica quartz which is used in our experiments.

When the intensity reduces to $1/e$ times the value of the initial intensity, the distance x is known as the penetration depth δ_p . If we consider the same for the electric field, the distance is known as the skin depth δ_e . We can see that both δ_p and δ_e are inversely proportional to the attenuation coefficient.

$$\frac{1}{\alpha} = \delta_p = \frac{\delta_e}{2} = \frac{\lambda_0}{4\pi k} \quad (3.15)$$

Even as the use of the quartz slide in front of and in contact with the infrared source was

able to reduce the inhomogeneities in the source infrared beam, it was much less intense than using the source just by itself. Subsequently this configuration was also dropped since the coiled filament source was getting damaged due to the quartz slide softening at the point of their contact and covering the filament locally, most likely due to the intense local temperature at the point of contact that exceeded the quartz slide's softening temperature.

3.2.4 Silicon nitride globar source

The next infrared source that we tried was a Scitec IR-Si253 20 Watt Silicon Nitride globar source with a right circular cylindrical geometry. It is shaped as a larger diameter solid cylinder presumably made of alumina whose melting point is beyond 2000°C, or another ceramic with a high melting temperature, upon which is stacked another solid cylinder of a smaller diameter which is the globar itself, with an active area of 2 mm (diameter) x 5 mm (height), as seen in Figure 3.28. The Silicon Nitride globar has an emissivity of 0.8, and can reach up to a temperature of 1170°C [232].



Figure 3.28: Scitec IR-Si 253 Silicon Nitride (Si_3N_4) globar source that can be operated up to a maximum temperature of 1170°C [232].

Since it was not possible to use the method of placing a glass or quartz slide in front of and in contact with the globar to obtain a more intense and more homogeneous secondary source due to temperature constraints at the contact interface, the choice of this source was due to the two considerations of geometry and maximum temperature. We chose to use an infrared source that had a higher operating temperature to obtain a source beam of higher intensity. The cylindrical geometry of the Silicon Nitride source would produce a homogeneous circular beam as well. However, it turned out that due to the stacked cylinder geometry with two different cylindrical radii, the circular beam was not completely

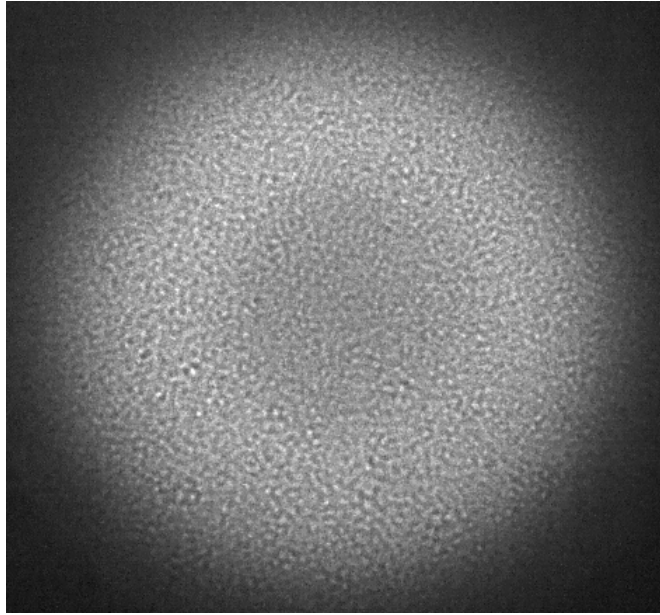


Figure 3.29: Longwave infrared speckle seen when using the Scitec IR-Si 253 silicon nitride (Si_3N_4) globar source, as shown in Figure 3.28, with concentric circular intensity inhomogeneities.

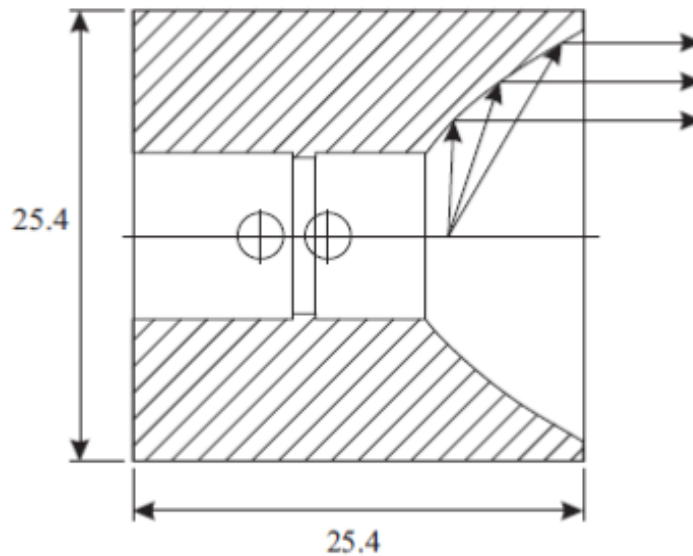


Figure 3.30: Scitec MC-234 parabolic reflector mount for Scitec IR-Si 253 silicon nitride (Si_3N_4) globar source, as shown in Figure 3.28, with a diameter of 25.4 mm and focal length of 3.0 mm.

homogeneous. The beam was comprised of two concentric disks whose relative intensity depended on the exact plane of the globar source being imaged by the camera, and it created

intensity artifacts like a bright central spot inside the circular beam or a bright central annulus outside the central beam, as shown in Figure 3.29. The use of a Scitec MC-234 parabolic reflector of diameter 25.4 mm, as shown in Figure 3.30, to alleviate this problem did not result in a significant improvement in the observation of a homogeneous intensity speckle pattern as well.

3.2.5 Silicon carbide globar source

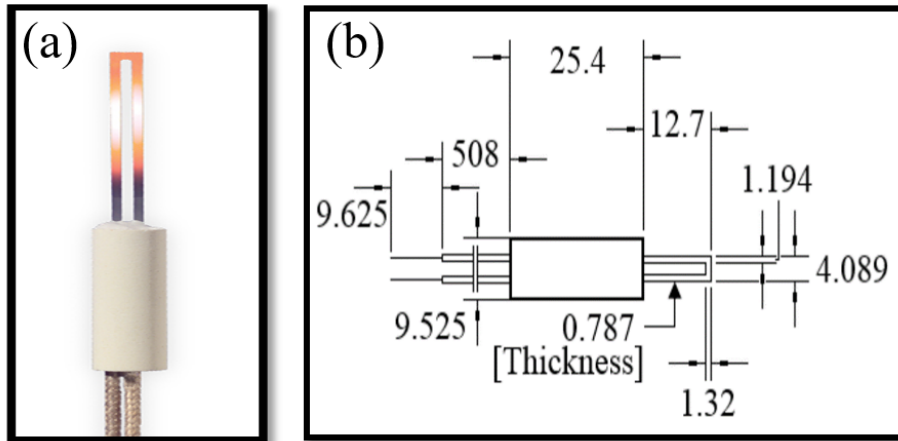


Figure 3.31: Scitec IR-Si 207 silicon carbide (SiC) globar source that can be operated up to a maximum temperature of 1455°C [232]: (a) upright view, and (b) sketch of geometrical dimensions (all in millimeter units) [233].

Finally, we settled on a Scitec IR-Si207 24 Watt Silicon Carbide globar source with an inverted U-shaped geometry, having an active area of 3 mm (width) x 4.4 mm (length), as shown in Figure 3.31. The Silicon Carbide globar has an emissivity of 0.8, and can be heated up to 1455°C, thereby producing a beam of higher intensity than the previous infrared sources. The U-shaped geometry is not ideal to achieve a homogeneous source. We had to trade-off the lack of a homogeneous source - arising from the irregular geometry (see Figure 3.31 [b]) - for a more intense source, in the face of a dearth of choice in obtaining commercial longwave infrared emitters suited for our experiment. Therefore, we had to conceive an optical configuration including a diaphragm to perform spatial selection that would allow us to overcome the inhomogeneity of the source geometry in the output source beam so as to obtain a homogeneous and intense circular beam capable of producing an almost ideal plane wavefront, as described in Section 3.3.

The temperature versus voltage curve for the silicon carbide globar is shown in Figure 3.32, while the emission versus wavelength characteristics for three different operating condi-

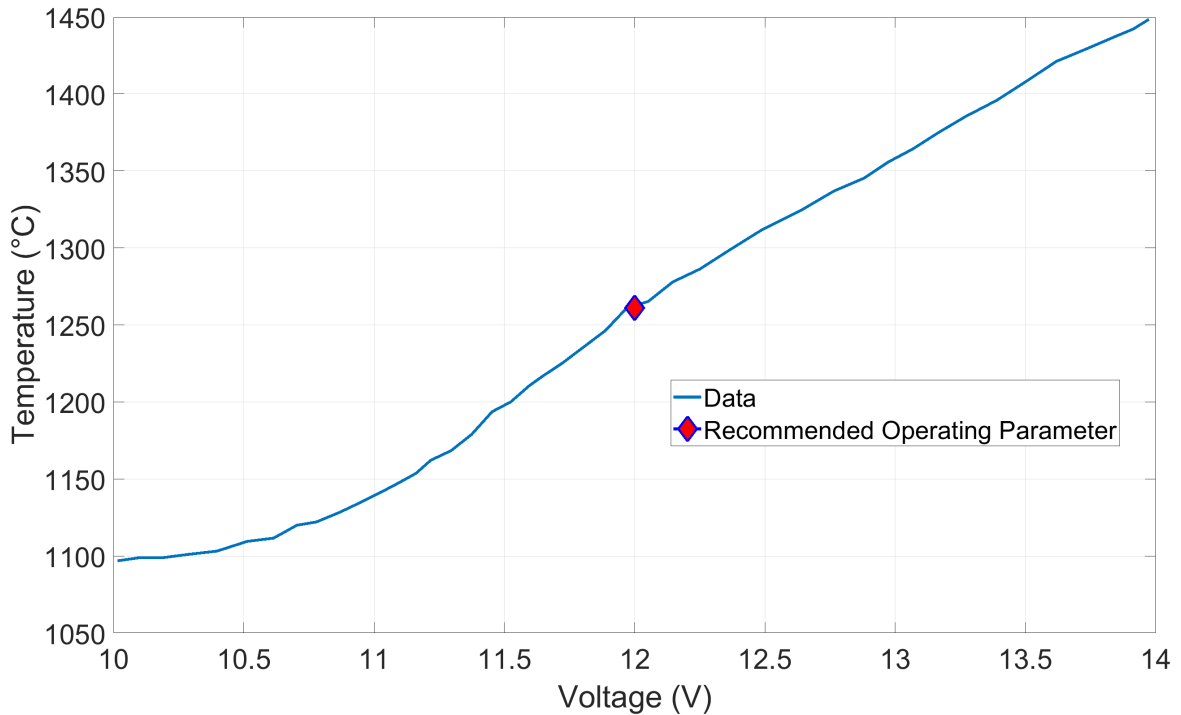


Figure 3.32: Temperature versus voltage plot for IR-Si 207 silicon carbide (SiC) global source, as shown in Figure 3.31 [233].

tions (voltage and current) are shown in Figure 3.33, where the red curve corresponding to 12 V voltage and 1.98 A current pertains to our usual operating conditions. It is instructive to consider the blackbody curves shown in Figure 3.20, and to see that even as increasing the temperature of the blackbody source shifts the peak wavelength of the emitted thermal radiation from the longwave infrared towards shorter wavelengths in the visible region of the electromagnetic spectrum, it still offers a large increase in the spectral radiance at wavelengths in the longwave infrared. A blackbody at room temperature (see the curve corresponding to $T = 300\text{ K}$ in Figure 3.20) emits about 100 times less thermal radiation in the longwave infrared (around $\lambda = 10\text{ }\mu\text{m}$) compared to a blackbody at a temperature of 1200 K. This enhances the source beam intensity in the longwave infrared and enables us to perform infrared speckle imaging with a better contrast. Thermal sources are known to have a rather limited luminance as their upper bound is given by blackbody radiation, with emissivity equal to 1. Alternatively the infrared radiation produced by a synchrotron does not suffer of the same problem while producing a very broad spectrum and a beam which is inherently collimated [234] [235].

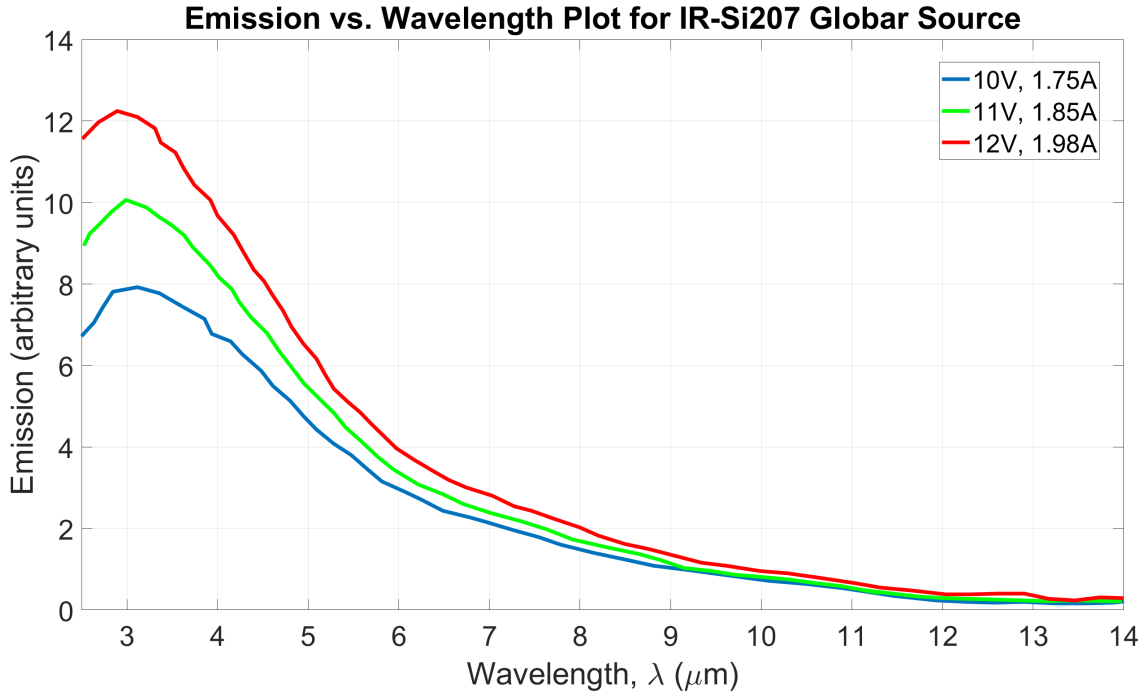


Figure 3.33: Emission versus wavelength plot for IR-Si 207 silicon carbide (SiC) globar source, at three different operating voltage and current conditions [233].

3.3 Point source

In addition to the requirement of optimizing an incoherent broadband longwave infrared source to produce a homogeneous beam, it is essential to obtain a source that is as close to an ideal point source as possible, in order to produce after collimation a close-to-ideal plane wavefront that will produce a reference speckle when passing through the scattering medium. While this is relatively easy to accomplish in the visible regime of the EM spectrum, with optical components in the visible regime available off-the-shelf, it is more difficult to realize this in the longwave infrared range. As shown in Section 3.2, the longwave infrared sources that were used were not point sources to begin with. The silicon nitride source, as described in Section 3.2.4, was the closest to being a point source but its use was discontinued due to its inability to produce a homogeneous source beam. An approximate point source would also reduce the spatial incoherence of the source, thereby improving the speckle contrast of the resulting reference speckle [236] [237] [238]. Consequently, it became necessary to use optical elements to produce experimentally a point source from the primary infrared source. An effective manner to do this is to use a diaphragm or iris which has a small aperture, which is also easily changeable for practical utility. In the course of the evolution of the setup and its optical components, different iris

apertures were used to create a good point source.

According to the van Cittert-Zernike theorem, the spatial coherence of an extended light source depends on the size of the emitter and its distance from the plane of observation. The spatial coherence area, A_c , is given by [239]:

$$A_c = \frac{D^2 \lambda^2}{\pi d^2} \quad (3.16)$$

where D is the distance between the source and the plane where the spatial coherence area is being calculated, d is the diameter of the light emitter, and λ is the wavelength of propagating light. This equation shows that the wavefronts from an extended source smooth out as they propagate away from the source, as is evident in the high spatial coherence of starlight due to the source stars being an astronomical distance away. In our case, since the wavelength is more or less fixed within the LWIR range, and the distance D cannot be extended significantly, the chief parameter to control is the diameter of the secondary thermal source which is controlled using the iris diaphragm's aperture diameter. For typical values of $D = 50$ mm, which is the distance between the iris and the collimating lens, $d = 1$ mm, which is the iris aperture diameter, the reference LWIR wavelength $\lambda = 10$ μm , we get a spatial coherence area of the secondary iris source of about 0.08 mm^2 at the collimating lens, which corresponds to a diameter of 320 μm . Increasing the iris aperture diameter to just 2 mm reduces this spatial coherence diameter to 80 μm . A more detailed discussion about coherence is presented in Section 3.3.1.

We used a Thorlabs ID25/M standard post-mounted iris diaphragm with black steel leaves that could be continuously varied to have an iris aperture diameter between 1 mm and 25 mm. The flexibility offered by this iris diaphragm enabled us to initially find a suitable aperture size such that the source could be obstructed as much as possible to be close to a point source without diminishing the intensity to a level where the speckle was not visible at all.

In a preliminary experimental configuration, the iris aperture diameter could not be reduced below 6 mm beyond which the intensity was too faint to observe a speckle. This led to the realization that additional optical elements were absolutely necessary to build an experimental setup with adequate intensity from the extant infrared sources without compromising heavily on the ability to obtain a point source.

We also used a Thorlabs ID50Z/M zero aperture post-mounted iris diaphragm that had a dual layer black steel leaf design with a continuous variability of the iris aperture from 0 mm (fully closed) to 50 mm. This iris was useful when we tried to reduce the aperture even below the minimum iris aperture diameter of 1 mm - that was possible with the Thorlabs ID25/M standard iris - to increase the spatial coherence of our source illumination. Due to the dual leaf design that places the leaves on two adjacent planes in the diaphragm, the iris aperture becomes elliptical when the diameter is between 1 mm and 0 mm, which alters the resulting wavefront from the approximate point source.

Since a point source can be approximated in reality using a pinhole, various fixed diameter iris apertures were fabricated by drilling in an aluminium sheet of thickness 0.5 mm. Aluminium has a low emissivity, of $\epsilon < 0.1$ [240], which is the case for many metals, and the radiation from the heated iris is therefore minimal. Various pinhole apertures with diameters between 5 mm - 1 mm, and 1000 μm to 10 μm were fabricated and used as irises. When the infrared source was placed in contact with glass or quartz slides, the aluminium sheet of pinhole apertures was also placed just in front of the source and the microscope slide in the direction of the camera to obtain a nearly point source. However, again, with the available infrared sources and the very small pinhole sizes, the beam intensity was too low to form a speckle, which prevented the pinholes from being used to augment the source infrared beam to be as similar as possible to one that would be obtained from a point source.

A Köhler illumination scheme of two lenses and two diaphragms was also tried but not adopted finally since a simpler setup with one lens and one iris diaphragm, became viable. As shown in Figure 3.2, an additional lens was placed between the blackbody source and the iris diaphragm (which serves as the secondary source) to form a magnified image of the source on the iris plane. This configuration enabled us to approximate a point source from an extended blackbody with adequate intensity to form a speckle pattern after undergoing scattering. We shall discuss in greater detail about coherence length and time now, especially for thermal radiation, and calculate estimates of these values for our experimental setup.

3.3.1 Coherence length and time

The coherence length of an electromagnetic wave is the distance along the propagation direction over which the wave retains a defined degree of temporal coherence. In other words, the phase relation between two points along the propagation axis follow a well-defined re-

lation ("phase memory") within the characteristic distance of the coherence length. The coherence length also characterises the upper limit of the range of optical path differences between waves within which wave interference produces a specified intensity contrast of the interference pattern. If the optical path difference between two waves is larger than the coherence length, the waves will not be considered coherent and will not interfere with each other. A larger value of the coherence length means that the wave is closer to the ideal case of a purely sinusoidal wave without phase fluctuations.

3.3.1.1 Coherence of light with Gaussian emission spectrum

Light that is not perfectly coherent, as is the case for all real sources, can be considered to have statistical phase discontinuities over the distance of the coherence length, which is inversely proportional to the frequency bandwidth of the light source.

The coherence length can be calculated by the equation:

$$L = \frac{c}{n\Delta f} \approx \frac{\lambda^2}{n\Delta\lambda} = C \frac{\lambda^2}{n\Delta\lambda} \quad (3.17)$$

where c is the speed of light in vacuum, n is the real (i.e. non-complex) refractive index of the medium of propagation, Δf is the source bandwidth, λ is the central wavelength of the radiation source, $\Delta\lambda$ is the spectral width of the source, and C is a constant that depends on the spectral emission profile of the source.

The coherence time of a broadband source is related to the coherence length as [241]:

$$\tau = \frac{L}{c} = \frac{C}{c} \frac{\lambda^2}{n\Delta\lambda} \quad (3.18)$$

When the emission spectrum of the source is considered to be Gaussian, the factor C for the coherence length L is close to 0.5. Depending on the assumptions used during the derivation, one gets $C = \frac{2\ln 2}{\pi} \approx 0.4413$ [242] or $C = \sqrt{\frac{2\ln 2}{\pi}} \approx 0.6643$ [241]. The coherence length of the light source also determines the axial image resolution. Shorter coherence lengths from broadband light sources provide finer resolution.

In an interferometric setup, the detected output interference signal is the electric field auto-

correlation of a light wave. In this case, the coherence length is defined as the full width at half maximum (FWHM) of the field autocorrelation. The interference fringe visibility V is defined in terms of the maximum intensity of oscillations, I_{max} , and the minimum intensity of oscillations, I_{min} , expressed mathematically as :

$$V = \frac{I_{max} - I_{min}}{I_{max} + I_{min}} \quad (3.19)$$

For a source with Gaussian emission spectrum having a FWHM spectral width of $\Delta\lambda$, an optical path difference of $\pm L$ will reduce the fringe visibility V by 50%. As the exact definition of the spectral width $\Delta\lambda$ is ambiguous, the coherence length is also defined in terms of a measurement carried out by a Michelson interferometer. The optical path length difference when a laser beam interferes with itself and produces a fringe visibility $V = \frac{1}{e} \approx 37\%$ is an alternative definition of the coherence length.

3.3.1.2 Coherence of thermal radiation

However, for a blackbody source, the emission spectrum is not Gaussian, but is described by the well-known Planck's law of blackbody radiation, as mentioned in Equation 3.9. Considering two-beam interference of thermal radiation in a Michelson interferometer, as shown in [243], with an optical path difference of $c\tau$ - with c being the light velocity and τ being the optical time difference - between the two beams, the intensity of the recombined wave $I(\tau)$ becomes:

$$I(\tau) = I_0 \frac{1}{2} \left[1 + \frac{\langle E(t) \cdot E(t - \tau) \rangle}{\langle [E(t)]^2 \rangle} \right] \quad (3.20)$$

where, I_0 is the incident wave intensity, t is time, E is the real component of the electric field vector, and the angular brackets $\langle \rangle$ denote a time average over the specified variable. The power spectrum of blackbody radiation, normalized to 1, is given by:

$$P(\nu) = \frac{15h^4\nu^3}{(\pi k_B T)^4 [e^{h\nu/k_B T} - 1]} \quad (3.21)$$

where, ν is the frequency of the blackbody radiation, $P(\nu)$ is the normalized power spec-

trum of the electric field $E(t)$, h is the Planck constant, k_B is the Boltzmann constant, and T is the absolute temperature of the blackbody source. Using the Wiener-Khintchine theorem [244] [245], the normalized self-coherence function $\frac{\langle E(t) \cdot E(t-\tau) \rangle}{\langle [E(t)]^2 \rangle}$ is related to the normalized power spectrum $P(\nu)$, which leads to the intensity ratio between the recombined wave and the incident wave being:

$$\frac{I(\tau)}{I_0} = \frac{1}{2} \left[1 + \frac{15}{\pi^4} \int_0^\infty \frac{x^3 \cos(2\pi k_B T \tau x / h)}{e^x - 1} dx \right] \quad (3.22)$$

From numerical calculations of Equation 3.22, it is shown in [243] that the coherence time τ_c and the coherence length l_c can be inferred by taking into account the threshold when the effects of interference are not significant. The coherence time and length of thermal radiation are then approximately defined as:

$$\tau_c \cong \frac{h}{4k_B T} \quad (3.23)$$

$$l_c = c\tau_c \cong \frac{hc}{4k_B T} \quad (3.24)$$

which shows that the coherence length and time are both inversely proportional to the temperature of the blackbody. The effective spectral width of the blackbody radiation $\Delta\nu$ and the coherence time τ_c are related to each other by a reciprocity inequality as established in [75]:

$$\tau_c \Delta\nu \geq \frac{1}{4\pi} \quad (3.25)$$

Defining the spectral width of blackbody radiation $\Delta\nu$ as the full width at half maximum (FWHM) of $P(\nu)$, from Equation 3.21, leads to a numerical result of the spectral width using Equation 3.23 as:

$$\Delta\nu = \frac{4.3k_B T}{h} \cong \frac{1}{\tau_c} \quad (3.26)$$

which shows that a decrease in the spectral width of blackbody radiation using a filter leads to an increase in the coherence length and time [243]. The numerical computation of Equation 3.22 shows that when the intensity of the recombined wave after interference is half that of the original incident wave, which in the case of monochromatic light corresponds to a quarter wavelength ($\lambda/4$) optical path difference between the interfering waves, then an effective wavelength of thermal radiation λ_{eff} can be defined as:

$$\lambda_{\text{eff}} = \frac{hc}{3.6k_B T} \approx \langle \lambda \rangle = \frac{\int_0^\infty \lambda B(\lambda, T) d\lambda}{\int_0^\infty B(\lambda, T) d\lambda} = \frac{hc}{2.7k_B T} \quad (3.27)$$

It can clearly be seen that λ_{eff} is approximately equal to the mean wavelength of thermal radiation $\langle \lambda \rangle$, with $B(\lambda, T)$ being the spectral density of blackbody radiation as defined in Equation 3.9.

Therefore, blackbody radiation that has not been filtered using a spectral filter can be considered to be composed of independent wave trains of finite length l_c which follow a random probability distribution. This length l_c is used as the definition of the coherence length for thermal radiation, and is also approximately equal to the effective wavelength (λ_{eff}) of the wave trains, as shown in Equation 3.27. After computing the constants in Equation 3.24, the coherence length can be simplified to read:

$$l_c T \cong 3600 \mu\text{m K} \quad (3.28)$$

which resembles the form of Wien's displacement law, which inversely relates the peak wavelength of the spectral radiance of blackbody radiation λ_{max} to the temperature T as:

$$\lambda_{\text{max}} T = 2898 \mu\text{m K} \approx 2900 \mu\text{m K} \quad (3.29)$$

Finally, we see that the coherence length and the effective, mean and peak wavelengths are all proportional to each other and are of the same order of magnitude:

$$l_c \approx 1.11 \lambda_{\text{eff}} \approx 1.48 \langle \lambda \rangle \approx 0.8 \lambda_{\text{max}} \quad (3.30)$$

Based on this, we now list the values of the coherence length and coherence time in Table 3.2 for our experimental conditions using the two different approaches described above to get order of magnitude estimates for the coherence variables. For the first case, we use the Equations 3.17 and 3.18 which assume a Gaussian emission spectrum, and consider three different values of the constant C , i.e. $C_1 = \frac{2\ln 2}{\pi} \approx 0.4413$, $C_2 = \sqrt{\frac{2\ln 2}{\pi}} \approx 0.6643$, and $C_3 = (C_1 + C_2)/2 = 0.5528$. The parameters we used to calculate the coherence values are the central wavelength $\lambda = 10 \mu\text{m}$, the spectral width $\Delta\lambda = 7 \mu\text{m}$ (i.e. between 7-14 μm), the refractive index of air at 10 μm , $n_{air,10\mu\text{m}} = 1.0003$ [246], and the speed of light in vacuum $c = 3 \times 10^8 \text{ m/s}$ which was divided by $n_{air,10\mu\text{m}}$ to get $c_{air,10\mu\text{m}}$. For the second case, we use Equations 3.24 and 3.23 for a blackbody radiation spectrum. The temperature T is calculated by using Wien's displacement law (see Equation 3.29) considering $\lambda_{max} = 10\mu\text{m}$, which gives $T = 290\text{K}$ to then calculate the coherence length, and $c_{air,10\mu\text{m}}$ is used to calculate the coherence time from the calculated coherence length.

Emission spectrum	Constant value	Coherence length (μm)	Coherence time (fs)
Gaussian	0.4413	6	21
	0.6643	9	32
	0.5528	8	26
Planck (Blackbody)	-	12	41

Table 3.2: Coherence length and coherence time values computed for longwave infrared radiation in air centred at 10 μm

We can see from Table 3.2 that the coherence lengths are all on the same order of magnitude as the reference wavelength of 10 μm of longwave infrared radiation. The coherence times also fall in the same order of magnitude range, a few tens of femtoseconds. As we have discussed above, the coherence length sets an upper limit on the optical path difference between two interfering waves to produce an interference pattern of adequate intensity contrast. In our case, the scattering medium has an average surface roughness on the order of 200 nm while the coherence length is at least 1 μm , even if we consider transmission through a Silicon wafer which has a refractive index of 3.47 (see Table 3.1), by dividing the coherence length calculated for propagation in air shown in Table 3.2 by Silicon's refractive index. This implies that the entire surface of our diffuser along the propagation direction falls within the coherence length scale, and thus will produce a speckle pattern.

3.3.1.3 Lateral coherence for speckle observation

It is also instructive to calculate the lateral angular range, i.e. perpendicular to the direction of propagation, within which two waves can produce an interference pattern at a fixed distance, from the coherence length. In Figure 3.34, the base of the isosceles triangle ADB forms a flat surface of the scatterer while the apex C is the observation plane for the speckle pattern. We consider that a wave from the point D travels to C with an optical path length equal to d_1 , while a wave from A to C will have an optical path length of d_2 . The optical path difference between the two waves will then be $\Delta d = d_2 - d_1 = d_1 \left(\frac{1}{\cos \theta} - 1 \right)$. To observe a speckle pattern, the optical path difference must satisfy the inequality $\Delta d \leq l_c \Rightarrow \frac{l_c}{d_1} + 1 \geq \sec \theta$ (where, $\sec \theta = \frac{1}{\cos \theta}$). Since the secant function is a monotonously increasing function between 0 to $\pi/2$, the inequality can be written as $\theta \leq \sec^{-1} \left(\frac{l_c}{d_1} + 1 \right)$. Considering l_c to be 12 μm (see Table 3.2) and d_1 to be 1,2,3 and 4 mm, which are the typical speckle observation plane distances of the camera from the diffuser's surface in our experiments, the values of θ turn out to be 9.0° , 6.4° , 5.2° and 4.5° respectively. Any two waves originating from points within the lateral distance $ad = d_1 \tan(\theta)$ will then be able to interfere with each other at c , and these distances for $d_1 = 1-4$ mm are 158 μm , 223 μm , 273 μm and 315 μm respectively. We can see therefore in our experiments that the lateral coherence length for speckle observation is much larger than the typical surface roughness, leading to the ability for waves from over a large area on the diffuser (compared to the surface roughness) to interfere with each other in producing the observed speckle pattern.

We shall now discuss about the final critical component of our setup which is the long-wave infrared camera that we use for speckle imaging, preceded by an overview of thermal camera technology, which is quite different from typical visible cameras.

3.4 Infrared detector

3.4.1 Bolometers

Bolometers are instruments that can detect thermal radiation and measure them by using a material whose electrical resistance is sensitive to temperature. It was first invented in 1878 by the astronomer and physicist Samuel Pierpont Langley with a temperature resolution down to $10^\circ \mu\text{C}$ [247] [248]. The essential components of a bolometer include an absorptive element which is connected to a constant temperature thermal reservoir through a thermal conductor. When thermal radiation impinges on the absorptive element, the temperature

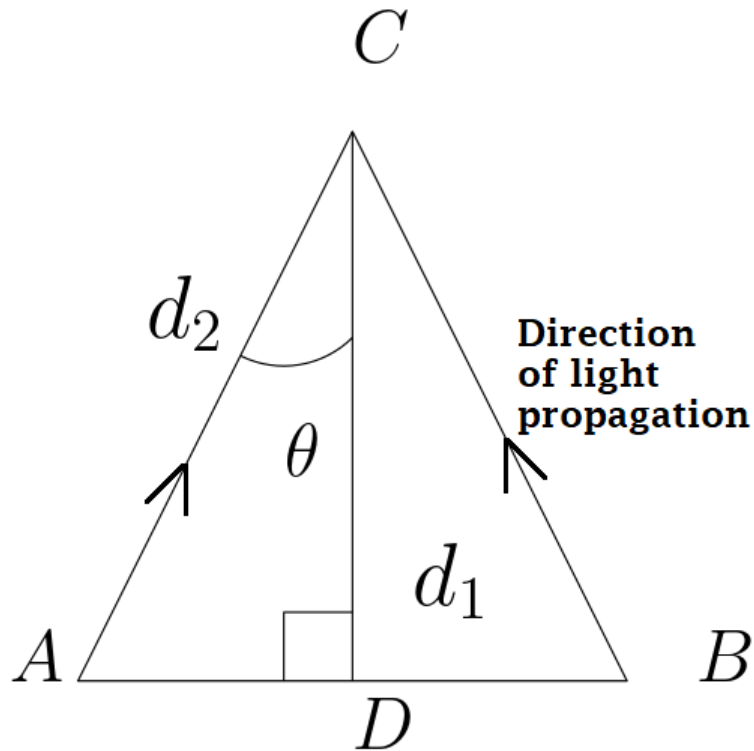


Figure 3.34: Lateral angular coherence range calculation sketch

of the absorber increases above the temperature of the thermal reservoir by an amount proportional to the absorbed power from the incident radiation. Considering that the heat capacity of the absorber is C , its initial temperature is T , the thermal conductance of the thermal link between the reservoir and absorber is G , and the power absorbed from the incident radiation is P , the temperature increase is equivalent to $\Delta T = P/G$. The thermal time constant of the system is $\tau = C/G$, which characterizes the response speed of the detector. The temperature increase is measured by a resistive thermometer which can be a separate material that is attached to the absorber or the absorbing material itself. The measured temperature increase then allows the calculation of the incident power absorbed by the relation above [249].

Bolometers are highly sensitive and have good energy resolution capabilities which are further improved if operated at cryogenic temperatures. There are usually two mechanisms that are employed to cool commercial bolometers - coolers based on the Stirling cycle [251] [252] and cooling using liquid nitrogen [253] - both of which make cameras based on these techniques more expensive, decrease their portability and make the imaging process more cumbersome.

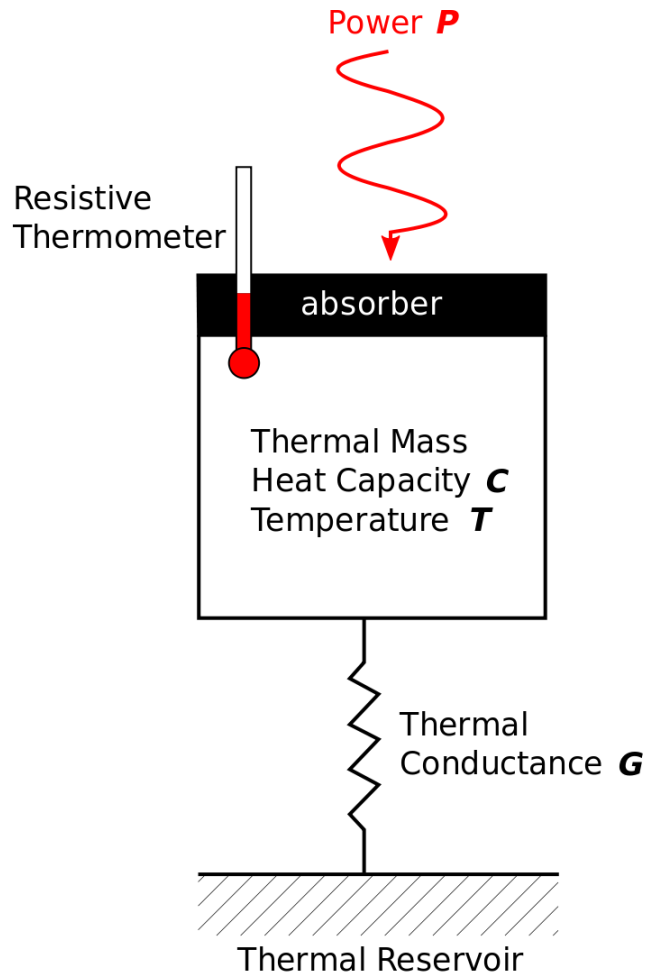


Figure 3.35: Schematic of a bolometer - essentially comprising a thermal radiation absorber connected to a thermal reservoir at a constant temperature through a thermal conductor - which is able to measure the power of incident thermal radiation by measuring the temperature change due to the incident radiation using a resistive thermometer [250].

3.4.2 Microbolometers

An improvement over the basic bolometer technology in the longwave infrared is the microbolometer [254]. A microbolometer is also a thermal sensor akin to a bolometer, i.e. based on the measurement of the thermal radiation using a temperature-dependent electrically resistive material, but it is an uncooled thermal sensing device. This has enabled the development of commercial uncooled thermal cameras with a thermal sensitivity in the order of a few milli Kelvins (mK) [255].

Microbolometers are arrays of individual pixels that detect longwave infrared radiation

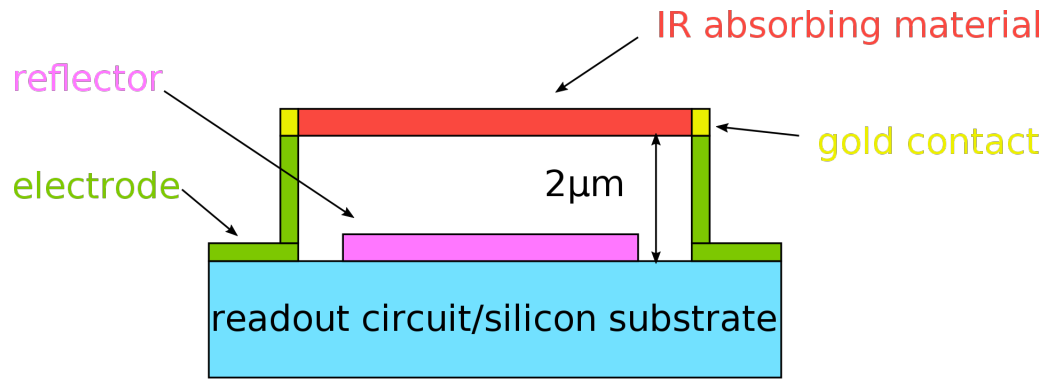


Figure 3.36: Cross-sectional scheme of a typical microbolometer pixel - consisting of a thermal absorber material that absorbs incident LWIR radiation which is placed above a substrate in a bridge structure to prevent thermal conduction with the substrate and readout circuitry below except for the tiny electrical contacts, thus eliminating the need for active cooling, and a reflector to redirect unabsorbed incident radiation to the absorber, all in a sealed vacuum enclosure [256].

between the wavelengths 7.5 - 14 μm . A single pixel consists of many layers in a bridge architecture on a substrate, each of which function similar to the essential components used in a bolometer. A typical microbolometer pixel is built using a silicon layer as the substrate which also comprises an integrated circuit for image readout. Thin L-shaped electrodes are manufactured by depositing a layer on the substrate and etching away the area to be removed later. The absorbing layer is deposited above the electrodes and connected to them by gold contacts. Different materials are used to make the absorbing layer, though any good absorber should have a high responsivity to convert the incoming thermal radiation to electrical signals while keeping the noise much lower than the signal. The bridge structure - with a hollow space of a few micrometers between the absorbing layer and the substrate - enables the absorber to be thermally isolated from the readout circuitry and allows it to function as a bolometer without requiring active cooling. A reflector layer is placed in contact with the substrate and below the absorber to redirect any unabsorbed light back to the absorber for maximum absorption of the incident thermal radiation. The whole microbolometer pixel array is enclosed in a vacuum to achieve thermal isolation and prevent air conduction between the thermistors and the readout integrated circuit, which could otherwise dampen the sensor responsivity, as well as to increase its lifespan by protecting the fragile thermistor array in vacuum [257] [258].

3.4.3 Microbolometer detector responsivity

The responsivity of the detector, which needs to be high, depends on a few key material properties of the absorber [259]:

- Temperature coefficient of resistance
- Pink noise characteristics
- Resistance

3.4.3.1 Temperature coefficient of resistance

A good detector needs to be manufactured from a material that exhibits a large resistance change when there is a small change in the temperature. This is quantified by the material's temperature coefficient of resistance (TCR) [259]. A material with a TCR that remains constant over the entire temperature range of the camera's operational conditions is also useful since it leads to reliable temperature measurements without the need to correct for the temperature dependence of the TCR. Additionally, as the absorber is heated, the resistance of the material must decrease, and so a material with a negative TCR is required. Materials with positive temperature coefficients (PTC) of resistance have limited lifetimes in harsh thermal control situations as they have low PTC intensity (i.e. the logarithm of the ratio of the maximum resistivity to the room temperature resistivity, which quantifies their operational range in terms of temperature, current and voltage) and poor PTC reproducibility [260]. The typical use of such materials is in high temperature ranges and not in the room temperature range [261] - which is our temperature range of interest, corresponding to the longwave infrared region. The absorbing thermal sensing detector of current commercial microbolometers are primarily made up of vanadium oxide (VO_x) which has a negative TCR of $\sim 2\%/K$ [262] and doped amorphous silicon (a-Si) with negative TCR values of $2\% - 5\%/K$ [263]. Even as some vanadium oxide detectors have higher TCR values like $6.5\%/K$ [264], boron-doped amorphous silicon is being increasingly used in place of vanadium oxide for large commercial microbolometer arrays. Boron-doped amorphous silicon has larger TCR values in general, and it is also fully compatible with the silicon complementary metal oxide semiconductor (CMOS) process that is used to make camera detectors industrially.

3.4.3.2 Pink (1/f) noise characteristics

The next important factor for the choice of an appropriate absorbing detector material in an uncooled microbolometer is the 1/f noise, also known as pink noise [265]. Pink noise carries an equal amount of noise energy for each frequency doubling or halving (octave) interval. In contrast, white noise has a constant power spectral density and has the same intensity at every frequency.

Thermal detectors undergo a change in their temperature when exposed to an incoming infrared radiation flux. To offset and monitor this change, the detectors are electrically biased using a bias current [266]. This electrical biasing leads to Joule heating which alters the resistance of the microbolometer. This self-heating process occurs over a very short duration compared to the thermal time constant of the microbolometer, but due to the bias power being much higher than the power of infrared radiation, it increases the temperature of the microbolometer significantly and results in a temperature drift driven by bias self-heating. As the heat generated from this Joule heating cannot be rapidly dissipated to the substrate by thermal conduction, there have been developments in the design of the readout circuit to compensate for the self-heating to improve imaging performance [267].

Increasing the detector bias leads to an improvement in the noise equivalent temperature difference (NETD), thus increasing its sensitivity. On the other hand, both responsivity and 1/f noise increase with the bias linearly. The NETD of a bolometer is defined as the temperature difference, between two large blackbodies placed next to each other and viewed by two-halves of the infrared imaging system, that is necessary to increase the output signal-to-noise ratio of the respective imaging half-arrays by unity [268]. The 1/f noise, therefore, limits the performance of the microbolometer detector by limiting the bias power that can be applied without increasing noise levels substantially [269]. Additionally, 1/f noise leads to detector drift and high spatial noise at low frequencies, which has a higher debilitating effect on target recognition than a similar amount of temporal noise.

Even if the detector temperature is stable and a calibration shutter is used, the spatial noise originating from 1/f noise causes a temporal degradation of performance. The coherence of the low frequency components also renders averaging over many samples ineffective in reducing the noise effectively. In contrast, averaging of white noise over many samples improves the signal to noise ratio. The effects of 1/f noise includes signal measurement uncertainties, spatial and temporal noise, and errors in non-uniformity correction, all of

which degrades imaging performance [270]. All these detrimental effects are the reason for choosing a detector which has the least $1/f$ noise given the other considerations [271].

3.4.3.3 Detector resistivity

The third important factor to be considered in choosing a highly responsive detector is the resistance of the detector material itself. It is necessary to use a material that has a low resistivity so that it can generate a higher detection current at a constant bias voltage. Secondly, the resistivity of a material also affects the Johnson-Nyquist noise, which adds to the total detector noise [272].

Johnson–Nyquist noise, also known as thermal noise, arises from the thermal motion of electrons (or charge carriers) inside an electrical conductor at equilibrium [273] [274]. Johnson-Nyquist noise is present in all electrical circuits, irrespective of applied voltage, and can be a limiting noise in some instruments [275]. It is an example of the general fluctuation-dissipation theorem in physical systems. Johnson-Nyquist noise power is linearly proportional to temperature, with increasing temperature leading to higher thermal noise power. In an ideal resistor, thermal noise has an approximately constant power spectral density, similar to white noise, except at very high frequencies (beyond 1 THz) [276], while in a finite bandwidth system, it approximates a Gaussian amplitude distribution. The resistivity values of typical detector materials like doped and undoped Vanadium oxide absorbers range from $0.01 \text{ } \Omega \text{ cm}$ to $10 \text{ } \Omega \text{ cm}$, which are in accordance with the requirements of state-of-the-art read-out circuitry for microbolometer arrays [277].

The reduction in the microbolometer pixel size over the years, and the proportional increase in the number of pixels per unit area leads to higher image resolution, but at the cost of a higher NETD since smaller pixels are less sensitive to incident infrared radiation. State-of-the-art microbolometer arrays have NETD values that are about 10 mK [278].

3.4.4 FLIR longwave infrared camera

A principal component of our experimental setup, and indeed the whole project, is our longwave infrared camera. We use a FLIR A655sc thermal infrared camera, shown in Figure 3.37, whose sensor is a focal plane array built using uncooled microbolometers of Vanadium Oxide (VoX). As discussed in Section 3.4.2, microbolometers are pixel arrays of sensors containing resistive elements that convert detected heat to electrical signals that can then form an image.

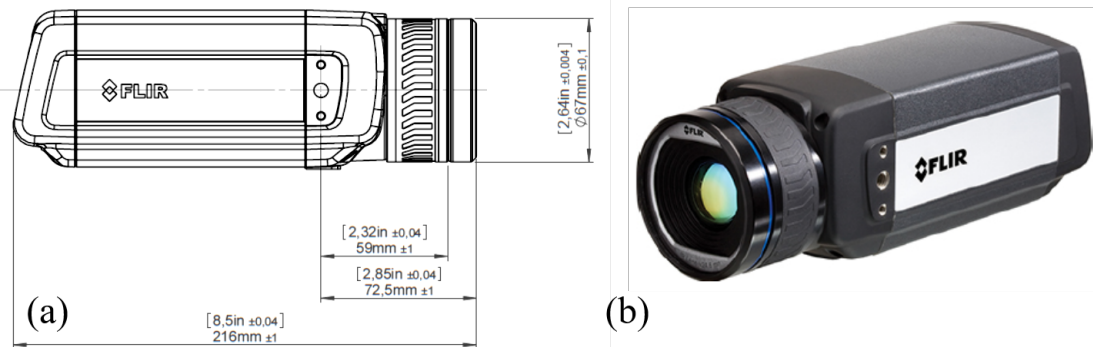


Figure 3.37: FLIR A655sc longwave infrared uncooled microbolometric camera: (a) sketch of geometrical dimensions, and (b) upright view, when used with the camera’s primary $f = 26.4$ mm lens [279].

The camera we use has 640×480 pixels with a 16 bit intensity-encoding dynamic and a frame rate of 50 Hz. It is possible to image at higher frequencies, though only by reducing the sensor area, with two windowing modes for imaging - one for 640×240 pixels at 100 Hz and the other for 640×120 pixels at 200 Hz. The size of each pixel is $17 \mu\text{m}$ across the diagonal. The incident infrared radiation is detected via an 8 ms rolling shutter readout. In a rolling shutter readout, all the pixels are not captured at the same time but the shutter records a subset of pixels sequentially over time in a specific direction until all the pixels have been acquired. It works in the entire LWIR spectral range from 7.5 to $14 \mu\text{m}$, and can detect temperatures between -40 and 650°C , with a thermal sensitivity or NETD of 30 mK . The accuracy of the camera’s temperature measurement is $\pm 2^\circ\text{C}$ or $\pm 2\%$ of the reading value. The emissivity of the camera can be varied and we usually set it to 0.92. It is quite compact - weighing 0.9 kg and measuring 216 mm (length) \times 73 mm (width) \times 75 mm (height). It is therefore comparatively much more portable than cooled thermal cameras, which require either a Stirling cycle engine or a liquid nitrogen supply for cooling. This compactness and portability arising from the uncooled microbolometer technology has been a key motivation for using this commercial LWIR camera to develop our imaging technique since it can be used in applications like those in industrial settings with greater ease than cooled thermal cameras.

The camera’s primary lens contains 3 aspheric lenses with a front lens diameter of 32 mm . The focal length is 24.6 mm with a minimum focus distance of 25 cm . This lens has an F-number of 1.0, which is the ratio between the focal length of the lens and the maximum diameter of the aperture or entrance pupil. The field of view is $25^\circ \times 19^\circ$ i.e. 31° across the

diagonal, and it has a spatial resolution or instantaneous field of view (IFOV) of $680 \mu\text{rad}$. The depth of field of this lens when the object plane is 50 cm away is ± 1 cm.

We also use a second close-up lens with the camera which has a magnification of 1.5x. This close-up objective lens contains 4 aspheric lenses with a front lens diameter of 52 mm. The focal length is 62 mm with a minimum focus distance of 46 mm, which is also our usual working distance for this lens. This lens has an F-number of 1.1. The field of view is 16 mm x 12 mm i.e. 22 mm across the diagonal, and it has a spatial resolution or instantaneous field of view (IFOV) of $25 \mu\text{m}$. The depth of field of this lens is $210 \mu\text{m}$, which makes it critically useful to image the longwave infrared speckles at a fixed plane. Indeed, the first longwave infrared speckle pattern that we observed using our setup, as shown in Figure 3.12, was obtained using this close-up lens.

3.4.5 Summary

In this chapter, we have looked at how the key elements of a speckle imaging system using scattering media were optimally developed and put together to build a longwave infrared speckle imaging setup - broadly, the scattering medium, the infrared source and the necessary optics to produce an approximate point source, the uncooled infrared camera and the associated infrared optics. The present experimental configuration, as shown in Figure 3.2, will then be utilized to carry out longwave infrared wavefront sensing, with the post-imaging processing and wavefront reconstruction being described in Chapter 4, as well as presenting the first results of LWIR wavefront sensing using speckle imaging demonstrated using the setup developed.

Chapter 4

Wavefront Reconstruction

Contents

4.1	Processing of the speckle images	89
4.2	Wavefront reconstruction algorithm	92
4.3	Angular memory effect characterization	94
4.3.1	Angular memory effect for varying diffuser - speckle imaging plane distances	100
4.4	Speckle grain size estimation	101
4.5	Lens phase imaging experiments	106
4.5.1	Reconstructed lens wavefronts	109
4.5.2	Wavefront sensing for various curvatures	112
4.5.3	Wavefront sensing with varying diffuser - speckle imaging plane distances	115
4.6	LWIR speckle imaging challenges	119
4.6.1	Camera noise analysis	119
4.6.2	Frame averaging of speckle images	124
4.6.3	Intensity inhomogeneities	125
4.6.4	Infrared focussing	126
4.7	Wavefront reconstruction of a complex phase mask	127
4.8	Qualitative and quantitative aspects of phase reconstruction	131

In Chapter 3, we have discussed the experimental setup developed for longwave infrared speckle imaging. In this chapter, we will look at the manner in which the speckle patterns are processed and treated to reconstruct phase images or wavefronts of infrared objects. We will discuss the speckle image processing and wavefront reconstruction algorithm, followed by a discussion on the first results in longwave infrared phase reconstruction. Some results about characterizations of the scattering media, additional results obtained from the reconstructed wavefronts after infrared speckle imaging, and future possibilities of work will be also briefly delved into.

4.1 Processing of the speckle images

The processing of data acquired in the form of speckle images produced when infrared light from a thermal source passes through a thin scattering medium after having been subjected to a possible deformation of its wavefront is one of the critical parts of this experimental project. Indeed, in any imaging experiment, just as it is essential to have an optimal experimental setup for the acquisition of images, it subsequently becomes necessary to treat these acquired images properly to derive physically meaningful and high fidelity results from the experiments. As the experimental setup has evolved over the course of this thesis project to achieve better phase imaging capabilities, so has the image processing workflow itself.

Since we carry out speckle imaging, and specifically in the longwave infrared, it is principally important to register the speckle pattern to the best possible accuracy and precision. While this is obviously limited by the camera sensor’s design and working conditions, the captured image can then be processed digitally to improve on this aspect or to at least prevent degradation in image quality in a subsequent part of the processing. The major issues in our image processing approach are to ensure that the speckle pattern that is captured is a relatively temporally static speckle, that the background signal and noise signal can be eliminated to the greatest possible degree in the acquired speckle images, and that these processed speckle patterns can then be used in the phase reconstruction algorithm we employ, to obtain physically viable and accurate results.

As discussed earlier, infrared images suffer from a strong background caused by camera technologies, but also by the fact that experiments are conducted in a non-zero Kelvin lab-

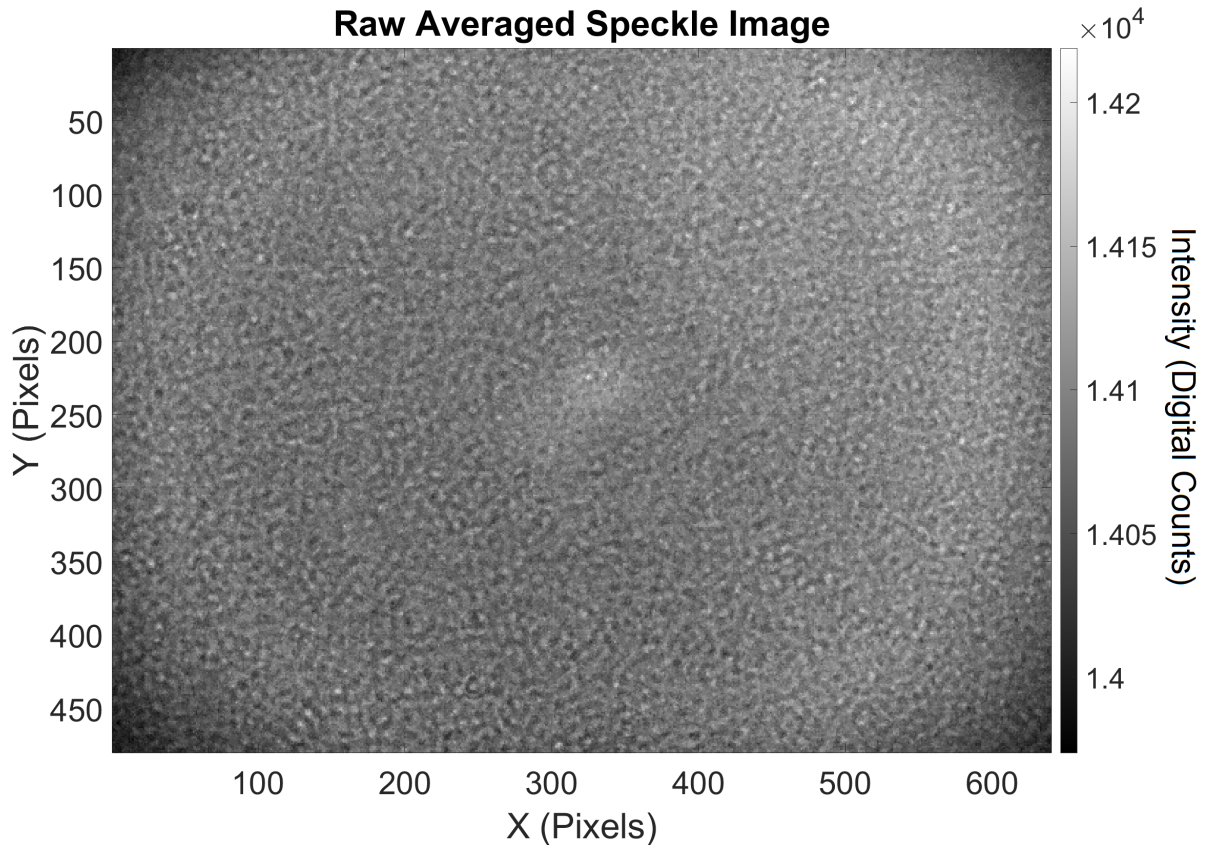


Figure 4.1: The mean of a single pixel over all 100 recorded raw image frames is calculated, for each of the 640 x 480 pixels, and the resulting image is considered the raw averaged speckle image.

oratory, where the environment emits infrared light. In a typical experiment, we capture movies of 100 frames at a frame rate of 50 Hz for the entire field of view of the camera sensor’s 640 x 480 pixels. Background images are taken with all the optics in place without the source beam, as a reference measurement of the signal from the environment and the associated camera noise. Similarly, a reference speckle pattern is captured when a plane wavefront from a thermal source illuminates the thin scatterer and a speckle pattern is formed after transmission. A sample speckle pattern is similarly captured, but with the plane wavefront being incident on a phase object (sample) which creates a distorted wavefront. The distorted wavefront is incident on the scatterer and the slightly altered speckle pattern, formed after transmission through the scatterer, is imaged by the camera as the sample speckle pattern.

The images are recorded by the camera and stored using its proprietary control software into the .seq format. The raw .seq files contain 100 frames of each speckle pattern imaged

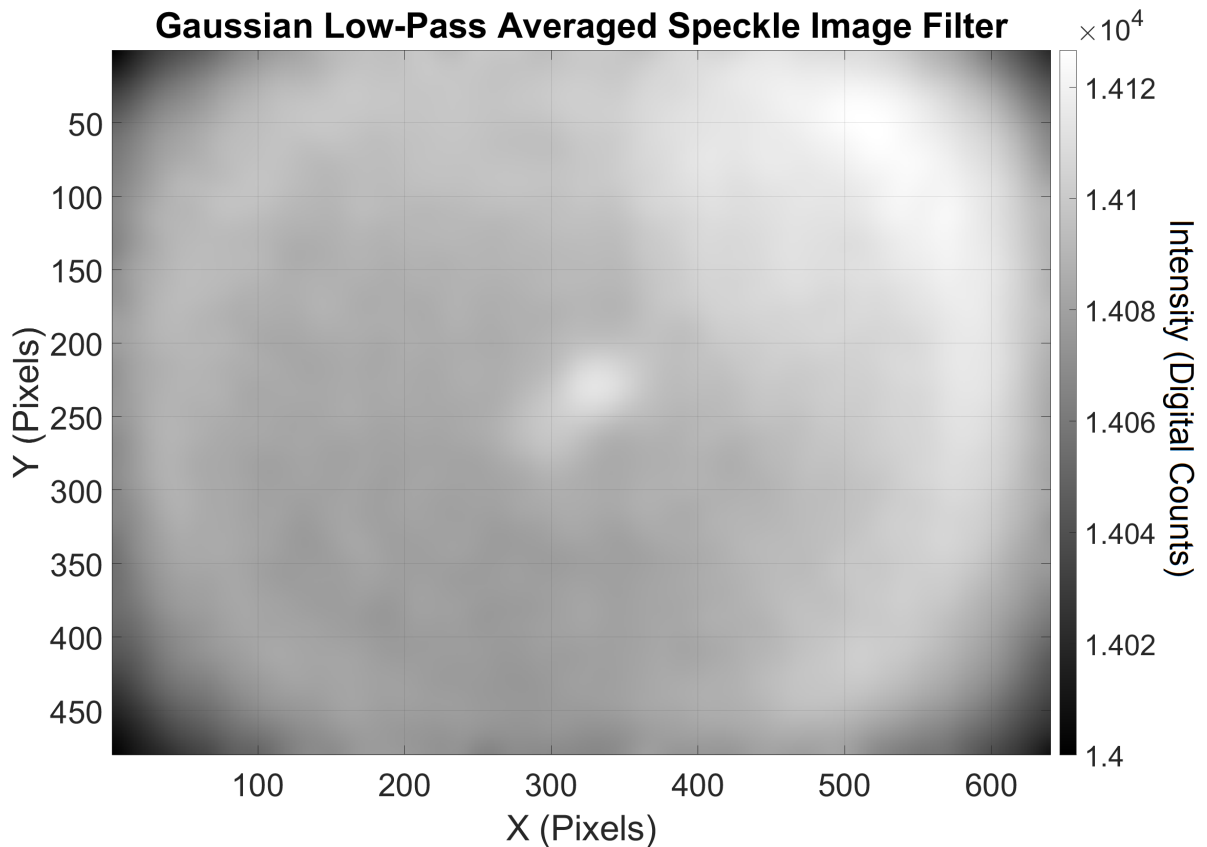


Figure 4.2: A Gaussian filter with $\sigma = 10$ pixels is used to smooth the raw averaged speckle image (shown in Figure 4.1), obtaining a low-pass filtered speckle image that contains the low spatial frequency components which are used as a subtractive mask for the final processed image (shown in Figure 4.3).

at 50 Hz. These files are then read by a simple MATLAB code, where every pixel's mean value is computed to obtain a composite image from all the acquired frames in the raw image sequence files. The averaged reference and sample speckle images are then individually passed through a Gaussian filtering routine. A Gaussian filter of $\sigma = 10$ pixels smooths the input speckle pattern (shown in Figure 4.1), and produces a filtered image mask where the low spatial frequency features are retained while the high spatial frequency features are filtered out. This smoothed image mask (shown in Figure 4.2) is then subtracted from the averaged original speckle pattern to remove the strong low spatial frequency features and retain higher spatial frequency details like the speckle grains themselves, and obtain the final high-pass filtered image (shown in Figure 4.3).

This filtering step ensures that some of the intensity inhomogeneities and vignetting effects on the boundaries of the image in the averaged speckle image are removed, thereby also

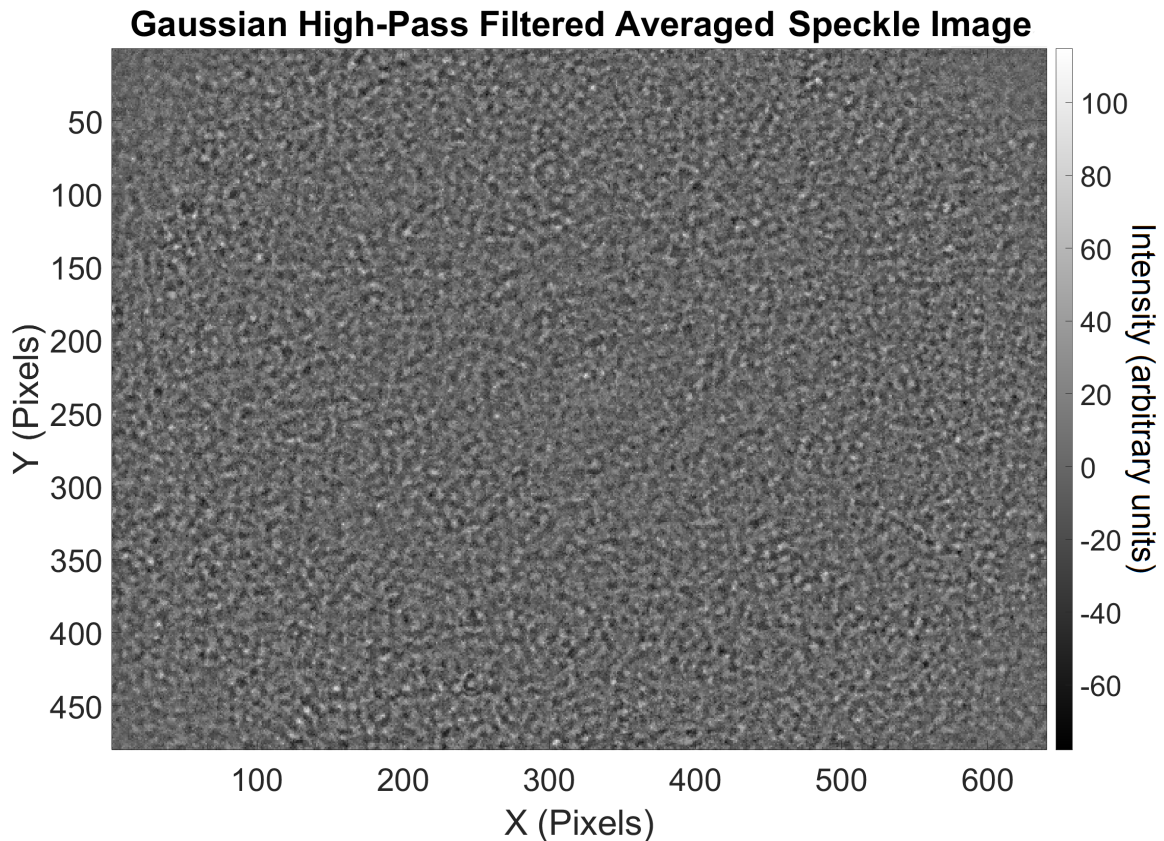


Figure 4.3: The low-pass Gaussian filtered image shown in Figure 4.2 is subtracted from the raw averaged speckle image (shown in Figure 4.1) to obtain the final processed image presented here. It corresponds to a Gaussian high-pass filtered speckle that has been removed of low spatial frequency intensity inhomogeneities while preserving the higher spatial frequency speckle grain features. Figures 4.1, 4.2 & 4.3 all depict images that correspond to the camera's 640 x 480 pixels measuring 10.88 mm x 8.16 mm on the camera sensor plane.

increasing the contrast of the speckle grains in the image. These filtered and averaged reference and sample speckle images are then used as input into the wavefront reconstruction algorithm to obtain the reconstructed wavefronts, as will be detailed in Section 4.2.

4.2 Wavefront reconstruction algorithm

We are interested in reconstructing the relative phase delay between a plane wavefront and a wavefront originating from a phase object that distorts a plane wavefront. This is achieved by using the different speckle patterns that are produced when the wavefronts are scattered and transmitted through a thin scattering medium in the two different conditions. The dis-

tortion of the reference plane wavefront due to the phase object induces small shifts in the speckle grains present in the reference speckle pattern. Hence, the map of the displacement field needs to be calculated from our measurements performed with and without a phase object.

The minuscule displacements of the speckle grains between the reference and sample speckle are computed using the diffeomorphic Demons algorithm. The algorithm uses effectors known as Demons to alter a deformable grid of the sample image to diffuse through the contours of the static reference image, ultimately trying to match the two, as discussed in Section 2.1.4.1. In our implementation, we utilize the Demons algorithm for non-rigid image registration, which is a part of the Matlab image processing toolbox and can be accessed through the function *imregdemons*. This algorithm employs iterative second-order gradient descent to minimize a mean squared difference function. To achieve multi-scale optimization and mitigate issues with local minima stagnation, we iteratively update and smooth the displacement vector map using Gaussian filters of diminishing dimensions. The algorithm calculates the displacement vectors using the gradient of the moving image and updates the deformation field accordingly. The integration step can be expressed as: $D(x, y) = D(x, y) + StepSize * \nabla M_{new}(x, y)$, where $D(x, y)$ is the deformation field, $StepSize$ is the step size, and $\nabla M_{new}(x, y)$ is the gradient of the updated moving image. The process continues until convergence, refining the deformation field and aligning the images.

The displacement field obtained from *imregdemons* is passed to another function in our code to perform the integration step and obtain the integrated gradient. This function computes the cumulative sum of gradients along the x and y directions for each pixel in the image. This results in a representation of the total gradient magnitude accumulated from a given reference point to each pixel location. The integrated gradient is obtained by integrating the gradients along a path from the reference point to the target pixel. The code uses the 2D Fast Fourier Transform (FFT) and its inverse (IFFT) to compute the gradients and perform the integration. The FFT operation converts the gradients from the spatial domain to the frequency domain. Then, the integration is performed by dividing the transformed gradients by the frequency components. Finally, the IFFT operation is applied with zero-padding, which converts the integrated gradient field back to the spatial domain, and the real component is obtained. The Demons algorithm is quite efficient in reconstructing the wavefront from the two speckle images and takes about 10 seconds for a single wavefront

reconstruction, which means that wavefront reconstruction can be possibly carried out in real-time for applications in which the dynamics evolves on the timescale of a few minutes and beyond.

4.3 Angular memory effect characterization

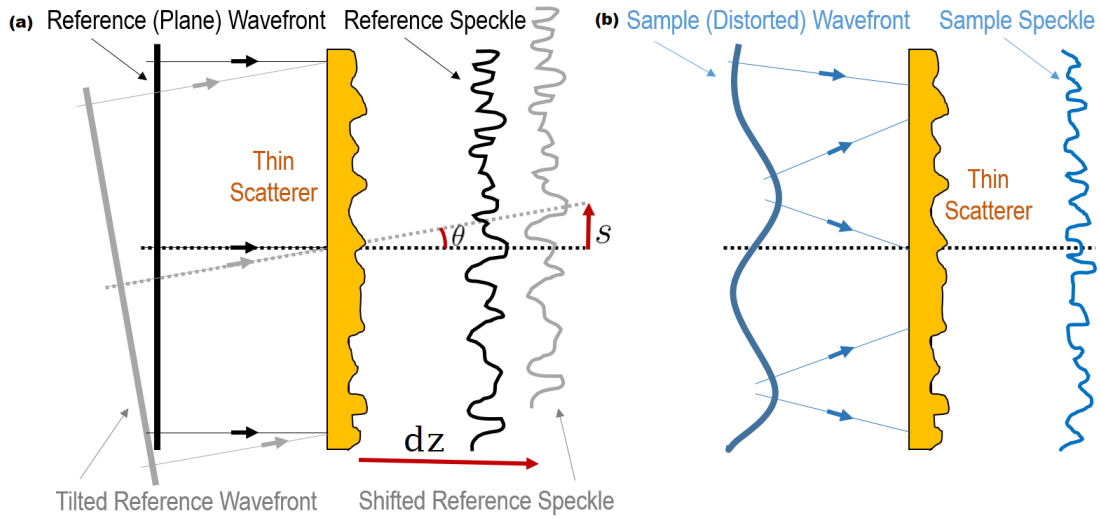


Figure 4.4: A speckle pattern is a unique fingerprint of the incident wavefront on a thin scattering medium. (a) A plane (reference) wavefront produces a reference speckle pattern after transmission through a thin surface scatterer, while a global tilt of the same plane wavefront by the angle θ also results in the same speckle pattern, only shifted by an amount $s = (dz)\theta$ at a distance dz , a phenomenon known as the angular memory effect. (b) A local tilt in the wavefront (induced by a sample) changes the speckle pattern and results in a distorted sample speckle which is different from the reference speckle pattern.

We shall now characterize the angular memory effect characteristics of our single side polished Silicon wafer diffuser. The angular memory effect is the phenomenon whereby a small global tilt in the input wavefront impinging on a thin scattering medium does not change the speckle pattern completely but only shifts the original speckle pattern in the transverse distance by an amount proportional to the tilt, as illustrated in Figure 4.4. It is a key characteristic of thin scattering media to have a high angular memory effect which enables precise wavefront sensing, due to a greater degree of correspondence between the incident wavefront's local phase information to the local speckle grain shifts in the captured speckle image. We wanted to experimentally measure the angular memory effect range of our diffuser to quantify this characteristic and verify that the diffuser we use satisfies the expected high memory effect shown by thin scatterers.

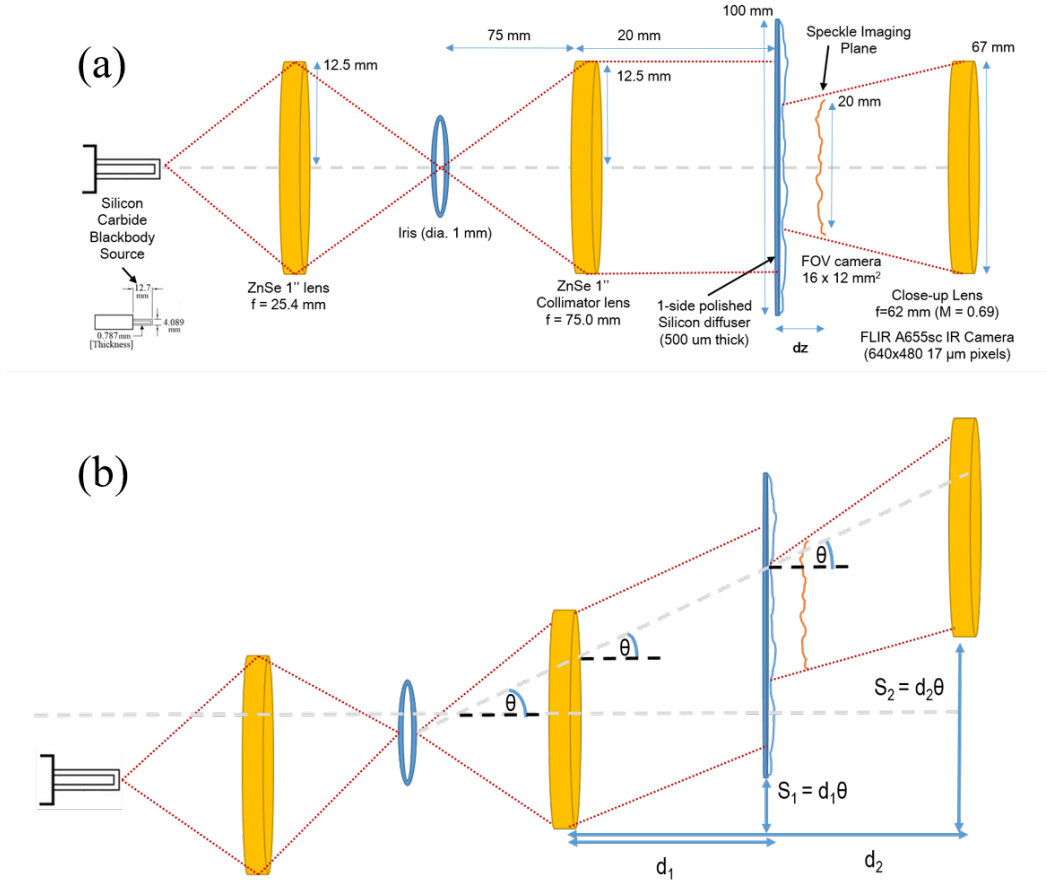


Figure 4.5: LWIR speckle imaging setup to characterize the angular memory effect of the scattering medium: (a) A blackbody source produces a plane wavefront which is incident on the scattering diffuser and forms a speckle that is imaged at a fixed imaging plane of a thermal camera. (b) To characterize the angular memory effect, we tilt a reference wavefront (a plane wavefront, in this case) globally by different angles, which is achieved by changing the position of the source, the secondary source image forming lens, and the iris in conjunction (to have the same intensity as the reference), which upon collimation forms a plane wavefront tilted by the variable angle θ . This tilted plane wavefront is incident on the diffuser, and the corresponding speckle pattern is imaged by the camera, with appropriate translations using micrometer translation stages to image the same speckle position. The resultant speckle pattern is identical to the reference speckle but has a global translation shift due to the global tilt of angle θ of the plane wavefront.

A specific wavefront produces a corresponding unique speckle pattern, whose relative grain positions do not change if the wavefront globally shifts by an angle θ . However, a local tilt in the wavefront produces a local deformation of the speckle pattern, which makes it possible to perform precise wavefront sensing as the speckle pattern is a unique fingerprint of the incident wavefront. The memory effect has been previously discussed in Section 2.1.4,

where the first reportage of the effect in literature is described, while the basic theoretical treatment regarding the effect is briefly reviewed in Section 2.2.2.3.

In our experiments to characterize the angular memory effect, using the setup described in Figure 4.5, we change the tilt angle θ of the plane wavefront in increments of 0.5° from the reference incidence angle of 0° (which corresponds to Figure 4.5 (a)) to 3.5° on either side of the optical axis. After the different speckle images are acquired which correspond to the different incidence angles of the plane wavefront on the diffuser, a small fixed window of the reference speckle image (typically 60×60 pixels around the central pixel) is cross-correlated with the shifted speckle images to find their maximum. The normalized cross-correlation of the two images gives us a measure of the similarity of the two speckle patterns, and is calculated as:

$$R_{xy}(m, n) = \frac{\sum_{i=1}^M \sum_{j=1}^N [x(i, j) - \bar{x}][y(i - m, j - n) - \bar{y}]}{\sqrt{\sum_{i=1}^M \sum_{j=1}^N [x(i, j) - \bar{x}]^2 \sum_{i=1}^M \sum_{j=1}^N [y(i, j) - \bar{y}]^2}} \quad (4.1)$$

where x and y are the input images, M and N are the dimensions of the input images, m and n are the row and column offsets, respectively, of the template with respect to the input image, and \bar{x} and \bar{y} are the means of the input images. The output of the function, $R_{xy}(m, n)$, represents the similarity of the template and the input image at each position. The maximum of the normalized auto-correlation function corresponds to the highest relative similarity between the reference speckle and the angular incidence speckle pattern, when the reference speckle pattern has been shifted by the same amount as the angular incidence speckle pattern has translated due to the memory effect. The position of the maximum of the normalized auto-correlation function therefore enables us to obtain this global speckle translation shift.

We see, in Figure 4.6, the maximum values of the normalized cross-correlation between the reference on-axis incidence speckle pattern and the individual shifted speckle patterns from off-axis incidences between 0.5° to 3.5° on either side of the optical axis, all of which are close to 1. The auto-correlation maxima values range between 0.90 and 0.97. The maximum normalized cross-correlation value of 1 would be theoretically expected for all the off-axis incidence speckle patterns, in the ideal case of them being exactly the same speckle pattern as the reference on-axis incidence speckle pattern with only a translation shift. We can see that our experimental angular memory effect results are in very good

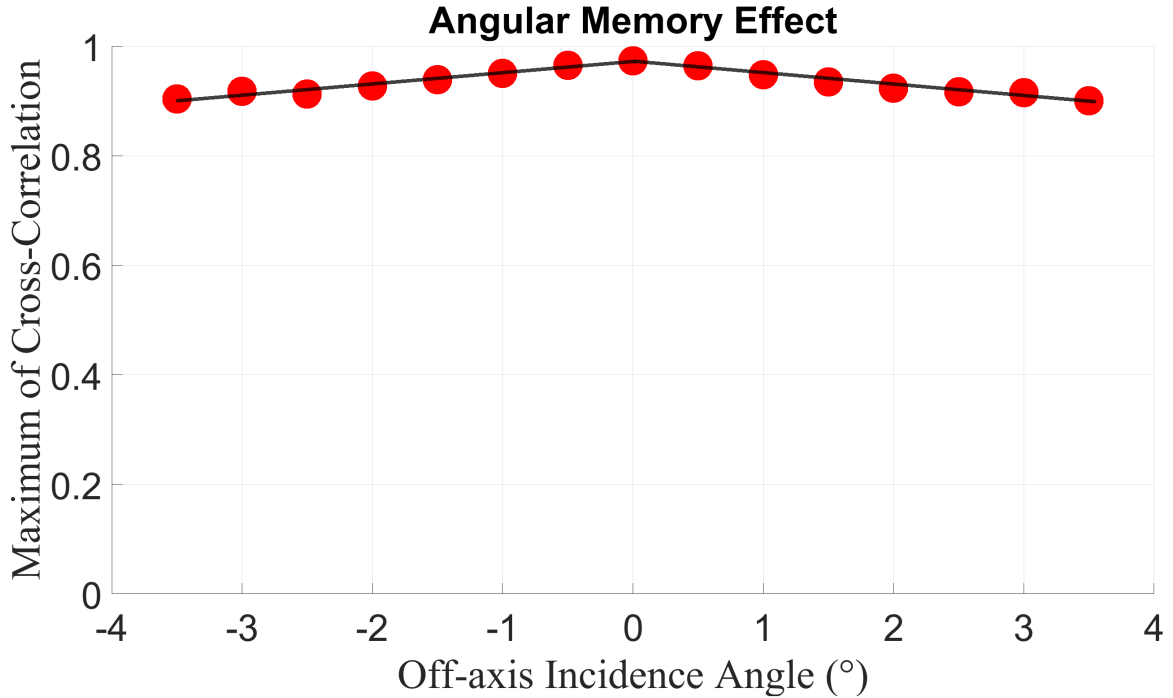


Figure 4.6: Angular memory effect characterization of a single side polished Silicon diffuser in an LWIR speckle imaging setup. With our diffuser, we see that the angular memory effect is satisfied over an angular range of about 3 degrees on either side of the axis. We quantify the cross-correlation of the off-axis speckles with the on-axis reference, and it turns out that our diffuser is very close to the infinite angular memory effect regime. The distance between the diffuser and the imaging plane of the camera (dz) is 4 mm, in this case.

agreement with the expected ideal scenario, which points out to a high angular memory effect for our single side polished Silicon wafer within a range of $\pm 3.5^\circ$ from the optical axis. This result implies that we can use our imaging setup to carry out wavefront reconstruction using the high fidelity of the speckle shifts that are due to the angular memory effect. This large angular memory effect permits a one-to-one correspondence from the incident wavefront’s local phase information to the local speckle grain shifts in the captured speckle image, thereby enabling precise wavefront sensing.

The cross-correlation between the reference speckle and the off-axis speckles gives us a quantitative estimate of the similarity between the speckle patterns, as we saw through the plot of the maximum values against the incidence angle in Figure 4.6. The position of the maximum of the cross-correlation functions, on the other hand, gives a measure of the global speckle translation shift between the reference and off-axis incidence speckles. As

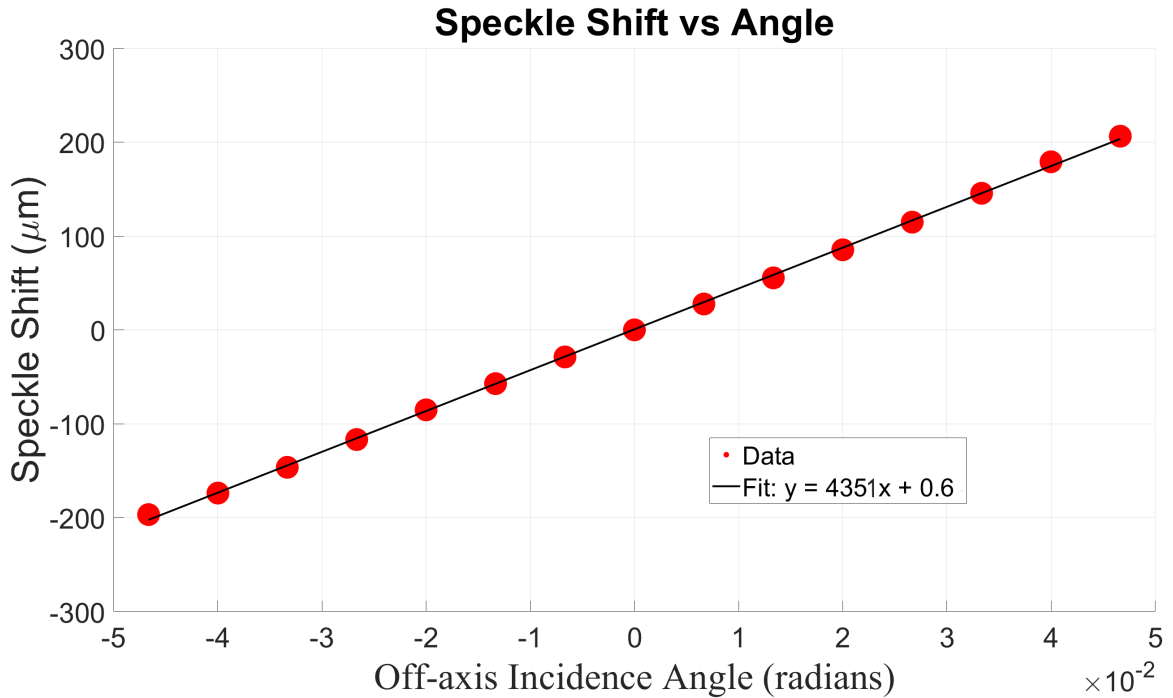


Figure 4.7: The estimated global speckle translation shift between an off-axis incidence speckle pattern and the reference on-axis speckle pattern is plotted against the incidence angle, which follows a well-defined linear relation, as expected in the angular memory effect range. A fit of the data points gives us an alternative experimental measurement of the distance between the diffuser and the speckle imaging plane of the camera, which is useful as a parameter for the Demons algorithm for wavefront reconstruction. The distance between the diffuser and the imaging plane of the camera (dz), as measured by a micrometer scale is 4 mm.

we have seen in Figure 4.4, the speckle shift s is a function of the incidence tilt angle θ and the distance between the diffuser and the imaging plane of the camera where the speckle is captured, dz . In the angular memory effect range, the relationship between the speckle shift and the tilt angle is expected to be linear, with the constant distance dz being the slope of the speckle shift versus tilt angle curve. In Figure 4.7, we use the experimental data from our angular memory effect characterization experiment to see if this linear relationship between the speckle shift and the tilt angle is satisfied, as well as estimating the value of dz using a linear fit to the data points. We see in the plot that the linear relationship is clearly satisfied, as expected, with the linear fit in close agreement with the experimental data. The speckle shift of the farthest off-axis incidence speckle with respect to the reference on-axis incidence speckle is less than 200 μm on either side of the optical axis, which corresponds to less than 10 pixels considering the pixel size of 17 μm , again alluding to the fairly large

angular memory effect regime we operate in. The slope of the fit gives a value of the distance between the diffuser and the speckle imaging plane to be 4.35 mm, as compared to the value of the same distance measured experimentally using a micrometer translation stage being 4.00 mm, which is 9% off and within experimental tolerance. In addition to reinforcing the validity of the angular memory effect regime of our diffuser in this imaging setup, the value of the distance from the fit also serves as an additional estimate of the distance value which is used as a calibration constant in the Demons algorithm.

It is pertinent to note here that the estimation of the value and position of the maxima of the 2-D normalized auto-correlation function between each off-axis incidence speckle and the reference on-axis incidence speckle was carried out by using a 2-D Gaussian fit of the peak of the normalized auto-correlation function to obtain a smoother and more symmetric precise estimate of the values. We can see in Figure 4.8 a glimpse of the difference introduced to the normalized cross-correlation function's peak upon being fitted by a 2-D Gaussian surface, by enabling a well-centred and localized estimation of the peak position.

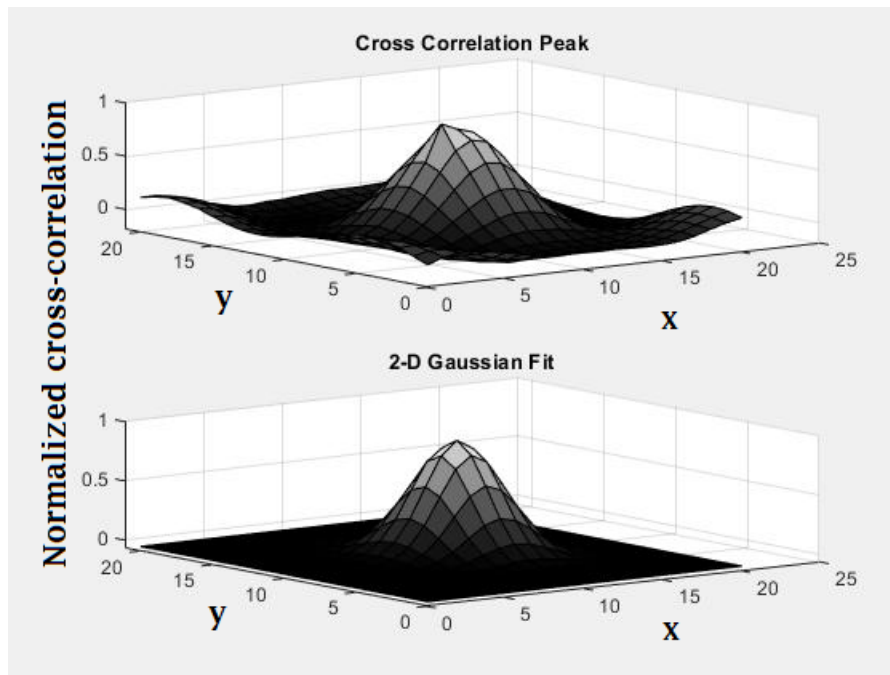


Figure 4.8: 2-D Gaussian surface fitting is employed to obtain a symmetric, smooth, and well-centred localization of the peak of the cross-correlation function between a reference on-axis incidence speckle and an off-axis incidence speckle for computing the maxima values, as shown in Figure 4.6, and the speckle shifts, as shown in Figure 4.7. The x and y axes are expressed in pixels, showing a window of 30 x 30 pixels around the maxima, and the z-axis is the normalized auto-correlation function's value.

4.3.1 Angular memory effect for varying diffuser - speckle imaging plane distances

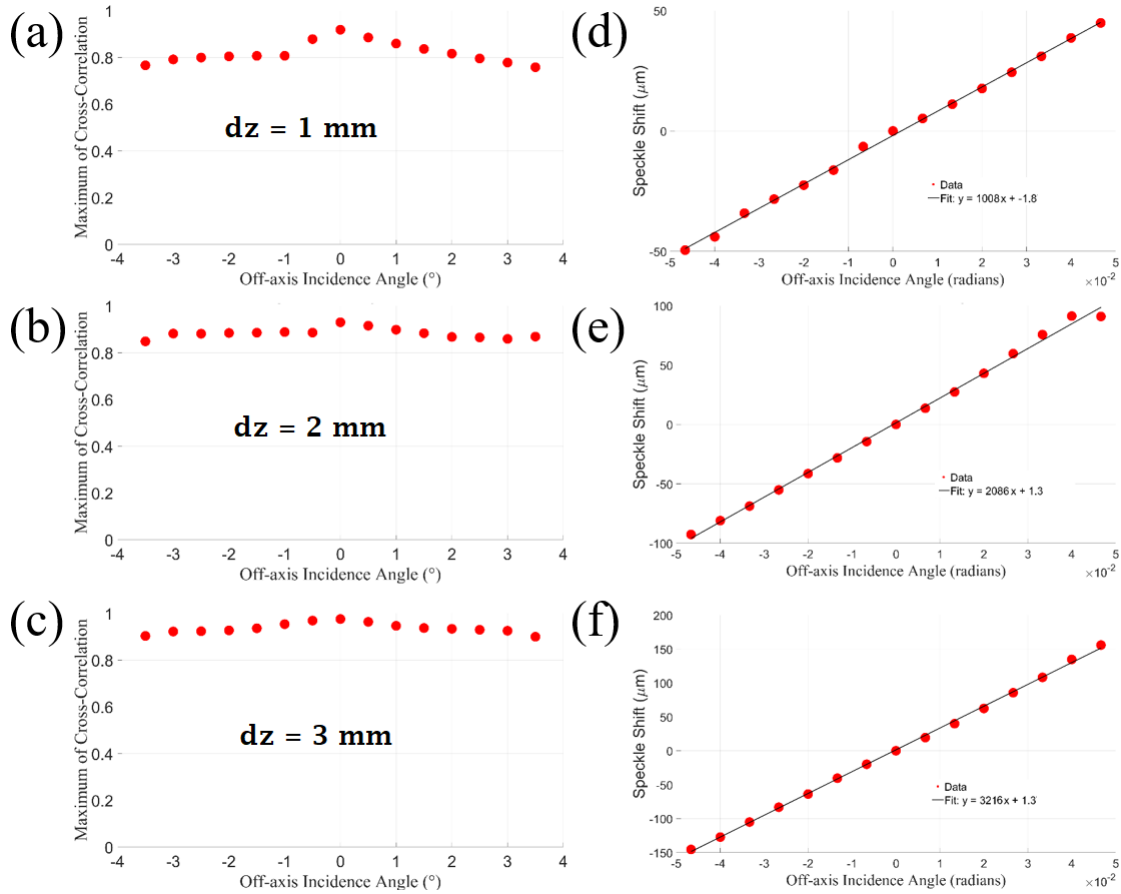


Figure 4.9: Angular memory effect experimental characterization at varying distances between the diffuser and the imaging plane of the camera where the speckle is observed, as denoted by dz in Figure 4.4: (a)-(c) are the cross-correlation maxima values for off-axis incidence speckles w.r.t. the reference on-axis speckle for distances $dz = 1, 2, 3$ mm, similar to Figure 4.6 where the same plot for $dz = 4$ mm is shown; (d)-(f) are the speckle translation shift versus incidence angle curves for distances $dz = 1, 2, 3$ mm, akin to Figure 4.7 which is for $dz = 4$ mm.

Figure 4.9 shows the characterization of the angular memory effect in our experiment by varying the distance between the diffuser and the speckle imaging plane of the camera. This allows to verify if the angular memory effect remains valid at varying distances and also to test the fidelity of the distance estimation from the linear fit between the speckle shift and tilt angle curve for different distances. As we can see in the plots (a), (b), and (c) of Figure 4.9, the curves depicting the maxima of the normalized cross-correlation are not significantly different from 4.6. On the corresponding plots to the right, in the (d), (e),

and (f) sub-plots of Figure 4.9, we see the same linear behaviour as in Figure 4.7. The value of the farthest off-axis incidence speckle shifts increase as the distance dz increases, which is as expected, and the values of the linear fit also closely match the micrometer scale measured distance values of $dz = 1, 2,$ and 3 mm. The difference between the measured distance values and the distance values estimated from the linear fit all remain less than 10%, with the difference decreasing with the decrease in the distance value. The slope of the linear fit for $dz = 1$ mm is 1.0 mm which is a difference of 1% w.r.t. the measured value, with the difference for the distance $dz = 2$ mm being 4%, for $dz = 3$ mm being 7% and for $dz = 4$ mm (shown in Figure 4.7) being 9%. These values are then used as an alternative value for the input parameter in the Demons algorithm where the distance dz is used as a calibration constant for the wavefront reconstruction process. Since the difference between the measured distance values and the estimated distance values from the linear fits of the angular memory effect experiment do not differ greatly, there is only a slight variation in the reconstructed wavefront results that we have discussed above. The slope increases with increasing dz due to the increase in sensitivity but the number of available phase pixels for imaging (i.e. the visible field) decreases, and the interplay between these factors produces the angular memory effect trends above. Additionally, this close agreement of the differently obtained distance values point to the fidelity of the value of the distance as the calibration constant, and also demonstrates a utility of the angular memory effect characterization itself.

4.4 Speckle grain size estimation

To complement our investigation of the memory effect, as discussed in Section 4.3, we have also characterized the average size of a speckle grain in our acquired LWIR speckle patterns, which is an important property of the speckle patterns. The value of the speckle grain size is critical in the resolution of the speckle by the camera, which also impacts the speckle intensity contrast. In order to obtain the average speckle grain size of the LWIR speckles imaged by our setup, we carry out a 2-D autocorrelation of the speckle image. The average radius of a plane cut of the peak (maxima) of the normalized autocorrelation function at the plane where the value of the normalized auto correlation function is 0.1 gives us an estimate of the speckle grain size for the image, as shown for visible speckles earlier [280].

In Figure 4.10, we see a sample speckle pattern when a spherical wavefront from a Zinc

Selenide (ZnSe) plano-convex lens of focal length 1 metre is incident on the diffuser to create such a speckle. The intensity values of the individual pixels are summed over 100 frames of the acquired LWIR speckle image to represent an average intensity value over each pixel. We then show the averaged intensity values of all the individual pixels in the figure, which are represented as digital counts that the camera records. The speckle shown in Figure 4.10, as well as the histogram representation of the same speckle in Figure 4.11 is unfiltered by the Gaussian filtering process described in Section 4.1. The autocorrelation function shown in Figure 4.12 is plotted after the raw speckle pattern (averaged over 100 frames) undergoes spatial filtering to reduce low spatial frequency intensity inhomogeneities, which we can see at the edges, for example. This should also give an idea of the necessity of carrying out spatial filtering in the image processing workflow to aid in obtaining speckles with better contrast.

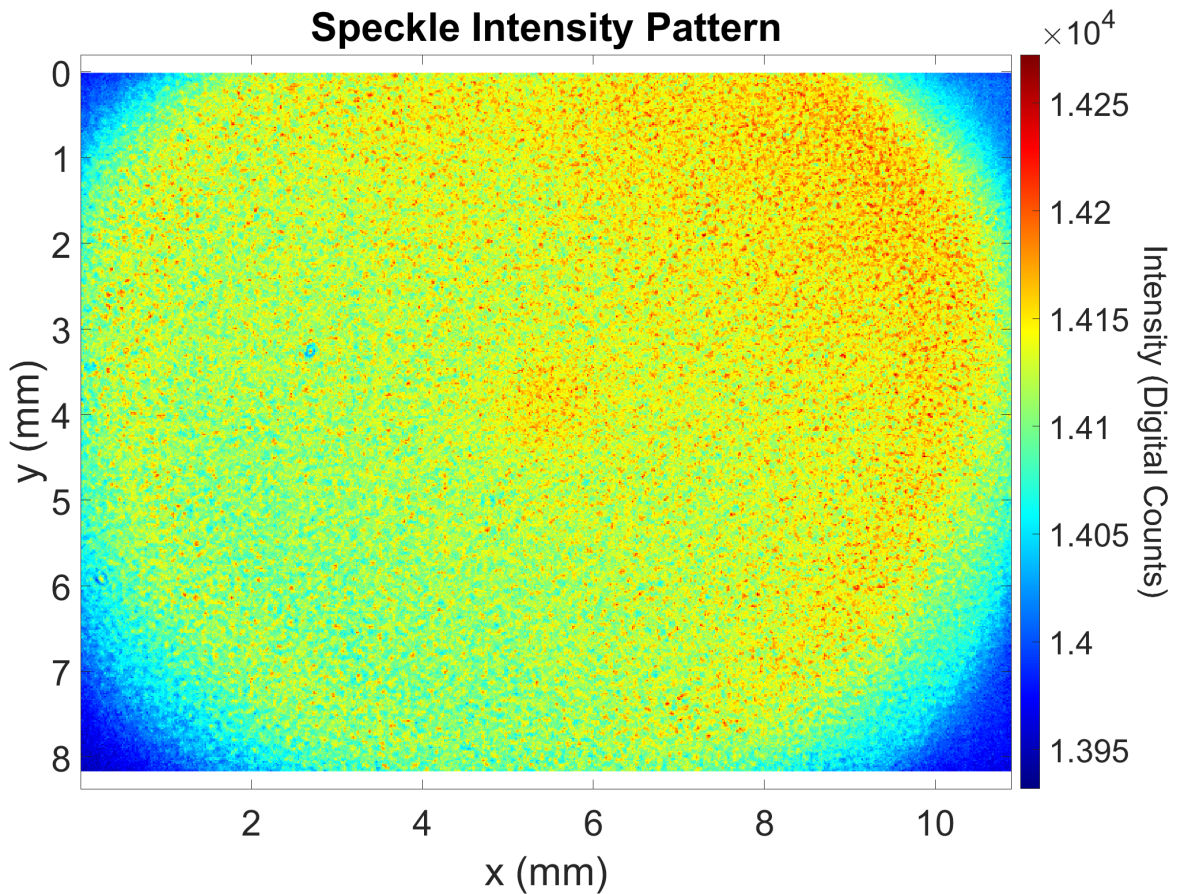


Figure 4.10: A representative speckle pattern when a spherical wavefront from a Zinc Selenide (ZnSe) lens of focal length 1 metre impinges on the diffuser which is placed at a distance of 1 mm from the speckle imaging plane. The x-axis represents 680 camera pixels and the y-axis represents 480 camera pixels.

Figure 4.11 shows the distribution of the pixel-wise averaged intensity values of the sample speckle pattern shown in Figure 4.10. The minimum value of the intensity is 13932 digital counts, while the maximum is 14272, with a mean of 14118, and standard deviation of 38 digital counts. The standard deviation of the intensity values is about 2% of the mean (calculated after the dark count of 13150 digital counts has been subtracted), which points to the fact that the intensity fluctuations are over a very small range of intensity values, and are therefore sensitive to camera resolution. We assume that the zero signal corresponds to the dark count value of the infrared radiation in our calculations of the statistical properties of the speckle image. The dark count value is taken from an LWIR image of a low emissivity aluminium sheet which approximately reflects a lower bound on the constant background signal that is incident on the thermal camera in our experimental room. The signal of interest associated to the speckle is thus superimposed on a very large offset produced by background thermal radiation. This is inherent to the use of a longwave infrared uncooled camera and is crucially different from speckle imaging at visible wavelengths, where the background is nearly zero and a large dynamic range is available to record the speckle image [51], as can be seen in Figure 4.11 (b). This reduces the contrast C of the speckle pattern, which is computed according to the equation $C = \frac{\sigma}{\langle I \rangle}$, and turns out to be 0.02 for the LWIR speckle as opposed to 0.91 for the visible speckle image.

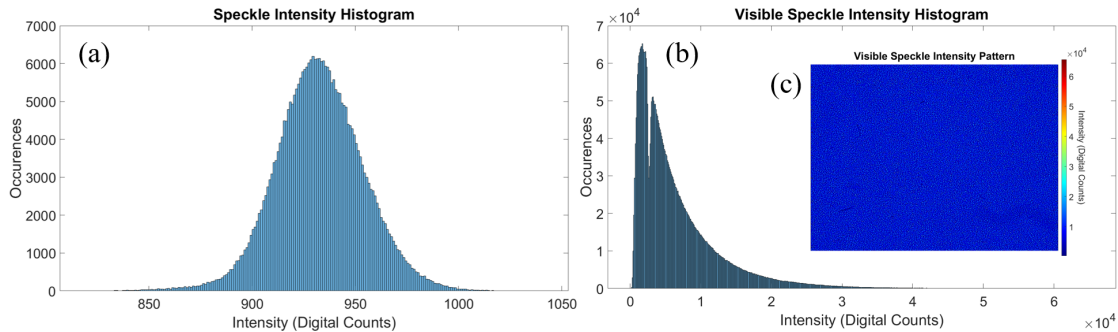


Figure 4.11: (a) Histogram of the occurrences of the digital count intensity values of an LWIR speckle pattern, as shown in Figure 4.10, compared with the (b) Histogram of a visible speckle pattern, as shown in the inset (c). The difference in the dynamic range between the LWIR speckle - whose intensity values have been subtracted by a dark count value of 13150 digital counts - and the visible speckle - is clearly visible.

The 2-D autocorrelation function of an image gives a quantitative estimate of the spatial dimensions over which the image has a high degree of similarity. It is well suited to determine the typical size of repeating features such as speckle grains in the absence of periodicity in the image. The computation of the normalized autocorrelation function, as shown in

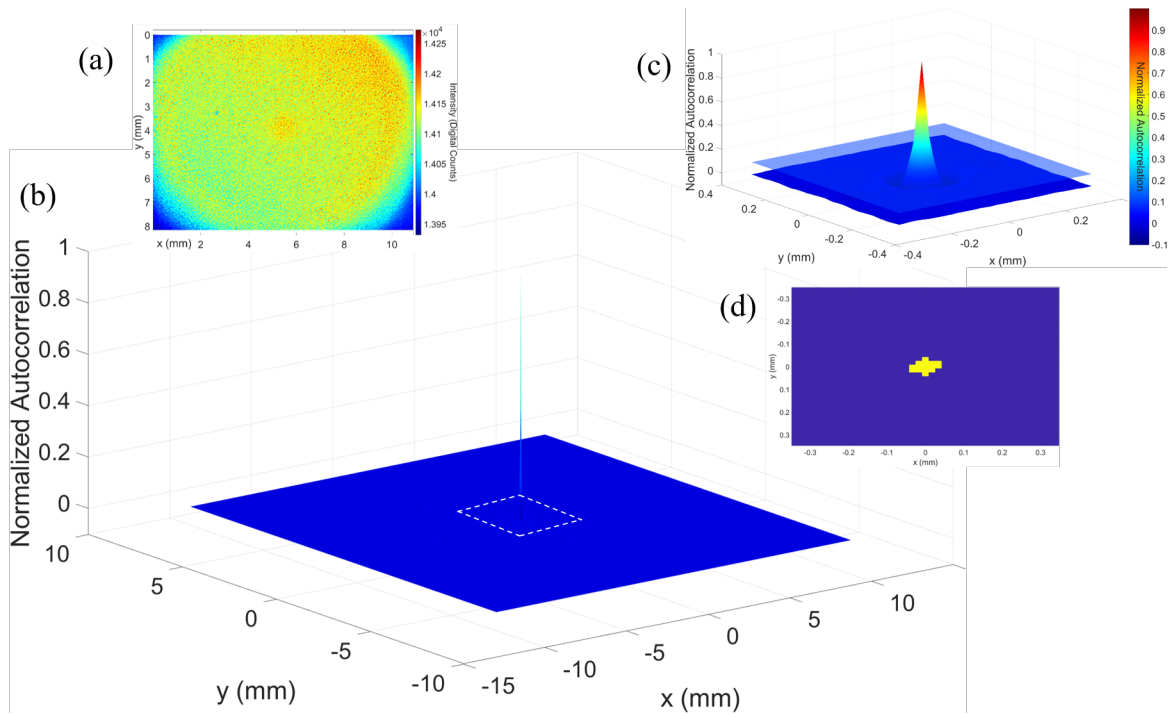


Figure 4.12: Speckle grain size estimate from the 2-D normalized autocorrelation function of a speckle intensity pattern: (a) shows the sample speckle pattern shown in Figure 4.10 which is used for the estimate, (b) depicts the 2-D normalized autocorrelation function of the image (a), with the sharp peak of the function shown at the centre. A magnified view of the 2-D normalized autocorrelation function at the centre, corresponding to the dotted region, is shown in the inset plot (c), with a plane cut made at the normalized autocorrelation value of 0.1 (shown as the translucent plane in (c)). The area of the normalized autocorrelation function at the plane corresponding to 0.1 is shown in (d) and is used to measure the radius of the peak to quantify the average speckle grain size.

Figure 4.12, enables us to find the characteristic size of a speckle grain by visualizing the sharp similarity in the region where a speckle grain overlaps with itself, and the subsequent sharp decline as the image shifts beyond the spatial dimension of a speckle grain. In the plot, we see that the peak of the normalized 2-D autocorrelation function has a very small radius compared to the full image size, and the features other than the peak are very weakly correlated. The sharp peak demonstrates that the speckle grains are the dominant periodic spatial feature in the image, which is also a result of reducing the low spatial frequency intensity contributions by Gaussian filtering. We make a plane cut at the normalized autocorrelation value of 0.1, which is just above the position where the peak juts out as the only feature, and then compute the area of the peak at that position. From this area A , the radius r of the peak can easily be found since $A = \pi r^2$. Since the autocorrelation peak represents

the image correlation arising just due to the speckle grains, we consider the radius of the peak width at this plane as the speckle grain size. It is important that the speckle grain size in one dimension (1D) is equal to at least two camera pixels, in order to satisfy the Nyquist-Shannon sampling criteria [281] [282] that requires a minimum sampling at half of the spatial frequency of an image to be able to fully resolve the image signal. If a single speckle grain falls on only one camera pixel, the small shift in the speckle grain position cannot be adequately sensed by the camera since the pixel will still report the position of the speckle grain on it. However, as the number of pixels on which a speckle grain is detected increases, the small speckle shifts can be sensed with a better accuracy.

The average speckle grain size of the speckle pattern shown in Figure 4.10 is computed to be $37.15\ \mu\text{m}$, which is 2.18 times the camera pixel pitch of $17\ \mu\text{m}$, thereby satisfying the Nyquist-Shannon sampling criteria. We can also see that the average size of a speckle grain is on the order of the reference LWIR wavelength of $10\ \mu\text{m}$.

The average speckle grain size values were computed for speckle images originating from a sample ZnSe lens of 1 metre focal length at different distances between the lens and the diffuser, as well as by varying the distance between the diffuser and the speckle imaging plane of the camera. The result of these measurements are shown in Figure 4.13. Each of the data points shows the mean of the speckle grain size computed from 20 sets of speckle images in each condition, and the error bars denote the standard deviation of the speckle grain size values. The dotted lines denote the grain sizes from speckle images acquired when a spherical wavefront from a sample lens is incident on the diffuser. The largest standard deviation among the errorbars is about $2.15\ \mu\text{m}$ corresponding to a mean of $38.3\ \mu\text{m}$ which is about 5.6% of the mean value. Most of the errorbars are not visible due to their much lower values compared to the mean, which demonstrates that the value of the average speckle grain size remains constant over multiple images and time, and is a characteristic feature of the speckle pattern in a given imaging condition.

The mean of the speckle grain sizes for reference speckle images, i.e. those speckle images which are produced by a plane wavefront impinging on the diffuser in the same imaging conditions except for the placement of the sample lens, are also shown by the solid lines. We can clearly see here that most of the speckle grain sizes are above $34\ \mu\text{m}$ which is the Nyquist-Shannon sampling limit for our system. The speckle grain sizes stay relatively similar for different positions of the sample lens with respect to the diffuser, for a fixed distance between the diffuser and the speckle imaging plane of the camera.

The mean of the grain size for the different positions of the sample lens at 1 mm distance between the diffuser and the imaging plane is $37.5 \mu\text{m}$ while the standard deviation is only $1.6 \mu\text{m}$ for them. The corresponding reference speckle images also have similar speckle grain sizes with the speckle images produced when the lens is placed. However, the key variation that we see in the speckle grain size is its increase when the distance between the diffuser and the camera's speckle imaging plane is increased, which is expected due to the larger distance between two points in the speckle imaging plane which subtend the same angle when the distance is increased [203]. This also has a positive effect on the speckle shift resolution, with one single speckle grain being sampled by more than 4 pixels in one dimension. The distance between the diffuser and the speckle imaging plane is though limited by the diminishing intensity of the speckle pattern as the distance is increased, even though at a distance of 4 mm as well, the speckle intensity is adequately intense to be used for phase reconstruction. We also clearly see from this analysis that the speckle grain size does not depend on the incident sample wavefront as the variation in the distance between the sample lens and the diffuser does not affect the speckle grain size, as well as the fact that there is no significant difference between the speckle grain sizes for the reference wavefront and the sample wavefront. This is an important result since a variation in the speckle grain sizes between the reference and sample speckle patterns would have made it much more difficult to accurately ascertain the speckle grain shifts, which ultimately allow us to reconstruct the sample wavefront.

The above analysis provides a quantitative characterization of the considerations that need to be taken into account to choose an optimal distance between the diffuser and the camera's speckling imaging plane for accurate phase reconstruction.

4.5 Lens phase imaging experiments

After discussing how LWIR speckle images are processed, and demonstrating that our LWIR speckle imaging using a Silicon diffuser has a high angular memory effect, we also looked at estimates of the speckle grain size which show that they are being sampled adequately. We shall now discuss how simple and fairly common infrared optical elements are used as phase objects to test the viability of using our novel longwave infrared speckle imaging experimental methodology for phase reconstruction.

A typical test experiment we have carried out uses infrared lenses as phase objects. Using

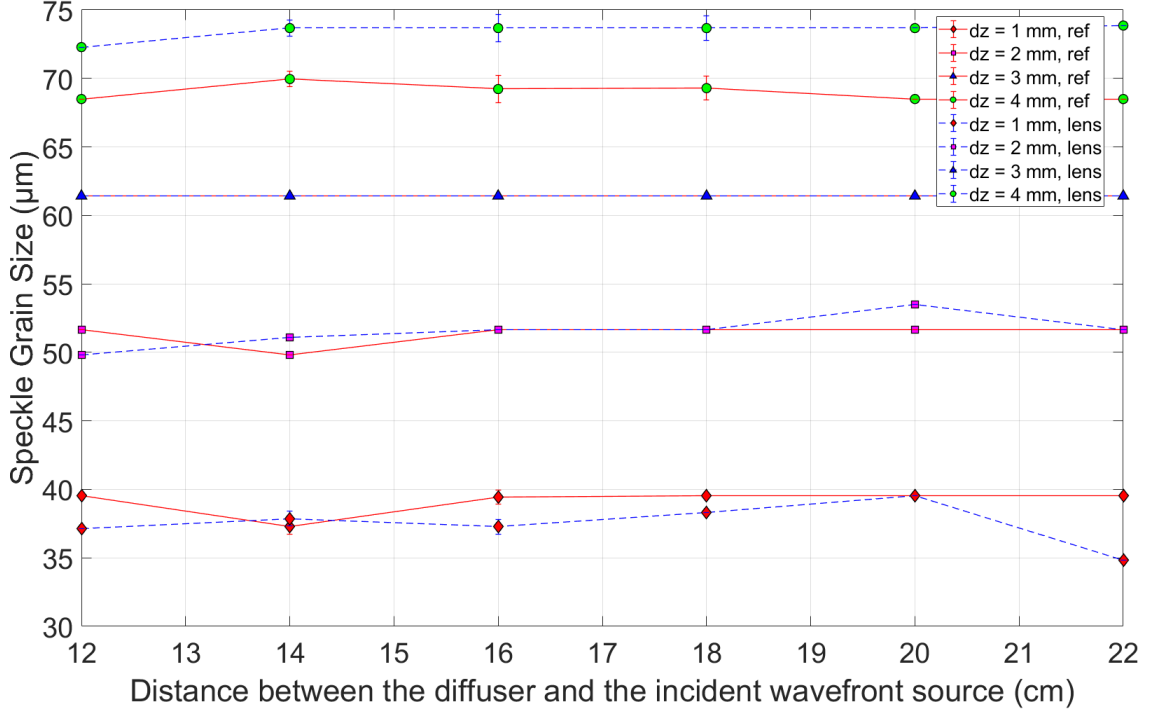


Figure 4.13: Speckle grain size comparison: The average speckle grain size is computed for different speckle images produced by a plane wavefront impinging on a diffuser (solid lines, denoted by ref in the legend) as well as those when a spherical wavefront from a Zinc Selenide (ZnSe) lens of focal length 1 m is incident on the diffuser (dotted lines, denoted by lens in the legend) at different distances between the lens and the diffuser (shown as the x-axis, with the corresponding reference speckle images being captured at the same positions without the lens) and at different distances between the diffuser and the camera’s imaging plane where the speckle is observed (denoted by the dz values 1-4 mm in the legend). Each of the data points is the mean speckle grain size value computed from 20 speckle images acquired in the same conditions, and the error bars depict the standard deviation of these 20 measurements for each data point.

the experimental setup in the configuration described in Figure 4.14, we first produce a plane wavefront from the thermal source which impinges on the diffuser directly. The transmitted speckle pattern is acquired and considered as the reference speckle pattern. The phase object, a Zinc Selenide (ZnSe) plano-convex lens, is subsequently placed in between the plane wavefront and the diffuser, with the planar side of the lens being towards the diffuser. The altered wavefront leads to a changed speckle pattern, which is acquired by the camera and treated as the sample speckle pattern, as depicted in the configuration in Figure 4.15. We will see in the following sections (Section 4.5.1) the geometry of the incident wavefronts from the different lenses, and the reconstructed lens wavefronts obtained from our phase reconstruction algorithm by using these speckle patterns.

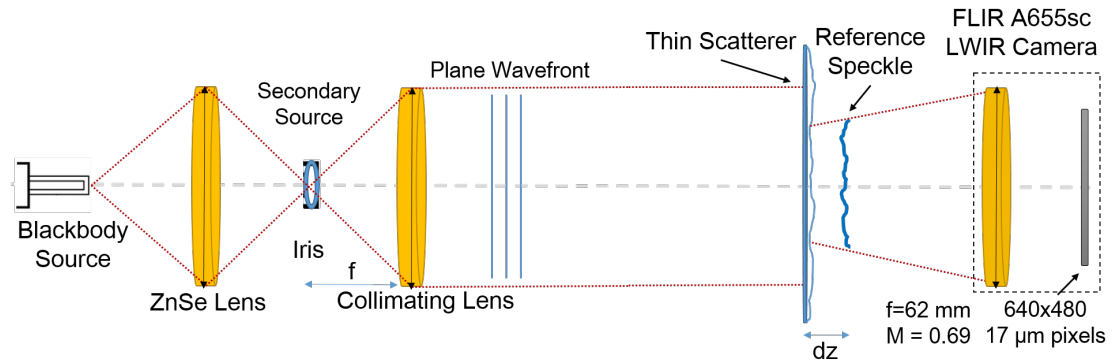


Figure 4.14: Experimental configuration for acquiring reference longwave infrared speckle images due to an incident plane wavefront arising from a thermal source.

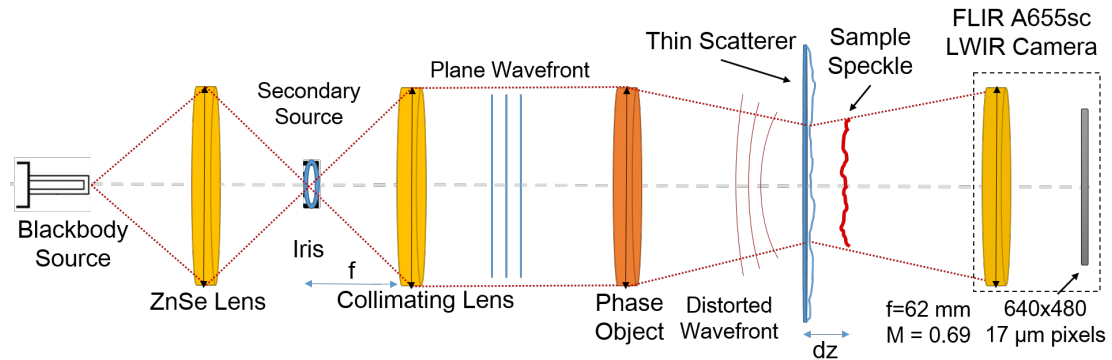


Figure 4.15: Experimental configuration for imaging the sample longwave infrared speckle pattern after a plane wavefront has been distorted by a phase object before incidence on the scattering medium.

In these experiments, the distances between the global source, the re-imaging lens for producing an image of the global on the iris, the iris that functions as the secondary source, and the collimating lens remain fixed. The plane wavefront that is then formed after the collimating lens is the same for different phase objects. The position of the phase objects (lenses) are varied in such a way that the distance between the lens and the diffuser change, which allows us to test the reconstruction of wavefronts with different radii of curvature from the same lens in an experiment. We also change the distance between the diffuser and the plane where the speckle is imaged by the camera, varying this distance from 1 mm to 2, 3 and 4 mm (labelled as the variable distance dz in Figures 4.14 and 4.15). This

allows us to explore the effect of changing the plane at which the speckle is intercepted for imaging through the camera. In order to do this, we move the diffuser itself which is mounted on a micrometer screw based translation stage while keeping the camera and its plane of imaging fixed.

4.5.1 Reconstructed lens wavefronts

4.5.1.1 Zinc Selenide (ZnSe) lens ($f = 1$ m)

A plano-convex ZnSe lens with a focal length of 1 metre placed between the plane wavefront and the diffuser produces a spherical wavefront that will converge to a focal point behind the diffuser and camera positions, as can be seen in Figure 4.16.

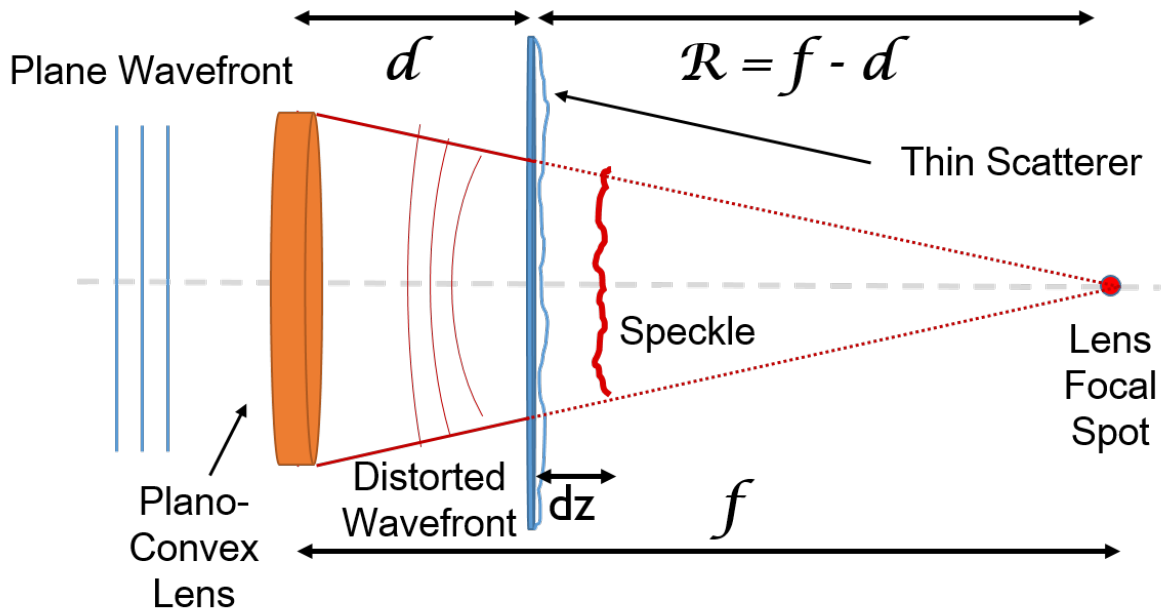


Figure 4.16: A plane wavefront is incident on a plano-convex lens, and the resulting wavefront is altered to become a converging spherical wavefront that would converge at the focal point of the lens.

Once the plane wavefront is incident on the lens, it forms the converging wavefront which then traverses a distance d before being incident on the diffuser.

The ideal wavefront that we expect to obtain by carrying out this experiment with the $f = 1$ m lens under the experimental conditions is depicted in Figure 4.17, while the actual reconstructed wavefront using the Demons algorithm in the same conditions is shown in Figure 4.18.

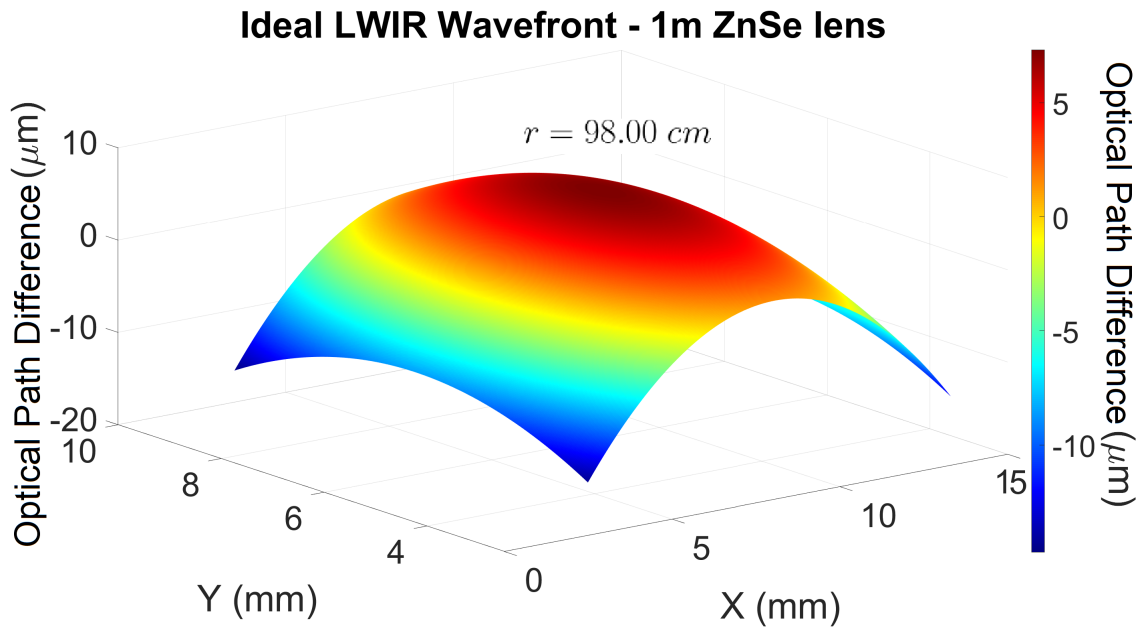


Figure 4.17: Ideal longwave infrared wavefront expected when the converging spherical wavefront from a plano-convex ZnSe $f = 1 \text{ m}$ lens is incident on the diffuser after traversing a distance of 2 cm between the lens and the diffuser.

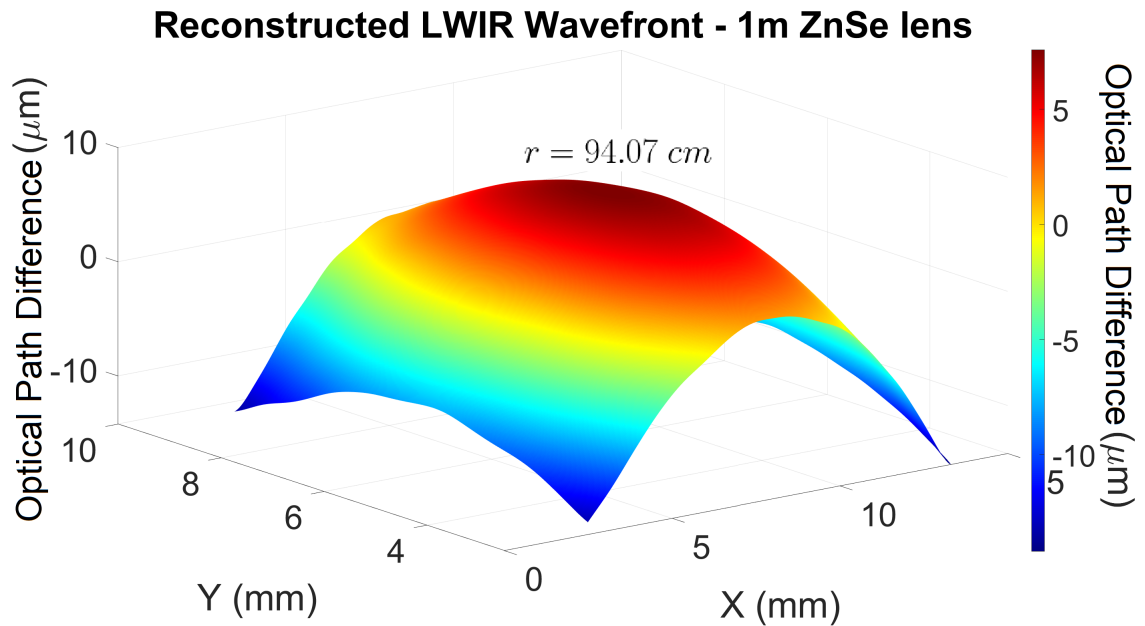


Figure 4.18: Reconstructed longwave infrared wavefront when a plano-convex ZnSe $f = 1 \text{ m}$ lens is placed 2 cm away from the diffuser and distorts a plane wavefront to form a converging spherical wavefront.

4.5.1.2 Wavefront radius of curvature estimation

The wavefront reconstruction algorithm measures the speckle grain shifts between the reference speckle and the sample speckle, and computes the optical path difference of the wavefront. While this result is useful to visualize the qualitative profile of the reconstructed wavefront, we need a way to have a quantitative estimate of the reconstructed wavefront profile. To do so, a surface fitting function is used to compute a least squares fit function to the reconstructed wavefront by assuming a spherical wavefront profile. The wavefront surface is approximated as the portion of the wavefront curvature that can be described by a sphere, which follows the equation:

$$w_c(x, y) = \sqrt{R^2 - (x^2 + y^2)} \quad (4.2)$$

where it is assumed that the sphere has a centre at $(x, y) = (0, 0)$. For a paraxial system, Equation 4.2 can be approximated as Equation 4.3 below:

$$w_c(x, y) \approx \frac{x^2 + y^2}{2R} \quad (4.3)$$

The fitting function used to fit the reconstructed wavefront to a sphere is defined as:

$$z'(x, y) = \frac{x^2 - x_0^2}{2R} + \frac{y^2 - y_0^2}{2R} + c \quad (4.4)$$

where, $z'(x, y)$ is the fit value of the optical path difference (OPD) at a point on the plane (x, y) , the centre of the sphere is at (x_0, y_0) , R is the radius of curvature of the wavefront, and c is a constant. The values of the variables x_0 , y_0 , R , and c are computed by minimizing the least squares difference between the value of $z'(x, y)$ and $z(x, y)$, which is the actual value of the optical path difference at a point obtained from the reconstructed wavefront. The value of R obtained from the spherical wavefront fitting routine is then compared with the ideal value of R that is expected according to the measurement conditions, as shown in Figure 4.16.

4.5.1.3 Zinc Selenide (ZnSe) lens ($f = 50$ cm)

We use a plano convex Zinc Selenide (ZnSe) lens of focal length, $f = 50$ cm, to validate the wavefront reconstruction experiment carried out with the ZnSe $f = 1$ m lens. The $f = 50$ cm lens is also placed between the plane wavefront and the diffuser in such a manner that it produces a converging spherical wavefront. The reconstructed wavefront, and the calculated value of the radius of curvature of the reconstructed wavefront from the $f = 50$ cm lens is shown in Figure 4.20. The ideal expected wavefront from the lens in the same experimental conditions is shown in Figure 4.19. The phase gradients of the wavefront emanating from the $f = 50$ cm lens are greater than those from the $f = 1$ m lens, as the convergence from the lens focusing is stronger when the focal length is lower. The value of the reconstructed wavefront's radius of curvature is then similarly, as in the case of the $f = 1$ m lens, calculated using the spherical wavefront fitting routine and compared with the expected ideal value of R , which shows that the reconstructed radius is in close agreement with the ideal expected radius.

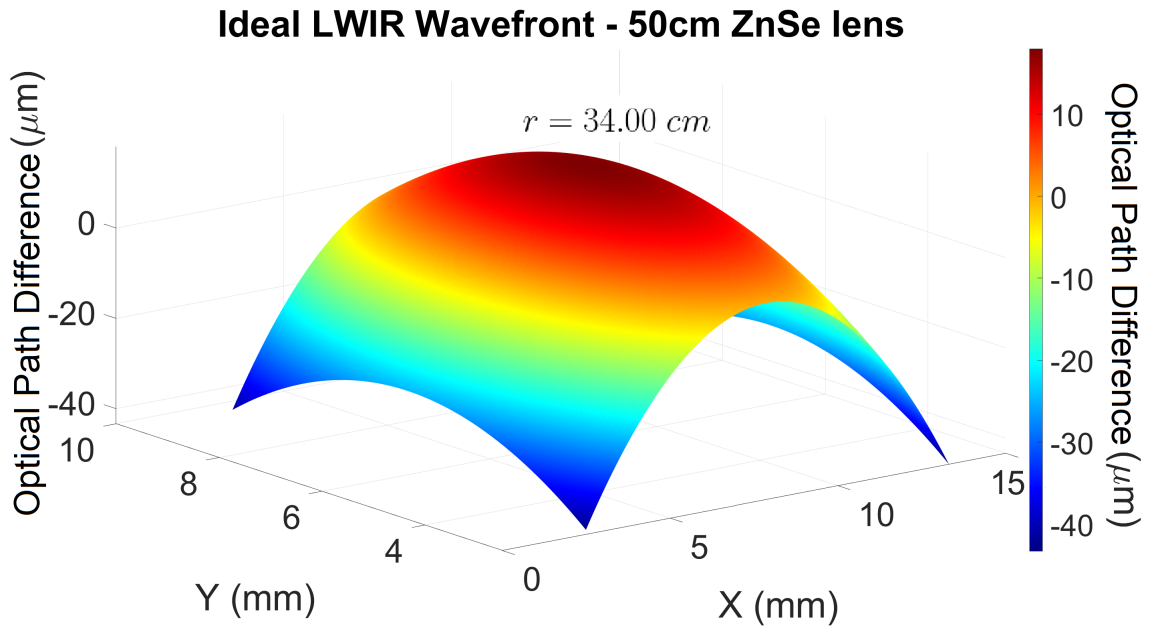


Figure 4.19: Ideal longwave infrared wavefront expected when the converging spherical wavefront from a plano-convex ZnSe $f = 50$ cm lens is incident on the diffuser after traversing a distance of 16 cm between the lens and the diffuser.

4.5.2 Wavefront sensing for various curvatures

In view of these first results demonstrating quantitative phase reconstruction in the long-wave infrared using the speckle imaging technique we have developed, we carried out

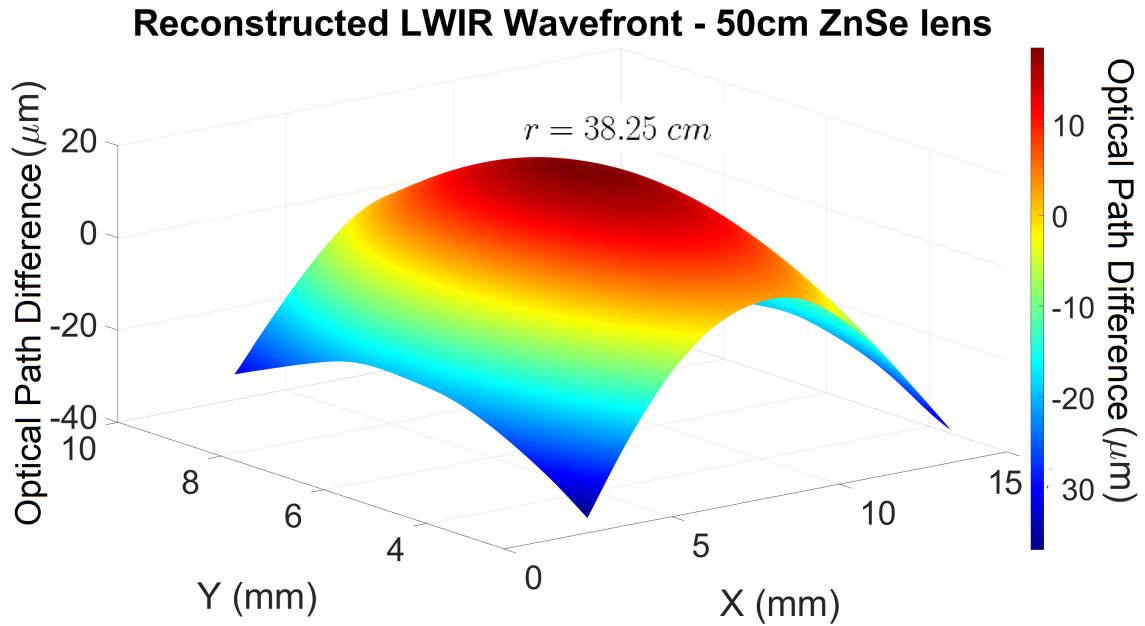


Figure 4.20: Reconstructed longwave infrared wavefront when a plano-convex ZnSe $f = 50$ cm lens is placed 16 cm away from the diffuser and distorts a plane wavefront to form a converging spherical wavefront.

experiments beyond these conditions to characterize and test the limits of our wavefront sensing methodology.

As elucidated in Figure 4.16, the radius of curvature of the impinging wavefront can be changed by varying the distance d , which allows us to test the reconstruction of sample wavefronts with different radii of curvature, by shifting the lens phase object itself amidst the LWIR speckle imaging setup shown in Figure 4.15. We now have a set of distinct wavefronts from the sample lens, each with a different radius of curvature, which impinges on the thin diffuser to form a distinct speckle pattern. We then analyse the speckle patterns to reconstruct the thermal wavefronts, as described earlier in this chapter.

In Figure 4.21, we can see the results of the experiment where a ZnSe lens of focal length $f = 1$ m is placed at distances between the lens and the diffuser varying from 12 to 22 cm. The distance between the lens centre and the diffuser is measured using a vernier caliper with a precision of 0.05 mm, with the lens centre being estimated by the lens' manufacturing design measurements, which means that there is a tolerance of about ± 0.1 mm in the distance measurements, that is lesser than 1% of the distance value itself. The sample ZnSe lens is placed at 2 cm intervals, and the data points represent the reconstructed radii of the different wavefronts impinging on the diffuser when such an experiment is carried out, with

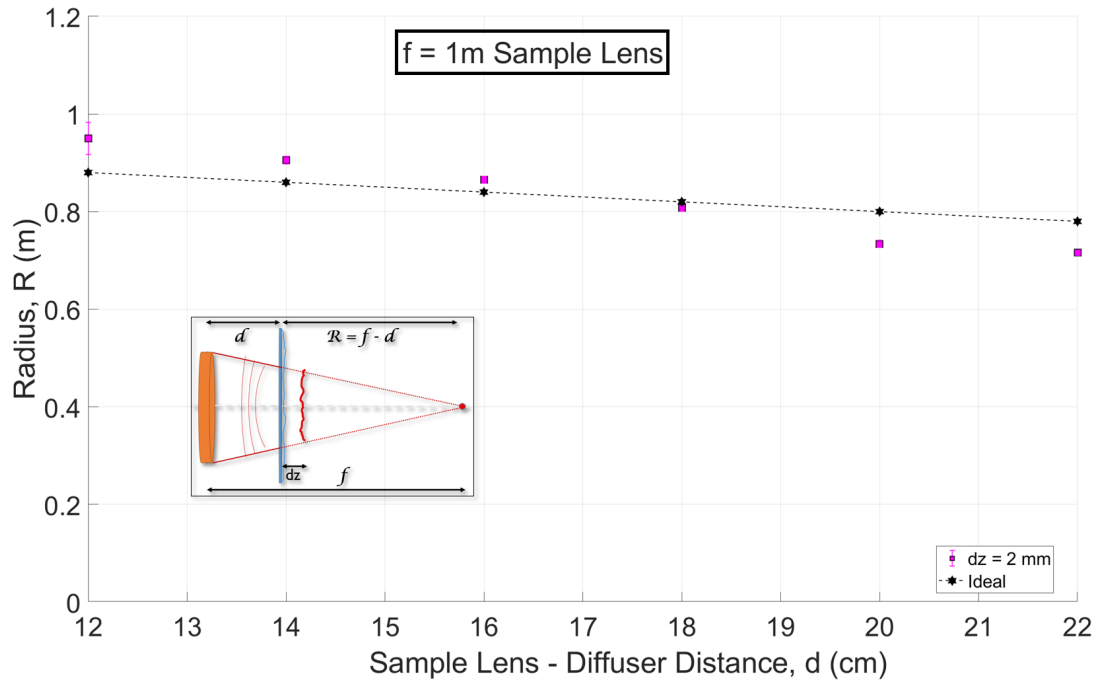


Figure 4.21: Comparison of the reconstructed wavefront’s fitted radius of curvature (R) at different distances (d) between the sample ZnSe lens of focal length 1 m and the diffuser, and at a fixed position (dz) of the speckle imaging plane. The inset depicts the different variables shown in the plot, as discussed earlier in Figure 4.16.

the distance between the diffuser and the plane where the speckle is imaged by the camera dz being constant - 2 mm in this case. The ideal radius of curvature of the impinging wavefront is shown by the straight black dotted line, which is a calculation of the expected wavefront radius of curvature based on the distance between the lens and the diffuser and the focal length of the lens, as shown in Figure 4.16.

For every set of measurements carried out with the varying lens to diffuser distances (d), as shown in Figure 4.21, the distance between the diffuser and the plane where the speckle is imaged by the camera (dz) is kept constant. Also, every data point shown in Figure 4.21 (except the ideal curve) results from the same measurement carried out 20 times separately to test the fidelity of the reconstructed values, with the standard deviation between these values being represented by the error bars plotted in the figure.

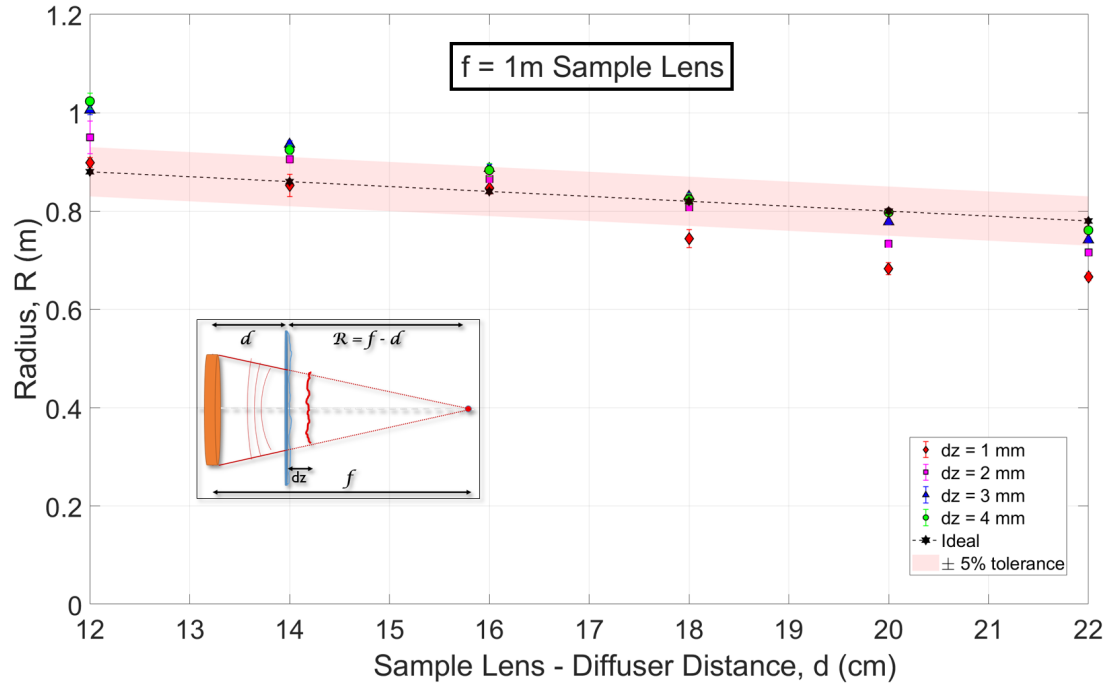


Figure 4.22: Comparison of the reconstructed wavefront's fitted radius of curvature (R) at different distances (d) between the sample ZnSe lens of focal length 1 m and the diffuser, and at different positions (dz) of the speckle imaging plane. The inset depicts the different variables shown in the plot, as discussed earlier in Figure 4.16. The $\pm 5\%$ tolerance band is calculated with respect to the ideal expected radii of curvature values as a reference.

4.5.3 Wavefront sensing with varying diffuser - speckle imaging plane distances

We also changed the distance between the diffuser and the plane where the speckle is imaged by the camera, shown as dz in Figure 4.16, to see how varying the distance between the diffuser and the camera affects the wavefront reconstruction process. In Figure 4.22, the four differently coloured lines (other than black) represent measurements similar to the ones described in Section 4.5.2, carried out at the varying lens-diffuser distances, but with the distance between the diffuser and the imaging plane of the camera being varied for each set of measurements, being fixed to 1 mm, 2 mm, 3 mm, and 4 mm. This distance between the diffuser and the imaging plane of the camera is measured by keeping the imaging plane of the camera fixed while the diffuser is moved by a micrometer screw mounted on a three-axis translation stage, with a precision of 0.01 mm. For every data point shown in Figure 4.22 as well, the measurements were carried out 20 separate times, and the error bars plotted in the figure depict their standard deviation. The highest standard deviation between the

reconstructed radii values for a particular data point, i.e. at a fixed distance between the lens and the diffuser, and a fixed distance between the diffuser and the camera's imaging plane, is 33 mm. While the mean values of the reconstructed radii can be seen from the plot directly, the difference between the reconstructed radii at every distance and the ideal estimated radius of curvature was calculated to quantify the deviation from this ideal value. The percentage differences of the absolute values of the reconstructed and ideal radii are between the maximum of 16.3% and a minimum value of 0.3%, with the average difference being 6.1%.

There is thus still room for improvement to achieve a very accurate measurement of the wavefront curvature using our method. However, we can consider that these first results are a success for our method considering the good qualitative agreement we obtain between our reconstructed wavefront and the ideal one. We recall that it is the first time that wavefront reconstruction is achieved in the longwave infrared using solely thermal radiation in a setup involving one single arm for the measurements with an uncooled bolometer camera, in striking contrast with other phase reconstruction methods such as digital holography which requires a reference arm.

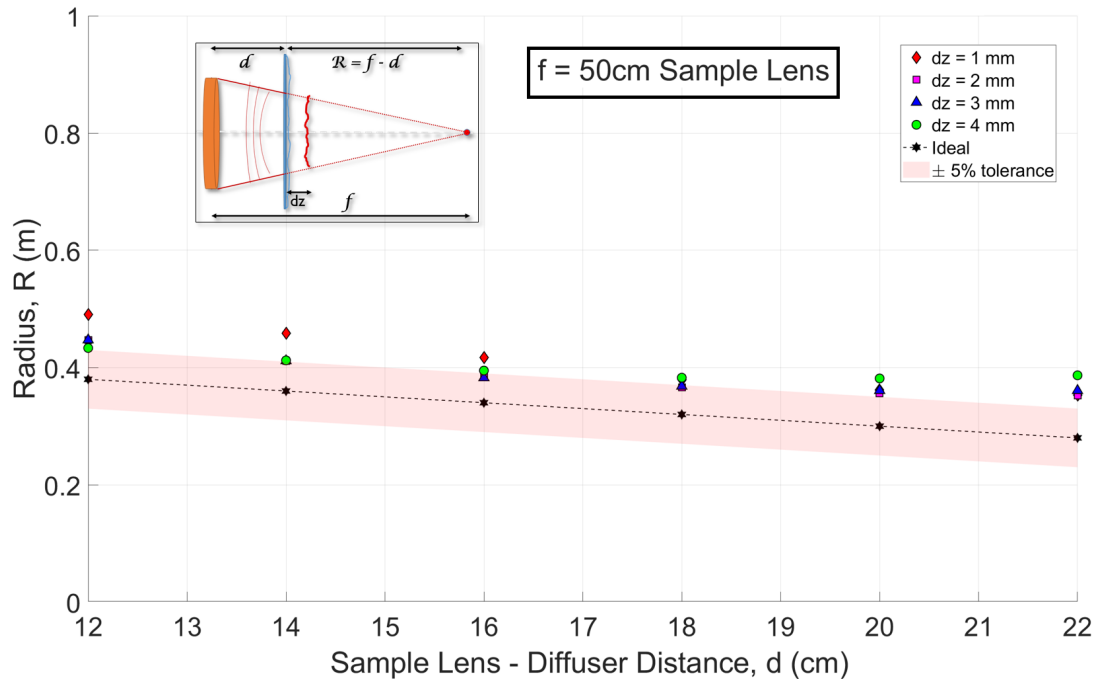


Figure 4.23: Comparison of the reconstructed wavefront's fitted radius of curvature R at different distances between the sample ZnSe lens of focal length 50 cm and the diffuser (d), and at different positions of the speckle imaging plane (dz).

In Figure 4.23, the results of a similar experiment, as described above, was carried out with a ZnSe lens of focal length $f = 50$ cm, with the lens and the diffuser being placed at distances between 12 to 22 cm apart from each other. The distance between the lens centre and the diffuser is measured using a vernier caliper with a precision of 0.05 mm, and the lens centre is estimated by the lens' manufacturing design measurements, with a tolerance of ± 0.1 mm in the distance measurements. Every data point shown in Figure 4.23 (except the ideal curve) is the result of a single measurement, which explains the lack of error bars (also for brevity), even as the measurements were repeated multiple times in separate experiments to achieve similar results.

We can see that the slope of the curves showing the reconstructed radii mimic that of the ideal estimated radii from the x-axis points 12 to 18 cm, which is followed by a change in the slope for all the curves to varying degrees between the x-axis points 18 to 22 cm. This is the case for all the different diffuser to camera imaging plane distances, with minor differences between each, but all of them having a gradient change at the x-axis 18 cm point.

Here, we also look at the difference between the reconstructed radii at every distance and the ideal estimated radius of curvature at the corresponding distance value. The percentage differences of the absolute values of the reconstructed and ideal radii are between the maximum of 38% and a minimum value of 12%, with the average difference being 20%. This value of the tolerance between the radii retrieved from our reconstructed wavefronts compared to the ideal geometrical radii expected in the different configurations is higher than that for the case of the $f = 1$ m lens, which necessitates further improvements. One explanation that might explain this trend is that as the focal length of the lens decreases, and the distance between the diffuser and the lens increases, the phase gradients are higher, which leads to a higher speckle grain shift and thus reaching a sensitivity limit for the phase reconstruction process. Indeed, we can see that upon dropping the data from the abscissa (x-axis) values 20 cm and 22 cm, the maximum difference between the reconstructed radii and ideal radii falls to 29% and the average also drops to 17%.

Figure 4.24 depicts the results of the wavefront reconstruction experiments discussed above for the $f = 1$ m lens and the $f = 50$ cm lens, with the reconstructed radii of curvature shown as a function of the ideal radii of curvature for each measurement. The ideal radii of curvature of the different wavefronts, plotted as the black dotted line in Figure 4.24, is therefore a linear curve around which are clustered the reconstructed radii values for

different lens - diffuser distances, signified by d in Figure 4.16, and for different diffuser - speckle imaging plane distances, labelled as dz in Figure 4.16.

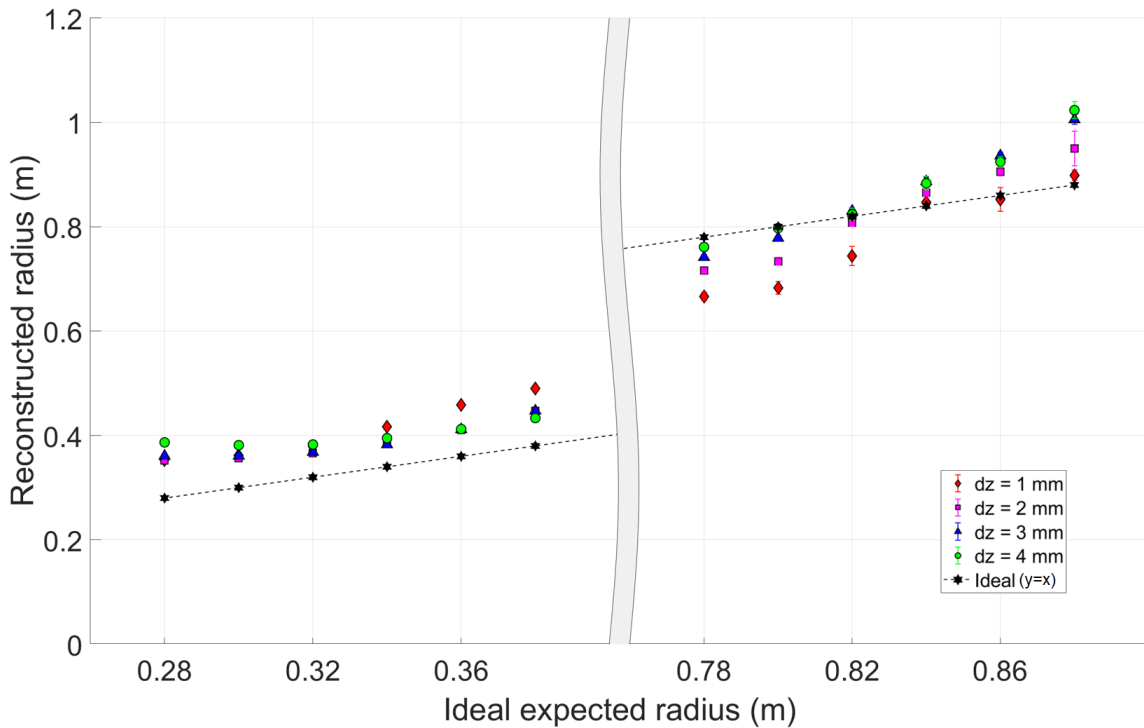


Figure 4.24: The reconstructed radii of curvature R of various different wavefronts from the $f = 1$ m and the $f = 50$ cm lenses, differing in their distance between the sample ZnSe lens and the diffuser (d), and also the distance between the diffuser and the speckle imaging plane (dz), are plotted against the ideal expected radii in every case, to signify the experimental validity of the linear relationship between the ideal and reconstructed radii. The black dotted line represents the ideal radii, with the x-axis kink in between separating the radii values from the $f = 50$ cm lens on the left from the $f = 1$ m lens' reconstructed radii values on the right.

We also tested wavefront reconstruction for other smaller lenses of focal lengths 20 cm and 5 cm. With the smaller focal length lenses, the wavefront reconstruction retrieves the qualitative profile of the spherical wavefronts quite well, and is able to distinguish when the wavefront curvature has an orientation (sign) change, even though the quantitative radii estimation is less accurate. These further experiments point to the need to improve upon and subsequently characterize the phase reconstruction limits of our wavefront reconstruction technique, which might also be limited by the Demons algorithm as well at high phase gradients within the constraints imposed by the optical system and the number of camera pixels that image a single speckle shift.

4.6 LWIR speckle imaging challenges

Up till here, we have discussed the development of the LWIR speckle imaging experimental setup, the wavefront reconstruction technique utilizing it, and seen the results that we have obtained in this first work on wavefront sensing in the LWIR using speckle imaging. We shall now look at a few of the specific challenges that we experienced working in the longwave infrared towards developing a speckle imaging technique, and mention some of the considerations that we worked upon to address them optimally within the constraints. The goal of this discussion is to share the experience we have gained in our work for future developments in the same field, as well as to highlight the key differences between LWIR speckle imaging and speckle imaging in the visible regime of the electromagnetic spectrum that need to be considered when transposing some of the techniques from the visible to the LWIR.

4.6.1 Camera noise analysis

The thermal camera that we use in our experimental setup is an uncooled microbolometer-based longwave infrared camera, as mentioned in greater detail in Section 3.4.4. While an optical camera is usually limited by shot noise, or the noise generated due to the statistical variation in the rate of incident photons arriving at the camera sensor, the noise in a thermal camera is characterized by the noise equivalent temperature difference (NETD), as explained in Section 3.4.3.2, which is essentially the lowest temperature difference resolvable by the camera sensor. The NETD of our camera according to the manufacturer's information is 0.03 °C or 30 mK (milli Kelvin). However, this figure is truly relevant for use cases where the camera is used to carry out thermometry by direct imaging of objects through their thermal radiation, while we use the LWIR camera to carry out phase reconstruction using speckle imaging. We therefore carried out alternative measurements from our imaging datasets to quantify the noise or fluctuations observed in the various images obtained using the thermal camera to have a better understanding of the camera's noise characteristics which are more relevant to our usage.

During imaging, we acquire a finite number of image frames instead of just one, and we carry out some statistical analysis on this stack of images, as represented in Figure 4.25. We define the pixel-wise mean, standard deviation, and the signal-to-noise ratio (SNR) over

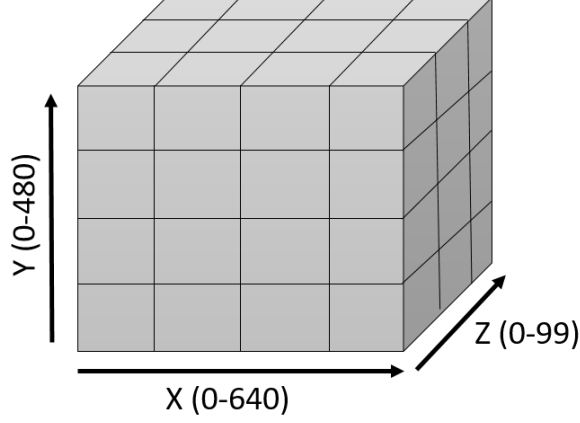


Figure 4.25: Schematic representation of an image stack that gives rise to one processed image in our experiments: during the acquisition of a typical image sequence using our thermal camera, we image over the 640 pixels x 480 pixels of the camera sensor and acquire a fixed number of image frames, typically around 100.

all the frames for a single speckle image sequence as:

$$\mu_{x,y} = \frac{1}{N_z} \sum_{z=1}^{N_z} p_{x,y,z} \quad (4.5)$$

$$\sigma_{x,y} = \sqrt{\frac{1}{N_z} \sum_{z=1}^{N_z} (p_{x,y,z} - \mu_{x,y})^2} \quad (4.6)$$

$$SNR_{x,y} = \frac{\mu_{x,y}}{\sigma_{x,y}} \quad (4.7)$$

where the value of a single pixel at a position (x, y) of the camera sensor and in an image frame z is $p_{x,y,z}$ and N_z is the number of acquired frames for each image sequence.

In Figure 4.26, we see the pixel-wise mean of the intensity values over 100 frames for a background image acquired by the camera. The background image is an image of our optical setup without the blackbody source being turned on, such that the signal detected by the camera is a measure of the thermal radiation incident on the camera sensor in the experimental room's conditions when not observing a speckle pattern. The mean of the intensity values over all the frames at a specific pixel position then represents the averaged

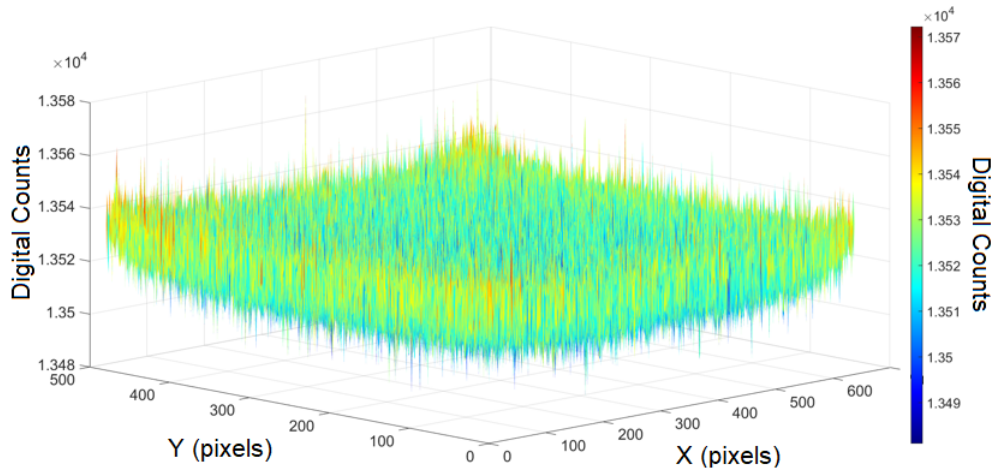


Figure 4.26: The pixel-wise mean of the intensity values over 100 frames of a background image (where the source is turned off) acquired by our camera is calculated according to Equation 4.5 and plotted here.

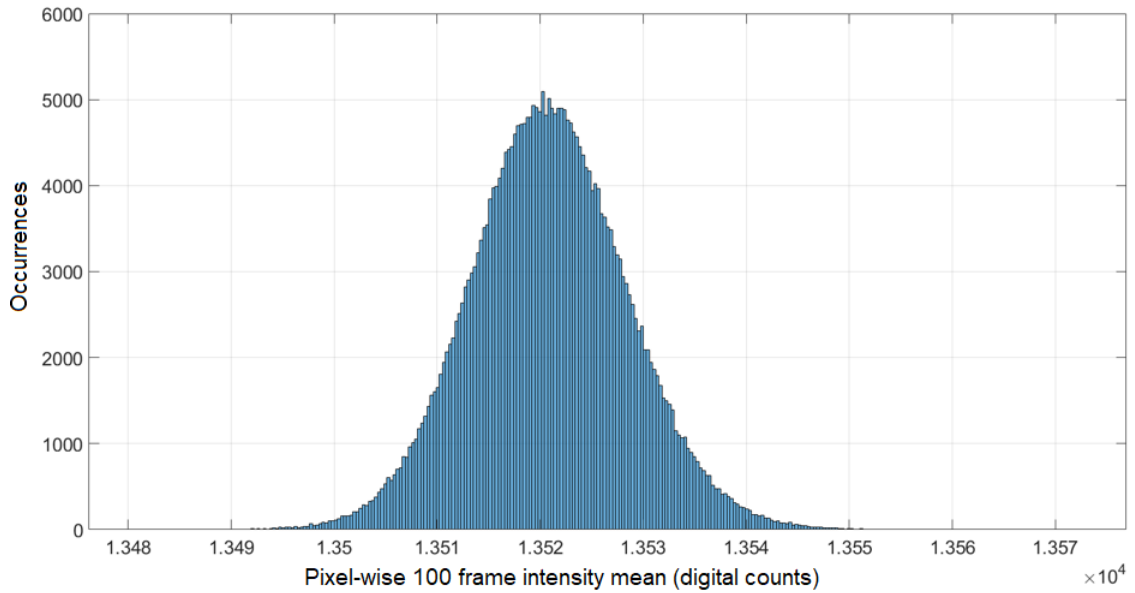


Figure 4.27: Histogram of the pixel-wise mean values over a 100 frame background image, as shown in Figure 4.26.

intensity of a specific pixel in an image that is used (in the case of a speckle pattern) for the wavefront reconstruction algorithm. Here, we see that the values of the pixel-wise mean is centered around 13520 digital counts, with a relatively minor variation across pixels, as can also be seen in the histogram of the pixel-wise mean values in Figure 4.27.

The standard deviation of the intensity values over the 100 frames for each pixel is shown

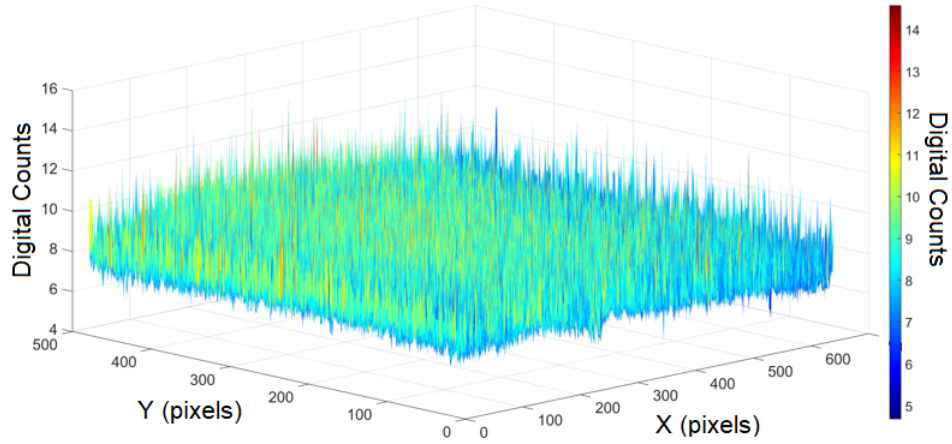


Figure 4.28: The pixel-wise standard deviation of the intensity values over 100 frames of a background image acquired by the thermal camera (with the source turned off) is calculated according to Equation 4.6 and plotted here.

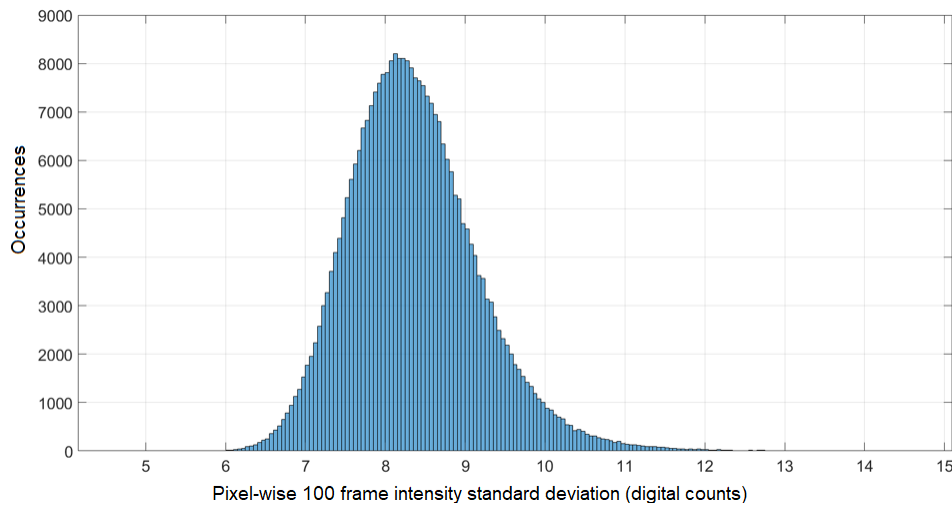


Figure 4.29: Histogram of the pixel-wise standard deviation values over a 100 frame background image, as shown in Figure 4.28.

in Figure 4.28, and the histogram of the distribution across all the pixels is shown in Figure 4.29. The average pixel-wise standard deviation over all the pixels is around 9 digital counts, which is about 3 orders of magnitude lower than the average value of the pixel-wise mean. This implies that the camera’s inherent image noise is quite low, and therefore, affords us a relatively good signal-to-noise ratio. The pixel-wise signal-to-noise ratio of the image stack, as defined in Equation 4.7, is plotted in Figure 4.30. The SNR values range from around 1100 to 2200.

We also calculated the pixel-wise standard deviation of the intensity values for three dif-

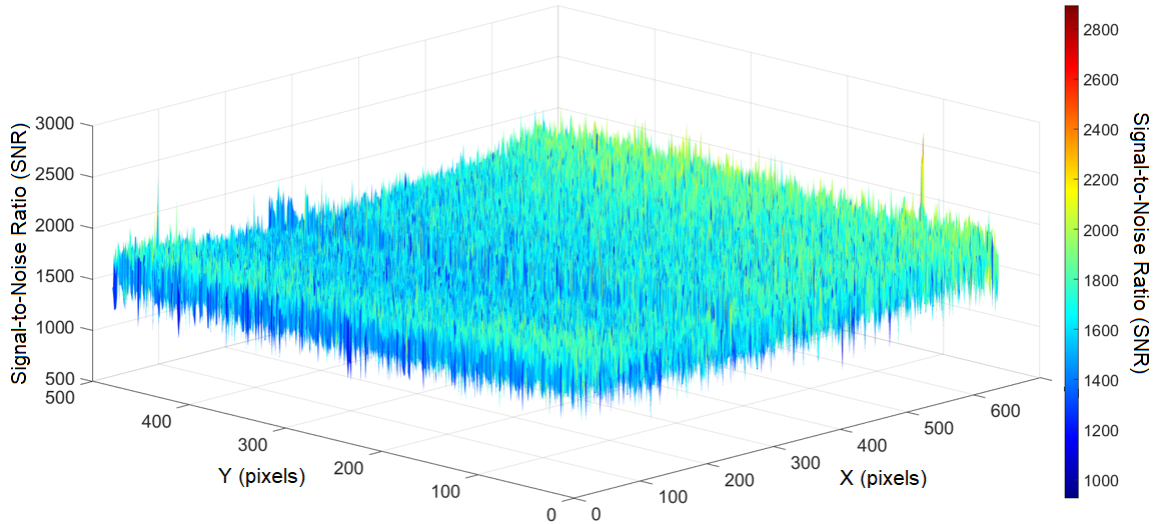


Figure 4.30: The signal-to-noise ratio (SNR) of every individual pixel over 100 frames is computed by using Equation 4.7 and the values of the pixel-wise mean and standard deviation, as shown in Figure 4.26 and Figure 4.28 respectively, and plotted here.

ferent imaging scenarios - one where the camera lens is closed to the environment using a lens cover (which is still an infrared emissive object itself at room temperature), one where the lens is able to image the optical setup except that the blackbody source is turned off, and a reference speckle when a plane wavefront impinging on the diffuser forms a speckle pattern - by acquiring 1000 frames for each of them, and computed the standard deviation values to be between $0.04\text{ }^{\circ}\text{C}$ and $0.19\text{ }^{\circ}\text{C}$, which are on the order of magnitude of the camera's NETD.

It is important to note here that even as the signal-to-noise ratio of the thermal images itself is not low, the difference between the background image (which is not a speckle pattern) and a speckle image is quite low. This is because the radiation emitted by the globar and collected by the collimation optics after passing through a 1 mm diaphragm is expanded to form a beam with a diameter of about 25 mm. This beam is then used to form the speckle after passing through the diffuser. The average mean intensity value over all the pixels and frames computed for 10 different background images (with the globar source switched off) is 13706 digital counts, while the same average mean intensity for 10 reference speckle images is 13721 digital counts and those for the lens-induced sample speckle patterns is 13725 counts. The average standard deviation for the intensity values of the background, reference speckle and sample speckle are 9, 22 and 24 digital counts, respectively. These values demonstrate that there is a high background signal present during our experiments

when the speckle images are measured, with similar digital count levels, which shows that the signal difference between the background and the speckle images is very low. The dynamic range over which the speckle is encoded is extremely low (about 20 digital counts with a noise level of 9 digital counts), compared to visible speckle images where typically there is a higher difference in the intensity values between the background and a sample image. The major difference is the absence of thermal background radiation at visible wavelengths at room temperature.

4.6.2 Frame averaging of speckle images

In the initial stages of our speckle imaging experiments, once we had observed LWIR speckle images through our experimental setup, we started acquiring multiple frames to average over and construct a speckle image which would improve the signal-to-noise ratio (SNR) of our speckle images. We therefore considered the number of frames over which the averaged speckle image would offer a significant increase in the SNR, since large image files would consume a great deal of memory in our storage media. In addition to the quest for knowing the optimal number of frames we needed to acquire, we also recorded images in the same experimental conditions over a period of time, to see the image SNR stability.

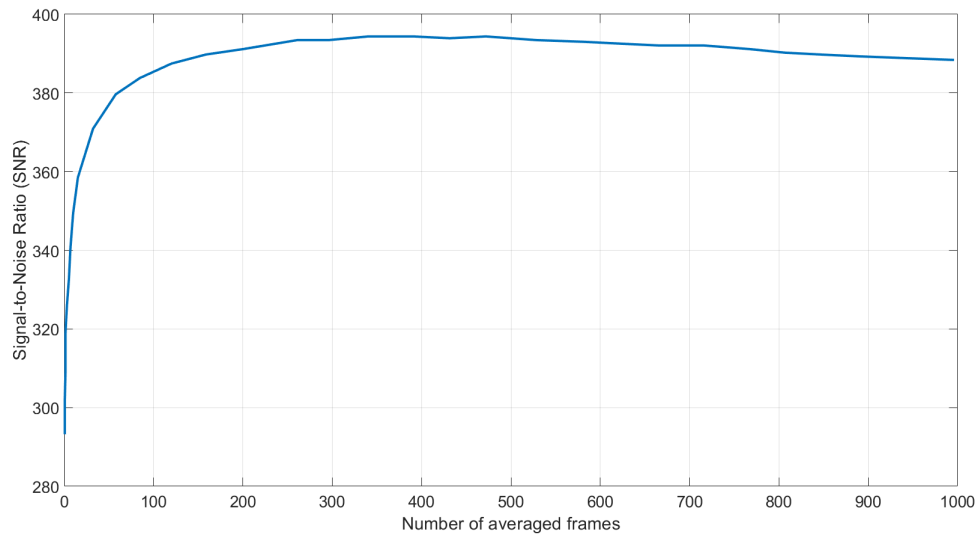


Figure 4.31: The average signal-to-noise ratio (SNR) values for a background image acquired by the thermal camera when an increasing number of acquired frames are pixel-wise averaged to obtain a pixel-wise mean intensity image.

In Figure 4.31, we see that the SNR increases sharply from about 250 to at least 320 as the

number of frames that are being averaged increase upto 100 averaged frames, and then the SNR values plateau and very slowly increase upto 1000 averaged frames. This measurement enabled us to only acquire 100 frames for each speckle image sequence as it was the optimal limit for a high image SNR without having to expend too much memory. Around 100 frames, we see that the SNR increase ranges from about 450 to 320 compared to the single frame image SNR value close to 250. We also saw that over time which ranges from 0 seconds to a little more than 30 hours, the image SNR shifts considerably, which signifies that there is a change in the temperature signal detected by the camera depending on the global temperature of the experimental room over time. Since the temperature and therefore the speckle image signal changes over time, it is imperative to carry out a single phase reconstruction experiment within a small window of time to avoid the speckle pattern from changing due to external temperature variations. This also means that we cannot capture a reference speckle as a single shot calibration for wavefront sensing of different samples, as this might alter the reconstructed wavefront result due to the external temperature variations. The typical timeframe for a single reference and sample speckle image sequence acquisition is about 10-15 seconds, depending on the time required to introduce the phase sample, at which scales the variation in the external temperature does not significantly alter the speckle image pattern to introduce phase reconstruction errors. We believe that it should be possible to carry out single-shot calibration of our wavefront sensing technique if the temperature of the surroundings is well-controlled, but the objective of developing our LWIR speckle imaging technique is the ability to deploy this method robustly in conditions where such a well-controlled constant temperature chamber is not available, as well.

4.6.3 Intensity inhomogeneities

We have discussed above how the acquisition of a speckle image has to deal with high background signals, and the very low difference in the thermal signal variations between different speckle images as well. In addition to these, there is also the challenge of having to remove intensity inhomogeneities from our speckle images, as well as vignetting effects on the edge of a speckle image due to the geometrical constraints of our imaging setup. We refer to Figure 4.1 which shows both of these issues, as well as Figure 4.10. We can see that there are large intensity features like a dark central spot as well as a dark annulus in Figure 4.1 which are not part of the speckle pattern and therefore need to be removed. We have already discussed in Section 4.1 how a 2-D Gaussian low-pass spatial frequency filter is used to remove these intensity inhomogeneities, as shown in Figure 4.2, to finally obtain

a filtered speckle image that does not contain these intensity features anymore, as seen in Figure 4.3. On the other hand, the vignetting effect seen prominently in the raw speckle image is partly removed by the Gaussian filter but still remains in the filtered image to a lesser extent. We altogether avoid using 100 pixels from each border or side of the speckle image by cropping the filtered image to only consider a central pixel area of 440 x 280 pixels for the wavefront reconstruction algorithm. This is also another issue that led us to obtain slightly erroneous results, which have been improved by cropping the edges without a significant loss of speckle information.

4.6.4 Infrared focussing

We would also like to briefly point out the difficulties in building the experimental setup for LWIR speckle imaging which stem primarily due to the lack of human vision intuition for the infrared. During the development of our experimental setup, it was difficult to estimate optical distances due to the inability to observe them with our eyes or simple tools that are pretty commonly available in an optics experimental laboratory. One example of this lack of vision capability in the infrared, with the only infrared imaging device available being our camera, was during the determination of the precise lens positions for the collimation of the blackbody source radiation to produce a plane wavefront for our speckle imaging experiments. While the difference between the focal length of a lens in the visible and the infrared can be calculated, which differs by about 10% with respect to the visible for a sample ZnSe lens of focal length 1 m, the lack of our intuition and vision in the infrared compounded the actual positioning of the optics since the effects of the experimental changes were not readily verifiable unless a full experiment had been carried out, while also keeping in mind the tolerances for the focal length variation of real lenses. After some searching, we were able to obtain a Thorlabs VRC6S MIR liquid crystal detector card in the wavelength range of 1.5 to >13.2 μm at room temperature, which enabled us to visualize the infrared focus of our optical lenses for easier experimental optimization. Even the choice of a phase object and a scattering medium in the longwave infrared is not only limited by the choice of materials, but also by the non-intuitive nature of their behaviour in a speckle imaging setup.

4.7 Wavefront reconstruction of a complex phase mask

In order to test our phase imaging technique beyond the use of simple infrared optical components that have a smoothly varying homogeneous phase gradient profile, we elected to fabricate a smiley pattern on a silicon substrate to investigate the possibility of phase imaging more complex samples.

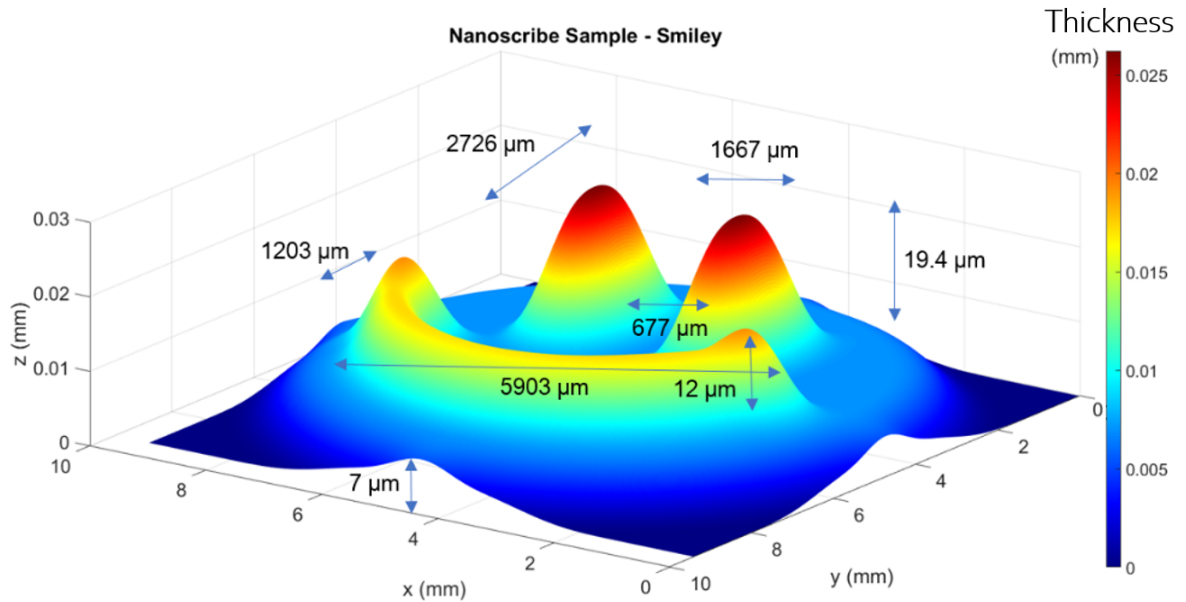


Figure 4.32: 3D design of smiley pattern with spatial gradients where the height is two orders of magnitude lesser than the lateral dimensions.

A smiley image was smoothed using a 2-D Gaussian smoothing kernel and the filtered image was then recast in 3D to create a smoothly varying smiley pattern with spatial gradients that were close to $1/100$, i.e. where the height is two orders of magnitude lesser than the lateral size of the features. The features of the smiley were designed to have a smooth phase gradient without abrupt or sharp phase jumps by maintaining the ratio between the height and the lateral dimensions, and with an amplitude in height on the order of the LWIR wavelength such that the optical path difference would also be less than or on the order of this wavelength. Considering that the refractive index of the SU(8) polymer used by the Nanoscribe to etch the smiley phase mask is 1.62 at the wavelength of $10\ \mu\text{m}$ [283] (see Figure 4.34), the approximate optical path difference for the smiley features turn out to be

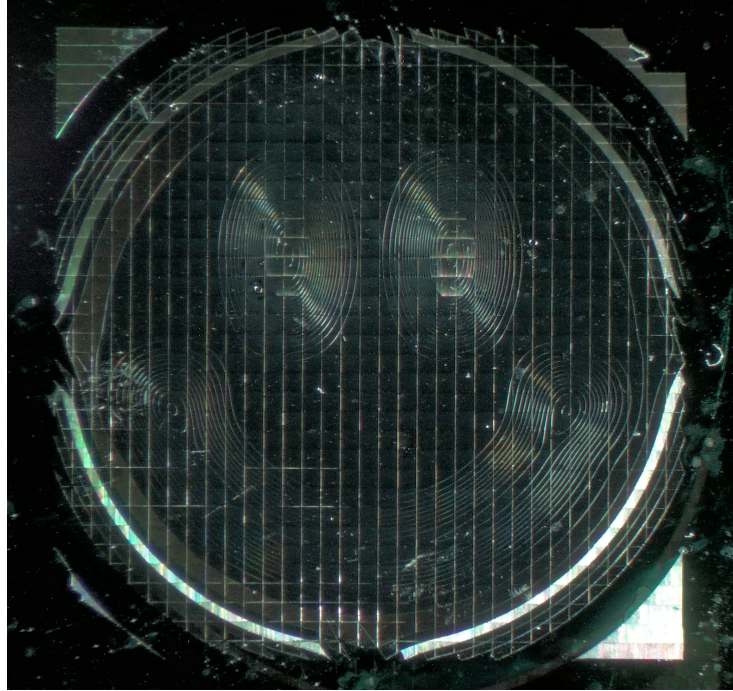


Figure 4.33: Optical microscope image of the fabricated smiley pattern on a double side polished silicon substrate, with the printed surface measuring 8.5 mm x 10.0 mm.

given by the equation:

$$\delta = \Delta L \times \Delta n = \Delta L \times (1.62 - 1) = 0.62\Delta L \quad (4.8)$$

where, δ is the optical path difference between a ray passing through the SU(8) phase mask and one outside it, ΔL is the difference in height of the phase mask features, and Δn is the refractive index difference between SU(8) and air. In our case, for the highest features of the smiley with a $\Delta L = 19.4 \mu\text{m}$, the optical path difference is $12 \mu\text{m}$, which is close to our reference wavelength of $10 \mu\text{m}$.

The three dimensional (3D) smiley pattern, as designed, is shown in Figure 4.32. The 3D smiley pattern was then used to print the design on a silicon wafer substrate using a Nanoscribe device, which employs two photon absorption to crosslink polymers for lithography. [284] A Nanoscribe device enables the fabrication of 3D micro and nanostructures through a process called direct laser writing, which involves using a femtosecond pulsed laser to induce polymerization in a photosensitive material. The laser beam is precisely focused on the surface of the material, creating a small volume of polymerized material at the focus

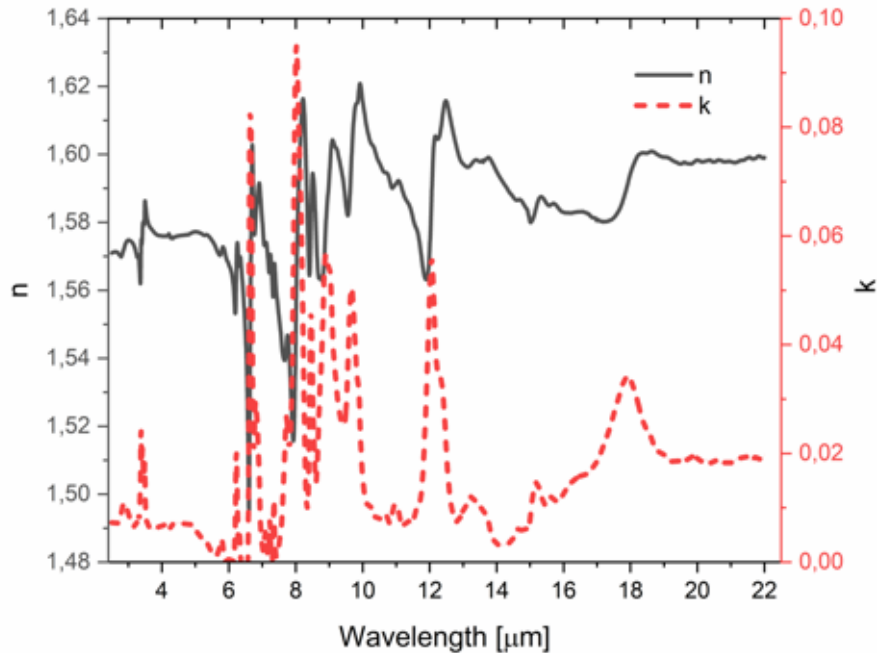


Figure 4.34: The refractive indices of SU(8) photoresist used for fabricating samples in a nanoscribe, from [283], which show that phase samples of a finite depth can be used as LWIR phase samples without significant light attenuation.

point. By moving the laser beam through the material and selectively polymerizing voxels, complex three-dimensional microstructures can be created layer by layer with high resolution and accuracy, greater design flexibility, and the ability to create complex geometries.

This 3D printing was performed by Dr. Justine Laurent from Gulliver laboratory at ESPCI, who is the engineer in charge of the NanoScribe setup. Upon a double side polished silicon wafer - with a diameter of 50.8 mm and thickness of 375-385 μm - an SU(8) photoresist was used to inscribe the smiley design. Care was taken to produce a smiley whose highest features were smaller than the penetration depth of approximately 40 μm for SU(8) at a wavelength of 10 μm [283]. An optical microscopy image of the smiley printed by the Nanoscribe is shown in Figure 4.33.

To carry out a phase imaging experiment with our setup for the smiley sample, we used a double side polished silicon wafer with nothing printed on it as a reference sample to obtain a reference speckle pattern. This step was necessary as not doing so introduced a significant non-uniform intensity difference between the reference speckle and the sample speckle due to the attenuation produced by the double side polished silicon wafer substrate. The

intensity difference introduces errors in the estimation of the speckle grain shift using the Demons algorithm and leads to a wrong phase reconstruction result. The sample speckle pattern was acquired by simply placing the printed smiley sample on the substrate between the plane wavefront and the diffuser.

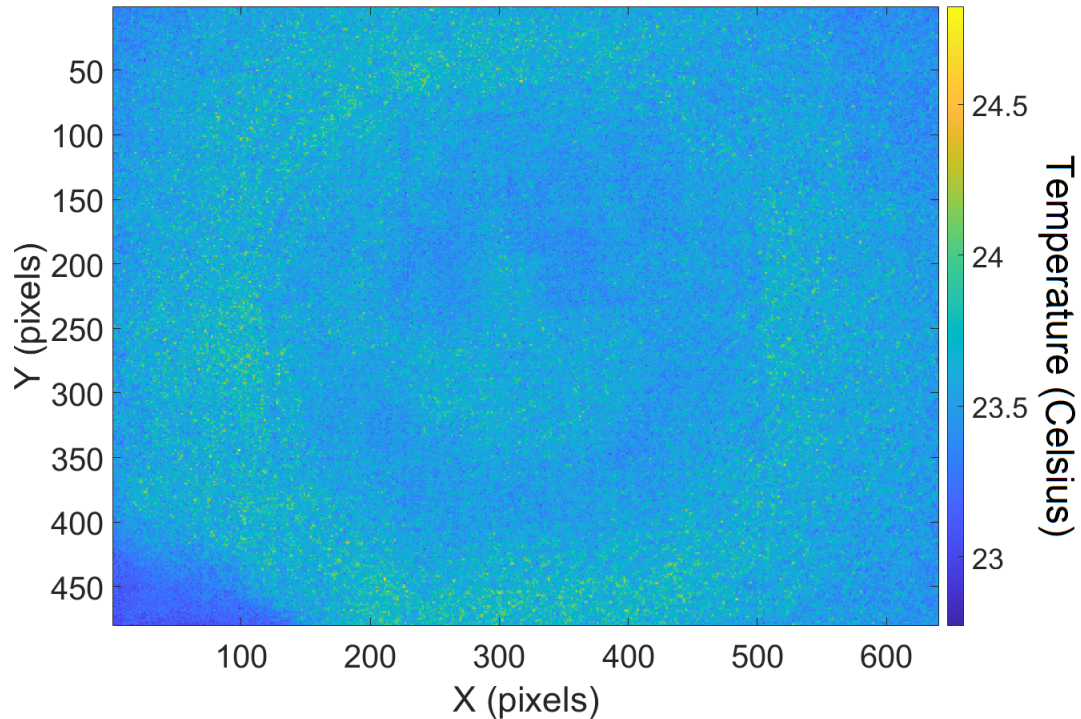


Figure 4.35: An LWIR image that shows the intensity information when the fabricated smiley pattern, as shown in Figure 4.33, is imaged using our LWIR camera, when placed in front of the diffuser and illuminated by a plane wavefront from our blackbody source.

An LWIR image of the smiley which is acquired through the diffuser upon illumination by a plane wavefront is shown in Figure 4.35. The intensity contrast of the image is quite low to be able to resolve the smiley itself, and especially its features. We can also see that the intensity difference between the darkest and brightest pixels in the intensity image does not cover a large dynamic range, and therefore, a precise delineation of the smiley pattern's features is difficult to obtain from the image intensity itself.

The speckle pattern however does contain embedded phase information in the intensity image itself, and using our wavefront reconstruction algorithm, as described in Section 4.2, it is then possible to reconstruct the wavefront from the smiley sample that is incident on the diffuser and creates the corresponding speckle pattern in transmission. The reconstructed wavefront from the smiley phase sample is shown in Figure 4.36. We can clearly see here

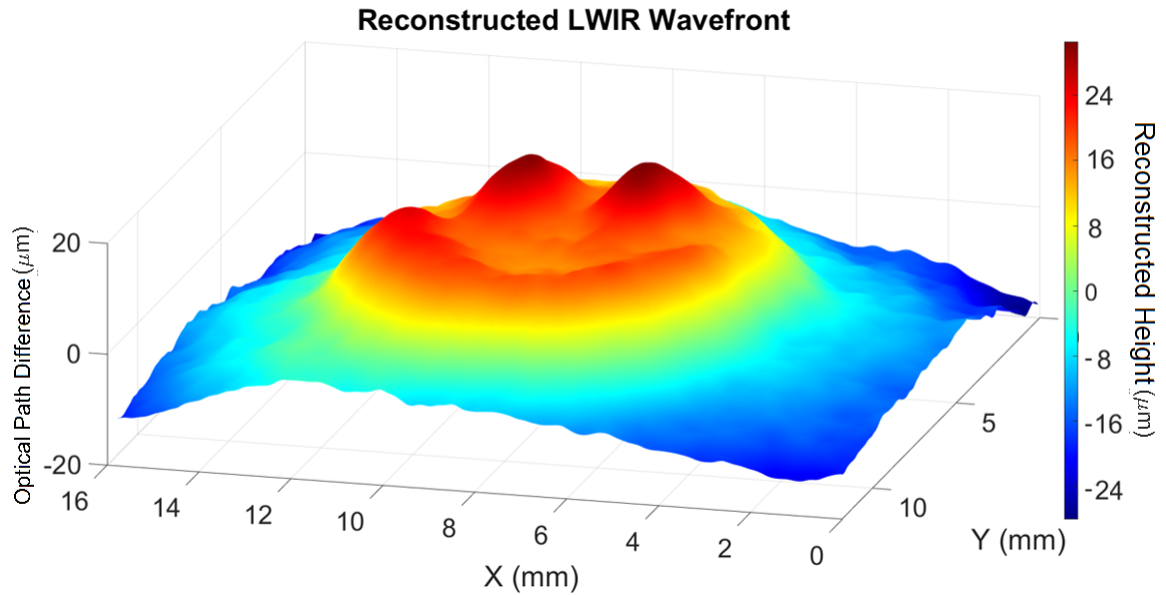


Figure 4.36: Reconstructed longwave infrared wavefront when a fabricated smiley pattern (as shown in Figures 4.32 & 4.33) is placed in front of the diffuser where it intercepts a plane wavefront and distorts its phase profile.

the main features of the smiley pattern itself, which gives a much more informative picture of the smiley pattern’s design in comparison to the intensity image shown in Figure 4.35.

This qualitative wavefront reconstruction of the patterned smiley on a double side polished Silicon substrate opens up the avenue for precise quantitative phase profiling, which will have interesting applications in reconstructing the surface characteristics of a Silicon wafer substrate sample whose intensity image reconstruction otherwise is not highly contrasted. Here, we can see another example of the complementary value of phase information for reconstructing a particular object when the usually imaged intensity information is unable to do so conventionally, and the utility of the diffuser’s ability to encode phase information of an object onto a speckle pattern upon transmission.

4.8 Qualitative and quantitative aspects of phase reconstruction

Wavefront reconstruction results using our LWIR speckle imaging setup based on the mapping of the slight displacements of the speckle grains induced by spatial variations of the phase have demonstrated the ability of our methodology to carry out quantitative phase

reconstruction in the case of infrared optical lenses with an average difference in the radius of curvature estimates of the spherical wavefronts with respect to the ideal expected radius by about 10%.

To quantify the phase noise in our imaging methodology, we compared the difference between the reconstructed wavefronts from two consecutive reference speckle images. We acquire 10 reference speckle images of 100 frames each, i.e. those speckles generated when a plane wavefront is incident on the diffuser and create a speckle pattern in transmission, and then we compute the pixel-wise mean of the speckle image intensity from the 100 frames for each reference speckle image. This averaged reference speckle is then Gaussian high-pass filtered to remove the low spatial frequency intensity features, as described in Section 4.1, and a border of 100 pixels width is removed from each side to neglect edge vignettes from the image. Each consecutive reference speckle pair then undergoes the wavefront reconstruction algorithm, which is described in Section 4.2. The reconstructed wavefront from two consecutive reference speckle images should ideally be a flat plane, in the absence of any noise. The 3-D reconstructed wavefront from a consecutive reference speckle pair is shown in Figure 4.37. We quantify this difference by plotting the standard deviation of this reconstructed wavefront for each pair, and the optical path difference range that is the difference between the highest and lowest reconstructed optical path difference values from the wavefront, in Figure 4.38.

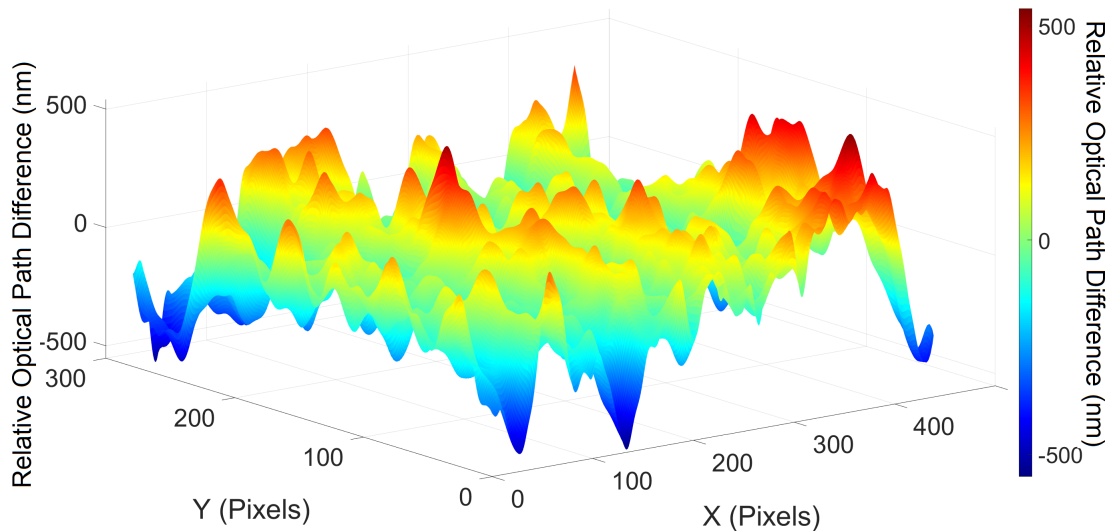


Figure 4.37: A 3-D surface plot of the reconstructed wavefront from two consecutive reference speckle images which shows the optical path difference between the two consecutive reference wavefronts which gave rise to these speckles.

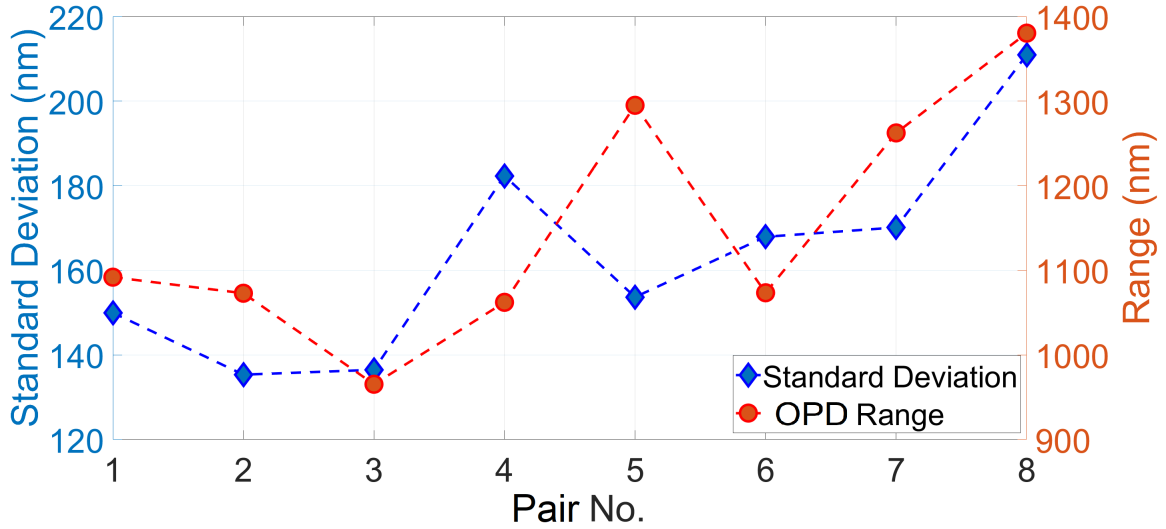


Figure 4.38: The optical path difference values for each reconstructed wavefront from a reference speckle pair, as shown in Figure 4.37, is computed for the 10 reference speckle images and their optical path difference range, i.e. the difference between the lowest and highest relative optical path difference value, and standard deviation are plotted.

We can see in Figure 4.37 that the optical path difference values are heterogeneously distributed, instead of showing any particular phase profile, as expected, while also demonstrating that the reconstructed wavefront profile is not flat but has an optical path difference between -500 and 500 nm. In Figure 4.38, we see that the optical path difference range between the lowest and highest optical path difference in the reconstructed reference speckle wavefront ranges from about 1000 nm to 1400 nm, while the standard deviation of the relative optical path difference lies between 140 nm and 210 nm. The average standard deviation of the optical path differences of the reconstructed wavefront pairs is 163 nm, while the average optical path difference range is 1150 nm. These optical path difference values are therefore the limiting relative optical path difference values we can observe with our present experimental setup and wavefront reconstruction algorithm.

We then carried out a similar analysis to find the optical path difference values between a reconstructed spherical wavefront, similar to the one shown in Figure 4.18, and the 2-D spherical fit to the reconstructed wavefront using Equation 4.4, to quantify the optical path difference fluctuations in one of our lens sample speckle images. The sample speckle image was acquired when a plane wavefront from our illumination source was incident on a sample Zinc Selenide (ZnSe) plano-convex lens of focal length 1 m, producing a spherical wavefront that created a speckle pattern upon transmission through the diffuser, and

was then acquired at the speckle imaging plane of the camera placed 1 mm away from the diffuser. Here, as well, the pixel-wise mean of the speckle image intensity from the 100 frames is computed to obtain an averaged sample speckle image, which is then Gaussian high-pass filtered, as described in Section 4.1, and a border of 100 pixels width is removed from each side to remove any influence from the edges. The sample speckle then undergoes the wavefront reconstruction algorithm, as described in Section 4.2, along with a reference speckle image in the same configuration but without the sample lens. The reconstructed wavefront in this case should be a spherical surface. The reconstructed spherical wavefront is then subjected to a 2-D spherical fit according to the Equation 4.4 to create a smooth surface, and also to estimate the radius of curvature of the reconstructed spherical wavefront, as discussed earlier in Section 4.5.1.2. The difference between this spherical fit surface and the reconstructed wavefront is computed, which gives us the residuals of the spherical wavefront fit, and these residual values also provide a measure of the optical path difference fluctuations within the reconstructed spherical wavefront compared to a smooth spherical surface.

The residuals of the reconstructed wavefront and its spherical fit surface is plotted in 3-D in Figure 4.39. We see in Figure 4.39 that the optical path difference range, or the difference between the lowest and highest relative optical path differences among the residual values is 1623 nm while the standard deviation of the optical path difference is 191 nm. In contrast, the optical path difference range of a reconstructed spherical wavefront and its spherical fit surface is 11667 nm and 10714 nm respectively, while the standard deviation is 2461 nm for the reconstructed wavefront and 2454 nm for the spherical fit surface. This indicates that the optical path difference range and the standard deviation between the reconstructed wavefront and the residuals arising from the difference between the reconstructed wavefront and the spherical fit has an order of magnitude difference, and therefore that our quantitative phase reconstruction are limited by the residuals which are about 10% of the reconstructed wavefront optical path difference values.

The standard deviation and optical path difference range of the residuals of the reconstructed wavefront and its spherical surface fit are computed for 8 sample speckle images, and shown in Figure 4.40. We see here that the optical path difference range values for the different sample speckle images range from about 1300 nm to 2100 nm with a mean of 1668 nm. The standard deviation of the residuals ranges from 170 nm to 260 nm, with a mean standard deviation of 195 nm.

A comparison between Figure 4.38 and Figure 4.40 demonstrates that the average standard deviation of the residuals for the $f = 1$ m sample lens spherical wavefronts and their spherical surface fits is of the same order of magnitude as the average standard deviation of the optical path differences between two reference speckles. Both the average optical path difference range and the average standard deviation are slightly lower for the reference speckles in comparison to the spherical wavefront residual optical path differences, which imply that our wavefront reconstruction results from the sample plano-convex lenses have a relatively high degree of precision within the constraints of the imaging system's inherent optical path difference fluctuations or noise.

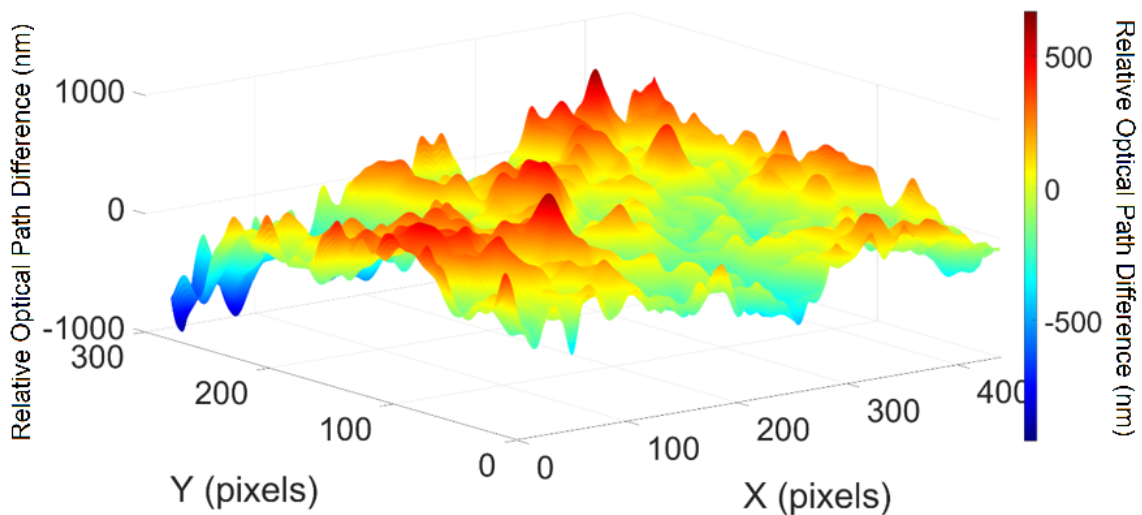


Figure 4.39: A 3-D surface plot of the residuals for a reconstructed spherical wavefront, that is the optical path difference between the reconstructed spherical wavefront and the spherical surface fit (according to Equation 4.4) for the reconstructed spherical wavefront emanating from a $f = 1$ m Zinc Selenide (ZnSe) lens.

While the wavefront reconstruction results for the ZnSe sample lenses of focal lengths $f = 1$ m and $f = 50$ cm are not only qualitatively similar to and representative of the expected wavefronts from these phase objects, they also demonstrate the quantitative reconstruction of the phase profiles of the incident wavefronts with a high degree of accuracy and appreciable precision within the experimental tolerance of our imaging methodology. However, in the case of other phase samples that we tested like ZnSe sample lenses of focal lengths $f = 20$ cm and $f = 5$ cm, even as the wavefront reconstruction shows qualitative agreement, there is further work that needs to be done to improve the quantitative phase reconstruction accuracy. In the case of the fabricated phase sample of the smiley, while the wavefront reconstruction qualitatively extracts the designed features of the smiley, and

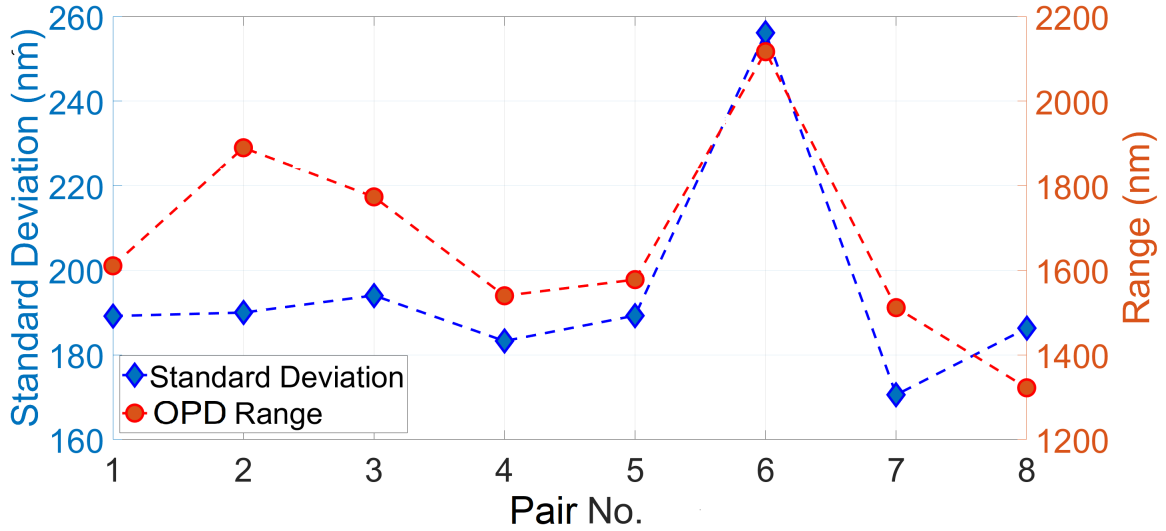


Figure 4.40: The optical path difference values for the residuals of the reconstructed spherical wavefront, as shown in Figure 4.39, is computed for 8 different sample lens ($f = 1$ m) speckle images and their optical path difference range, i.e. the difference between the lowest and highest relative optical path difference value, and standard deviation are plotted.

shows the ability to reconstruct an LWIR sample's features by recovering the phase profile in the absence of intensity contrast, the quantitative optical path difference profile needs to be characterized by an alternative LWIR wavefront sensing technique to attest to its accuracy.

We see in Figure 4.41 the reconstructed wavefront when a sample ZnSe plano-convex lens of focal length $f = 5$ cm is placed 1 cm away from a diffuser, and in Figure 4.42 the reconstructed wavefront when the same lens is placed 9 cm away from the diffuser. We can see in Figure 4.16 that when a plano-convex lens is placed at a distance d from the diffuser which is lesser than the focal length of the lens, the radius of curvature of the incident wavefront on the diffuser is positive and a converging spherical wavefront is expected to be reconstructed. On the other hand, if the distance d between the diffuser and the lens exceeds the focal length of the lens, the converging wavefront from the plano-convex lens is focused at the focal point of the lens and then emerges as a diverging wavefront with a negative radius of curvature, according to the convention in Figure 4.16. The same behaviour is demonstrated in Figure 4.41 where the reconstructed wavefront matches the expected converging spherical wavefront, while the reconstructed wavefront in Figure 4.42 shows the case where the expected wavefront is a diverging spherical wavefront. While this qualitative difference between the incident wavefronts is reproduced in the reconstructed wavefronts, enabling

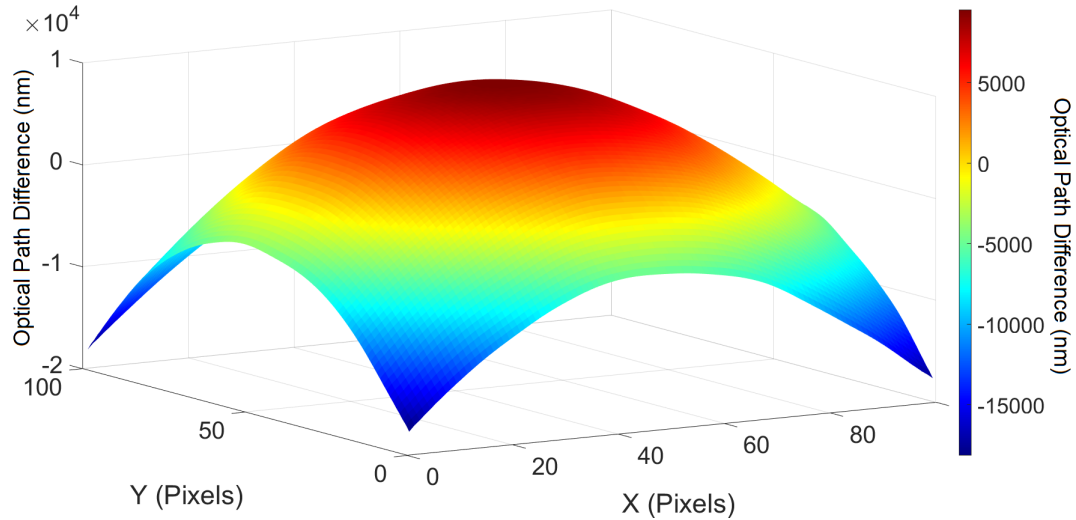


Figure 4.41: The reconstructed wavefront obtained using LWIR speckle imaging when a ZnSe lens of focal length $f = 5$ cm is placed 1 cm away from a diffuser, which creates a converging spherical wavefront that is incident on the diffuser, forming a speckle in transmission that is acquired at the imaging plane of the camera placed 1 mm away on the other side of the diffuser. The central 100×100 pixels of the speckle image containing the reduced size speckle are used for the wavefront reconstruction and shown here.

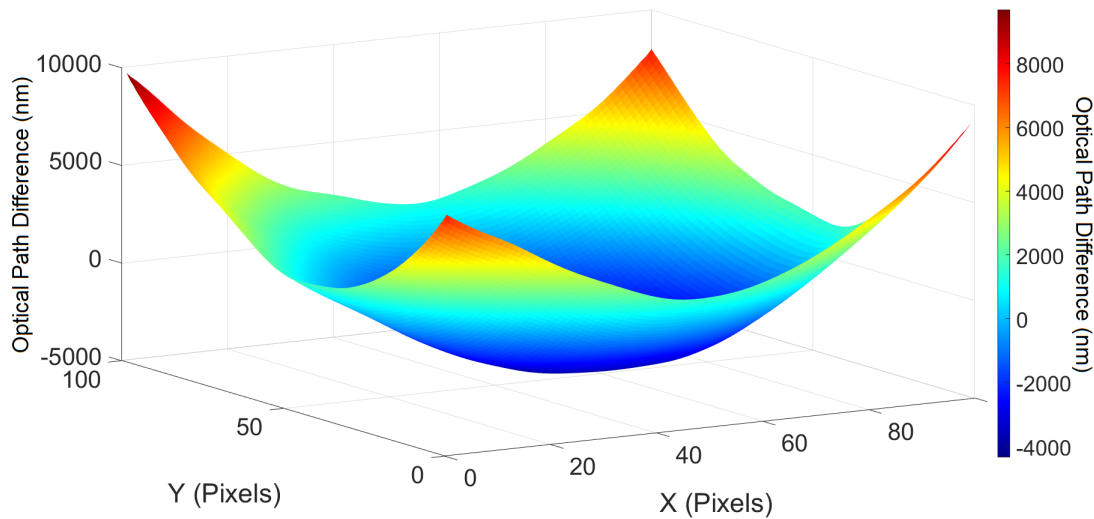


Figure 4.42: The reconstructed wavefront obtained using LWIR speckle imaging when a ZnSe lens of focal length $f = 5$ cm is placed 9 cm away from a diffuser, which creates a diverging spherical wavefront that is incident on the diffuser after first being focused at the lens' focal point in between the lens and the diffuser, forming a speckle in transmission that is acquired at the imaging plane of the camera placed 1 mm away on the other side of the diffuser. The central 100×100 pixels of the speckle image containing the reduced size speckle are used for the wavefront reconstruction and shown here, as well.

the visualization of a change in the incident wavefront profile, a more accurate estimation of the precise lens position from the reconstructed wavefront itself would need further work for accurate quantification of the reconstructed wavefront profile. The origin of this challenge seems to be the higher phase gradients in the incident wavefront experienced when undergoing transmission through smaller focal length lenses that produces stronger speckle shifts, whose speckle shift estimation and subsequent wavefront reconstruction then is limited by the ability to resolve in the speckle image the difference between a speckle shift and an overlap between shifted speckle grains. The height gradients in case of both the $f = 1$ m and $f = 50$ cm ZnSe lenses, as well as the smiley, were on the order of $1/100$, i.e. where the spatial size of the sample phase object along the axis of propagation of light is two orders of magnitude lower than the size along a plane perpendicular to the axis of propagation. A better understanding of the optical path difference limits that our present imaging method can achieve is an important future objective to improve the quantitative wavefront reconstruction quality for our experiments.

4.9 Summary

We have seen in this Chapter how the LWIR speckle imaging experimental setup, whose development we looked at in Chapter 3, has been used for phase reconstruction by utilizing the Demons algorithm for LWIR wavefront reconstruction. We discussed the image processing workflow that is carried out after the acquisition of the raw speckle images for them to be fed into the Demons algorithm. The angular memory effect was characterized subsequently, which shows that our scattering medium has a large angular memory effect range and we carry out our experiments in a regime where the speckle shift in an angular memory effect experiment is linearly proportional to the angular tilt of the incident wavefront throughout our scattering medium's spatial extent observed by the camera. We also carried out an analysis of the speckle grain sizes to see that they were satisfying sampling criteria, and that their sizes reflected the distance between the diffuser and the imaging plane of the camera, a parameter which is used for the wavefront reconstruction algorithm and is independently also obtained from the angular memory effect characterization.

This was followed by a discussion of the phase imaging experiments we conducted using ZnSe sample infrared lenses, to demonstrate the first results in LWIR wavefront sensing using speckle imaging. These first results showed that speckle imaging in the longwave infrared is capable of carrying out wavefront sensing, as in the visible, and that many of

the theoretical and experimental concepts developed in the visible regime could be successfully adapted to the LWIR for wavefront sensing. A slew of further experiments are done to characterize these first results in more detail, and we see that the radius of curvature estimates of the reconstructed wavefronts matched closely with the values expected by geometrical optics. We then delve into some challenges that we experienced in carrying out LWIR speckle imaging, and the lessons learnt from carrying out this work, while also emphasizing that the transposition of an imaging technique from the visible to the LWIR is not initially a happy marriage, with the complementary advantages of the wavefront regime and the imaging technique needing to optimize and adapt to the constraints in each of them to obtain a holistically successful result.

We finally discuss the fabrication of a customized sample phase mask to test our imaging methodology over non-regular (or, not spherically symmetric) phase samples like a smiley made of SU(8) polymer on a silicon substrate. We have not only seen here the accurate qualitative wavefront reconstructed from the smiley sample, but also seen that how a low-contrast intensity sample in the LWIR can be investigated to obtain complementary phase information using our wavefront sensing method. We then discuss the qualitative and quantitative aspects of our phase reconstruction technique and their limitations, which would form the basis for further developments to this technique.

Chapter 5

General conclusions and outlook

Contents

5.1 Future prospects	143
---------------------------------------	------------

In this thesis, we sought to develop a speckle-based wavefront sensing system in the long-wave infrared (LWIR), that can reconstruct thermal wavefronts by carrying out LWIR phase imaging through scattering media.

In Chapter 1 of this manuscript, we first looked at longwave infrared radiation and its manifest utility in thermal imaging, atmospheric and space applications, and spectroscopy. We also looked at some recent examples of infrared imaging in a non-line-of-sight light propagation context and noted that these have been limited to the near infrared (NIR) and the mid infrared (MIR). A discussion of recent developments demonstrating the necessity of characterizing tailored infrared emitters then demonstrated the need for developing similar techniques in the LWIR as well.

In Chapter 2, we traced the development of techniques for the retrieval of the phase of light - in order to obtain complementary information to the intensity of light - like holography and modern digital holography for phase imaging applications. The alternative approach of wavefront sensing for phase imaging was subsequently described, through the development of wavefront sensors and most recently, by imaging through complex media. The field of visible imaging through complex media and specific developments in visible wavefront sensing were described. This formed the groundwork for our work on LWIR phase

imaging.

In Chapter 2, after an introduction to the basic physical principles involved in the formation of speckles, which arise due to light propagation through scattering media, we took inspiration from visible speckle imaging to carry out phase reconstruction of objects through a scattering medium. Specifically, in Section 2.2, we looked at the formation of speckles, their statistical parameters, the memory effect of thin scatterers and speckle grain characteristics. In order to develop a compact LWIR wavefront sensor based on speckle imaging, which would also allow us to study speckle-based imaging in the thermal infrared from 8 to 14 μm , we then discussed the development of the experimental setup. While the physics of visible speckle imaging is theorized to work similarly at wavelengths that do not pertain to the visible region of the electromagnetic (EM) spectrum, the difficulty in obtaining readily available optical components in the longwave infrared, and more generally the difficulties inherent to LWIR imaging, brought forth experimental challenges that are described in detail in Chapter 3. The development of our LWIR speckle imaging setup and the progressive refinement of the experimental setup were then delved into in detail for the key experimental building blocks for infrared speckle imaging. These include the development of an appropriate scattering medium, the choice of a good infrared source, and a discussion of the uncooled microbolometer camera, which is a technology that makes broadband compact thermal imaging possible. Once the experimental setup was described in Chapter 3, we elucidated on our first experiments in LWIR speckle imaging, and the results obtained in those experiments in Chapter 4.

In Chapter 4, we began by looking at the image processing of the acquired LWIR speckle images from our experimental setup and briefly discussed the Demons algorithm which we used for wavefront reconstruction. Subsequently, phase imaging experiments that we conducted with sample infrared optical lenses were described, and we saw that the wavefronts that we reconstructed through LWIR speckle imaging demonstrated wavefront sensing through a scattering medium in the longwave infrared for the first time, to the best of our knowledge. We carried out wavefront reconstruction experiments using Zinc Selenide (ZnSe) lenses. Wavefronts of different radii of curvature were reconstructed, after LWIR speckle images were acquired through the two sample lenses in the experimental setup, in order to test the fidelity of our LWIR phase reconstruction method, and we saw that the reconstructed values of the wavefront radii of curvature were in close agreement with the expected ideal values of the radii for the wavefronts. We also probed how the wavefront

reconstruction functioned when the speckle pattern was intercepted at different distances by the camera, after LWIR light transmission through the scattering medium.

In Section 4.3, we experimentally characterized our Silicon wafer diffuser's angular memory effect characteristics; it being a key attribute of thin scatterers that makes them highly effective for wavefront sensing and phase imaging. In our case, we experimentally observed that the single side polished Silicon wafer diffuser has a high angular memory effect, which subsequently enabled us to carry out precise wavefront reconstruction, using the high fidelity of the speckle shifts that are due to the large angular memory effect of the thin diffuser. We also analysed the speckle grain sizes for our experimental conditions and in addition to satisfying the sampling limits for speckle imaging and wavefront reconstruction, they also showed that the speckle grain sizes are on the order of the light wavelength, as is theoretically estimated.

In Section 4.6, we shed light on some of the specific challenges we had to contend with in developing an LWIR wavefront sensing technique based on speckle imaging. The analysis of the thermal camera's noise characteristics highlighted the relatively low signal and image contrast in infrared speckle imaging, due to a high infrared background which was ever present during our experimental speckle image acquisitions. To improve the signal-to-noise ratio of our LWIR speckle images, we settled on frame averaging to improve the LWIR speckle image contrast. We noticed that the LWIR background image, which was acquired without an infrared source and emanated from the thermal radiation of the experimental area, and the reference speckle image which was acquired without any phase sample but with the experimental setup in place and the infrared source turned on, both exhibited a change in their global mean image intensity values that depended on the room temperature. It does not hamper carrying out similar experiments spread over time if the reference and sample speckle images are acquired consecutively at the same time - which takes a few minutes - and which is the method we employed in our experiments. Subsequently, a brief commentary on intensity inhomogeneities in our speckle images and the use of spatial filtering to reduce them was presented, followed by a description of how our (human) inability to visualize the infrared increased the complexity of placing infrared optical components in their correct positions to ensure proper light focussing, which we ameliorated to a great degree with a rudimentary IR optical focussing aid.

The LWIR speckle-based phase imaging modality is further tested by fabricating a structured phase mask - a smiley pattern, which we used to reconstruct the wavefront of such a

phase sample. It served as another example of the complementary value of phase information for reconstructing a particular object when the usually imaged intensity information is unable to do so conventionally, and demonstrated the diffuser's ability to encode phase information of an object onto a speckle pattern upon transmission.

The quantitative aspects of wavefront reconstruction using our methodology are then presented to round off the discussion of these first experiments and successful experimental results in longwave infrared wavefront reconstruction using a scattering medium for speckle imaging. The key findings of the work presented in this manuscript demonstrate that our objective of developing a speckle imaging system using complex scattering media in the longwave infrared region of the electromagnetic spectrum, has been successfully realised. It has opened up the avenue towards reconstructing thermal wavefronts for more complex phase samples, and for an improved understanding of longwave infrared speckle-based phase imaging.

5.1 Future prospects

While we have seen at a glance some of the avenues where future work will be needed to advance this technique, we begin on a footing where this first work has shown the possibilities for using the longwave infrared to carry out wavefront sensing using speckle imaging. We begin with some of the immediate work that will be carried out ahead, and also point towards developments that will carry this broad field towards utilitarian applications as well as further investigations into the field of infrared speckle imaging.

One of the first phase samples that we want to subsequently test is a fabricated phase sample of an USAF target pattern which is used for optical resolution characterization. The phase design of this sample, as shown in Figure 5.1, is highly irregular and discontinuous compared to the samples we have tested till now, and it will be a test of the phase resolution and sensitivity capabilities of our LWIR speckle imaging-based wavefront sensing technique.

A more application-oriented experiment would be to try to characterize structures on a Silicon substrate like integrated circuits or resistors on substrates, as can be seen in Figure 5.2, which would enable thermal imaging of visually opaque samples as shown in some previous work using a different thermal imaging technique [285]. Here, the idea would be to use the temperature dependence of the refractive index which modifies the optical

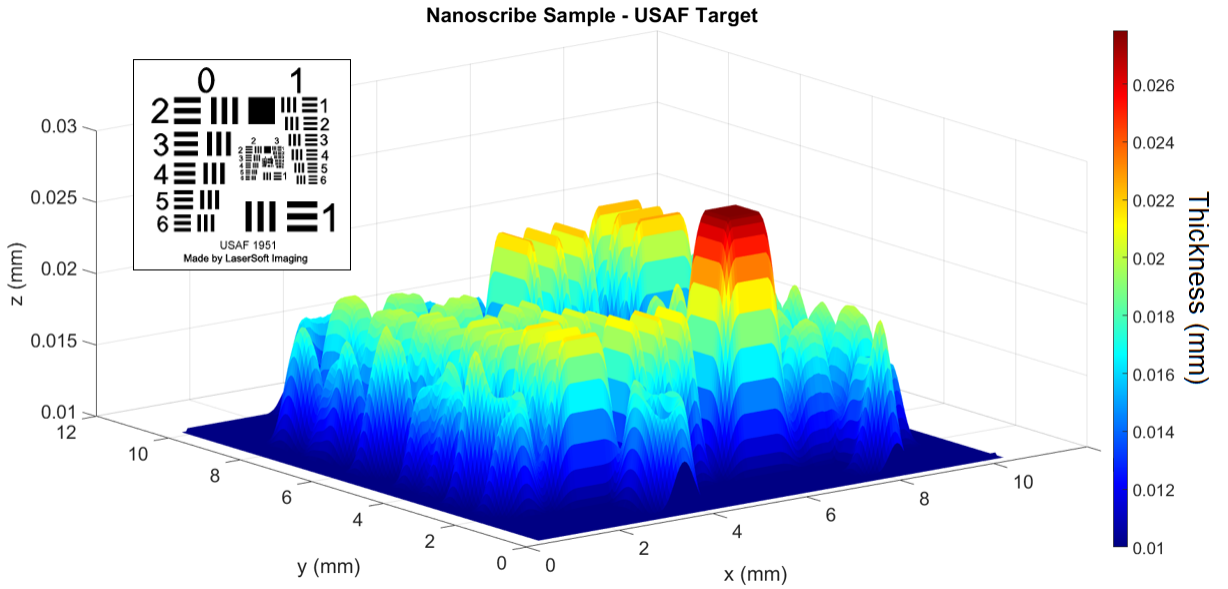


Figure 5.1: A 1951 USAF resolution test chart sample used as the design for a nanoscribe fabricated phase sample.

phase. Therefore, temperature - in Silicon, for instance - could be deduced from phase measurements rather than from intensity measurements as usual.

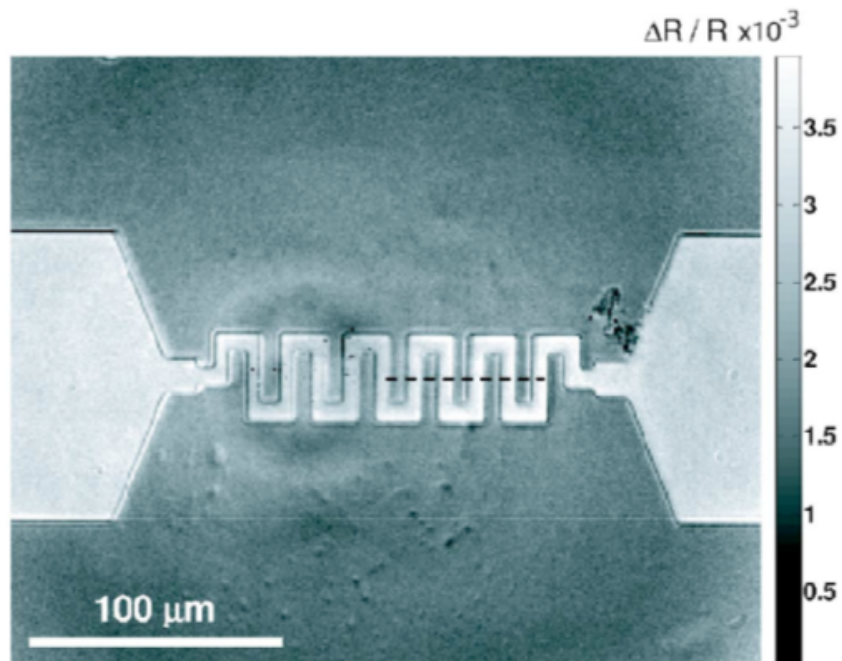


Figure 5.2: Thermal image of a gold resistor obtained through a 500 μm silicon substrate, from [285].

We also wanted to use infrared filters to see if we could carry out spectroscopic studies. However, for the infrared filters that we tried, the intensity of the speckle pattern was too low. We need to therefore figure out how to investigate carrying out LWIR speckle imaging with higher intensity sources, which was until now limited due to the camera sensor's sensitivity to large incident thermal radiation.

An additional aspect of this work, that could be investigated in the future, concerns the modelling of speckle patterns. Based on an analytical model, as described in appendix A, the near-field speckle was calculated for visible speckles. Carrying out a similar analysis for LWIR speckles can be used to compare with and enhance the theoretical understanding of experimental LWIR speckles, and also utilize such calculations to fine tune our technique and test new applications.

In this manuscript, we have described the development of a novel longwave infrared speckle imaging system that is capable of reconstructing thermal wavefronts. We have also seen the need for such techniques for practical applications, and this work also opens the avenue to carrying out further experiments in the LWIR by utilizing speckle imaging for imaging through scattering media and investigating speckle physics in the LWIR. In addition, it has also broadened the utility of speckle-based wavefront sensing techniques for multi-spectral applications in different domains. The emerging innovative field of computational imaging and lensless imaging [286] has shown transformative applications that are promising for potential applications in the LWIR, if they can be adapted to our LWIR wavefront sensing technique. Many other research ideas at the cutting-edge of visible speckle physics might also be amenable for translating to the LWIR, after the challenges in the LWIR are worked upon. We hope this thesis will be of use in future research in the broad domain of infrared phase imaging.

Bibliography

- [1] A. Shilova, *Development of Serial Protein Crystallography with Synchrotron Radiation*. PhD thesis, Dec. 2016.
- [2] H. Obrig and A. Villringer, “Beyond the Visible—Imaging the Human Brain with Light,” *Journal of Cerebral Blood Flow & Metabolism*, vol. 23, pp. 1–18, Jan. 2003.
- [3] D. R. Rhiger, “HgCdTe Long-Wave Infrared Detectors,” in *Semiconductors and Semimetals*, vol. 84, pp. 303–331, Elsevier, 2011.
- [4] D. Socolinsky, L. Wolff, J. Neuheisel, and C. Eveland, “Illumination invariant face recognition using thermal infrared imagery,” in *Proceedings of the 2001 IEEE Computer Society Conference on Computer Vision and Pattern Recognition. CVPR 2001*, vol. 1, pp. I–I, Dec. 2001.
- [5] J. A. Hackwell, D. W. Warren, R. P. Bongiovi, S. J. Hansel, T. L. Hayhurst, D. J. Mabry, M. G. Sivjee, and J. W. Skinner, “LWIR/MWIR imaging hyperspectral sensor for airborne and ground-based remote sensing,” in *Imaging Spectrometry II*, vol. 2819, pp. 102–107, International Society for Optics and Photonics, Nov. 1996.
- [6] T. S. Kleine, T. Lee, K. J. Carothers, M. O. Hamilton, L. E. Anderson, L. Ruiz Diaz, N. P. Lyons, K. R. Coasey, W. O. Parker Jr., L. Borghi, M. E. Mackay, K. Char, R. S. Glass, D. L. Lichtenberger, R. A. Norwood, and J. Pyun, “Infrared Fingerprint Engineering: A Molecular-Design Approach to Long-Wave Infrared Transparency with Polymeric Materials,” *Angewandte Chemie International Edition*, vol. 58, no. 49, pp. 17656–17660, 2019.
- [7] “Infrared window,” *Wikipedia*, Oct. 2022.

- [8] A. Rogalski, "History of infrared detectors," *Opto-Electronics Review*, vol. 20, pp. 279–308, Sept. 2012.
- [9] M. Akhloofi, A. Bendada, and J.-C. Batsale, "State of the art in infrared face recognition," *Quantitative InfraRed Thermography Journal*, vol. 5, pp. 3–26, June 2008.
- [10] A. Kylili, P. A. Fokaides, P. Christou, and S. A. Kalogirou, "Infrared thermography (IRT) applications for building diagnostics: A review," *Applied Energy*, vol. 134, pp. 531–549, Dec. 2014.
- [11] "Review: Application of Infrared Thermography in Livestock Monitoring." <https://doi.org/10.13031/trans.13068>.
- [12] J. A. Shaw, P. W. Nugent, J. Johnson, J. J. Bromenshenk, C. B. Henderson, and S. Debnam, "Long-wave infrared imaging for non-invasive beehive population assessment," *Optics Express*, vol. 19, pp. 399–408, Jan. 2011.
- [13] S. Komatsu, A. Markman, A. Mahalanobis, K. Chen, and B. Javidi, "Three-dimensional integral imaging and object detection using long-wave infrared imaging," *Applied Optics*, vol. 56, pp. D120–D126, Mar. 2017.
- [14] G. J. Tattersall, "Infrared thermography: A non-invasive window into thermal physiology," *Comparative Biochemistry and Physiology Part A: Molecular & Integrative Physiology*, vol. 202, pp. 78–98, Dec. 2016.
- [15] J. Verstockt, S. Verspeek, F. Thiessen, W. A. Tjalma, L. Brochez, and G. Steenackers, "Skin Cancer Detection Using Infrared Thermography: Measurement Setup, Procedure and Equipment," *Sensors*, vol. 22, p. 3327, Jan. 2022.
- [16] J. Kerr, "Review of the effectiveness of infrared thermal imaging (thermography) for population screening and diagnostic testing of breast cancer," p. 60.
- [17] C. C. Joyal and M. Henry, "Long-Wave Infrared Functional Brain Imaging in Human: A Pilot Study," *The Open Neuroimaging Journal*, vol. 7, pp. 1–3, Jan. 2013.
- [18] R. Boonstra, C. J. Krebs, S. Boutin, and J. M. Eadie, "Finding Mammals Using Far-Infrared Thermal Imaging," *Journal of Mammalogy*, vol. 75, pp. 1063–1068, Nov.

1994.

- [19] R. Usamentiaga, P. Venegas, J. Guerediaga, L. Vega, J. Molleda, and F. G. Bulnes, “Infrared Thermography for Temperature Measurement and Non-Destructive Testing,” *Sensors*, vol. 14, pp. 12305–12348, July 2014.
- [20] E. Faye, F. Rebaudo, D. Yáñez-Cajo, S. Cauvy-Fraunié, and O. Dangles, “A toolbox for studying thermal heterogeneity across spatial scales: From unmanned aerial vehicle imagery to landscape metrics,” *Methods in Ecology and Evolution*, vol. 7, no. 4, pp. 437–446, 2016.
- [21] A. A. Gowen, B. K. Tiwari, P. J. Cullen, K. McDonnell, and C. P. O’Donnell, “Applications of thermal imaging in food quality and safety assessment,” *Trends in Food Science & Technology*, vol. 21, pp. 190–200, Apr. 2010.
- [22] C. A. MacCarley, B. M. Hemme, and L. Klein, “Evaluation of Infrared and Millimeter-wave Imaging Technologies Applied to Traffic Management,” *SAE Transactions*, vol. 109, pp. 373–382, 2000.
- [23] J. N. Munday, “Tackling Climate Change through Radiative Cooling,” *Joule*, vol. 3, pp. 2057–2060, Sept. 2019.
- [24] W. Li and S. Fan, “Nanophotonic control of thermal radiation for energy applications [Invited],” *Optics Express*, vol. 26, p. 15995, June 2018.
- [25] L. Mescia and A. Massaro, “New Trends in Energy Harvesting from Earth Long-Wave Infrared Emission,” *Advances in Materials Science and Engineering*, vol. 2014, p. e252879, Aug. 2014.
- [26] J. V. Taranik, M. F. Coolbaugh, and R. G. Vaughan, “An Overview of Thermal Infrared Remote Sensing with Applications to Geothermal and Mineral Exploration in the Great Basin, Western United States,” in *Remote Sensing and Spectral Geology* (R. Bedell, A. P. Crósta, and E. Grunsky, eds.), vol. 16, p. 0, Society of Economic Geologists, Jan. 2009.
- [27] D. Manolakis, M. Pieper, E. Truslow, R. Lockwood, A. Weisner, J. Jacobson, and T. Cooley, “Longwave Infrared Hyperspectral Imaging: Principles, Progress, and

- Challenges,” *IEEE Geoscience and Remote Sensing Magazine*, vol. 7, pp. 72–100, June 2019.
- [28] P. G. Lucey, T. J. Williams, M. Mignard, J. Julian, D. Kobubun, G. Allen, D. Hampton, W. Schaff, M. J. Schlangen, E. M. Winter, W. B. Kendall, A. D. Stocker, K. A. Horton, and A. P. Bowman, “AHI: An airborne long-wave infrared hyperspectral imager,” in *Airborne Reconnaissance XXII*, vol. 3431, pp. 36–43, SPIE, Nov. 1998.
- [29] V. Farley, A. Vallières, M. Chamberland, A. Villemaire, and J.-F. Legault, “Performance of the FIRSAT: A long-wave infrared hyperspectral imaging sensor,” in *Optically Based Biological and Chemical Detection for Defence III*, vol. 6398, pp. 164–174, SPIE, Oct. 2006.
- [30] D. Manolakis, S. Golowich, and R. S. DiPietro, “Long-Wave Infrared Hyperspectral Remote Sensing of Chemical Clouds: A focus on signal processing approaches,” *IEEE Signal Processing Magazine*, vol. 31, pp. 120–141, July 2014.
- [31] A. Pavelchek, R. G. Trissel, J. Plante, and S. Umbrasas, “Long-wave infrared (10-micron) free-space optical communication system,” in *Free-Space Laser Communication and Active Laser Illumination III*, vol. 5160, pp. 247–252, SPIE, Jan. 2004.
- [32] Z. Yang, O. Gulbitten, P. Lucas, T. Luo, and S. Jiang, “Long-Wave Infrared-Transmitting Optical Fibers,” *Journal of the American Ceramic Society*, vol. 94, no. 6, pp. 1761–1765, 2011.
- [33] S. P. Mahulikar, H. R. Sonawane, and G. Arvind Rao, “Infrared signature studies of aerospace vehicles,” *Progress in Aerospace Sciences*, vol. 43, pp. 218–245, Oct. 2007.
- [34] R. P. White, “Infrared deicing system for aircraft,” July 2000.
- [35] M. Taguchi, T. Fukuhara, T. Imamura, M. Nakamura, N. Iwagami, M. Ueno, M. Suzuki, G. L. Hashimoto, and K. Mitsuyama, “Longwave Infrared Camera on-board the Venus Climate Orbiter,” *Advances in Space Research*, vol. 40, pp. 861–868, Jan. 2007.
- [36] L. Nemes, “INFRARED EMISSION SPECTROSCOPY OF CARBON VAPORS

AND PLASMAS, A SHORT OVERVIEW,” *Contributions, Section of Natural, Mathematical and Biotechnical Sciences*, vol. 38, pp. 27–32, June 2017.

- [37] J. Cutts and R. Capps, “Space science applications of infrared detector technology: A review,” in *1990 Fourth International Conference on Advanced Infrared Detectors and Systems*, pp. 125–131, June 1990.
- [38] *Scientific Examination of Art: Modern Techniques in Conservation and Analysis*. National Academies Press, Jan. 2005.
- [39] J. Wilder, P. Phillips, C. Jiang, and S. Wiener, “Comparison of visible and infra-red imagery for face recognition,” in *Proceedings of the Second International Conference on Automatic Face and Gesture Recognition*, pp. 182–187, 1996.
- [40] T. Maeda, Y. Wang, R. Raskar, and A. Kadambi, “Thermal Non-Line-of-Sight Imaging,” in *2019 IEEE International Conference on Computational Photography (ICCP)*, (Tokyo, Japan), pp. 1–11, IEEE, May 2019.
- [41] C. M. Cornelius and J. P. Dowling, “Modification of Planck blackbody radiation by photonic band-gap structures,” *Physical Review A*, vol. 59, pp. 4736–4746, June 1999.
- [42] J.-J. Greffet, R. Carminati, K. Joulain, J.-P. Mulet, S. Mainguy, and Y. Chen, “Coherent emission of light by thermal sources,” *Nature*, vol. 416, pp. 61–64, Mar. 2002.
- [43] M. Laroche, C. Arnold, F. Marquier, R. Carminati, J.-J. Greffet, S. Collin, N. Bardou, and J.-L. Pelouard, “Highly directional radiation generated by a tungsten thermal source,” *Optics Letters*, vol. 30, pp. 2623–2625, Oct. 2005.
- [44] M. Makhsiyani, P. Bouchon, J. Jaeck, J.-L. Pelouard, and R. Häidar, “Shaping the spatial and spectral emissivity at the diffraction limit,” *Applied Physics Letters*, vol. 107, p. 251103, Dec. 2015.
- [45] L. Abou-Hamdan, C. Li, R. Haidar, V. Krachmalnicoff, P. Bouchon, and Y. D. Wilde, “Hybrid modes in a single thermally excited asymmetric dimer antenna,” *Optics Letters*, vol. 46, pp. 981–984, Mar. 2021.

- [46] J. S. Chivian, R. N. Claytor, and D. D. Eden, “Infrared holography at $10.6\mu\text{m}$,” *Applied Physics Letters*, vol. 15, pp. 123–125, Aug. 1969.
- [47] G. Rousset, J. Primot, and J. C. Fontanella, “Visible wavefront sensor development,” *LEST Foundation, Technical Report*, vol. 28, pp. 17–33, Jan. 1987.
- [48] S. Rotter and S. Gigan, “Light fields in complex media: Mesoscopic scattering meets wave control,” *Reviews of Modern Physics*, vol. 89, p. 015005, Mar. 2017.
- [49] M. Rueckel, J. A. Mack-Bucher, and W. Denk, “Adaptive wavefront correction in two-photon microscopy using coherence-gated wavefront sensing,” *Proceedings of the National Academy of Sciences*, vol. 103, pp. 17137–17142, Nov. 2006.
- [50] O. Katz, P. Heidmann, M. Fink, and S. Gigan, “Non-invasive single-shot imaging through scattering layers and around corners via speckle correlations,” *Nature Photonics*, vol. 8, pp. 784–790, Oct. 2014.
- [51] P. Berto, H. Rigneault, and M. Guillon, “Wavefront sensing with a thin diffuser,” *Optics Letters*, vol. 42, p. 5117, Dec. 2017.
- [52] Y. Park, C. Depeursinge, and G. Popescu, “Quantitative phase imaging in biomedicine,” *Nature Photonics*, vol. 12, pp. 578–589, Oct. 2018.
- [53] W. T. Chen, A. Y. Zhu, V. Sanjeev, M. Khorasaninejad, Z. Shi, E. Lee, and F. Capasso, “A broadband achromatic metalens for focusing and imaging in the visible,” *Nature Nanotechnology*, vol. 13, pp. 220–226, Mar. 2018.
- [54] P. Lalanne and P. Chavel, “Metalenses at visible wavelengths: Past, present, perspectives,” *Laser & Photonics Reviews*, vol. 11, no. 3, p. 1600295, 2017.
- [55] C. N. H. Candia and B. Gutiérrez-Medina, “Direct Imaging of Phase Objects Enables Conventional Deconvolution in Bright Field Light Microscopy,” *PLOS ONE*, vol. 9, p. e89106, Feb. 2014.
- [56] G. Popescu, “Chapter 5 Quantitative Phase Imaging of Nanoscale Cell Structure and Dynamics,” in *Methods in Cell Biology*, vol. 90, pp. 87–115, Elsevier, 2008.
- [57] W. J. Croft, *Under the Microscope: A Brief History of Microscopy*. World Scientific,

2006.

- [58] “Micrographia : Or, Some physiological descriptions of minute bodies made by magnifying glasses. With observations and inquiries thereupon.” <https://digital.sciencehistory.org/works/9g54xj51s>.
- [59] H. Gest, “The discovery of microorganisms by Robert Hooke and Antoni Van Leeuwenhoek, fellows of the Royal Society,” *Notes and Records of the Royal Society of London*, vol. 58, pp. 187–201, May 2004.
- [60] G. Popescu, *Quantitative Phase Imaging of Cells and Tissues*. McGraw-Hill Biophotonics, New York: McGraw-Hill, 2011.
- [61] E. Abbe, “Beiträge zur Theorie des Mikroskops und der mikroskopischen Wahrnehmung,” *Archiv für Mikroskopische Anatomie*, vol. 9, pp. 413–468, Dec. 1873.
- [62] K. I. Willig, R. R. Kellner, R. Medda, B. Hein, S. Jakobs, and S. W. Hell, “Nanoscale resolution in GFP-based microscopy,” *Nature Methods*, vol. 3, pp. 721–723, Sept. 2006.
- [63] E. Betzig, G. H. Patterson, R. Sougrat, O. W. Lindwasser, S. Olenych, J. S. Bonifacino, M. W. Davidson, J. Lippincott-Schwartz, and H. F. Hess, “Imaging intracellular fluorescent proteins at nanometer resolution,” *Science (New York, N.Y.)*, vol. 313, pp. 1642–1645, Sept. 2006.
- [64] M. J. Rust, M. Bates, and X. Zhuang, “Sub-diffraction-limit imaging by stochastic optical reconstruction microscopy (STORM),” *Nature Methods*, vol. 3, pp. 793–796, Oct. 2006.
- [65] M. G. L. Gustafsson, “Nonlinear structured-illumination microscopy: Wide-field fluorescence imaging with theoretically unlimited resolution,” *Proceedings of the National Academy of Sciences*, vol. 102, pp. 13081–13086, Sept. 2005.
- [66] E. Betzig, J. K. Trautman, T. D. Harris, J. S. Weiner, and R. L. Kostelak, “Breaking the Diffraction Barrier: Optical Microscopy on a Nanometric Scale,” *Science*, vol. 251, pp. 1468–1470, Mar. 1991.

- [67] J. R. Lakowicz, ed., *Principles of Fluorescence Spectroscopy*. Boston, MA: Springer US, 2006.
- [68] R. Y. Tsien, “The green fluorescent protein,” *Annual Review of Biochemistry*, vol. 67, pp. 509–544, 1998.
- [69] J. B. Pawley, ed., *Handbook Of Biological Confocal Microscopy*. Boston, MA: Springer US, 2006.
- [70] M. Marvin, “Microscopy apparatus,” Dec. 1961.
- [71] A. Dubois and C. Boccara, “[Full-field OCT],” *Medecine sciences*, vol. 22, pp. 859–864, Oct. 2006.
- [72] V. Ronchi, “Forty Years of History of a Grating Interferometer,” *Applied Optics*, vol. 3, pp. 437–451, Apr. 1964.
- [73] F. Zernike, “Phase contrast, a new method for the microscopic observation of transparent objects,” *Physica*, vol. 9, pp. 686–698, July 1942.
- [74] F. Zernike, “Phase contrast, a new method for the microscopic observation of transparent objects part II,” *Physica*, vol. 9, pp. 974–986, Dec. 1942.
- [75] M. Born and E. Wolf, *Principles of Optics: Electromagnetic Theory of Propagation, Interference and Diffraction of Light*. Elsevier, June 2013.
- [76] D. Gabor, “A New Microscopic Principle,” *Nature*, vol. 161, pp. 777–778, May 1948.
- [77] “File:Holograph-record.svg - Wikipedia.” <https://commons.wikimedia.org/wiki/File:Holograph-record.svg>.
- [78] R. Collier, *Optical Holography*. Elsevier, June 2013.
- [79] “Holography,” *Wikipedia*, Oct. 2022.
- [80] E. N. Leith and J. Upatnieks, “Wavefront Reconstruction with Continuous-Tone Objects*,” *Journal of the Optical Society of America*, vol. 53, p. 1377, Dec. 1963.

- [81] E. N. Leith and J. Upatnieks, "Wavefront Reconstruction with Diffused Illumination and Three-Dimensional Objects*," *Journal of the Optical Society of America*, vol. 54, p. 1295, Nov. 1964.
- [82] E. N. Leith and J. Upatnieks, "Photography by Laser," *Scientific American*, vol. 212, no. 6, pp. 24–35, 1965.
- [83] Yu. N. Denisyuk and L. M. Alexandrova, "My Way in Holography," *Leonardo*, vol. 25, no. 5, pp. 425–430, 1992.
- [84] T. Huang, "Digital holography," *Proceedings of the IEEE*, vol. 59, pp. 1335–1346, Sept. 1971.
- [85] L. Yaroslavsky and J. Astola, *Introduction to Digital Holography*. Bentham Science Publishers, 2009.
- [86] J. W. Cooley and J. W. Tukey, "An algorithm for the machine calculation of complex Fourier series," *Mathematics of computation*, vol. 19, no. 90, pp. 297–301, 1965.
- [87] G. Strang, "Wavelets," *American Scientist*, vol. 82, no. 3, pp. 250–255, 1994.
- [88] "HOLOPHILE, INC., The History and Development of Holography, hologram, holograms, holography, holography exhibitions, holographic images, 3-D, 3-dimensional images, Hologram, Holograms, Holography, Holography Exhibitions, Holographic Images, 3-D, 3-Dimensional Images." <http://holophile.com/history.htm>.
- [89] E. N. Leith and J. Upatnieks, "Reconstructed Wavefronts and Communication Theory*," *JOSA*, vol. 52, pp. 1123–1130, Oct. 1962.
- [90] T. Tishko, T. Dmitry, and T. Vladimir, *Holographic Microscopy of Phase Microscopic Objects: Theory and Practice*. WORLD SCIENTIFIC, May 2011.
- [91] J. W. Goodman and R. W. Lawrence, "DIGITAL IMAGE FORMATION FROM ELECTRONICALLY DETECTED HOLOGRAMS," *Applied Physics Letters*, vol. 11, pp. 77–79, Aug. 1967.
- [92] U. Schnars and W. Jüptner, "Direct recording of holograms by a CCD target and

- numerical reconstruction,” *Applied Optics*, vol. 33, pp. 179–181, Jan. 1994.
- [93] S. Y. Suck, *Digital Heterodyne Holography for Plasmonic Nanostructures*. PhD thesis, Université Pierre et Marie Curie - Paris VI, Nov. 2011.
- [94] N. Rahbany, I. Izeddin, V. Krachmalnicoff, R. Carminati, G. Tessier, and Y. De Wilde, “One-Shot Measurement of the Three-Dimensional Electromagnetic Field Scattered by a Subwavelength Aperture Tip Coupled to the Environment,” *ACS Photonics*, vol. 5, pp. 1539–1545, Apr. 2018.
- [95] C. J. Mann, L. Yu, C.-M. Lo, and M. K. Kim, “High-resolution quantitative phase-contrast microscopy by digital holography,” *Optics Express*, vol. 13, pp. 8693–8698, Oct. 2005.
- [96] E. Cuche, F. Bevilacqua, and C. Depeursinge, “Digital holography for quantitative phase-contrast imaging,” *Optics Letters*, vol. 24, p. 291, Mar. 1999.
- [97] W. Xu, M. H. Jericho, I. A. Meinertzhagen, and H. J. Kreuzer, “Digital in-line holography for biological applications,” *Proceedings of the National Academy of Sciences*, vol. 98, pp. 11301–11305, Sept. 2001.
- [98] V. Balasubramani, M. Kujawińska, C. Allier, V. Anand, C.-J. Cheng, C. Depeursinge, N. Hai, S. Juodkazis, J. Kalkman, A. Kuś, M. Lee, P. J. Magistretti, P. Marquet, S. H. Ng, J. Rosen, Y. K. Park, and M. Ziemczonok, “Roadmap on Digital Holography-Based Quantitative Phase Imaging,” *Journal of Imaging*, vol. 7, p. 252, Dec. 2021.
- [99] G. Popescu, Y. Park, N. Lue, C. Best-Popescu, L. Deflores, R. R. Dasari, M. S. Feld, and K. Badizadegan, “Optical imaging of cell mass and growth dynamics,” *American Journal of Physiology-Cell Physiology*, vol. 295, pp. C538–C544, Aug. 2008.
- [100] E. Absil, G. Tessier, M. Gross, M. Atlan, N. Warnasooriya, S. Suck, M. Coppey-Moisan, and D. Fournier, “Photothermal heterodyne holography of gold nanoparticles,” *Optics Express*, vol. 18, pp. 780–786, Jan. 2010.
- [101] N. Warnasooriya, F. Joud, P. Bun, G. Tessier, M. Coppey-Moisan, P. Desbiolles,

- M. Atlan, M. Abboud, and M. Gross, "Imaging gold nanoparticles in living cell environments using heterodyne digital holographic microscopy," *Optics Express*, vol. 18, pp. 3264–3273, Feb. 2010.
- [102] J. Lu, Y. Zeng, X. Chang, Y. Hong, and X. Hu, "Quantitative phase imaging of cells through turbid media based on infrared digital holographic microscopy," *Applied Physics Express*, vol. 14, p. 035004, Feb. 2021.
- [103] A. M. Beigzadeh, M. R. R. Vaziri, and F. Ziaie, "Modelling of a holographic interferometry based calorimeter for radiation dosimetry," *Nuclear Instruments and Methods in Physics Research Section A: Accelerators, Spectrometers, Detectors and Associated Equipment*, vol. 864, pp. 40–49, Aug. 2017.
- [104] R. L. Powell and K. A. Stetson, "Interferometric Vibration Analysis by Wavefront Reconstruction," *JOSA*, vol. 55, pp. 1593–1598, Dec. 1965.
- [105] Y. Kuznetsova, A. Neumann, and S. R. J. Brueck, "Imaging interferometric microscopy—approaching the linear systems limits of optical resolution," *Optics Express*, vol. 15, pp. 6651–6663, May 2007.
- [106] M. Lang and H. Eschler, "Gigabyte capacities for holographic memories," *Optics & Laser Technology*, vol. 6, pp. 219–224, Oct. 1974.
- [107] J. E. Baldwin and C. A. Haniff, "The application of interferometry to optical astronomical imaging," *Philosophical Transactions of the Royal Society of London. Series A: Mathematical, Physical and Engineering Sciences*, May 2002.
- [108] P. Hayward, *Culture, Technology & Creativity in the Late Twentieth Century*. Indiana University Press, 1990.
- [109] M. Paturzo, V. Pagliarulo, V. Bianco, P. Memmolo, L. Miccio, F. Merola, and P. Ferraro, "Digital Holography, a metrological tool for quantitative analysis: Trends and future applications," *Optics and Lasers in Engineering*, vol. 104, pp. 32–47, May 2018.
- [110] T. Tahara, X. Quan, R. Otani, Y. Takaki, and O. Matoba, "Digital holography and its multidimensional imaging applications: A review," *Microscopy*, vol. 67, pp. 55–67,

Apr. 2018.

- [111] O. Matoba, X. Quan, P. Xia, Y. Awatsuji, and T. Nomura, “Multimodal Imaging Based on Digital Holography,” *Proceedings of the IEEE*, vol. 105, pp. 906–923, May 2017.
- [112] B. Javidi, A. Carnicer, A. Anand, G. Barbastathis, W. Chen, P. Ferraro, J. Goodman, R. Horisaki, K. Khare, M. Kujawińska, R. Leitgeb, P. Marquet, T. Nomura, A. Ozcan, Y. Park, G. Pedrini, P. Picart, J. Rosen, G. Saavedra Tortosa, N. T. Shaked, A. Stern, E. Tajahuerce, L. Tian, G. Wetzstein, and M. Yamaguchi, “Roadmap on digital holography,” Oct. 2021.
- [113] P. Ferraro, “Infrared Digital Holography as New 3D Imaging Tool for First Responders and Firefighters: Recent Achievements and Perspectives,” in *CLEO: 2014*, (San Jose, California), p. AW1P.6, OSA, 2014.
- [114] A. Pelagotti, M. Paturzo, A. Geltrude, M. Locatelli, R. Meucci, P. Poggi, and P. Ferraro, “Digital holography for 3D imaging and display in the IR range: Challenges and opportunities,” *3D Research*, vol. 1, p. 6, Nov. 2011.
- [115] T. L. Nguyen, S. Pradeep, R. L. Judson-Torres, J. Reed, M. A. Teitell, and T. A. Zangle, “Quantitative Phase Imaging: Recent Advances and Expanding Potential in Biomedicine,” *ACS Nano*, vol. 16, pp. 11516–11544, Aug. 2022.
- [116] B. C. Platt and R. Shack, “History and principles of Shack-Hartmann wavefront sensing,” *Journal of Refractive Surgery (Thorofare, N.J.: 1995)*, vol. 17, no. 5, pp. S573–577, 2001 Sep-Oct.
- [117] N. Bareket and L. T. James, “Wavefront Sensors And Deformable Mirrors For Visible Wavelengths,” in *1980 Technical Symposium East* (W. J. Cuneo, ed.), (Washington, D.C.), pp. 4–13, Aug. 1980.
- [118] F. Roddier, *Adaptive Optics in Astronomy*. Cambridge University Press, June 1999.
- [119] R. J. Collier, “Program of the 1971 Spring Meeting of the Optical Society of America,” *Journal of the Optical Society of America*, vol. 61, p. 648, May 1971.

- [120] P.-T. R. G. Ernst Dorn, *Zeitschrift für Instrumentenkunde*. Springer, 1904.
- [121] E. Moreno-Barriuso and R. Navarro, “Laser Ray Tracing versus Hartmann–Shack sensor for measuring optical aberrations in the human eye,” *JOSA A*, vol. 17, pp. 974–985, June 2000.
- [122] T. Kohnen and D. D. Koch, *Cataract and Refractive Surgery*. Springer Science & Business Media, Sept. 2006.
- [123] V. F. Pamplona, A. Mohan, M. M. Oliveira, and R. Raskar, “NETRA: Interactive display for estimating refractive errors and focal range,” *ACM Transactions on Graphics*, vol. 29, pp. 77:1–77:8, July 2010.
- [124] B. Masson, L. McMackin, J. Wissler, and K. Bishop, “Study of a round jet using a Shack-Hartmann wavefront sensor,” in *33rd Aerospace Sciences Meeting and Exhibit*, (Reno,NV,U.S.A.), American Institute of Aeronautics and Astronautics, Jan. 1995.
- [125] P. Feautrier, P. Y. Kern, R. J. Dorn, G. Rousset, P. Rabou, S. Laurent, J.-L. Lizon, E. Stadler, Y. Magnard, O. Rondeaux, M. Cochard, D. Rabaud, A. Delboulbe, P. Puget, and N. N. Hubin, “NAOS visible wavefront sensor,” in *Adaptive Optical Systems Technology*, vol. 4007, pp. 396–407, SPIE, July 2000.
- [126] J. W. Hardy, “Adaptive optics: A progress review,” in *San Diego, '91, San Diego, CA* (M. A. Ealey, ed.), (San Diego, CA), pp. 2–17, Dec. 1991.
- [127] P. Feautrier, J.-L. Gach, M. Downing, P. Jorden, J. Kolb, J. Rothman, T. Fusco, P. Balard, E. Stadler, C. Guillaume, D. Boutolleau, G. Destefanis, N. Lhermet, O. Pacaud, M. Vuillermet, A. Kerlain, N. Hubin, J. Reyes, M. Kasper, O. Ivert, W. Suske, A. Walker, M. Skegg, S. Derelle, J. Deschamps, C. Robert, N. Vedrenne, F. Chazalet, J. Tanchon, T. Trollier, A. Ravex, G. Zins, P. Kern, T. Moulin, and O. Preis, “Advances in detector technologies for visible and infrared wavefront sensing,” in *SPIE Astronomical Telescopes + Instrumentation* (B. L. Ellerbroek, E. Marchetti, and J.-P. Véran, eds.), (Amsterdam, , Netherlands), pp. 84470Q–84470Q–33, Sept. 2012.
- [128] W. J. Bates, “A wavefront shearing interferometer,” *Proceedings of the Physical So-*

ciety, vol. 59, p. 940, Nov. 1947.

- [129] J. Primot and L. Sogno, “Achromatic three-wave (or more) lateral shearing interferometer,” *JOSA A*, vol. 12, pp. 2679–2685, Dec. 1995.
- [130] J. Primot and N. Guérineau, “Extended Hartmann test based on the pseudoguiding property of a Hartmann mask completed by a phase chessboard,” *Applied Optics*, vol. 39, pp. 5715–5720, Nov. 2000.
- [131] J.-C. Chanteloup, “Multiple-wave lateral shearing interferometry for wave-front sensing,” *Applied Optics*, vol. 44, p. 1559, Mar. 2005.
- [132] D. Huang, K. A. Leslie, D. Guest, O. Yeshcheulova, I. J. Roy, M. Piva, G. Moriceau, T. A. Zangle, R. S. Lo, M. A. Teitell, and J. Reed, “High-Speed Live-Cell Interferometry: A New Method for Quantifying Tumor Drug Resistance and Heterogeneity,” *Analytical Chemistry*, vol. 90, pp. 3299–3306, Mar. 2018.
- [133] H. Yu, J. Park, K. Lee, J. Yoon, K. Kim, S. Lee, and Y. Park, “Recent advances in wavefront shaping techniques for biomedical applications,” *Current Applied Physics*, vol. 15, pp. 632–641, May 2015.
- [134] P. Bon, G. Maucort, B. Wattellier, and S. Monneret, “Quadriwave lateral shearing interferometry for quantitative phase microscopy of living cells,” *Optics Express*, vol. 17, pp. 13080–13094, July 2009.
- [135] P. Bon, N. Bourg, S. Lécart, S. Monneret, E. Fort, J. Wenger, and S. Lévêque-Fort, “Three-dimensional nanometre localization of nanoparticles to enhance super-resolution microscopy,” *Nature Communications*, vol. 6, p. 7764, July 2015.
- [136] K. Underwood, J. C. Wyant, and C. L. Koliopoulos, “Self-Referencing Wavefront Sensor,” in *Wavefront Sensing*, vol. 0351, pp. 108–114, SPIE, Aug. 1983.
- [137] M. E. Riley and M. A. Gusinow, “Laser beam divergence utilizing a lateral shearing interferometer,” *Applied Optics*, vol. 16, pp. 2753–2756, Oct. 1977.
- [138] G. Baffou, P. Bon, J. Savatier, J. Polleux, M. Zhu, M. Merlin, H. Rigneault, and S. Monneret, “Thermal Imaging of Nanostructures by Quantitative Optical Phase

- Analysis,” *ACS Nano*, vol. 6, pp. 2452–2458, Mar. 2012.
- [139] G. Baffou, J. Polleux, H. Rigneault, and S. Monneret, “Super-Heating and Micro-Bubble Generation around Plasmonic Nanoparticles under cw Illumination,” *The Journal of Physical Chemistry C*, vol. 118, pp. 4890–4898, Mar. 2014.
- [140] P. Bon, S. Aknoun, S. Monneret, and B. Wattellier, “Enhanced 3D spatial resolution in quantitative phase microscopy using spatially incoherent illumination,” *Optics Express*, vol. 22, pp. 8654–8671, Apr. 2014.
- [141] G. Baffou, E. B. Ureña, P. Berto, S. Monneret, R. Quidant, and H. Rigneault, “Deterministic temperature shaping using plasmonic nanoparticle assemblies,” *Nanoscale*, vol. 6, pp. 8984–8989, July 2014.
- [142] S. Khadir, P. Bon, D. Vignaud, E. Galopin, N. McEvoy, D. McCloskey, S. Monneret, and G. Baffou, “Optical Imaging and Characterization of Graphene and Other 2D Materials Using Quantitative Phase Microscopy,” *ACS Photonics*, vol. 4, pp. 3130–3139, Dec. 2017.
- [143] S. Khadir, S. Khadir, D. Andrén, P. C. Chaumet, S. Monneret, N. Bonod, M. Käll, A. Sentenac, and G. Baffou, “Full optical characterization of single nanoparticles using quantitative phase imaging,” *Optica*, vol. 7, pp. 243–248, Mar. 2020.
- [144] J. P. Gordon, H. J. Zeiger, and C. H. Townes, “The Maser—New Type of Microwave Amplifier, Frequency Standard, and Spectrometer,” *Physical Review*, vol. 99, pp. 1264–1274, Aug. 1955.
- [145] T. H. Maiman, “Stimulated Optical Radiation in Ruby,” *Nature*, vol. 187, pp. 493–494, Aug. 1960.
- [146] L. Allen and D. G. C. Jones, “An analysis of the granularity of scattered optical maser light,” *Physics Letters*, vol. 7, pp. 321–323, Dec. 1963.
- [147] J. W. Goodman, “Some fundamental properties of speckle*,” *JOSA*, vol. 66, pp. 1145–1150, Nov. 1976.
- [148] D. Gabor, “Laser Speckle and Its Elimination,” *IBM Journal of Research and Devel-*

opment, vol. 14, pp. 509–514, Sept. 1970.

- [149] A. Ishimaru, *Wave Propagation and Scattering in Random Media. Volume 1 - Single Scattering and Transport Theory*, vol. 1. Jan. 1978.
- [150] A. P. Gibson, J. C. Hebden, and S. R. Arridge, “Recent advances in diffuse optical imaging,” *Physics in Medicine & Biology*, vol. 50, p. R1, Feb. 2005.
- [151] I. Freund, “Looking through walls and around corners,” *Physica A: Statistical Mechanics and its Applications*, vol. 168, pp. 49–65, Sept. 1990.
- [152] J. W. Goodman, *Statistical Optics*. John Wiley & Sons, May 2015.
- [153] A. Labeyrie, “Attainment of Diffraction Limited Resolution in Large Telescopes by Fourier Analysing Speckle Patterns in Star Images,” *Astronomy and Astrophysics*, vol. 6, p. 85, May 1970.
- [154] D. Huang, E. A. Swanson, C. P. Lin, J. S. Schuman, W. G. Stinson, W. Chang, M. R. Hee, T. Flotte, K. Gregory, C. A. Puliafito, and J. G. Fujimoto, “Optical Coherence Tomography,” *Science*, vol. 254, pp. 1178–1181, Nov. 1991.
- [155] W. B. Bridges, P. T. Brunner, S. P. Lazzara, T. A. Nussmeier, T. R. O’Meara, J. A. Sanguinet, and W. P. Brown, “Coherent Optical Adaptive Techniques,” *Applied Optics*, vol. 13, pp. 291–300, Feb. 1974.
- [156] J. W. Hardy, *Adaptive Optics for Astronomical Telescopes*. Oxford University Press, 1998.
- [157] J. C. Dainty, *Laser Speckle and Related Phenomena*. Springer Science & Business Media, Dec. 2013.
- [158] M. Fink, “Time reversal of ultrasonic fields. I. Basic principles,” *IEEE Transactions on Ultrasonics, Ferroelectrics, and Frequency Control*, vol. 39, pp. 555–566, Sept. 1992.
- [159] I. M. Vellekoop and A. P. Mosk, “Focusing coherent light through opaque strongly scattering media,” *Optics Letters*, vol. 32, pp. 2309–2311, Aug. 2007.

- [160] I. M. Vellekoop, “Controlling the propagation of light in disordered scattering media,” July 2008.
- [161] I. M. Vellekoop, A. Lagendijk, and A. P. Mosk, “Exploiting disorder for perfect focusing,” *Nature Photonics*, vol. 4, pp. 320–322, May 2010.
- [162] N. Savage, “Digital spatial light modulators,” *Nature Photonics*, vol. 3, pp. 170–172, Mar. 2009.
- [163] I. M. Vellekoop and A. P. Mosk, “Universal Optimal Transmission of Light Through Disordered Materials,” *Physical Review Letters*, vol. 101, p. 120601, Sept. 2008.
- [164] E. N. Leith and J. Upatnieks, “Holographic Imagery Through Diffusing Media,” *Journal of the Optical Society of America*, vol. 56, p. 523, Apr. 1966.
- [165] Z. Yaqoob, D. Psaltis, M. S. Feld, and C. Yang, “Optical phase conjugation for turbidity suppression in biological samples,” *Nature Photonics*, vol. 2, pp. 110–115, Feb. 2008.
- [166] S. M. Popoff, G. Lerosey, R. Carminati, M. Fink, A. C. Boccara, and S. Gigan, “Measuring the Transmission Matrix in Optics: An Approach to the Study and Control of Light Propagation in Disordered Media,” *Physical Review Letters*, vol. 104, p. 100601, Mar. 2010.
- [167] C. Park, J.-H. Park, C. Rodriguez, H. Yu, M. Kim, K. Jin, S. Han, J. Shin, S. H. Ko, K. T. Nam, Y.-H. Lee, Y.-H. Cho, and Y. Park, “Full-Field Subwavelength Imaging Using a Scattering Superlens,” *Physical Review Letters*, vol. 113, p. 113901, Sept. 2014.
- [168] S. Popoff, G. Lerosey, M. Fink, A. C. Boccara, and S. Gigan, “Image transmission through an opaque material,” *Nature Communications*, vol. 1, p. 81, Sept. 2010.
- [169] S. Feng, C. Kane, P. A. Lee, and A. D. Stone, “Correlations and Fluctuations of Coherent Wave Transmission through Disordered Media,” *Physical Review Letters*, vol. 61, pp. 834–837, Aug. 1988.
- [170] I. Freund, M. Rosenbluh, and S. Feng, “Memory Effects in Propagation of Optical

Waves through Disordered Media,” *Physical Review Letters*, vol. 61, pp. 2328–2331, Nov. 1988.

- [171] L. Devaud, M. Guillon, I. Gusachenko, and S. Gigan, “Chromato-axial memory effect in step-index multimode fibers,” *APL Photonics*, vol. 6, p. 126105, Dec. 2021.
- [172] J.-P. Thirion, “Image matching as a diffusion process: An analogy with Maxwell’s demons,” *Medical Image Analysis*, vol. 2, pp. 243–260, Sept. 1998.
- [173] X. Pennec, P. Cachier, and N. Ayache, “Understanding the “Demon’s Algorithm”: 3D Non-rigid Registration by Gradient Descent,” in *Medical Image Computing and Computer-Assisted Intervention – MICCAI’99* (G. Goos, J. Hartmanis, J. van Leeuwen, C. Taylor, and A. Colchester, eds.), vol. 1679, pp. 597–605, Berlin, Heidelberg: Springer Berlin Heidelberg, 1999.
- [174] T. Vercauteren, X. Pennec, A. Perchant, and N. Ayache, “Diffeomorphic demons: Efficient non-parametric image registration,” *NeuroImage*, vol. 45, pp. S61–72, Mar. 2009.
- [175] “Estimate displacement field that aligns two 2-D or 3-D images - MATLAB imregdemons - MathWorks France.” <https://fr.mathworks.com/help/images/ref/imregdemons.html>.
- [176] B. Redding, S. F. Liew, R. Sarma, and H. Cao, “Compact spectrometer based on a disordered photonic chip,” *Nature Photonics*, vol. 7, pp. 746–751, Sept. 2013.
- [177] S. K. Sahoo, D. Tang, and C. Dang, “Single-shot multispectral imaging with a monochromatic camera,” *Optica*, vol. 4, p. 1209, Oct. 2017.
- [178] H. Cao, “Perspective on speckle spectrometers,” *Journal of Optics*, vol. 19, p. 060402, June 2017.
- [179] Z. Xu, Z. Wang, M. E. Sullivan, D. J. Brady, S. H. Foulger, and A. Adibi, “Multimodal multiplex spectroscopy using photonic crystals,” *Optics Express*, vol. 11, p. 2126, Sept. 2003.
- [180] T. S. Kao, S. D. Jenkins, J. Ruostekoski, and N. I. Zheludev, “Coherent Control of

- Nanoscale Light Localization in Metamaterial: Creating and Positioning Isolated Subwavelength Energy Hot Spots,” *Physical Review Letters*, vol. 106, p. 085501, Feb. 2011.
- [181] T. Čižmár, M. Mazilu, and K. Dholakia, “In situ wavefront correction and its application to micromanipulation,” *Nature Photonics*, vol. 4, pp. 388–394, June 2010.
- [182] S. M. Popoff, A. Aubry, G. Lerosey, M. Fink, A. C. Boccara, and S. Gigan, “Exploiting the Time-Reversal Operator for Adaptive Optics, Selective Focusing, and Scattering Pattern Analysis,” *Physical Review Letters*, vol. 107, p. 263901, Dec. 2011.
- [183] M. P. Georges, “Speckle interferometry in the long-wave infrared for combining holography and thermography in a single sensor: Applications to nondestructive testing: The FANTOM Project,” in *Optical Measurement Systems for Industrial Inspection IX*, vol. 9525, pp. 343–357, SPIE, June 2015.
- [184] J.-F. Vandenrijt, C. Thizy, I. Alexeenko, G. Pedrini, J. Rochet, B. Vollheim, I. Jorge, P. Venegas, I. López, W. Osten, and M. P. Georges, “Mobile speckle interferometer in the long-wave infrared for aeronautical nondestructive testing in field conditions,” *Optical Engineering*, vol. 52, p. 101903, Apr. 2013.
- [185] H.-C. Liu and S. Zhang, “Computational ghost imaging of hot objects in long-wave infrared range,” *Applied Physics Letters*, vol. 111, p. 031110, July 2017.
- [186] M. Georges, J.-F. Vandenrijt, C. Thizy, I. Alexeenko, G. Pedrini, J. Rochet, B. Vollheim, I. Jorge, P. Venegas, I. Lopez, and W. Osten, “Simultaneous Temperature and Deformations Measurements Using Long-Wave Infrared Speckle Interferometry: A Novel Hybrid Technique for Industrial Nondestructive Testing,” in *Fringe 2013* (W. Osten, ed.), (Berlin, Heidelberg), pp. 917–920, Springer, 2014.
- [187] J.-F. Vandenrijt, C. Thizy, and M. P. Georges, “Vibration analysis by speckle interferometry with CO₂ lasers and microbolometers arrays,” in *Imaging and Applied Optics 2014 (2014)*, Paper DTh4B.8, p. DTh4B.8, Optica Publishing Group, July 2014.
- [188] W. Boucher, G. Bourgeois, M. Deprez, E. Homassel, and B. Wattellier, “Recent

developments in IR metrology using quadri wave lateral shearing interferometry,” in *Optifab 2015*, vol. 9633, pp. 494–500, SPIE, Oct. 2015.

- [189] M. Georges, “Long-Wave Infrared Digital Holography,” in *New Techniques in Digital Holography*, ch. 6, pp. 219–254, John Wiley & Sons, Ltd, 2015.
- [190] J.-F. Vandenrijt, C. Thizy, P. Queeckers, F. Dubois, D. Doyle, and M. P. Georges, “Long-wave infrared digital holographic interferometry with diffuser or point source illuminations for measuring deformations of aspheric mirrors,” *Optical Engineering*, vol. 53, p. 112309, Apr. 2014.
- [191] A. Dixit, A. K. Agarwal, and P. K. Dwivedi, “Optical Performance Evaluation of Infrared Microlens by Direct Wavefront Sensing at LWIR Wavelength,” in *ICOL-2019* (K. Singh, A. K. Gupta, S. Khare, N. Dixit, and K. Pant, eds.), Springer Proceedings in Physics, (Singapore), pp. 303–306, Springer, 2021.
- [192] C. Kiiikka, D. R. Neal, J. Kincade, R. Bernier, T. Hull, D. Chaney, S. Farrer, J. Dixon, A. Causey, and S. Strohl, “The JWST infrared Scanning Shack Hartman System: A new in-process way to measure large mirrors during optical fabrication at Tinsley,” in *Space Telescopes and Instrumentation I: Optical, Infrared, and Millimeter*, vol. 6265, pp. 1107–1117, SPIE, July 2006.
- [193] A. Kudryashov, A. Alexandrov, A. Rukosuev, V. Samarkin, P. Galarneau, S. Turbide, and F. Châteauneuf, “Extremely high-power CO₂ laser beam correction,” *Applied Optics*, vol. 54, pp. 4352–4358, May 2015.
- [194] S. Divitt, D. F. Gardner, and A. T. Watnik, “Imaging around corners in the mid-infrared using speckle correlations,” *Optics Express*, vol. 28, p. 11051, Apr. 2020.
- [195] A. T. Watnik and D. F. Gardner, “Wavefront Sensing in Deep Turbulence,” *Optics and Photonics News*, vol. 29, pp. 38–45, Oct. 2018.
- [196] “Methods and apparatuses for wavefront reconstruction.” https://scholar.google.fr/citations?view_op=view_citation&hl=fr&user=bbqh_NgAAAAJ&sortby=pubdate&citation_for_view=bbqh_NgAAAAJ:1sJd4Hv_s6UC.
- [197] “Phasics.” <https://phasics.com>.

- [198] A. Bhattacharya, *Design of a Stable Optical System with an Injection-Locked Laser to Cool Quantum Gases to Ultracold Temperatures*. Thesis, Dept. of Physics, Apr. 2019.
- [199] “Ultrasound,” *Wikipedia*, Mar. 2023.
- [200] S. A. El-said and A. T. Azar, “Speckles Suppression Techniques for Ultrasound Images,” *Journal of Medical Imaging and Radiation Sciences*, vol. 43, pp. 200–213, Dec. 2012.
- [201] J. S. Lee, L. Jurkevich, P. Dewaele, P. Wambacq, and A. Oosterlinck, “Speckle filtering of synthetic aperture radar images: A review,” *Remote Sensing Reviews*, vol. 8, pp. 313–340, Feb. 1994.
- [202] K. Pearson, “The Problem of the Random Walk,” *Nature*, vol. 72, pp. 294–294, July 1905.
- [203] J. W. Goodman, *Speckle Phenomena in Optics: Theory and Applications*. Roberts and Company Publishers, 2007.
- [204] A. Goetschy and R. Pierrat, *Light Waves in Complex Media: From Biological Tissues to Cold Atoms*. Sorbonne University Master LUMI Course Notes, 2019.
- [205] S. S. Chandrasekhar, *Radiative Transfer*. New York : Dover Publications, 1960.
- [206] A. P. Mosk, A. Lagendijk, G. Lerosey, and M. Fink, “Controlling waves in space and time for imaging and focusing in complex media,” *Nature Photonics*, vol. 6, pp. 283–292, May 2012.
- [207] “Optical Glass N-BK7 Optical Material.” <https://www.crystran.co.uk/optical-materials/optical-glass-n-bk7-and-others>.
- [208] E. Hecht, *Optics*. Boston: Pearson Education, Inc, 5 ed ed., 2017.
- [209] “The Correct Material for Infrared (IR) Applications.” <https://www.edmundoptics.com/knowledge-center/application-notes/optics/the-correct-material-for-infrared-applications>.

- [210] J. L. T. a. K. M. K. LLC, Janos Technology, “Common Infrared Optical Materials and Coatings: A Guide to Properties, Performance, and Applications.” https://www.photonics.com/Articles/Common_Infrared_Optical_Materials_and_Coatings_A/a25495.
- [211] “Zinc Selenide (ZnSe) Windows.” https://www.thorlabs.com/newgrouppage9.cfm?-objectgroup_id=3981.
- [212] “Sodium Chloride Windows | Edmund Optics.” <https://www.edmundoptics.com/f/sodium-chloride-nacl-windows/14170/>.
- [213] M. Leonetti, A. Grimaldi, S. Ghirga, G. Ruocco, and G. Antonacci, “Scattering Assisted Imaging,” *Scientific Reports*, vol. 9, p. 4591, Mar. 2019.
- [214] B. Choi, T. L. Ringold, and J. Kim, “Methods to Enhance Laser Speckle Imaging of High-Flow and Low-Flow Vasculature,” p. 8, 2012.
- [215] M. Khorasaninejad, W. T. Chen, A. Y. Zhu, J. Oh, R. C. Devlin, C. Roques-Carnes, I. Mishra, and F. Capasso, “Visible Wavelength Planar Metalenses Based on Titanium Dioxide,” *IEEE JOURNAL OF SELECTED TOPICS IN QUANTUM ELECTRONICS*, vol. 23, no. 3, p. 16, 2017.
- [216] G. Gohari, A. Mohammadi, A. Akbari, S. Panahirad, M. R. Dadpour, V. Fotopoulos, and S. Kimura, “Titanium dioxide nanoparticles (TiO₂ NPs) promote growth and ameliorate salinity stress effects on essential oil profile and biochemical attributes of *Dracocephalum moldavica*,” *Scientific Reports*, vol. 10, p. 912, Jan. 2020.
- [217] N. Jayarambabu, “Germination and Growth Characteristics of Mungbean Seeds (*Vigna radiata* L.) affected by Synthesized Zinc Oxide Nanoparticles,” *International Journal of Current Engineering and Technology*, vol. 4, p. 5, Oct. 2014.
- [218] P. Dubey, P. Sharma, and V. Kumar, “FTIR and GC–MS spectral datasets of wax from *Pinus roxburghii* Sarg. needles biomass,” *Data in Brief*, vol. 15, pp. 615–622, Dec. 2017.
- [219] “High transmission silicon for infrared optical applications - Sil’tronix Silicon Technologies.” <https://www.sil-tronix-st.com/en/news/High-transmission-silicon->

for-infrared-optical-applications.

- [220] “Surface Roughness Measurement—Parameters | Olympus.” <https://www.olympus-ims.com/en/metrology/surface-roughness-measurement-portal/parameters/>.
- [221] M. Planck and M. Masius, *The Theory of Heat Radiation*. Philadelphia, P. Blakiston’s Son & Co, [c1914].
- [222] M. Massoud, *Engineering Thermofluids: Thermodynamics, Fluid Mechanics, and Heat Transfer*. Springer Science & Business Media, Dec. 2005.
- [223] “Wayback Machine.” <https://web.archive.org/web/20090711135115/http://www.monarchserver.com/TableofEmissivity.pdf>, July 2009.
- [224] G. De Falco, G. Moggia, M. Sirignano, M. Commodo, P. Minutolo, and A. D’Anna, “Exploring Soot Particle Concentration and Emissivity by Transient Thermocouples Measurements in Laminar Partially Premixed Coflow Flames,” *Energies*, vol. 10, p. 232, Feb. 2017.
- [225] “Infrared Source IR-30 Series.” <https://scitec.uk.com/irsources/IR-3X-series>.
- [226] “Large Microscope Slides and Cover Glasses, Racks, Staining Dishes, Storage Boxes.” https://www.tedpella.com/histo_html/slides-large.aspx.
- [227] M. Rubin, “Optical properties of soda lime silica glasses,” *Solar Energy Materials*, vol. 12, pp. 275–288, Sept. 1985.
- [228] “Micro-Tec glass microscope slides.” <https://www.microtonano.com/Micro-Tec-glass-microscope-slides.php>.
- [229] S. Popova, T. Tolstykh, and V. Vorobev, “Optical characteristics of amorphous quartz in the 1400-200 cm⁻¹ region,” *Opt. Spectrosc*, vol. 33, pp. 444–445, 1972.
- [230] R. Kitamura, L. Pilon, and M. Jonasz, “Optical constants of silica glass from extreme ultraviolet to far infrared at near room temperature,” *Applied Optics*, vol. 46, pp. 8118–8133, Nov. 2007.
- [231] “Microscope Slides - Specialty Quartz, Petrographic, Plastic, Spot, Cavity.”

https://www.tedpella.com/histo_html/specialty-slides.aspx.

- [232] “IR Source IR-SiX Series.” <https://scitec.uk.com/irsources/IR-SiX-series>.
- [233] “IR-SX Series Silicon Nitride/Carbide Steady State IR sources.” <http://www.hawkeyetechnologies.com/source-selection/irsx/>.
- [234] H. A. Bechtel, E. A. Muller, R. L. Olmon, M. C. Martin, and M. B. Raschke, “Ultrabroadband infrared nanospectroscopic imaging,” *Proceedings of the National Academy of Sciences*, vol. 111, pp. 7191–7196, May 2014.
- [235] F. Huth, M. Schnell, J. Wittborn, N. Ocelic, and R. Hillenbrand, “Infrared-spectroscopic nanoimaging with a thermal source,” *Nature Materials*, vol. 10, pp. 352–356, May 2011.
- [236] K. Kim, S. Bittner, Y. Zeng, S. F. Liew, Q. Wang, and H. Cao, “Electrically pumped semiconductor laser with low spatial coherence and directional emission,” *Applied Physics Letters*, vol. 115, p. 071101, Aug. 2019.
- [237] H. Cao, R. Chriki, S. Bittner, A. A. Friesem, and N. Davidson, “Complex lasers with controllable coherence,” *Nature Reviews Physics*, vol. 1, pp. 156–168, Feb. 2019.
- [238] *Optical Interferometry for Biology and Medicine*.
- [239] A. R. Thompson, J. M. Moran, and G. W. Swenson, “Van Cittert–Zernike Theorem, Spatial Coherence, and Scattering,” in *Interferometry and Synthesis in Radio Astronomy* (A. R. Thompson, J. M. Moran, and G. W. Swenson Jr., eds.), Astronomy and Astrophysics Library, pp. 767–786, Cham: Springer International Publishing, 2017.
- [240] “Table of emissivity of various surfaces - transmetra.” https://www.transmetra.ch/images/transmetra_pdf/publikationen_literatur/pyrometrie-thermografie/emissivity_table.pdf.
- [241] W. Drexler and J. G. Fujimoto, eds., *Optical Coherence Tomography*. Cham: Springer International Publishing, 2015.
- [242] C. Akcay, P. Parrein, and J. P. Rolland, “Estimation of longitudinal resolution in optical coherence imaging,” *Applied Optics*, vol. 41, pp. 5256–5262, Sept. 2002.

- [243] A. Donges, “The coherence length of black-body radiation,” *European Journal of Physics*, vol. 19, pp. 245–249, May 1998.
- [244] N. Wiener, “Generalized harmonic analysis,” *Acta Mathematica*, vol. 55, pp. 117–258, Dec. 1930.
- [245] A. Khintchine, “Korrelationstheorie der stationären stochastischen Prozesse,” *Mathematische Annalen*, vol. 109, pp. 604–615, Dec. 1934.
- [246] R. J. Mathar, “Refractive index of humid air in the infrared: Model fits,” *Journal of Optics A: Pure and Applied Optics*, vol. 9, pp. 470–476, Apr. 2007.
- [247] S. P. S. P. Langley, *The "Bolometer"*. New York, The Society, 1881.
- [248] S. P. Langley, “The Bolometer and Radiant Energy,” *Proceedings of the American Academy of Arts and Sciences*, vol. 16, pp. 342–358, 1880.
- [249] G. Eppeldauer, A. L. Migdall, and C. L. Cromer, “Characterization of a High Sensitivity Composite Silicon Bolometer,” *Metrologia*, vol. 30, pp. 317–320, Jan. 1993.
- [250] “Bolometer,” *Wikipedia*, Aug. 2022.
- [251] D. Thombare and S. Verma, “Technological development in the Stirling cycle engines,” *Renewable and Sustainable Energy Reviews*, vol. 12, pp. 1–38, Jan. 2008.
- [252] T. Jitsufuchi, “Development of a cooled infrared camera for measuring volcanic SO₂ gas concentration and temperature distributions,” in *2021 IEEE International Geoscience and Remote Sensing Symposium IGARSS*, pp. 7860–7863, 2021.
- [253] G. B. Dalton, M. Caldwell, A. K. Ward, M. S. Whalley, G. Woodhouse, R. L. Edeson, P. Clark, S. M. Beard, A. M. Gallie, S. P. Todd, J. M. D. Strachan, N. N. Bezawada, W. J. Sutherland, and J. P. Emerson, “The VISTA infrared camera,” in *SPIE Astronomical Telescopes + Instrumentation* (I. S. McLean and M. Iye, eds.), (Orlando, Florida, USA), p. 62690X, June 2006.
- [254] K. C. Liddiard, “The active microbolometer: A new concept in infrared detection,” in *Microelectronics: Design, Technology, and Packaging*, vol. 5274, pp. 227–238, SPIE, Mar. 2004.

- [255] D. F. Murphy, A. Kennedy, M. Ray, R. Wyles, J. Wyles, J. F. Asbrock, C. Hewitt, D. V. Lue, T. Sessler, J. S. Anderson, D. Bradley, R. Chin, H. Gonzales, C. L. Pere, and T. Kostrzewa, "Resolution and sensitivity improvements for VOx microbolometer FPAs," in *Infrared Technology and Applications XXIX*, vol. 5074, pp. 402–413, SPIE, Oct. 2003.
- [256] "Microbolometer," *Wikipedia*, Nov. 2022.
- [257] C. Liu, J. Fu, Y. Hou, Q. Zhou, and D. Chen, "A Self-Calibration Method of Microbolometer With Vacuum Package," *IEEE Sensors Journal*, vol. 20, pp. 8570–8575, Aug. 2020.
- [258] "How are FLIR's microbolometer arrays packaged? Are they under vacuum? Why?." <https://www.flir.com/support-center/oem/how-are-flirs-microbolometer-arrays-packaged-are-they-under-vacuum-why/>.
- [259] D. Neikirk, J. Campbell, A. de Lozanne, H. Marcus, and B. Streetman, "FAR-INFRARED AND SUB-MILLIMETER MICROBOLOMETER DETECTORS," p. 4.
- [260] J.-W. Zha, D.-H. Wu, Y. Yang, Y.-H. Wu, R. K. Y. Li, and Z.-M. Dang, "Enhanced positive temperature coefficient behavior of the high-density polyethylene composites with multi-dimensional carbon fillers and their use for temperature-sensing resistors," *RSC Advances*, vol. 7, no. 19, pp. 11338–11344, 2017.
- [261] J. Li, C. Chang, X. Li, Y. Li, and G. Guan, "A New Thermal Controlling Material with Positive Temperature Coefficient for Body Warming: Preparation and Characterization," *Materials*, vol. 12, p. 1758, May 2019.
- [262] R. Jimenez, M. Moreno, A. Torres, A. Morales, A. Ponce, D. Ferrusca, J. Rangel-Magdaleno, J. Castro-Ramos, J. Hernandez-Perez, and E. Cano, "Fabrication of Microbolometer Arrays Based on Polymorphous Silicon–Germanium," *Sensors*, vol. 20, p. 2716, May 2020.
- [263] T. Zhou, Y. Zuo, K. Qiu, J. Zheng, and Q. Wang, "Potential of Ti doped hydrogenated amorphous Si film with suitable resistivity and high TCR for microbolometer applications," *Vacuum*, vol. 119, pp. 30–33, Sept. 2015.

- [264] B. Wang, J. Lai, H. Li, H. Hu, and S. Chen, "Nanostructured vanadium oxide thin film with high TCR at room temperature for microbolometer," *Infrared Physics & Technology*, vol. 57, pp. 8–13, Mar. 2013.
- [265] J. T. J. T. Timpe, *Measurement and Analysis of 1/f Noise in Uncooled Microbolometers*. Thesis, Massachusetts Institute of Technology, 2000.
- [266] M. Alhussein and S. I. Haider, "Simulation and Analysis of Uncooled Microbolometer for Serial Readout Architecture," *Journal of Sensors*, vol. 2016, pp. 1–13, 2016.
- [267] W. J. Parrish and J. T. Woolaway II, "Improvements in uncooled systems using bias equalization," in *AeroSense '99* (B. F. Andresen and M. Strojnik, eds.), (Orlando, FL), p. 748, July 1999.
- [268] F. Niklaus, C. Vieider, and H. Jakobsen, "MEMS-based uncooled infrared bolometer arrays: A review," in *Photonics Asia 2007* (J.-C. Chiao, X. Chen, Z. Zhou, and X. Li, eds.), (Beijing, China), p. 68360D, Nov. 2007.
- [269] M. Kohin and N. R. Butler, "Performance limits of uncooled VO_x microbolometer focal plane arrays," in *Defense and Security* (B. F. Andresen and G. F. Fulop, eds.), (Orlando, FL), p. 447, Aug. 2004.
- [270] C. M. Hanson, "Implications of 1/f noise in uncooled thermal imaging," in *Infrared Technology and Applications XLIV* (G. F. Fulop, C. M. Hanson, P. R. Norton, B. F. Andresen, and J. L. Miller, eds.), (Orlando, United States), p. 51, SPIE, May 2018.
- [271] H. Ryu, S. Kwon, S. Cheon, S. M. Cho, W. S. Yang, and C. A. Choi, "Evaluation of 1/f Noise Characteristics for Si-Based Infrared Detection Materials," *ETRI Journal*, vol. 31, no. 6, pp. 703–708, 2009.
- [272] J. C. Mather, "Bolometer noise: Nonequilibrium theory," *Applied Optics*, vol. 21, pp. 1125–1129, Mar. 1982.
- [273] J. B. Johnson, "Thermal Agitation of Electricity in Conductors," *Physical Review*, vol. 32, pp. 97–109, July 1928.
- [274] H. Nyquist, "Thermal Agitation of Electric Charge in Conductors," *Physical Review*,

vol. 32, pp. 110–113, July 1928.

- [275] B. Jacobsen, “Thermal noise in multi-section radio links,” *Proceedings of the IEE - Part C: Monographs*, vol. 105, pp. 139–150(11), Mar. 1958.
- [276] J. Barry, E. Lee, and D. Messerschmitt, *Digital Communication*. Springer US, 2012.
- [277] N. Émond, A. Hendaoui, and M. Chaker, “Low resistivity $W_x V_{1-x} O_2$ -based multilayer structure with high temperature coefficient of resistance for microbolometer applications,” *Applied Physics Letters*, vol. 107, p. 143507, Oct. 2015.
- [278] W. A. Radford, D. F. Murphy, J. A. Finch, K. Hay, A. Kennedy, M. Ray, A. A. Sayed, J. Wyles, R. Wyles, J. B. Varesi, E. A. Moody, and F. Cheung, “Sensitivity improvements in uncooled microbolometer FPAs,” in *AeroSense '99* (B. F. Andresen and M. Strojnik, eds.), (Orlando, FL), p. 119, July 1999.
- [279] “FLIR A655sc High-Resolution Science Grade LWIR Camera | Teledyne FLIR.” <https://www.flir.com/products/a655sc?vertical=rd+science&segment=solutions>.
- [280] V. Parigi, E. Perros, G. Binard, C. Bourdillon, A. Maître, R. Carminati, V. Krachmalnicoff, and Y. De Wilde, “Near-field to far-field characterization of speckle patterns generated by disordered nanomaterials,” *Optics Express*, vol. 24, p. 7019, Apr. 2016.
- [281] H. Nyquist, “Certain Topics in Telegraph Transmission Theory,” *Transactions of the American Institute of Electrical Engineers*, vol. 47, pp. 617–644, Apr. 1928.
- [282] C. Shannon, “Communication in the Presence of Noise,” *Proceedings of the IRE*, vol. 37, pp. 10–21, Jan. 1949.
- [283] S. Ashraf, I. Niskanen, B. Kanyathare, E. Vartiainen, C. Mattsson, R. Heikkilä, and G. Thungström, “Determination of complex refractive index of SU-8 by Kramers–Kronig dispersion relation method at the wavelength range 2.5–22.0 μm ,” *Journal of Quantitative Spectroscopy and Radiative Transfer*, vol. 224, pp. 309–311, Feb. 2019.
- [284] S. Maruo, O. Nakamura, and S. Kawata, “Three-dimensional microfabrication with two-photon-absorbed photopolymerization,” *Optics Letters*, vol. 22, pp. 132–134,

Jan. 1997.

- [285] G. Tessier, S. Holé, and D. Fournier, “Quantitative thermal imaging by synchronous thermorefectance with optimized illumination wavelengths,” *Applied Physics Letters*, vol. 78, pp. 2267–2269, Apr. 2001.
- [286] V. Boominathan, J. T. Robinson, L. Waller, and A. Veeraraghavan, “Recent advances in lensless imaging,” *Optica*, vol. 9, pp. 1–16, Jan. 2022.
- [287] J.-J. Greffet and R. Carminati, “Relationship between the near-field speckle pattern and the statistical properties of a surface,” *Ultramicroscopy*, vol. 61, pp. 43–50, 1995.
- [288] J. Laverdant, S. Buil, B. Bérini, and X. Quélin, “Polarization dependent near-field speckle of random gold films,” *Physical Review B*, vol. 77, p. 165406, Apr. 2008.
- [289] J.-J. Greffet, “Scattering of electromagnetic waves by rough dielectric surfaces,” *Physical Review B*, vol. 37, pp. 6436–6441, Apr. 1988.
- [290] J.-J. Greffet and R. Carminati, “Image formation in near-field optics,” *Progress in Surface Science*, vol. 56, pp. 133–237, Nov. 1997.

Appendix A

Analytical Modelling of Speckle

This appendix presents the key ideas relating the surface topography of a random rough surface to the near-field speckle intensity using first-order perturbation theory. The theory was developed by Greffet and Carminati [287], and has been used for the analysis of the near-field speckle properties random gold films by Laverdant et al. [288].

A.1 Speckle generation due to scattering from a rough surface

The scattering of light during transmission through random rough surfaces results in a complex intensity pattern. This intensity pattern displays irregular fluctuations, and is known as a speckle. The near-field speckle pattern originates from the residual roughness of the scattering medium's surface. A direct relationship between the near-field speckle pattern and the statistical properties of a random rough scattering surface was shown by Greffet and Carminati [287].

A.1.1 Scatterer topography and correlation function

The correlation function is first defined for the near-field intensity, and then it is shown that the power spectral density of the intensity can be obtained by multiplying the power spectral density of the surface topography by a transfer function, whose explicit form is derived. Speckle contrast is also shown to be proportional to the root-mean-squared (rms)

roughness of the surface, and that the contrast decreases when either the temporal or spatial coherence of the illuminating beam is reduced.

A random rough surface is defined as a surface whose height $z = S(\mathbf{r}_{\parallel})$ at a point \mathbf{r}_{\parallel} is a random variable with zero mean (i.e. $\langle S(\mathbf{r}_{\parallel}) \rangle = 0$) and a Gaussian probability density function. The rms height is called the roughness, δ , and the correlation function is:

$$\langle S(\mathbf{r}_{\parallel})S(\mathbf{r}'_{\parallel}) \rangle = \delta^2 C(|\mathbf{r}'_{\parallel} - \mathbf{r}_{\parallel}|) \quad (\text{A.1})$$

The surface is assumed to be isotropic, stationary and random, characterized by the correlation length a , with the correlation function depending only on $|\mathbf{r}'_{\parallel} - \mathbf{r}_{\parallel}|$.

Due to the translational invariance of the surface, the Fourier transform is defined on a finite area A of the surface profile $S(\mathbf{r}_{\parallel})$. The Fourier transforms of $S_A(\mathbf{r}_{\parallel})$ and $C(|\mathbf{r}'_{\parallel} - \mathbf{r}_{\parallel}|)$ are:

$$S_A(\mathbf{r}_{\parallel}) = \frac{1}{4\pi^2} \int d(\mathbf{k}_{\parallel}) S_A(\mathbf{k}_{\parallel}) e^{-i\mathbf{k}_{\parallel} \cdot \mathbf{r}_{\parallel}} \quad (\text{A.2})$$

$$C(|\mathbf{u}|) = \int d(\mathbf{k}_{\parallel}) g(\mathbf{k}_{\parallel}) e^{-i\mathbf{k}_{\parallel} \cdot \mathbf{u}} \quad (\text{A.3})$$

The Weiner-Khinchin theorem relates the Fourier transform of the correlation function, $g(\mathbf{k}_{\parallel})$, to the power spectral density of the surface:

$$\lim_{A \rightarrow \infty} \frac{\langle S_A(\mathbf{k}_{\parallel}) S_A(-\mathbf{k}_{\parallel}) \rangle}{A} = 4\pi^2 \delta^2 g(\mathbf{k}_{\parallel}) \quad (\text{A.4})$$

A.1.2 First-order perturbation theory to compute transmitted electric field

The near-field can be computed using a first-order perturbation approach if the ratio $\delta/\lambda < 0.05$. To first-order in δ/λ , the scattered field is linear to the surface spectrum. The scattered field then itself is a random variable, with the fluctuations in the near-field intensity

giving rise to a near-field speckle. The near-field speckle originates from random intensity variations due to the random roughness of the surface, in contrast to a far-field speckle which has universal statistical properties.

We consider an incident wave E_{inc} coming from $z < S(x, y)$, $\varepsilon = \varepsilon_2$ illuminating an interface separating two dielectric media. The transmitted wave E_t in $z > S(x, y)$, $\varepsilon = \varepsilon_1$ is expanded on a plane wave basis:

$$\mathbf{E}_t(\mathbf{r}) = \int d(\mathbf{k}_{\parallel}) \mathbf{e}_t(\mathbf{k}_{\parallel}) e^{i(\mathbf{k}_{\parallel} \cdot \mathbf{r}_{\parallel}) + \gamma_1 z} \quad (\text{A.5})$$

where, $\gamma_1 = \sqrt{\varepsilon_1 \omega^2 / c^2 - \mathbf{k}_{\parallel}^2}$ with $Im(\gamma_1) > 0$ & $Re(\gamma_1) > 0$, $\mathbf{r} = (x, y, z)$ and $\mathbf{r} = (x, y)$. We need to find the unknown $\mathbf{e}_t(\mathbf{k}_{\parallel})$. As $\nabla \cdot E = 0$, $\mathbf{e}_t(\mathbf{k}_{\parallel}) \cdot \mathbf{k}_{\parallel} = 0$, and only two components are needed to describe the field, \mathbf{e}_t can be split into the two s- and p-components as:

$$\mathbf{e}_t(\mathbf{k}_{\parallel}) = e_{t,s}(\mathbf{k}_{\parallel}) \mathbf{a}_{t,s}(\mathbf{k}_{\parallel}) + e_{t,p}(\mathbf{k}_{\parallel}) \mathbf{a}_{t,p}(\mathbf{k}_{\parallel}) \quad (\text{A.6})$$

where,

$$\mathbf{a}_{t,s}(\mathbf{k}_{\parallel}) = \mathbf{a}_z \times \mathbf{k}_{\parallel} / |\mathbf{k}_{\parallel}| \quad (\text{A.7})$$

$$\mathbf{a}_{t,p}(\mathbf{k}_{\parallel}) = \mathbf{a}_{t,s}(\mathbf{k}_{\parallel}) \times \frac{\mathbf{k}_{\parallel} + \gamma_1 \mathbf{a}_z}{n_1 k_0} \quad (\text{A.8})$$

with, $n_1 = \sqrt{\varepsilon_1}$, $Im(n_1) > 0$ and $\mathbf{a}_z = \hat{z}$.

To get a perturbative solution to Equation A.5, the field is expanded in powers of δ/λ :

$$\mathbf{e}_t(\mathbf{k}_{\parallel}) = \mathbf{e}_t^{(0)}(\mathbf{k}_{\parallel}) + \mathbf{e}_t^{(1)}(\mathbf{k}_{\parallel}) \quad (\text{A.9})$$

Using the boundary condition [289], the Fresnel transmission factors for the zero-order

field are recovered:

$$\begin{bmatrix} e_{t,s}^{(0)} \\ e_{t,p}^{(0)} \end{bmatrix} = \begin{bmatrix} \frac{2\gamma_2^{inc}}{\gamma_1^{inc} + \gamma_2^{inc}} & 0 \\ 0 & \frac{2n_1 n_2 \gamma_2^{inc}}{\varepsilon_1 \gamma_2^{inc} + \varepsilon_2 \gamma_1^{inc}} \end{bmatrix} \begin{bmatrix} e_s^{inc} \\ e_p^{inc} \end{bmatrix} \quad (\text{A.10})$$

where, $\gamma_2 = \sqrt{\varepsilon_2 \omega^2 / c^2 - \mathbf{k}_{\parallel}^2}$ with $Im(\gamma_2) > 0$ & $Re(\gamma_2) > 0$. The first-order contribution can be written as:

$$\mathbf{e}_t^{(1)}(\mathbf{k}_{\parallel}) = S(\mathbf{k}_{\parallel}^{inc} - \mathbf{k}_{\parallel}) L(\mathbf{k}_{\parallel}, \mathbf{k}_{\parallel}^{inc}) \mathbf{e}_{inc} \quad (\text{A.11})$$

where, L is a linear operator connecting the s- and p-components of the electric field:

$$\begin{bmatrix} e_{ts}^{(1)}(\mathbf{k}_{\parallel}) \\ e_{tp}^{(1)}(\mathbf{k}_{\parallel}) \end{bmatrix} = i \frac{\gamma_2 - \gamma_1}{4\pi^2} S(\mathbf{k}_{\parallel}^{inc} - \mathbf{k}_{\parallel}) R^{-1}(\mathbf{k}_{\parallel}, \mathbf{k}_{\parallel}) R(\mathbf{k}_{\parallel}, \mathbf{k}_{\parallel}^{inc}) \begin{bmatrix} t_s e_s^{inc} \\ t_p e_p^{inc} \end{bmatrix} \quad (\text{A.12})$$

where, the operator R is:

$$R(\mathbf{k}_{\parallel}, \mathbf{k}'_{\parallel}) = -n_2^2 \frac{\omega^2}{c^2} \begin{bmatrix} \hat{\mathbf{k}}_{\parallel} \cdot \hat{\mathbf{k}}'_{\parallel} & \frac{\gamma_1(\hat{\mathbf{k}}'_{\parallel})}{n_1 \omega / c} \hat{\mathbf{k}}'_{\parallel} \cdot (\mathbf{a}_z \times \hat{\mathbf{k}}_{\parallel}) \\ \frac{\gamma_2(\hat{\mathbf{k}}_{\parallel})}{n_2 \omega / c} \hat{\mathbf{k}}_{\parallel} \cdot (\mathbf{a}_z \times \hat{\mathbf{k}}'_{\parallel}) & \frac{\gamma_1(\hat{\mathbf{k}}'_{\parallel}) \gamma_2(\hat{\mathbf{k}}_{\parallel}) (\hat{\mathbf{k}}'_{\parallel} \cdot \hat{\mathbf{k}}_{\parallel}) + |\mathbf{k}_{\parallel}| |\mathbf{k}'_{\parallel}|}{n_1 n_2 \omega^2 / c^2} \end{bmatrix} \quad (\text{A.13})$$

The expression of the scattered field is finally obtained by introducing [Equation A.11](#) in [Equation A.5](#):

$$\mathbf{E}_t^{(1)}(\mathbf{r}) = \int d(\mathbf{k}_{\parallel}) S(\mathbf{k}_{\parallel}^{inc} - \mathbf{k}_{\parallel}) e^{i\gamma_1 z} \left\{ L(\mathbf{k}_{\parallel}, \mathbf{k}_{\parallel}^{inc}) \mathbf{e}_{inc} \right\} e^{i(\mathbf{k}_{\parallel} \cdot \mathbf{r}_{\parallel})} \quad (\text{A.14})$$

A.1.3 Scatterer topography and speckle contrast

The near-field intensity is the square modulus of the electric field:

$$I(\mathbf{r}_{\parallel}, z) = |\mathbf{E}_t^{(0)}(\mathbf{r}_{\parallel}, z) + \mathbf{E}_t^{(1)}(\mathbf{r}_{\parallel}, z)|^2 \quad (\text{A.15})$$

and to first order in δ/λ :

$$I(\mathbf{r}_{\parallel}, z) = |\mathbf{E}_t^{(0)}(\mathbf{r}_{\parallel}, z)|^2 + 2\text{Re}\{\mathbf{E}_t^{(1)}(\mathbf{r}_{\parallel}, z) \cdot \mathbf{E}_t^{(0)*}(\mathbf{r}_{\parallel}, z)\} \quad (\text{A.16})$$

which can be written as a constant zero-order term and a first-order term in δ/λ :

$$I(\mathbf{r}_{\parallel}, z) = I^{(0)}(z) + I^{(1)}(\mathbf{r}_{\parallel}, z) \quad (\text{A.17})$$

and which shows that the zero-order term has no contribution in image modulation when constant height scans are carried out.

In order to relate the near-field intensity's correlation function to the spectral power density of the surface, we first write the intensity correlation function at constant height:

$$\langle I(\mathbf{r}_{\parallel})I(\mathbf{r}_{\parallel} + \mathbf{u}) \rangle = \langle I^{(0)}I^{(0)} \rangle + \langle I^{(1)}(\mathbf{r}_{\parallel})I^{(1)}(\mathbf{r}_{\parallel} + \mathbf{u}) \rangle \quad (\text{A.18})$$

Neglecting the constant zero-order term and the cross-term contribution, and using [Equation A.16](#), [Equation A.14](#) & [Equation A.4](#), we get:

$$\langle I^{(1)}(\mathbf{r}_{\parallel})I^{(1)}(\mathbf{r}_{\parallel} + \mathbf{u}) \rangle = \text{Re}\left\{ \int \delta^2 g(\mathbf{k}_{\parallel}) F(\mathbf{k}_{\parallel}) e^{i(\mathbf{k}_{\parallel} \cdot \mathbf{u})} d(\mathbf{k}_{\parallel}) \right\} \quad (\text{A.19})$$

where, $F(\mathbf{k}_{\parallel})$ is a filter function that depends on the polarization, observation height and

the incident field wavevector, given by:

$$\begin{aligned}
F(\mathbf{k}_{\parallel}) = & 2[\mathbf{e}_t^{(0)*} \cdot L(\mathbf{k}_{\parallel}^{inc} - \mathbf{k}_{\parallel}, \mathbf{k}_{\parallel}^{inc}) \mathbf{e}_{inc}] e^{i\gamma_1(\mathbf{k}_{\parallel}^{inc} - \mathbf{k}_{\parallel})z} \\
& \left\{ \mathbf{e}_t^{(0)} \cdot L^*(\mathbf{k}_{\parallel}^{inc} - \mathbf{k}_{\parallel}, \mathbf{k}_{\parallel}^{inc}) \mathbf{e}_{inc}^* e^{-2Im[\gamma_1(\mathbf{k}_{\parallel}^{inc})] - i\gamma_1^*(\mathbf{k}_{\parallel}^{inc} - \mathbf{k}_{\parallel})z} \right. \\
& \left. + \mathbf{e}_t^{(0)*} \cdot L^*(\mathbf{k}_{\parallel}^{inc} + \mathbf{k}_{\parallel}, \mathbf{k}_{\parallel}^{inc}) \mathbf{e}_{inc} e^{-2i\gamma_1^*(\mathbf{k}_{\parallel}^{inc})z + i\gamma_1(\mathbf{k}_{\parallel}^{inc} + \mathbf{k}_{\parallel})z} \right\}
\end{aligned} \tag{A.20}$$

The filter function depends both on the incident wave vector and the incident frequency, conveying all the information about the illuminating beam's spatial and temporal coherence.

A useful characterization of a speckle is the ratio between the fluctuations of the intensity and the average intensity. This is the speckle contrast, defined as:

$$C_I = \frac{\sqrt{\langle I^2 \rangle - \langle I \rangle^2}}{\langle I \rangle} = \frac{\sqrt{\langle I^{(1)2} \rangle}}{I^{(0)}} \tag{A.21}$$

Putting $\mathbf{u} = 0$, we obtain $\langle I^{(1)} I^{(1)} \rangle$ and it is evident that the speckle contrast is proportional to the roughness δ .

Using this perturbative approach, a speckle simulated from a random rough surface profile does not turn out to be isotropic. This is due to the dependence of $F(\mathbf{k}_{\parallel})$ on the direction of \mathbf{k}_{\parallel} , whereas the power spectral density depends only on the modulus of \mathbf{k}_{\parallel} .

Experimentally, it is known that the speckle contrast decreases as the temporal coherence length of the illumination decreases, and this can be simulated by an average filter function $F(\mathbf{k}_{\parallel})$ integrated over the spectrum of the source. Simulations show that the speckle contrast also reduces similarly as the spatial coherence is reduced.

From equation 2.25, we know that the speckle grain size is proportional to the wavelength of the incident light. In our case, we consider the reference wavelength to be 10 μm , which is also the order of magnitude of the speckle grain size. We also know that under certain conditions of the validity of first-order perturbation theory to model scattering on rough surfaces, the speckle contrast is linearly proportional to the roughness of the scattering medium [287] [290]. We chose to work with a surface scatterer instead of a volume scat-

terer so as to draw from previous work carried out in the visible regime [51] using thin diffusers which have a higher angular memory effect, as discussed in Section 2.2.2.3.

RÉSUMÉ

Le rayonnement infrarouge à ondes longues (LWIR), entre 7 et 14 μm , permet l'imagerie passive et constitue une gamme spectrale cruciale pour la spectroscopie. L'imagerie infrarouge (IR) a de nombreuses applications dans les domaines de la thermographie, de la détection aérienne et atmosphérique, de la détection des défauts et des tests médicaux non invasifs. Les motifs de tavelures, ou "speckle", permettent de détecter la phase ou l'intensité en utilisant des milieux diffusants complexes - aux longueurs d'onde visibles et infrarouges. Nous avons mis au point une nouvelle configuration d'imagerie du front d'onde, en utilisant un milieu diffusif mince et une caméra microbolométrique non refroidie travaillant dans la gamme LWIR. En exploitant le fort effet mémoire de diffuseurs minces, les déformations locales de la figure de speckle permettent de remonter à une information quantitative sur les gradients locaux de la phase optique. Ceux-ci sont ensuite intégrés en deux dimensions pour reconstruire le profil du front d'onde. Nous avons démontré avec succès la reconstruction d'un front d'onde LWIR dans des échantillons optiques infrarouges, allant de lentilles optiques et jusqu'à des échantillons de phase complexes. Le dispositif expérimental et la technique sont caractérisés, en gardant à l'esprit leur utilité pour des applications futures prometteuses dans l'imagerie à travers des milieux visuellement non transparents tels que les semi-conducteurs, les surfaces nano-électroniques et les optiques pour l'infrarouge.

MOTS CLÉS

Imagerie de phase, Imagerie infrarouge, Imagerie de front d'onde, Milieux complexes

ABSTRACT

Long wave infrared (LWIR) radiation between 7-14 μm allows passive imaging and is the fingerprint region for spectroscopy. Infrared (IR) imaging has wide-ranging applications in thermography, airborne atmospheric sensing, fault detection, and non-invasive medical testing. However, existing cameras are only sensitive to the amplitude, but not to the phase of IR radiation. The technique of speckle imaging enables the detection of phase or intensity through complex scattering media - at visible and IR wavelengths. We have developed a novel broadband LWIR speckle imaging configuration for wavefront sensing, utilizing a thin diffusive medium and an uncooled microbolometric camera. Taking advantage of the large angular memory effect of the diffuser, deformations in the speckle image can be ascribed to local variations in the phase of the impinging wavefront. The spatial shifts of the speckle grains in the images are registered using a rapid diffeomorphic image registration algorithm, generating a high-resolution mapping of the local phase gradients. The local phase gradients are then integrated in 2-D to reconstruct the wavefront profile. We have successfully demonstrated thermal wavefront reconstruction using LWIR speckle imaging in infrared optical samples, ranging from optical lenses to fabricated complex phase samples. The experimental setup and technique are characterized, keeping in mind its utility for promising future applications in imaging through visually non-transparent media like semiconductor wafers, engineered nano-electronic surfaces, and infrared optics.

KEYWORDS

Phase imaging, Infrared imaging, Wavefront sensing, Complex media